

A Unified Probabilistic Assessment of Wind Reserves for Islanded Microgrids

© Maxwell L. Little

A Thesis submitted to the School of Graduate Studies in partial fulfillment of the requirements for the degree of Masters of Engineering

Department of Electrical Engineering

School of Graduate Studies

Faculty of Engineering and Applied Science

Memorial University of Newfoundland

October 2017

St. John's Newfoundland and Labrador

Abstract

This thesis presents an analytical and numerical framework for the unified probabilistic assessment of wind reserves with a focus on the applications of wind generation in islanded microgrids. A multivariate nonparametric kernel density estimation algorithm is proposed to generate probabilistic models of a site's wind resource, electrical demand and the performance of installed wind generation. These models are numerically combined to evaluate the capability of wind generation to act as a dynamic reserve by predicting its performance when used for demand response, secondary generation and frequency regulation in an islanded microgrid. The proposed modeling framework captures multivariate cross-correlation, nonstationary environmental and load behavior, as well as multimodality in their underlying probability distributions. A case study is conducted using field data from Cartwright in order to validate the proposed algorithms. The case study results include probabilistic predictions of wind generation effectiveness for varying load profiles and generation capacity. PLEXIM simulation software is used to implement a model microgrid to demonstrate the integration of wind generation and its regulatory capabilities. The proposed algorithm has applications in power system planning and operation, and it provides probabilistic data for use in energy management and optimization of microgrids.

Acknowledgements

I wish to acknowledge the academic and financial support of my supervisor Dr. Kevin Pope. I am also grateful to Dr. John Quaiocoe for his technical advice.

I acknowledge S.F. Rabbi for his personal and professional support as I navigated graduate school for the first time. I also send a heartfelt thank you to my parents (Lloyd and Linda Little) as well as my sister Kaitlyn. Your support throughout my program is appreciated - I would not have reached this point otherwise.

Table of Contents

List of Figures and Tables	viii
Chapter 2	viii
Chapter 3	ix
Chapter 4	x
Chapter 5	xii
Chapter 6	xiv
Nomenclature	xvii
Chapter 1: Introduction	1
1.1 Thesis Objectives	4
1.2 List of Publications	4
1.3 Thesis Organization	5
Chapter 2: Analysis and Probabilistic Modeling of Wind Resources.....	9
2.1: Introduction.....	9
2.2: Wind Resource Modeling – Overview	10
2.2.1: Wind Turbine Behavior	12
2.3: Probabilistic Modeling of Wind Velocity.....	16

2.4: Bivariate Modeling	19
2.5: Analysis of Nonstationary Behavior	23
2.6: Frequency Domain Analysis	26
2.6.1: The Discrete-Time Fourier Transform	29
2.6.2: Statistical Analysis of Spectral Residuals	31
2.6.3: Nonstationary Feature Identification	39
2.7: Multidimensional Wind Resource Modeling	40
2.7.1: Multivariate Optimized Nonparametric Probabilistic Modeling	42
2.7.2: A Time-Variant Bivariate Wind Resource Model	46
2.7.3: Model Validation	50
2.8: Conclusions	54
Chapter 3: Probabilistic Assessment of Wind Reserves	56
3.1: Introduction	56
3.2: Probabilistic Demand Modeling	58
3.2.1: Overview of Electrical Demand	59
3.2.2: Stationary Probabilistic Load Modeling	62
3.2.3: Nonstationary Behavior of Load Profiles	64
3.2.4: Frequency Domain Analysis	67
3.2.5: Time-Variant Probabilistic Load Modeling	70

3.2.6: Probabilistic Assessment of Load Profiles	77
3.3: Probabilistic Wind Reserve Assessment.....	87
3.3.1: Wind Turbine Power Output Modeling	87
3.3.2: Probabilistic Load Pickup.....	92
3.4: Applications of Wind Reserves	101
3.5: Conclusions.....	103
Chapter 4: Modeling, Simulation and Control of Islanded Microgrids	104
4.1: Introduction.....	104
4.2: Microgrid Topology.....	105
4.2.1: Overview of Distributed Generation.....	105
4.2.2: Microgrid Implementation – AC and DC	107
4.2.3: Islanding.....	109
4.3: Analysis, Modeling and Control of Microgrids.....	111
4.3.1: Grid Forming in Microgrids.....	112
4.3.2: Grid Synchronization and Interconnection of Distributed Generation	118
4.3.4: Microgrid Support using Distributed Generation	132
4.4: Integration of Wind Generation into Islanded Microgrids	136
4.4.1: Overview of Wind Turbine Generators	136
4.4.2: Modeling and Control of Direct-Drive PMSG Wind Turbines	140

4.4.3: Grid Interconnection using Back to Back Power Converters	146
4.5: Conclusions.....	151
Chapter 5: Cartwright – A Case Study: Resource Modeling	152
5.1: Introduction.....	152
5.2: The Wind Resource Model	154
5.3: Wind Reserve Assessment.....	175
5.3.1: The Load Profile	175
5.3.2: Probabilistic Reserve Modeling.....	194
5.4: Conclusions.....	222
Chapter 6: Cartwright – A Case Study: PLEXIM Implementation	223
6.1: Introduction.....	223
6.2: Implementation of Demand Response in a Microgrid.....	224
6.3: Wind Turbine Interconnection in PLEXIM.....	245
6.4: Conclusions.....	256
7.1 Thesis Contribution.....	263
7.2: Future Work.....	264
References.....	265
Chapter 1	265
Chapter 2.....	265

Chapter 3	267
Chapter 4	268

List of Figures and Tables

Chapter 2

Figure 2.1: A Nonparametric Distribution Wind Velocity Model	19
Figure 2.2: A probabilistic model of Air Density	22
Figure 2.3: Nonparametric modeling of wind velocity subsets	24
Table 2.1: Distribution Moments of Wind Velocity Subsets	26
Figure 2.4: A Flow Chart of the Frequency Domain Analysis Algorithm	28
Figure 2.5: Single-Sided Magnitude Spectrum of Wind Velocity	30
Figure 2.6: Probability Distribution Model of Magnitude Residuals	33
Figure 2.7: Logarithmic Mean of the Wind Velocity Magnitude Spectrum	35
Table 2.2: Statistically Significant Magnitude Residuals	36
Figure 2.8: Magnitude Residual Frequency Autocorrelation	37
Figure 2.9: Spectrally Identified Variance Signals	38
Figure 2.10: Simple Joint Wind/Density Probabilistic Model	40
Figure 2.11: Wind/Density Correlation Distribution	41
Figure 2.12: Effects of Bandwidth on Kernel Density Estimators	44

Figure 2.13: A Bivariate Probabilistic Wind/Density Model	45
Figure 2.14: The Bivariate Wind Resource Model	48
Figure 2.15: A time-variant model of site wind power density	49
Figure 2.16: Model Correlations	52
Figure 2.17: Distribution of Correlation Coefficients of Probabilistic Models	53

Chapter 3

Figure 3.1: Sample Demand Data	59
Figure 3.2: Demand Probability Distribution Models	62
Table 3.1: Stationary Probabilistic Load Model Prediction Errors	64
Figure 3.3: Probability Distributions of Demand Subsets	65
Table 3.2: Distribution Moments of Load Subsets	66
Figure 3.4: Demand Amplitude Spectrum	68
Figure 3.5: Seasonal and Diurnal Demand Variance	69
Figure 3.6: Probabilistic Demand Distribution	74
Table 3.3: General Demand Data Probabilistic Prediction Statistics	75

Figure 3.7: Probability Distribution of Prediction Statistics	76
Table 3.4: Demand Subset Probabilistic Prediction Statistics	77
Figure 3.8: An Example Demand CDF	78
Figure 3.9: Microgrid Load Profiles	79
Figure 3.10: Expected Values	82
Figure 3.11: Probabilistic Demand Models	84
Figure 3.12: Expected Value of Secondary Demand	85
Figure 3.13: Normalized Probabilistic Wind Turbine Output	90
Figure 3.14: Expected Wind Turbine Capacity Factor	92
Figure 3.15: Probabilistic Comparisons of Demand and Wind Generation	96
Figure 3.16: Energy Balance Distribution (250 kW Generation)	99
Figure 3.17: Energy Balance Distribution (500 kW Generation)	100

Chapter 4

Figure 4.1: Distributed Generation	106
Figure 4.2: (a) AC and (b) DC Microgrid Topologies	108

Figure 4.3: (a) Grid Connected vs. (b) Islanded Microgrids	110
Figure 4.4: Microgrid Simulation Topology in PLEXIM	112
Figure 4.5: Grid Forming Diesel Generator	114
Figure 4.6: Diesel Generator Excitation Controller	117
Figure 4.7: Diesel Engine Governor	118
Figure 4.8: SOGI Configuration	120
Figure 4.9: The SOGI-QSG	120
Figure 4.10: Gain-Normalized FLL Configuration in PLEXIM	121
Figure 4.11: DSOGI-FLL with PNSG in PLEXIM	123
Figure 4.12: PLEXIM Implementation of the Instantaneous Power Theory	126
Figure 4.13: VSI Controller Architecture	126
Figure 4.14: VSI Current Controller	127
Figure 4.15: Distributed Generation Interconnection Topology	128
Figure 4.16: Voltage and Frequency Droop Regulation in PLEXIM	134
Figure 4.17: Wind Turbine Types	138
Figure 4.18: PMSG Control and Modeling Topology in PLEXIM	141
Figure 4.19: Q-axis stator current controller in PLEXIM	143

Figure 4.20: Dynamic Wind Turbine Model in PLEXIM	146
Figure 4.21: Back-to-Back Converter Architecture in PLEXIM	147
Figure 4.22: DC-Link Voltage Controller in PLEXIM	150

Chapter 5

Figure 5.1: Cartwright Microgrid Architecture	154
Figure 5.2: Probabilistic Wind Resource Model for Cartwright	158
Figure 5.3: Cartwright's Wind Power Density	160
Figure 5.4: Probabilistic Power Output of the NPS-100c-21 in Cartwright	163
Figure 5.5: Probability of Quiescent Operation – NPS-100c-21 at Cartwright	165
Figure 5.6: Probabilistic Power Output of the NPS-100c-24 in Cartwright	(a) 166
	(b) 167
	(c) 168
	(d) 169
Figure 5.7: Probability of Quiescent Operation – NPS-100c-24 at Cartwright	171
Figure 5.8: Expected Capacity Factor	(a) 172

	(b)	174
Figure 5.9: Cartwright Demand Distribution	(a)	176
	(b)	177
	(c)	178
	(d)	179
Figure 5.10: Base, Secondary and Peak Demand in Cartwright	(a)	181
	(b)	182
	(c)	184
	(d)	185
Figure 5.11: Secondary Demand Distribution in Cartwright	(a)	186
	(b)	187
	(c)	188
	(d)	289
Figure 5.12: Peak Demand Distribution in Cartwright	(a)	290
	(b)	291
	(c)	292
	(d)	293

Figure 5.13: Power Balance Distribution in Cartwright – NPS-100c-21	296
Figure 5.14: Power Balance Distribution in Cartwright – NPS-100c-24	298
Figure 5.15: Power Balance Distribution in Cartwright – NPS-100c-21 (500 kW)	200
Figure 5.16: Power Balance Distribution in Cartwright – NPS-100c-24 (500 kW)	202
Figure 5.17: Probability of Meeting Secondary Reserve Requirements (1)	203
Figure 5.18: Probability of Meeting Secondary Reserve Requirements (2)	207
Figure 5.19: Peak Power Balance Distribution – NPS-100c-21	210
Figure 5.20: Peak Power Balance Distribution – NPS-100c-24	212
Figure 5.21: Peak Power Balance Distribution – NPS-100c-21 (500 kW)	214
Figure 5.22: Peak Power Balance Distribution – NPS-100c-24 (500 kW)	216
Figure 5.23: Probability of Meeting Peak Shaving Reserve Requirements (1)	218
Figure 5.24: Probability of Meeting Peak Shaving Reserve Requirements (2)	221

Chapter 6

Figure 6.1: Microgrid Demand Profile	225
Figure 6.2: Synchronous Generator Power Output	226

Figure 6.3: Grid Frequency	228
Figure 6.4: Active Power from Droop Regulator	229
Figure 6.5: Performance Comparison of Microgrid Frequency Regulation	231
Figure 6.6: Microgrid Voltage Error	233
Figure 6.7: Reactive Power from Droop Regulator	234
Figure 6.8: Performance Comparison of Microgrid Voltage Regulation	236
Figure 6.9: Grid Synchronization Performance	237
Figure 6.10: Inverter Terminal Current (Stationary Frame)	239
Figure 6.11: Inverter Currents during Grid Interconnection	241
Figure 6.12: Inverter Currents during Demand Increase	243
Figure 6.13: Inverter Currents during Demand Decrease	244
Figure 6.14: DC Link Current	246
Figure 6.15: DC Link Voltage during Load Variation	248
Figure 6.16: DC Link Voltage during Reference Change	249
Figure 6.17: PMSG Stator Currents	250
Figure 6.18: PMSG Stator Currents during Load Variation	251
Figure 6.19: PMSG Stator Currents during DC Link Reference Change	252

Figure 6.20: Converter Terminal Voltages	253
Figure 6.21: Converter Terminal Voltages during Load Variation	254
Figure 6.22: Converter Terminal Voltages during DC Link Reference Change	255

Nomenclature

Chapter 2

P	Aerodynamic Power
ρ	Air Density
A	Swept Area
v	Wind Velocity
C_p	Wind Turbine Power Coefficient
T_{shaft}	Wind Turbine Driveshaft Torque
c	Blade Chord Length
B	Number of Blades
V_{rel}	Blade-Relative Wind Velocity
φ	Angle of Relative Wind
C_L	Airfoil Lift Coefficient
C_D	Airfoil Drag Coefficient
r	Radial Blade Location

R	Turbine Blade Radius
$\dot{\theta}$	Angular Velocity
β	Blade Pitch Angle
λ	Tip-Speed Ratio
J	Polar Moment of Inertia
$\ddot{\theta}$	Angular Acceleration
a	Weibull Scale Parameter
b	Weibull Shape Parameter
b_r	Rayleigh Scale Parameter
μ	Mean
σ	Standard Deviation
K	Kernel Function
n	Index Number
N	Number of Dataset Samples
h_n	Kernel Bandwidth Parameter
$\hat{\sigma}$	Dataset Standard Deviation

E	Expected Value
p_m	Model Probability Function
p_e	Empirical Probability Function
x_i	Dataset Sample
p_{tur}	Instantaneous Wind Turbine Output Power
P_c	Wind Turbine Power Curve
p_d	Partial Pressure of Dry Air
M_d	Molecular Mass of Dry Air
p_v	Vapor Pressure of Water
M_v	Molecular Mass of Water
R_g	Universal Gas Constant
T	Temperature
R_H	Relative Humidity
p_{vsat}	Saturation Vapor Pressure of Water
p	Barometric Pressure
x_s	Stationary Base Dataset Sample

$x_{\sigma 1 \dots \sigma n}$	Periodic Variance Functions within a Nonstationary Dataset
V	DTFT of Wind Velocity Data
K_f	DTFT Frequency Index
f_s	Sample Frequency
P_{var}	Variance Period
f	Frequency
F_{mean}	DTFT Logarithmic Moving Average
M	Logarithmic Averaging Window Upper Bound
L	Logarithmic Averaging Window Lower Bound
P_{res}	Residual Occurrence Probability
d	Distance from the Logarithmic Mean
μ_e	Extreme Value Location Parameter
σ_e	Extreme Value Scale Parameter
p_{val}	Observation P-Value
σ_1	Diurnal Cycle Variance Function
σ_2	Seasonal Cycle Variance Function

T_1	Diurnal Cycle Variance Period
T_2	Seasonal Cycle Variance Period
$x_{\sigma 1}$	Reconfigured Dataset using Diurnal Variance
$x_{\sigma 1 \sigma 2}$	Reconfigured Dataset using Diurnal and Seasonal Variance
j	Diurnal Phase Index
k	Seasonal Phase Index
f_G	Gaussian Mixture Model
φ_σ	Gaussian Mixture Component
x_c	Kernel Function Centre Point
H	Gaussian Mixture Covariance Matrix
H_k	Kernel Covariance Matrix
f_k	Kernel Density Estimate
N_α	Inverse Sum of Squares
G_p	Hessian Operator
tr	Trace Operator
R_E	Bivariate Environmental Dataset

$R_{E\sigma_1\sigma_2}$	Feature-Extracted Bivariate Environmental Dataset
m	Length of Data Subsets
$F_{K\sigma_1\sigma_2}$	Multidimensional Bivariate KDE Model Object
n_v	Size of Wind Velocity Observation Space
n_ρ	Size of Air Density Observation Space
R^2	Correlation Coefficient
i_c	CDF Observation Index
i_e	ECDF Observation Index

Chapter 3

x	A general variable of interest
α	Gamma Distribution Scale Parameter
B	Gamma Distribution Shape Parameter
Γ	Gamma Function
μ	Generalized Extreme Value Location Parameter

σ	Generalized Extreme Value Scale Parameter
ξ	Generalized Extreme Value Shape Parameter
L	A Nonstationary Pseudorandom Variable
p_L	A Time-Variant Probability Distribution of Electrical Demand
$L_{\sigma_1\sigma_2}$	Demand Data Variance Features
$F_{L\sigma_1\sigma_2}$	Demand Data Probabilistic Model
$p_1:p_n$	Demand Distribution Observation Points
$C_{L\sigma_1\sigma_2}$	Demand Data Cumulative Distribution Function
P_t	Wind Turbine Output Space
ρ_{set}	Vector of Potential Air Density Observations
V_{set}	Vector of Potential Wind Velocity Observations
ρ_{base}	The Base Air Density
F_t	Probabilistic Wind Turbine Output Model
F_{Pt}	Time Variant Wind Turbine Output Model
P_o	Discrete Wind Turbine Output Power Bins
ε	Bind Width

E_{Pt}	Expected Wind Turbine Output Power
P_{bal}	Power Balance Condition Space
P_{TO}	Vector of Discrete Wind Turbine Output Values
P_{LO}	Vector of Discrete Electrical Demand Values
Pr_{bal}	Probabilistic Power Balance Model
G_R	Wind Generation Reserve Requirement
P_c	Base Generation Profile
P_R	Probability of Sufficient Wind Generation
P_{FW}	Probabilistic Frequency Regulation Capability

Chapter 4

E	Closed Loop System Transfer Function
G	System Plant Transfer Function
H	System Feedback Transfer Function
s	Laplace Domain
K_{Ie}	Exciter Integral Gain
K_E	Exciter Feedback Gain

C	PI Controller Transfer Function
V^*	Direct-Axis Generator Terminal Reference Voltage
V	Direct-Axis Generator Terminal Voltage
C_E	Excitation Controller Transfer Function
T	Steady State Generator Excitation Behavior
T_e	Generator Electrical Time Constant
K_p	Controller Proportional Gain
K_i	Controller Integral Gain
S	SOGI Transfer Function
k	SOGI Gain
ω'	SOGI Resonance Frequency
v	SOGI Input Voltage
v'	Direct Component of SOGI Input Voltage
qv'	Quadrature Component of SOGI Input Voltage
$V_{\alpha+}$	Positive Sequence Alpha Axis Grid Voltage
$V_{\beta+}$	Positive Sequence Beta Axis Grid Voltage

V_{α}	Alpha Axis Grid Voltage
V_{β}	Beta Axis Grid Voltage
qV_{α}	Quadrature Alpha Axis Grid Voltage
qV_{β}	Quadrature Beta Axis Grid Voltage
$V_{\alpha-}$	Negative Sequence Alpha Axis Grid Voltage
$V_{\beta-}$	Negative Sequence Beta Axis Grid Voltage
P	Active Power
Q	Reactive Power
I_{α}	Alpha Axis Inverter Terminal Current
I_{β}	Beta Axis Inverter Terminal Current
G_{PR}	PR Controller Transfer Function
K_R	Controller Resonant Gain
ω_0	PR Controller Resonant Frequency
$V_{\alpha T}^*$	Alpha-Axis Inverter Terminal Voltage Reference
$V_{\beta T}^*$	Beta-Axis Inverter Terminal Voltage Reference
I_{α}^*	Alpha Axis Inverter Terminal Current Reference

I_{β}^*	Beta Axis Inverter Terminal Current Reference
L_1	Inverter-Side LCL Filter Inductance
R	LCL Filter Shunt Resistance
C	LCL Filter Shunt Capacitance
L_2	Grid-Side LCL Filter Inductance
$I_{\alpha\beta S}$	Stationary Frame LCL Filter Shunt Branch Currents
$V_{\alpha\beta 1}$	Stationary Frame LCL Filter Shunt Branch Voltages
$I_{\alpha\beta E}$	Stationary Frame Inverter Terminal Current Tracking Error
$\alpha - \delta$	Symbolic Compound Variables
$A - F$	Additional Symbolic Compound Variables
P_{Inv}	Inverter Output Active Power
Q_{Inv}	Inverter Output Reactive Power
k_{DP}	Active Power Droop Coefficient
k_{DQ}	Reactive Power Droop Coefficient
f	Grid Frequency
f^*	Grid Reference Frequency

v_{sd}	Direct-Axis PMSG Stator Voltage
v_{sq}	Quadrature-Axis PMSG Stator Voltage
L_{sd}	Direct-Axis PMSG Stator Inductance
L_{sq}	Quadrature-Axis PMSG Stator Inductance
R_s	PMSG Stator Resistance
i_{sd}	Direct-Axis PMSG Stator Current
i_{sq}	Quadrature Axis PMSG Stator Current
φ_m	PMSG Magnet Flux
y_{sd}	Direct-Axis Decoupled Substitute Control Variable
y_{sq}	Quadrature-Axis Decoupled Substitute Control Variable
ω_e	PMSG Electrical Frequency
T_e	PMSG Electromagnetic Torque
p	Number of Pole Pairs in the PMSG Rotor
J	PMSG Wind Turbine System Moment of Inertia
T_{tur}	Wind Turbine Mechanical Torque
$T_{friction}$	Friction Torque

C_t	Wind Turbine Torque Coefficient
κ	Intermediate Symbolic Variable
V_{dc}	DC Link Voltage
I_{rect}	Controlled Rectifier Output Current
I_{inv}	Inverter Input Current
C_{Link}	DC Link Capacitance
P_G	PMSG Terminal Power
P_R	Controller Rectifier Output Power

Chapter 1: Introduction

Wind energy is a significant and increasing component of global electricity generation. Continuing concerns regarding climate change, air pollution and the future availability of fossil fuels are influencing the global electricity market towards an increased contribution from renewable energy. Advances in the electrical and mechanical wind turbine assemblies (including larger, more efficient and cheaper designs), research into energy storage technology, continued improvements in the design and control of power electronic converters as well as steady improvements in electrical machinery are continually improving the practical and economic feasibility of wind generation. In general, a wind generation installation falls into two major categories – transmission connected (where the wind energy output is connected to a large grid through transmission infrastructure) and islanded (where the wind energy supplies a local distribution grid). Transmission-connected systems are generally in the form of large wind farms, operated by industry to supply energy to utilities. Islanded wind energy systems are used to provide energy to remote communities that are isolated from the transmission system.

Transmission-connected wind generation is a relatively mature field, with large wind farms being constructed throughout the windier regions of the world. However, a considerable fraction of the world population remains isolated from transmission grids instead being supplied by islanded microgrids – smaller electricity distribution systems which cannot access transmission infrastructure. The installation of wind generation into

these islanded microgrids presents a unique set of technical challenges. The lack of transmission-level connection requires the microgrid to fully supply the load-side active and reactive power demand. Suboptimal design has a magnified effect on the economic performance, power quality and reliability of islanded microgrids. Advances in wind generation has made it cost and performance-competitive with conventional generation in transmission-interconnected systems. The economic benefit of wind energy in islanded microgrids is maintained - the high cost of fuel transportation and reduced efficiency of smaller, distribution scale generators offsets the technical challenges inherent to the system topology.

The installation of wind energy into islanded microgrids is defined by its applications within the larger system. Power-electronic interconnected wind generation has fast active and reactive power ramping capability, leading to applications in microgrid frequency and voltage regulation. Islanded microgrids are especially susceptible to contingencies requiring this regulatory action due to a lack of the stabilizing influence of the transmission grid. In addition, many microgrids have highly variable demand profiles due to intermittent commercial and industrial loads, such as mines, processing plants or mills. Therefore, wind generation is also well-suited as a dynamic reserve for demand response and peak shaving. However, the chaotic and intermittent nature of wind generator output requires considerable engineering effort with respect to microgrid integration. Planning the integration of wind generation into an islanded microgrid requires algorithms that predict power system performance during any reasonable operating condition. The demand profile and wind energy availability must be modeled to allow optimization of system

configuration. Current research in this field focuses on deterministic and probabilistic modeling, where techniques such as machine-learning algorithms and statistical tools are applied for demand and wind power forecasting to predict future system behavior [1]-[5]. These methods are best suited for short term planning of existing systems as opposed to the assessment of long-term reserve capability. Machine learning is computationally expensive and unreliable during uncommon conditions that differ from previously extracted features.

The drawbacks of deterministic modeling can be addressed by probabilistic approaches. Probabilistic power system planning estimates the probability of various system contingencies through analysis of the space of possible system behavior. Some preliminary research has been conducted in this area, including probabilistic demand forecasting [2] and studies on the effects of wind-based demand response on existing transmission systems [3], [5]. However, none of the previous studies focused on developing a probabilistic model combining demand profile and wind power availability for demand response and frequency regulation in islanded microgrids. A unified probabilistic framework for the probabilistic assessment of wind reserves for applications within islanded microgrids is needed to address these deficiencies. The proposed methodology will be validated using analytical and numerical simulations. As a final method of validation, a case study using field data from an islanded microgrid is conducted to evaluate the use of wind generation as a dynamic reserve, including its probabilistic performance and physical implementation within the existing electrical generation and distribution system.

1.1 Thesis Objectives

The continued push towards the implementation of renewable generation in combination with advances in microgrid control and operation technology has created a need for additional research in the integration of wind reserves into islanded microgrids. This thesis seeks to provide improved probabilistic wind reserve assessment algorithms for use in islanded microgrids, including advanced multidimensional wind resource models, probabilistic wind reserve assessment techniques, studies into microgrid topologies and control, as well as a case study which validates the utility of the proposed methodologies. The overarching objective is to provide an analysis and modeling framework for the probabilistic prediction of the performance of an islanded microgrid when wind generation is installed as a dynamic reserve, allowing analysis of the feasibility of wind as well as providing a starting point for system optimization.

1.2 List of Publications

The following publications are related to work included within this thesis:

[1] **Little, M., Rabbi, S.F.**, Pope, K. and Quaiocoe, J, “A Novel Probabilistic Assessment of Wind Reserves for Demand Response and Frequency Regulation in Islanded Microgrids.”

In IEEE IAS Annual Meeting, Cincinnati Ohio, October 2nd-5th, 2017.

- [2] **Little, M.** and Pope, K., "Performance Modeling for Wind Turbines Operating in Harsh Conditions", *International Journal of Energy Research*, Early Access, Published August 17th, 2016
- [3] **Little, M.** and Pope, K "Modeling Wind Turbine Performance with Recursive Parameter Estimation", in *CSME International Congress*, Kelowna, BC, June 26th-29th, 2016.
- [4] **Little, M.** and Pope, K., "Frequency Domain Analysis for the Statistical Assessment of Wind Resources", in *CCECE*, Vancouver, Canada, May 15th-18th, 2016.
- [5] **Little, M.** and Pope, K., 'Modeling Seasonal Wind Resource Variation in a Maritime-Influenced Humid Continental Climate,' in *Newfoundland Electrical and Computer Engineering Conference* , St. John's, NL, November 5th, 2015.

1.3 Thesis Organization

This thesis is organized as a series of Chapters, each covering a separate aspect of wind reserve assessment and its application into islanded microgrids. Literature surveys are included within each individual Chapter to improve the compartmentalization of the thesis and allow a reader to conduct a more focused study into each aspect of the overarching theme of wind reserve assessment. Chapter 1 introduces the thesis and includes the thesis objectives and organization. The remainder of the thesis is organized as follows:

- Chapter 2 presents a novel multidimensional probabilistic wind resource modeling framework. Existing wind resource modeling techniques are reviewed, including Weibull, nonparametric and multivariable mixture models. Deficiencies in these methods are identified and addressed by the development of a time-variant, multivariate nonparametric probabilistic model that includes the effects of both wind velocity and air density. Both time and frequency-domain analysis techniques are used to identify statistically significant nonstationary behavior within the site wind regime, allowing probabilistic models to be created that maintain accuracy throughout the modeling period. The developed modeling framework is validated using sample data and shown to produce a superior probabilistic fit in comparison to existing techniques, providing probabilistic predictions of wind power density, wind turbine output and the likelihood of various environmental contingencies.
- Chapter 3 presents a novel wind reserve assessment algorithm for use in islanded microgrids. The modeling methodology presented in Chapter 2 is extended to the analysis of electrical demand data. The demand profile is probabilistically organized, identifying the base, secondary and peak demand including its probabilistic time-variance. The previously developed wind resource model is then combined with this demand profile using a novel probabilistic algorithm that identifies the time-variant probability of adequate wind reserves for applications such as frequency regulation, demand response and peak shaving. The information provided by this modeling algorithm is shown to be fundamentally different from standard deterministic approaches and has applications in power system planning and microgrid operation.

- Chapter 4 presents a review of the analytical and numerical modeling of islanded microgrids. The nature of distributed generation, microgrid topologies and the principle of islanding is reviewed. Subsequently, microgrid operation and control techniques including grid forming, grid synchronization and the interconnection of distributed generators are investigated and implemented within a PLEXIM simulation environment. The use of droop-based microgrid support using power inverters is also reviewed with a focus on using wind energy as a dynamic reserve for microgrid stabilization. The interconnection topologies for various wind turbine designs are overviewed, with the Direct-Drive PMSG wind turbine identified as the optimal topology for use in islanded microgrids. The control and grid connection of this turbine design is investigated, including back-to-back converter control, LCL power filters and DC Link voltage stabilization. The simulation environment presented in this Chapter is designed for use in evaluating the performance of dynamic wind reserves, allowing site-specific case studies to be conducted.
- Chapter 5 conducts a case study in probabilistic wind reserve assessment using data from Cartwright, a remote community in Labrador. As an islanded microgrid, Cartwright's unique demand and wind resource profiles are modelled using the algorithms and methods presented in Chapters 2 and 3 to evaluate the ability of wind generation to act as a dynamic reserve for demand response, peak shaving, microgrid frequency regulation and/or microgrid voltage regulation. Significant time-variance in the probabilistic wind reserve is identified and correlated with seasonal and diurnal cycles. The effects of different wind turbine designs and

capacity amounts are also investigated, producing a time-variant probabilistic power balance model which allows quantification of the resultant wind reserve.

- Chapter 6 concludes the case study presented in Chapter 5 by implementing a model of Cartwright's microgrid in a PLEXIM simulation environment. Wind energy is used to implement demand response, droop-based frequency regulation and voltage regulation using the control and simulation topology presented in Chapter 4. In addition, the power electronic based control of a direct-drive PMSG wind turbine is implemented to demonstrate the required interconnection topology for wind energy installation. The simulation environment verifies the wind reserve applications presented in the previous Chapters, validating the utility of the probabilistic assessment algorithm by demonstrating the design applications when implemented in islanded microgrids.
- Chapter 7 concludes the thesis, reviewing the thesis contributions and presenting avenues of future investigation.

Chapter 2: Analysis and Probabilistic Modeling of Wind

Resources

2.1: Introduction

Wind energy a significant and increasing component to global renewable generation. Concerns of climate change, air pollution and fossil-fuel availability is influencing continued wind turbine installation. Additionally, advances in wind turbine design (including size and efficiency), energy storage technology and power electronics are continually improving the practical and economic feasibility of wind generation. The installation of grid-connected wind energy systems (WES) falls into two major categories: transmission connected (where the wind energy output is connected to a large grid through transmission infrastructure) and islanded (where the wind energy supplies a local distribution grid). Transmission-connected systems are generally in the form of large wind farms, operated by industry to supply energy to national utilities. Islanded wind energy systems are used to provide energy to remote communities that are isolated from the transmission system. The economic benefit of islanded wind energy is magnified by the high cost of fuel transportation, causing increased financial viability and reducing environmental impacts.

The development of islanded wind energy systems (IWES) carries a unique set of challenges. The lack of transmission-level connection requires the IWES to fully supply the load-side active and reactive power demand. Suboptimal design has a magnified effect

on the performance of the IWES. The time-variant, intermittent wind resource must be accurately modelled and compared with demand. Probabilistic contingencies must be evaluated to ensure reliable system operation and the performance of IWES must be predicted throughout the life of the system to allow design and control optimization. At a fundamental level, IWES design and optimization requires an accurate, probabilistic model of the time-variant site wind resource capable of predicting wind turbine power output throughout operation.

2.2: Wind Resource Modeling – Overview

Wind resource modeling is the process of determining the statistical properties of site wind observations and predicting their effects on wind turbine performance. Wind resource modeling is conducted using varying methodologies with the intent of optimizing the Wind Energy System (WES) design. Pre-feasibility studies [1]-[6] are conducted by simulating system profiles (including generation, storage and demand modeling) to determine the economic and practical feasibility of wind generation installations. A very wide range of potential WES designs exist [7, 8], including both wind-only renewable generation, hybrid wind / solar, wind / hydro as well as more esoteric options such as wind / biomass and solar / biomass. Each WES design presents unique challenges with respect to grid connection, system configuration and design optimization. The WES design process requires a detailed model of system performance. This is accomplished through component modeling [9]

followed by system design, simulation and optimization [10], [11]. Using this method, the economic and technical behavior of system components are input into a series of optimization equations and performance constraints. Conditions such as renewable fraction, unmet load, storage requirements and system capital cost are used to evaluate the viability and performance of the WES. Recently, advanced optimization techniques such as genetic algorithms, artificial neural networks and fuzzy logic have been used to obtain an optimal system design [11]-[13]. While the performance of these optimization algorithms is generally sufficient, a common limitation is the lack of an accurate simulation of each hybrid system's performance over the evaluation interval.

At a coarse level, wind energy atlases [15], [16] detail global wind energy potential, suggesting regions worthy of further investigation. Probabilistic models such as the Weibull Distribution [17]–[20], approximate the long-period wind statistics, with parameters selected using either probabilistic (maximum-likelihood [21], percentile estimation [22]) or direct (least-squares) estimation algorithms. The model estimates annual energy production and the capacity factor of an installed wind turbine. Additional techniques such as Fractional Weibull distribution modeling [23] and distribution suitability analysis [24, 25] fit site-specific distributions that represent non-Weibull behavior. This type of single-distribution wind resource modeling is widely used for initial site selection and feasibility analysis. However, additional environmental variables such as air density and Reynolds number influence wind turbine performance, inducing significant model error. Bivariate wind / density distribution models [26]-[28] correctly assume a correlation between wind velocity and air density, producing a more accurate estimate of

wind turbine annual energy production. These models can be used to predict wind turbine performance given knowledge of their aerodynamic characteristics.

2.2.1: Wind Turbine Behavior

Wind turbines are non-linear, multivariate systems with varying performance depending on local aerodynamic condition (turbulence, wind shear and wake effects, etc.). The effects of these conditions are difficult to measure, exhibiting time-variance and multivariate interaction. It is not feasible to construct an operational process model that includes parameters representing all operational variables. When modeling a site's wind resource, major effects are attributed to wind velocity, air density, the wind turbine's mechanical rotation speed and the associated mechanical torque. The former two factors influence the energy available – the latter define operating regions where this energy can be safely extracted. The interaction between these variables must be modeled to allow air density performance correction, analysis of wind shear and turbulence effects and eventual modeling of wind turbine electrical characteristics based on aerodynamic performance.

Rotor dynamics formulation

The total power available from the wind is calculated by the total kinetic energy passing through the turbine within a given time interval. The available power is

$$P = \frac{1}{2} C_p \rho A v^3 \quad (1)$$

where ρ , A , v , and C_p represent the air density, turbine swept area, wind velocity and power coefficient, respectively. The wind velocity and air density are assumed to be constant across the swept area – shear and turbulence must be modelled numerically using computational fluid dynamics (CFD) software. For the purposes of wind resource modeling, blade element momentum theory (BEM) [29] is sufficiently accurate. BEM theory integrates the aerodynamic force along the turbine blades to predict shaft torque as a function of wind velocity, rotational speed and the wind turbine's airfoil geometry:

$$T_{shaft} = \int_0^R \frac{1}{2} \rho c V_{rel}^2 B r (C_L \sin \varphi - C_D \cos \varphi) dr \quad (2)$$

where c , B , V_{rel} , φ represent the chord length, number of blades, relative wind velocity and angle of relative wind. The variables C_L and C_D are the airfoil's lift and drag coefficients, generally obtained from manufacturer test data and/or CFD studies. The integral limits are the turbine hub ($r = 0$) and the blade tip ($r = R$). The relative velocity can be expressed in terms of the wind velocity, radial position and turbine angular rotational velocity:

$$V_{rel} = v(1 - \frac{\dot{\theta}r}{v}) \quad (3)$$

where $\dot{\theta}$ represents the angular velocity. The angle of relative wind φ is a function of V_{rel} and r and depends on the physical design of the turbine blade (including blade twist). The blade pitch angle, β , affects the angle of relative wind. Furthermore, the lift and drag coefficients are functions of the angle of relative wind and v , $\dot{\theta}$, r and β . Completing the definite integral in (2) results in the turbine output torque being a function of v , R , $\dot{\theta}$ and β , in addition to ρ , c and B .

The analytical effects of v and $\dot{\theta}$ can be combined into a dimensionless parameter - the tip-speed ratio (λ):

$$\lambda = \frac{\dot{\theta}R}{v} \quad (4)$$

This assumption is verified by a numerical study of large wind turbines [30] and simplifies analytical analysis of wind turbine performance. The aforementioned shaft torque, T_{shaft} , is related to the angular blade acceleration:

$$T_{shaft} = J\ddot{\theta} \quad (5)$$

where J is the turbine's polar moment of inertia. Using the relation between torque and power, the shaft power is related to the angular acceleration and angular velocity:

$$P = J\dot{\theta}\ddot{\theta} \quad (6)$$

(6) can be combined with (1) and (4) to relate the dynamic performance of the wind turbine to the environmental operating conditions,

$$J\dot{\theta}\ddot{\theta} = \frac{C_p\rho\pi R^5\dot{\theta}^3}{2\lambda^3} \quad (7)$$

Rearranging, the instantaneous angular acceleration can be expressed as a function of the turbine efficiency, radius, air density, rotational speed and tip-speed ratio. Removing all variables except angular acceleration from the left-hand side, the following equation can predict turbine rotor dynamics [29],

$$\ddot{\theta} = \frac{C_p\rho\pi R^5\dot{\theta}^2}{2J\lambda^3} \quad (8)$$

The relation presented in (8) identifies the dynamic relation between wind turbine performance and environmental conditions. This relation bridges the gap between environmental conditions and wind turbine performance, allowing the dynamic behavior of a wind turbine to be modelled given knowledge of the wind turbine's environment.

2.3: Probabilistic Modeling of Wind Velocity

The prediction of wind turbine performance requires substantial knowledge of the statistical properties of the wind velocity. At a fundamental level, wind is a chaotic process. From moment to moment, the measured wind velocity can unpredictably vary due to influences from terrain, structures and simple fluid interaction – processes which are difficult to observe and even more difficult to model. However, the wind is a physical process which obeys a set of governing equations – energy supplied by the solar flux is dissipated by kinetic and thermal processes throughout the atmosphere. While deterministic prediction is difficult, this underlying dependence leads to the statistical modeling of wind velocity as a random variable, defined by a probability distribution and autocorrelation function. Probability distributions are functions expressing the likelihood of encountering any particular value of a random variable given independent, non-disruptive observations.

In general, probability distribution modeling uses parametric distribution functions. These probability distributions are defined as closed-form analytical functions involving a small number of free parameters. The Weibull, Rayleigh and Lognormal distributions (among others) belong to this distribution type. Parametric distributions such as these are simple to model, reasonably easy to fit to a dataset and can easily be subjected to analytical statistical techniques such as MAE, MAPE or RMSE fit-closeness analysis or various data transforms. However, the solution space defined by parametric probability distributions is limited by their requirement for closed-form analytical expressions. Multimodal, discrete or discontinuous probability density functions are not easily modelled parametrically.

Instead, numerical techniques have been developed to produce nonparametric probability distributions. The most commonly used such method is Kernel Smoothing.

The Kernel smoothing distribution [35] provides a close approximation to an observed probability distribution by modeling each data point as an instance of a base Kernel function. The kernel function K can be the Gaussian distribution, a triangle, box, or one of various other parametric distributions. The Kernel distribution is developed by summation of all kernel instances produced by the dataset, developing the following functional form:

$$f_k(v, h_n) = \frac{1}{Nh_n} \sum_{i=1}^n K[(v - v_i)/h_n] \quad (9)$$

where N is the number of discrete dataset samples, K is the kernel function and h_n is the bandwidth smoothing parameter. For further analysis, it is assumed that the standard normal (Gaussian distribution is used as the Kernel smoothing function – an appropriate selection for datasets which are relatively close to Gaussian in nature:

$$K(v | \mu, \sigma^2) = \frac{1}{\sigma\sqrt{2\pi}} e^{-\frac{(v-\mu)^2}{2\sigma^2}} \quad (10)$$

where μ and σ represent the sample mean and standard deviation, respectively. The standard deviation of the kernel function is referred to as the bandwidth - it influences the bias and variance of the final probability distribution estimate. Proper bandwidth selection is vital to avoid over or underfitting the sample data. Assuming that the actual sample distribution is Gaussian (or similar) and using the Gaussian kernel function, the optimal bandwidth can be approximated as [36]:

$$h = \left(\frac{4\hat{\sigma}^5}{3N}\right)^{\frac{1}{5}} \quad (11)$$

where $\hat{\sigma}$ is the dataset's standard deviation and N is the dataset size. When n is large, accurate bandwidth optimization is possible without knowledge of the underlying distribution [36]. For non-Gaussian distributions, numerical bandwidth estimators are required to ensure an accurate distribution fit.

Figure 2.1 displays a nonparametric kernel smoothing distribution fitted to the wind velocity dataset. Using a Gaussian Kernel function and a smoothing bandwidth of 0.7408, an extremely close fit is observed. Unlike the previously investigated parametric probability distributions, the kernel smoothing algorithm successfully matches the location and magnitude of the distribution mode. In addition, the slight multimodality evident within the dataset is captured, with small secondary peaks evident at wind velocities near 5 and 15 knots. Finally, the nonparametric distribution accurately models the probabilistic roll-off observed at high wind velocities. As this region holds the majority of the available wind energy, accuracy here is paramount. Nonparametric distributions are vulnerable to bandwidth errors, however they are suitable for wind velocity analysis due to the large number of data samples and continuous nature of the underlying probability distribution.

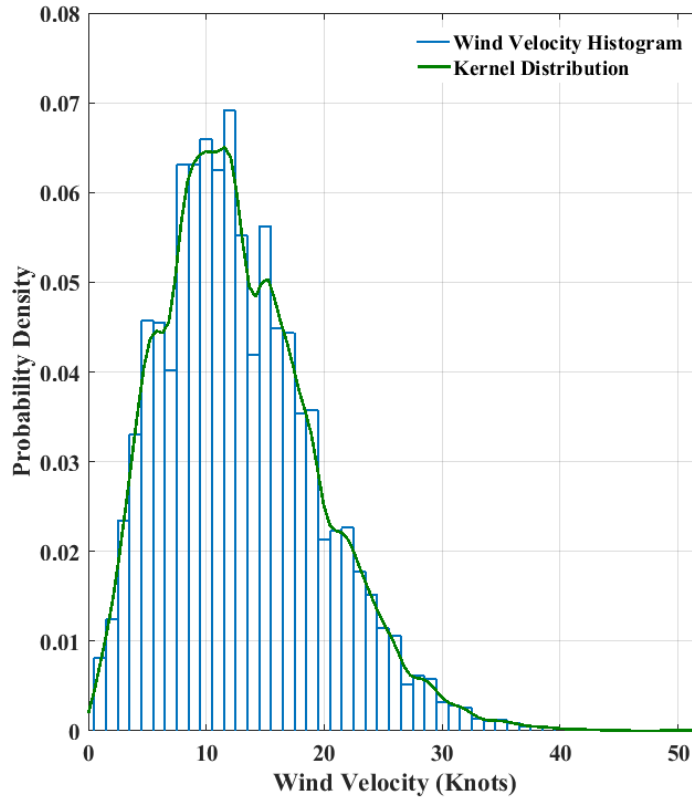


Figure 2.1: A Nonparametric Distribution Wind Velocity Model

2.4: Bivariate Modeling

The numerical prediction of wind turbine performance involves the calculation of the expected output power. Generalizing the wind turbine efficiency [39] and environmental variables as time-variant functions, the instantaneous output power can be expressed as:

$$p_{tur}(t) = \frac{1}{2} C_p(t) \rho(t) A v(t)^3 \quad (12)$$

where $C_p(t)$, $\rho(t)$, and $v(t)$ represent the instantaneous power coefficient, air density, and wind velocity, respectively. The variable A represents the turbine's swept area. This relation indicates that the site air density is important for wind resource modeling, having a

significant effect on both the available wind power, the general wind power density and the captured power of an operational wind turbine.

The time-variant power coefficient $C_p(t)$ is difficult to analytically predict, varying with turbine rotation speed, blade pitch angle, Reynold's number and wind velocity [40, 41]. This issue has been addressed by wind turbine manufacturers. The performance of each wind turbine design is experimentally measured, resulting in a performance function known as a power curve. The power curve $P_c(v(t))$ relates the wind turbine's steady-state power output to the wind velocity. The power curve is taken at a standard air density. Including the effects of air density and substituting the wind turbine power curve, the wind turbine power output expression reduces to:

$$p_{tur}(t) = \rho(t)P_c(v(t)) \quad (13)$$

where the air density is normalized by the base manufacturer value (normally 1.225 kg/m³) and both variables expressed as functions of time. Using the ideal gas law [42] approximation, the density of the air can be expressed as:

$$\rho = \frac{(p_d M_d + p_v M_v)}{R_g T} \quad (14)$$

where ρ is the air density, p_d is the partial pressure of dry air, M_d is the molecular mass of dry air, p_v is the vapor pressure of water vapour and M_v is the molecular mass of water. The variables R_g and T represent the universal gas constant and temperature, respectively. The partial pressure of water vapour is related to the saturation vapor pressure and the relative humidity as follows:

$$p_v = R_H p_{vsat} \quad (15)$$

where R_H is the relative humidity and p_{vsat} is the saturation water vapor pressure. The saturation pressure of water vapor is a function of temperature, and is approximated as [42]:

$$p_{vsat} = 610.78 * 10^{\frac{7.5T}{T+237.3}} \quad (16)$$

The partial pressure of dry air (p_d) is the remaining pressure when p_{vsat} is subtracted from the measured barometric pressure p . If the dew point temperature is available, the vapor pressure can be calculated as:

$$p_v = 610.78 * 10^{\frac{7.5T_d}{T_d+237.3}} \quad (17)$$

Substituting Eqs. (22) to (25) into Eq. (21) the turbine power output can be expressed as:

$$p_{tur}(t) = \frac{[(p - p_v)M_d + (610.78 * 10^{\frac{7.5T_d}{T_d+237.3}})M_v] P_c(v(t))}{RT} \quad (18)$$

Equation 26 is used for the time-series prediction of wind turbine performance. It includes the effects of multiple environmental variables to improve power output prediction accuracy.

The relationship between air density and wind turbine power output requires any probabilistic wind resource model to be bivariate in nature, including both wind velocity and air density. Air density data is probabilistically modelled to investigate the degree of variation and the underlying probability distribution. Figure 2.2 displays both Gaussian and Kernel distribution air density models. The air density histogram displays significant probability density between values of 1.14 and 1.35 kg/m^3 – a significant degree of variability. Probabilistically, a Gaussian distribution is the best parametric fit. However, the nonparametric Kernel distribution more accurately reflects the true probability distribution. The degree of variability evident combined with its probabilistic behavior

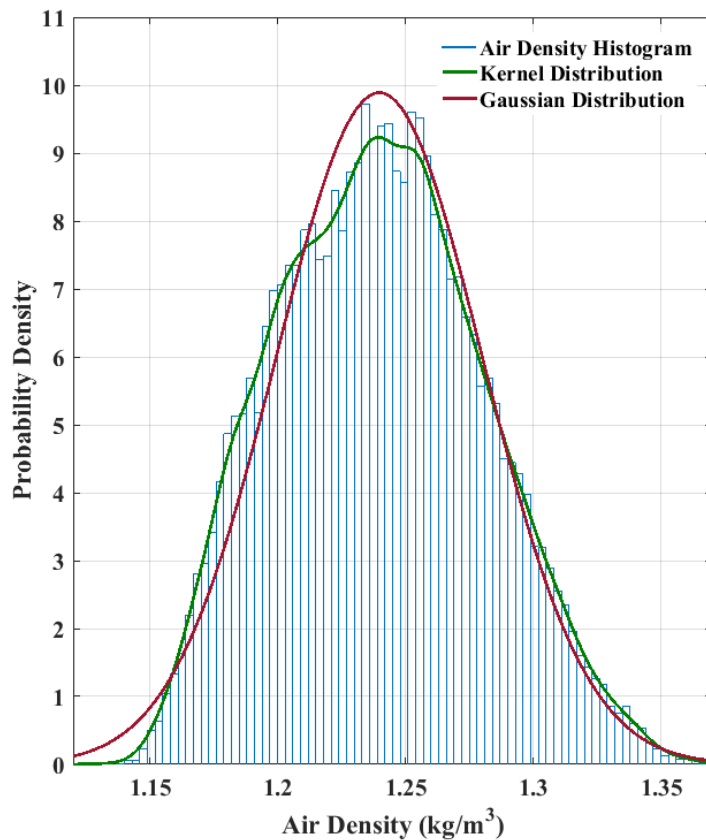


Figure 2.2: A probabilistic model of Air Density

indicates that a full, bivariate model must be developed to accurately model a site's wind resource.

2.5: Analysis of Nonstationary Behavior

Previously, probabilistic analysis has been conducted with the assumption that both wind velocity and air density data are stationary signals. A stationary signal has constant statistical properties – a stationary random variable can be defined using the same probability distribution regardless of the time of observation. This assumption significantly simplifies probabilistic analysis, reducing a wind resource model to a single bivariate probability distribution. The assumption of stationarity must be investigated to ensure its validity – otherwise important information is lost when modeling the wind resource. As the model dataset is comprised of environmental measurements, subsets are drawn corresponding to measurement periods at diametrically opposite seasonal and diurnal phases. Non-stationary behavior is most likely to present itself by comparing these extremes. A nonparametric kernel distribution is fitted to four 244-element wind velocity subsets, with the resulting distribution compared to that of the entire 43824-element dataset. In addition, the first four empirically determined distribution moments (mean, standard deviation, skewness and kurtosis) are compared. Any variation among these parameters indicates non-stationary behavior.

Figure 2.3 displays the Kernel distribution fits of each dataset, calculated using the smoothing bandwidth determined in MATLAB's "ksdensity" function [43]. Significant variation is evident between each subset and the primary dataset. Two distinct distribution groups are evident – Sets 2 and 3 are probabilistically similar, as well as sets 4 and 5. Interestingly, Set 1 (the complete dataset) appears to split the difference between the two. Based on the observation times, this suggests a seasonal pattern is present in the probabilistic model of wind velocity, superimposed on a weaker diurnal signal. However, while these patterns can be surmised based on the distribution fits, a more rigorous analysis is required to validate their presence and to detect any additional periodic patterns.

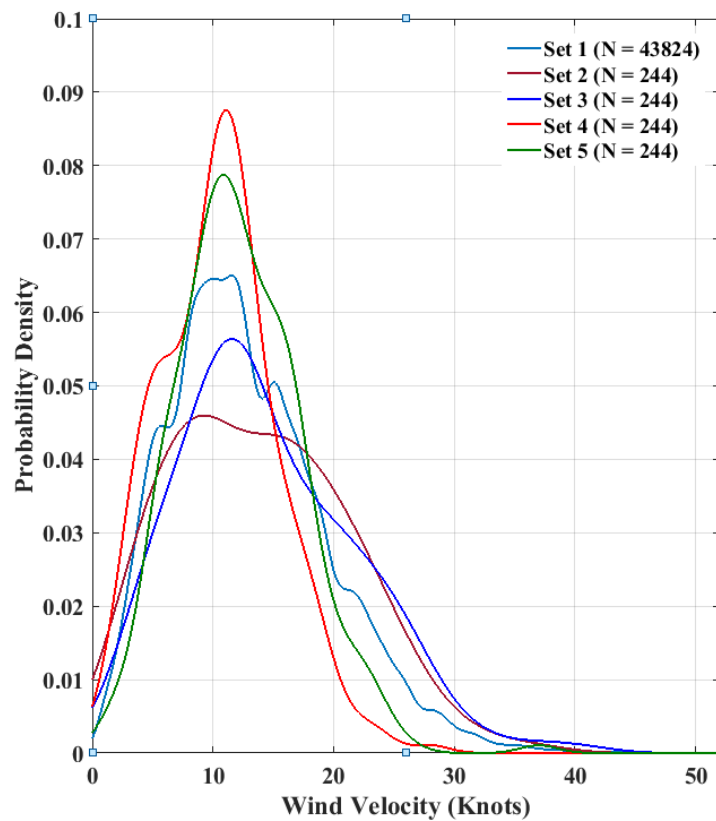


Figure 2.3: Nonparametric modeling of wind velocity subsets

The degree of observed probabilistic variance is displayed in Table 2.1. The mean, standard deviation, skewness and kurtosis of each distribution is calculated and compared. The mean wind velocity shows significant variation across the datasets, ranging from 10.49 for set 4 (corresponding to early morning in the summer) to 14.51 in set 3 (corresponding to late afternoon during mid-winter). The diurnally opposite equivalents have mean values of 12.22 and 13.84, respectively. The entire dataset has a mean value of 12.93. Essentially, the mean wind velocity is higher during the winter months. Similar behavior is evident in the standard deviations, skewness and kurtosis data, indicating that the shape of the wind velocity probability distribution significantly varies over time. The standard deviation ranges from 4.79 to 7.34, indicating a large temporal change in wind velocity variance. The distribution skewness values are always positive (indicating a left-skewed probability distribution with a long right tail) and large enough to indicate significant asymmetry in the wind velocity. The distribution Kurtosis varies from 2.62 to 4.54, indicating time-variance between platykurtic (kurtosis < 3) and leptokurtic (kurtosis > 3) behavior. The Kurtosis values suggest the frequency of outliers, indicating the likelihood of damaging wind events or periods of prolonged calm. In all cases, the degree of statistical time-variance indicates that further investigation of non-stationary behavior is required. This analysis is conducted within the frequency domain.

Table 2.1: Distribution Moments of Wind Velocity Subsets

Observation Set	Mean	Std. Deviation	Skewness	Kurtosis
1 (N = 43824)	12.9274	6.5713	0.7185	3.6046
2 (N = 244)	13.8648	7.3054	0.4156	2.6218
3 (N = 244)	14.5082	7.3403	0.6590	3.2654
4 (N = 244)	10.4877	4.7941	0.3748	3.1735
5 (N = 244)	12.2213	5.0950	0.6588	4.5378

2.6: Frequency Domain Analysis

The nonstationary behavior of wind velocity requires augmented time-variant probabilistic modeling algorithms. The statistical properties of an environmental data set (such as wind velocity and/or air density) are time-varying and chaotic. To analyze nonstationary behavior, environmental data can be modeled as a general discrete nonstationary dataset, $x(n)$, comprised of a stationary base dataset, $x_s(n)$, with nonstationary behavior modeled as superimposed periodic features, $x_{\sigma_1 \dots \sigma_n}$. The nonstationary variance periods, $\sigma_1 \dots \sigma_n$ which exist within $x(n)$ must be identified to allow probabilistic modeling algorithms to accurately reflect nonstationary behavior. Preliminary work in the identification of wind velocity variance [44] identified considerable turbine performance

variance occurring throughout the course a seasonal cycle. A frequency-domain study [45] defined wind turbine power spectra spanning hourly and daily timescales. An analysis framework based around wide-band frequency domain study of a large environmental dataset is capable of identifying and quantifying any periodic variance contributors, allowing more advanced time-variant probabilistic analysis of the nonstationary site wind resource. Figure 2.4 presents a flow chart of the frequency domain analysis algorithm presented in this section.

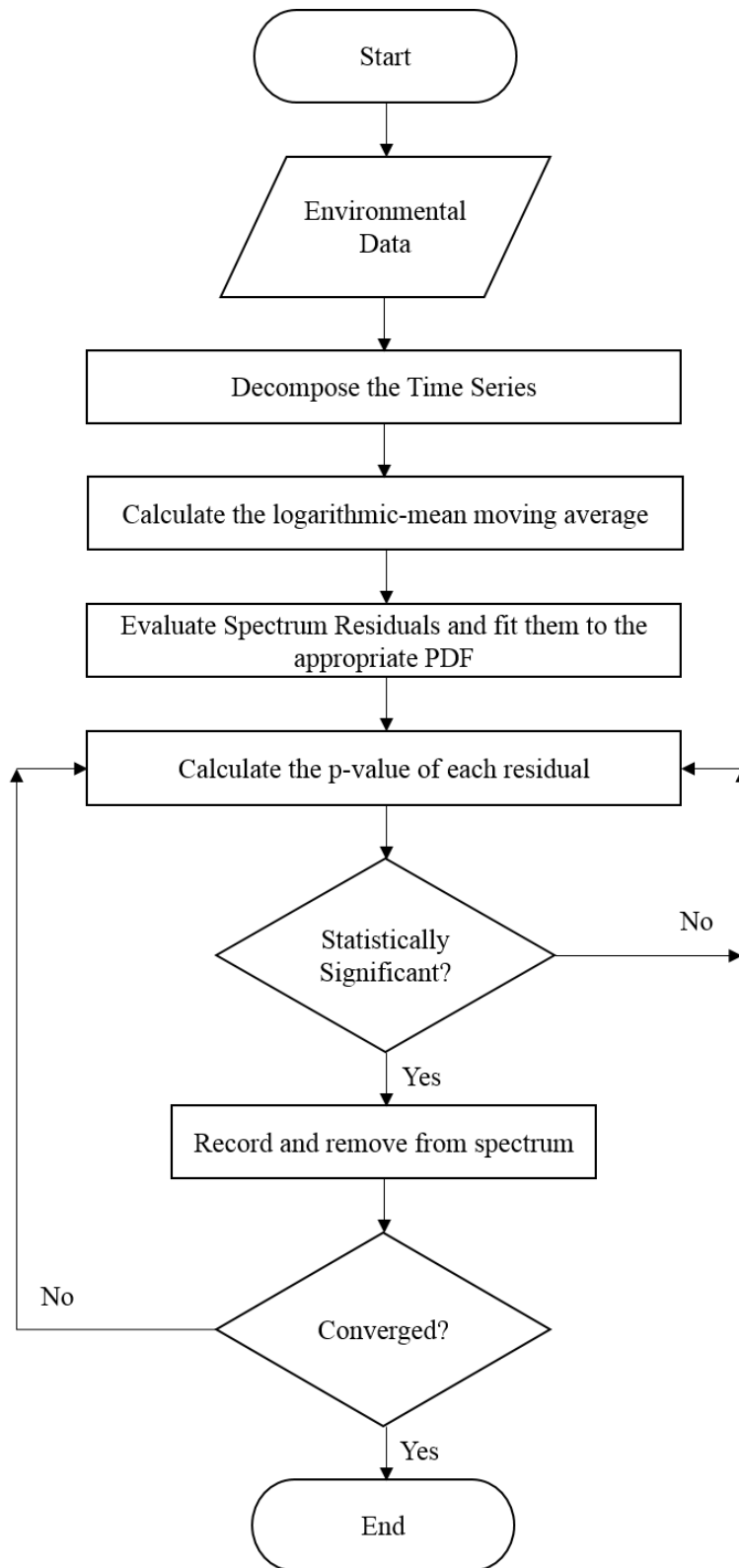


Figure 2.4: A Flow Chart of the Frequency Domain Analysis Algorithm

2.6.1: The Discrete-Time Fourier Transform

The discrete-time Fourier transform (DTFT) is used to extract the frequency spectrum of the nonstationary environmental dataset $v(n)$:

$$V(k) = \sum_{n=0}^{N-1} v(n) \cdot e^{-j2\pi\left(\frac{kn}{N}\right)}, \quad 0 \leq k_f < N \quad (19)$$

where $V(k)$ represents the complex DTFT observation at point k_f and n the time-domain observation index. The DTFT is best suited for wide-band frequency analysis, providing superior frequency resolution at the expense of unnecessary time-series analysis. The DTFT frequency resolution is determined by the dataset size N and the sample frequency, f_s . The Nyquist sampling theorem limits the range of detectable variance periods:

$$\frac{2}{f_s} \leq p_{var} \leq Nf_s \quad (20)$$

where p_{var} is the variance period of interest. The observed variance frequency indices are defined as:

$$K_f = \frac{n}{Nf_s} \quad 0 \leq n \leq \frac{N}{2} \quad (21)$$

The magnitude and phase of the complex function $V(k)$ details the periodic variance contribution at the observation frequency.

Figure 2.5 displays the single-sided DTFT magnitude spectrum (with the DC mean removed) of an 8-year wind velocity dataset, comprised of the 5 years from the previous section with the addition of the three previous years. The larger dataset is selected to better isolate annual or semi-annual trends (if they exist). The range of variance periods is from 2 hours (the sample Nyquist period) to 8 years. In general, the frequency spectrum is a combination of $1/f$ noise, white noise and Kolmogorov pink noise ($f^{-5/3}$) with superimposed random amplitude variance. Four significant variance contributors are visually evident, corresponding to periods of 1 year, 1 day, 12 hours and 8 hours. The 1-year variance period has the highest amplitude (of roughly 1 knot on the single-sided FFT), indicating a large seasonal variance signal. The remaining spectrum peaks are related to diurnal variance –

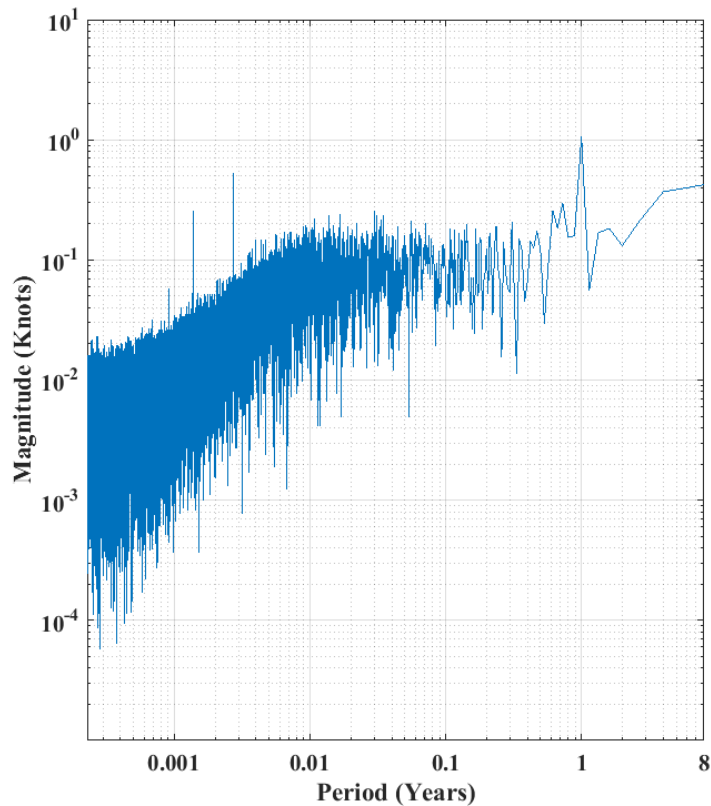


Figure 2.5: Single-Sided Magnitude Spectrum of Wind Velocity

the presence of harmonics above the fundamental 24-hour signal indicates a more complex, non-sinusoidal variance pattern. Statistical analysis of the magnitude spectrum is required to quantify and validate these peaks, ensuring that they are not statistical artifacts and allowing their use in probabilistic modeling.

2.6.2: *Statistical Analysis of Spectral Residuals*

The general frequency-amplitude correlation within the wind velocity spectrum is concealed by considerable random noise. The noise is an expected property of relatively random and chaotic processes with little auto-regressive behavior or band-limitation – such as environmental data. A logarithmic moving average algorithm (Eqs. 30 - 32) is developed to remove the random noise, extracting the mean DTFT frequency-magnitude correlation function. The width of the averaging window is set to a fixed logarithmic distance, ensuring that an equal-ratio bandwidth is used to produce the mean magnitude function regardless of the core observation frequency.

$$F_{mean}(k) = \frac{1}{M - L} \sum_{i=L}^M F(i) \quad (22)$$

$$\log(L) = \log(k) - \frac{1}{2} \quad (23)$$

$$\log(M) = \log(k) + \frac{1}{2} \quad (24)$$

The removal of magnitude noise allows the presence of statistically significant variance frequencies to be evaluated through analysis of the spectral residuals. The set of logarithmic distances between each DTFT magnitude observation and its equal-frequency logarithmic mean is assumed to be a stationary random variable (due to the loss of time information when using the DTFT) that has an associated probability distribution function. The assumption of randomness in the magnitude noise is verified through analyzing the frequency autocorrelation function. Within the wind velocity magnitude spectrum, frequencies with a significant contribution to the overall variance will appear as outliers to the associated probability distribution.

Figure 2.6 displays a histogram of the magnitude residuals (in logarithmic form) superimposed with a fitted probability distribution function. The residual distribution closely approximates a two-parameter extreme value distribution:

$$P_{res}(d, \mu_e, \sigma_e) = \sigma_e^{-1} e^{\frac{d - \mu_e}{\sigma_e}} e^{-e^{\frac{d - \mu_e}{\sigma_e}}} \quad (25)$$

where d is the logarithmic distance from the mean, μ_e is the distribution location parameter and σ_e is the distribution scale parameter. The fitted extreme value distribution has a location parameter of 0.0522 and a scale parameter of 0.2251. This distribution type is asymmetrical about the mean and is related to the Weibull distribution through a logarithmic transform. It represents the probability of encountering magnitude noise, of any particular amplitude, at a specific observation frequency. The occurrence probability of each frequency observation is calculated by substituting the residual magnitude, d , into the probability density function, $P_{res}(d, \mu_e, \sigma_e)$. Repeating this process over the entire single-sided DTFT produces $N/2$ independent probability observations spanning the frequencies defined in Eq. (28).

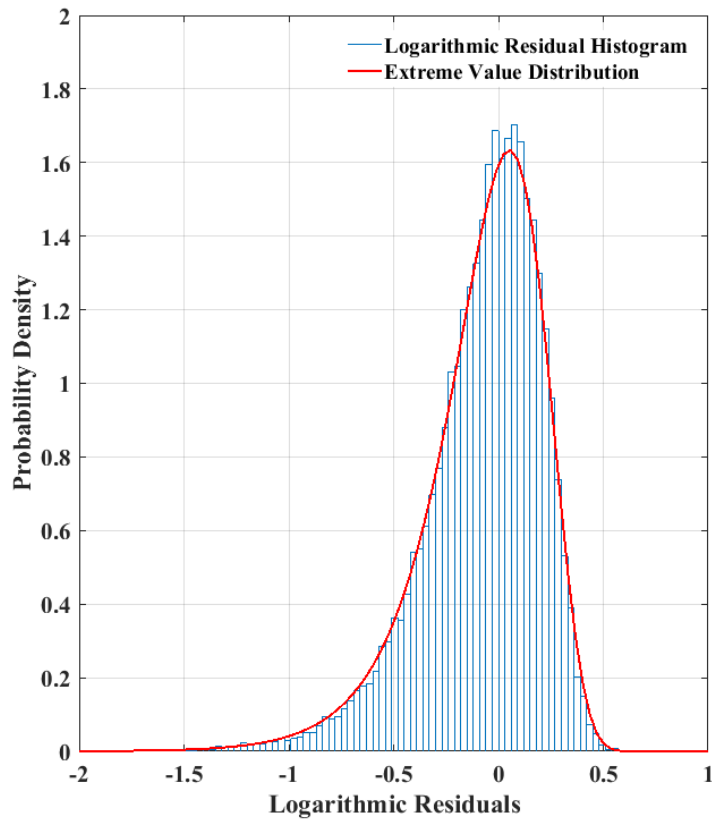


Figure 2.6: Probability Distribution Model of Magnitude Residuals

The statistical significant of each noise observation calculated to evaluate its statistical significance. The p-magnitude is used to quantify this value:

$$p_{val}(n) = \{1 - P_{res}(d(n), \mu_e, \sigma_e)\}^{N/2} \quad (26)$$

where $p_{val}(n)$ is the observation p-value. Residuals with a p-value less than 0.05 are considered statistically significant – they are significantly less likely than the largest outlier expected from a dataset of size N. The presence of any statistically significant noise observations indicating that a periodic trend exists in the underlying time-domain data with a period defined by the associated frequency.

Identification of any significant variance frequencies suggest the random-process assumption of original filtering algorithm was violated. The logarithmic moving average DTFT magnitude is disproportionately shifted towards the high-magnitude outliers. An iterative process is used where any statistically significant residuals are excluded from the filtering algorithm, separating their contribution from the underlying noise behavior. The value of $F_{mean}(k)$ is calculated using the remaining observations. The magnitude of any significant variance observation is corrected by subtracting the co-located mean magnitude from the original observation. The iterative process continues until a repeated residual evaluation fails to identify a previously-unknown magnitude outlier. The final identified outlier frequencies represent the wind regime's statistically significant periodic variation.

Figure 2.7 displays the corrected logarithmic mean amplitude spectrum. The original magnitude spectrum and the uncorrected logarithmic mean are superimposed. The corrected logarithmic mean shows a smooth transition between low-frequency 1/f noise (at

periods greater than 4 months), white noise (at periods between 4 months and 4 days), Kolmogorov pink noise (periods between 4 days and 6 hours) and high-frequency white noise (at periods less than 6 hours). The effect of removing the statistically significant variance frequencies is visible, especially that due to the seasonal-cycle variability. The frequency/magnitude behavior of the wind velocity data is a measure of the intermittency in the wind resource, with the energy contained within each band a measure of the overall wind velocity variability expected at different observation frequencies.

Table 2.2 displays the statistically significant variance signals, their probability of occurrence and the resulting observation p-value. Signals with extremely low probabilities of occurrence indicate that a chance observation is unlikely, signaling a greater degree of

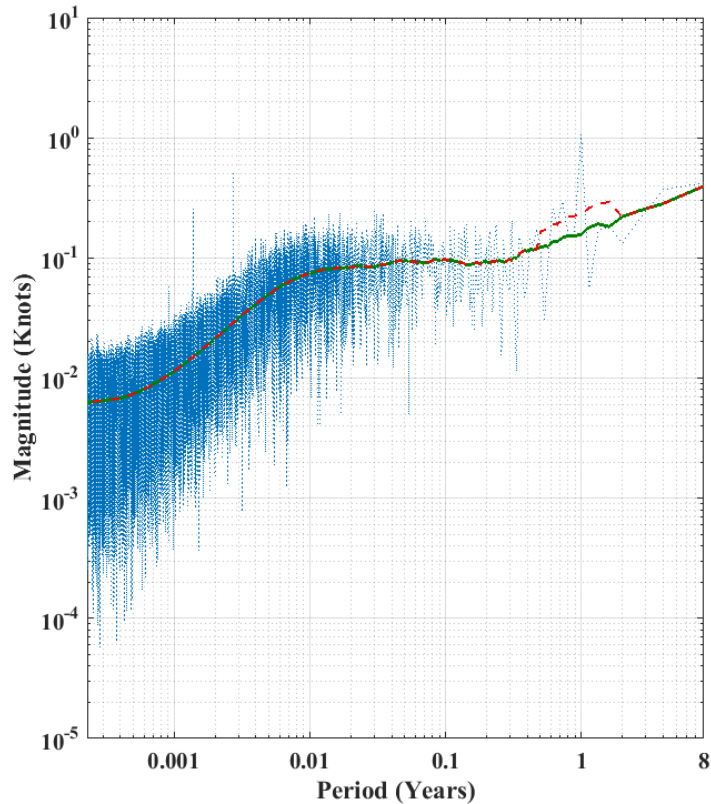


Figure 2.7: Logarithmic Mean of the Wind Velocity Magnitude Spectrum

statistical significance. The iterative filtering algorithm identifies statistically significant variance at observation periods of 1 year, 1 day, 12 hours and 8 hours, with occurrence probabilities of 2.10×10^{-14} , 5.97×10^{-100} , 2.89×10^{-109} and 1.51×10^{-8} , respectively. Given the sample size ($N = 70124$), these observations all have P-values significantly less than 0.05, indicating statistical significance. The identified statistically significant variance signal corresponds to a nearly sinusoidal seasonal variance signal with a superimposed, more complex diurnal signal with harmonic distortion. Some minor non-stochastic variance may exist at additional frequencies, however, the original wind data and DTFT algorithm lacks the magnitude and frequency resolution to isolate them from the underlying magnitude noise.

Table 2.2: Statistically Significant Magnitude Residuals

Index	Period (h)	Probability	P-Value
2923	24	2.89×10^{-109}	0
5845	12	5.97×10^{-100}	0
9	8766	2.10×10^{-14}	7.40×10^{-10}
8775	8	1.51×10^{-8}	0.000530
8759	8	1.56×10^{-6}	0.0533

The assumption of random, extreme-value distributed noise superimposed on the log-mean frequency spectrum is verified by calculating the frequency autocorrelation of both the observation magnitudes and phases. Figure 2.8 displays the magnitude autocorrelation signal. The maximum non-zero lag autocorrelation is less than 0.2, with no significant

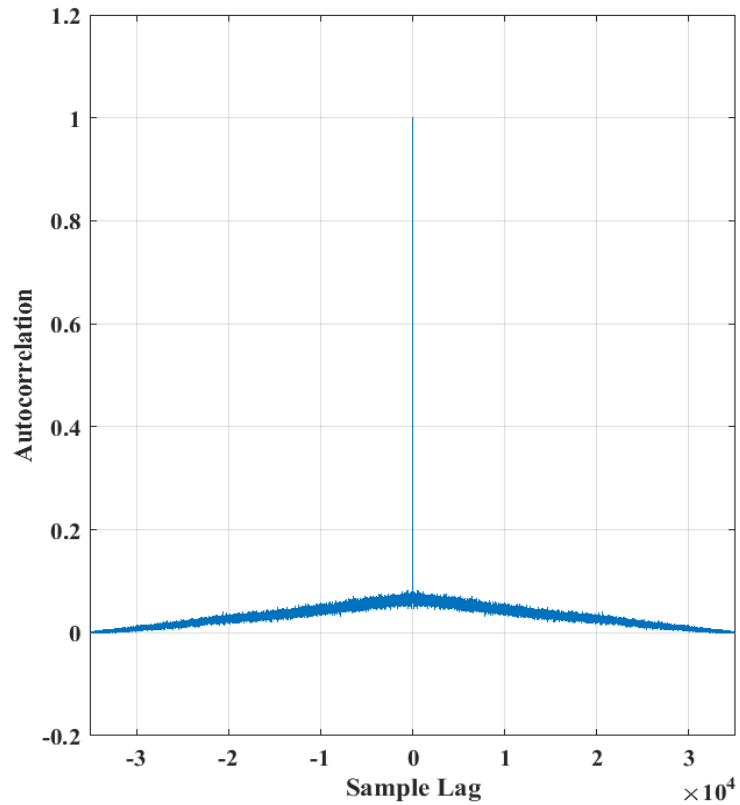


*Figure 2.8: Magnitude Residual Frequency
Autocorrelation*

outliers in correlation magnitude. Within the limits imposed by a finite random process with band-dependant variance, the autocorrelation signal is consistent with the assumption that the magnitude residuals are accurately modeled as an extreme-value distributed random variable. Therefore, the wind velocity data is modeled (in the frequency domain) as this random variable superimposed on the site-specific large bandwidth variance function.

Figure 2.9 displays the identified statistically significant variance signals reconstructed into the time domain. The signal amplitude determines the amount of variance – the signal phase places this variance within the appropriate (annual or diurnal) time frame. In this case, a phase of 0 degrees corresponds to January 1st and 12:00 a.m., respectively. A seasonal variability with an amplitude of 2 knots and a phase of roughly -5 degrees is present, indicating a significant statistical wind velocity maxima which occurs during December. The minima occurs during June, with a mean wind velocity value approximately 4 knots lower. The diurnal signal is more complex, with significant second and third harmonics of variable phase distorting the underlying sinusoidal pattern. The diurnal signal has a peak to peak amplitude of roughly 2.5 knots, with a maxima at roughly 12 pm and a

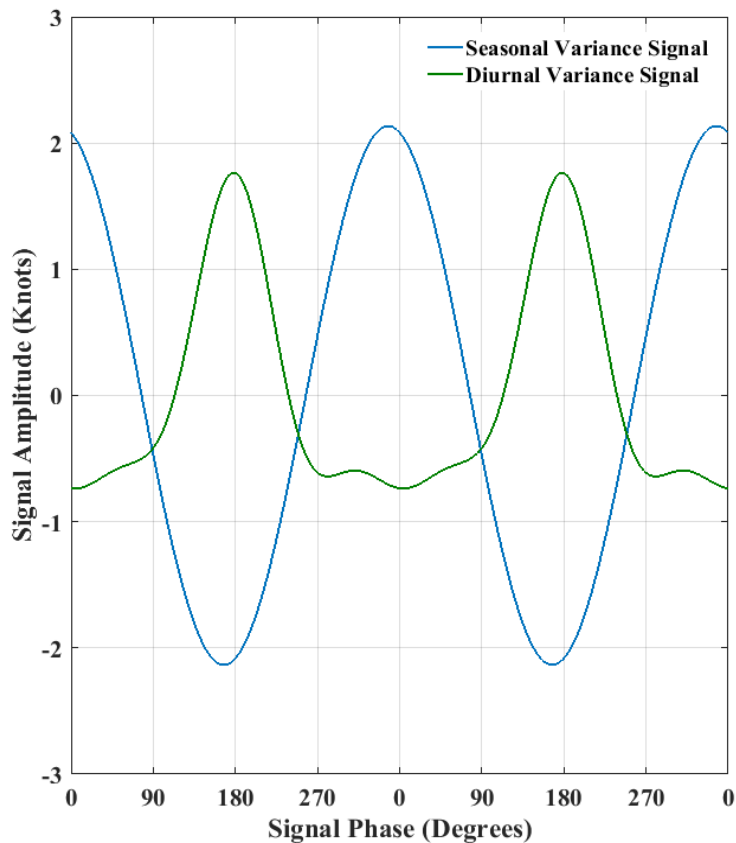


Figure 2.9: Spectrally Identified Variance Signals

minimum between 6 p.m. and 6 a.m. However, these are rough approximations of the true nonstationary behavior. To identify the effect the identified variance has on the probabilistic nature of the wind resource, a feature extraction algorithm is required.

2.6.3: Nonstationary Feature Identification

The frequency domain analysis algorithm identified statistically significant nonstationary variance periods, σ_1 and σ_2 , corresponding to diurnal and seasonal patterns. A bivariate environmental dataset (comprised of wind velocity and air density data) must be decomposed in such a manner as to isolate the effect of this nonstationary variance. To model the diurnal-cycle variance contributor σ_1 , the length N bivariate environmental dataset, $[x_1(n) \ x_2(n)]$, must span at least one full period, T_1 . The dataset can be reconfigured from a discrete time series into a $k \times n \times 2$ matrix,

$$\begin{bmatrix} x_{\sigma_1}(k, n, 1) \\ x_{\sigma_1}(k, n, 2) \end{bmatrix} = \begin{bmatrix} x_1(n + (k - 1)T_1) \\ x_2(n + (k - 1)T_1) \end{bmatrix} \quad 0 < n \leq T_1 \quad (27)$$

The feature extraction algorithm is applied recursively to capture joint probabilistic variance existing at sufficiently spaced periods. Assuming the second variance contributor σ_2 has a period $T_2 \geq 2T_1$, the following multidimensional dataset is generated:

$$\begin{bmatrix} x_{\sigma_1\sigma_2}(j, k, n, 1) \\ x_{\sigma_1\sigma_2}(j, k, n, 2) \end{bmatrix} = \begin{bmatrix} x_{\sigma_1}(j, n + (k - 1)T_2, 1) \\ x_{\sigma_1}(j, n + (k - 1)T_2, 2) \end{bmatrix} \quad (28)$$

where $x_{\sigma_1\sigma_2}$ is a 4-dimensional matrix. Each plane indexed (j, k) contains n bivariate data samples, providing the data organization required for probabilistic modeling.

2.7: Multidimensional Wind Resource Modeling

The joint probability distribution of two uncorrelated random variables is calculated analytically by multiplying the individual marginal distributions. In the bivariate (wind velocity and air density) case, the result is a two-dimensional condition space with an associated matrix of probability values. Using marginal distributions calculated by applying the unidimensional Kernel smoothing algorithm to each environmental dataset,

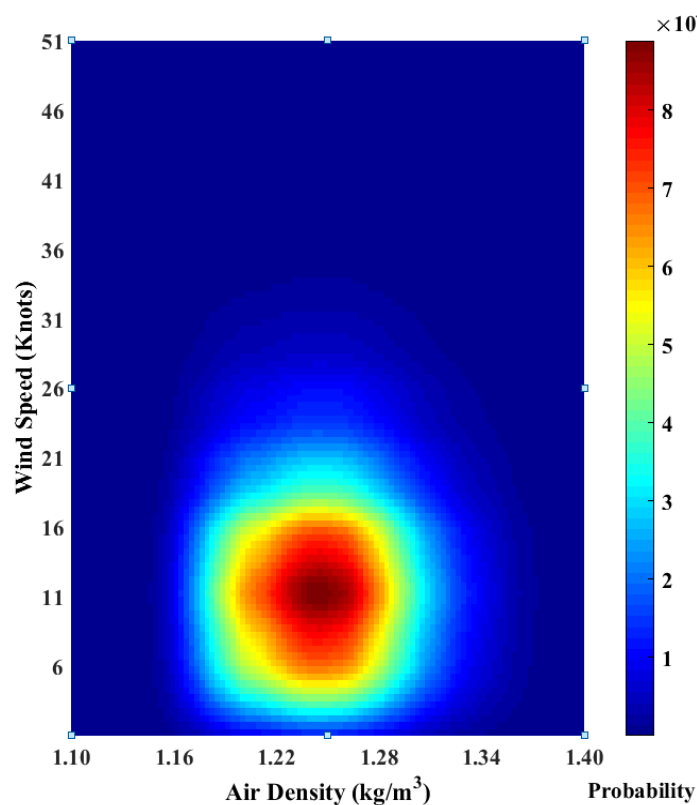


Figure 2.10: Simple Joint Wind/Density Probabilistic Model

the joint wind velocity/air density distribution is determined. Figure 2.10 displays the developed probability distribution. This distribution is strongly unimodal, with a peak at a wind velocity of ~ 12 knots and an air density of ~ 1.25 kg/m^3 . The occurrence probability monotonically decreases with displacement from these conditions, with the effect of each marginal distribution visible within the overall shape of the bivariate distribution. Assuming that wind velocity and air density are uncorrelated, this joint distribution produces an accurate model of the site wind resource

The assumption of variable independence is tested by examining the correlation coefficient between each seasonal/diurnal subset of the environmental data. This process examines the time-variant correlation between the site wind velocity and air density. Figure

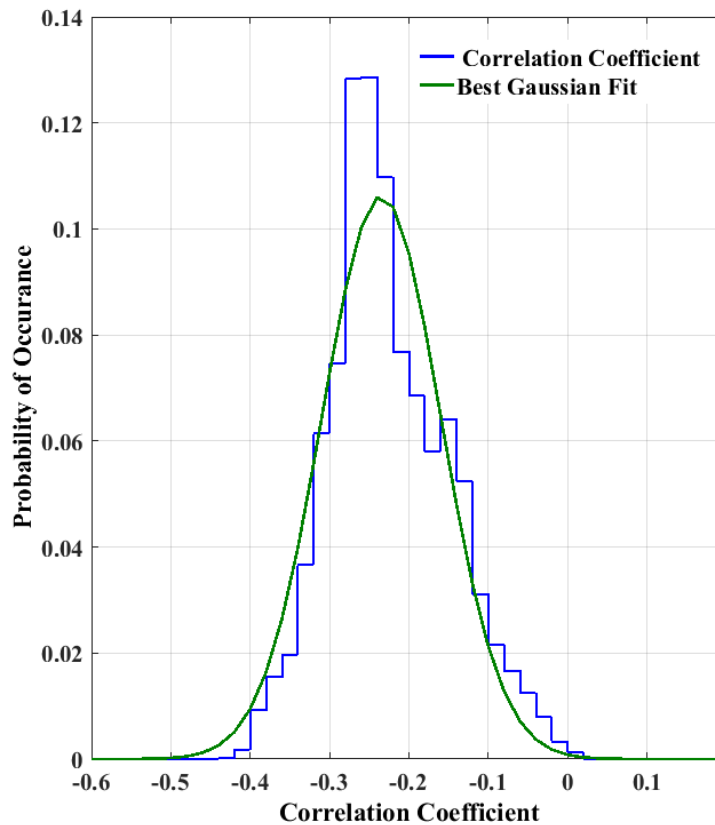


Figure 2.11: Wind/Density Correlation Distribution

2.1.1 displays the distribution of correlation coefficients and a Gaussian approximation. The wind velocity and air density datasets are negatively correlated, with a mean correlation coefficient of roughly -0.2. The observed correlation coefficients range from 0 to -0.4, indicating a moderate (but significant) negative correlation between environmental variables. The distribution does not include zero within 2 standard deviations of the mean, strongly suggesting that the result is statistically significant. This correlation exists through essentially all of the seasonal/diurnal subsets, indicating that a joint distribution model must include variable dependence to accurately reflect the true site environmental conditions and accurately estimate the wind resource. This is accomplished through the use of a multidimensional, optimized nonparametric probabilistic modeling algorithm.

2.7.1: Multivariate Optimized Nonparametric Probabilistic Modeling

The kernel smoothing algorithm presented earlier can be generalized to multiple dimensions. Treating each data point as a zero-covariance Gaussian distribution, a n -dimensional multivariate Kernel Density Estimate (KDE) can be expressed as a Gaussian mixture model [46],

$$f_G(x) = \sum_{i=1}^N x_i \varphi_H(x - x_i) \quad (29)$$

where

$$\varphi_H(x - x_c) = (2\pi)^{-\frac{n}{2}} |H|^{-\frac{1}{2}} e^{(-1/2)(x-x_c)^T H^{-1} (x-x_c)} \quad (30)$$

represents the selected Gaussian kernel function centered at the point x_c and with a covariance matrix H . The Kernel Density Estimate (KDE) is developed by convolving the sample distribution $f_G(x)$ with a Gaussian kernel that has a covariance matrix H_k (the kernel bandwidth) [47]:

$$f_k(x) = \sum_{i=1}^N x_i \varphi_{H+H_k}(x - x_c) \quad (31)$$

The model is a multivariate approximation of the underlying probability density developed by the summation of N Gaussian kernels centered at each observation. The accuracy of the KDE is dependent on the kernel bandwidth. Appropriate bandwidth selection is vital to the development of an optimal probabilistic model.

A popular method of evaluating the accuracy of the KDE $f_k(x)$ is the asymptotic mean integrated square error (AMISE), as presented in [48],

$$AMISE = (4\pi)^{-\frac{n}{2}} |H|^{-\frac{1}{2}} N_\alpha^{-1} + \frac{1}{4} n^2 \int tr^2 \{HG_p(x)\} dx \quad (32)$$

where tr is the trace operator, $G_p(x)$ is the Hessian of the underlying multivariate probability distribution and N_α is defined as [47]

$$N_\alpha = \left[\sum_{i=1}^N \alpha_i^2 \right]^{-1} \quad (33)$$

The optimal bandwidth of the KDE is determined by minimizing the AMISE. Matej et al. [46] present a on-line, computationally efficient method of bandwidth optimization which is used to generate the required KDEs.

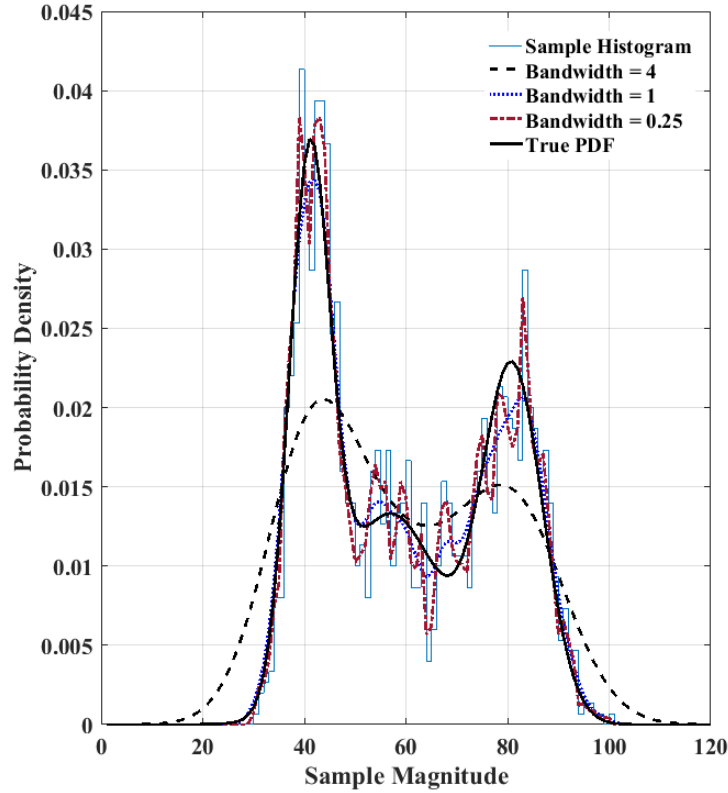


Figure 2.12: Effects of Bandwidth on Kernel Density Estimators

Figure 2.12 displays the effect of bandwidth selection on the KDE fitting algorithm. The true PDF is generated as a summation of three Gaussian distributions with varying mean and standard deviation parameters. For each distribution, 500 random points are generated and used as input to the univariate version of the KDE algorithm Eqs. (12-14). Three bandwidths are selected to demonstrate the effect on fitting accuracy: 0.25, 1 and 4. The smallest bandwidth shows clear over-fitting behavior, while the largest bandwidth shows significant underfit. The best overall approximation is shown by the KDE with a bandwidth of 1. The optimal bandwidth varies based on the quantity of samples and their underlying distribution, and will tend to minimize the probability of over or under-fitting the true distribution given a random, finite sample set.

Figure 2.13 displays the bivariate kernel distribution generated using the total wind velocity and air density datasets. It is observed that the distribution significantly departs from the product of the marginal distributions, validating the observed correlation. While the distribution shape is similar, the actual joint probability values are substantially different, covering a wider range of potential conditions and introducing secondary modes to the general distribution. The more complex joint distribution model provides more accurate information for use in wind resource assessment and modeling. However, the nonstationary behavior revealed in the previous sections must be taken into account. A time-variant extension to this multidimensional probabilistic model is required to fully define the site wind resource.

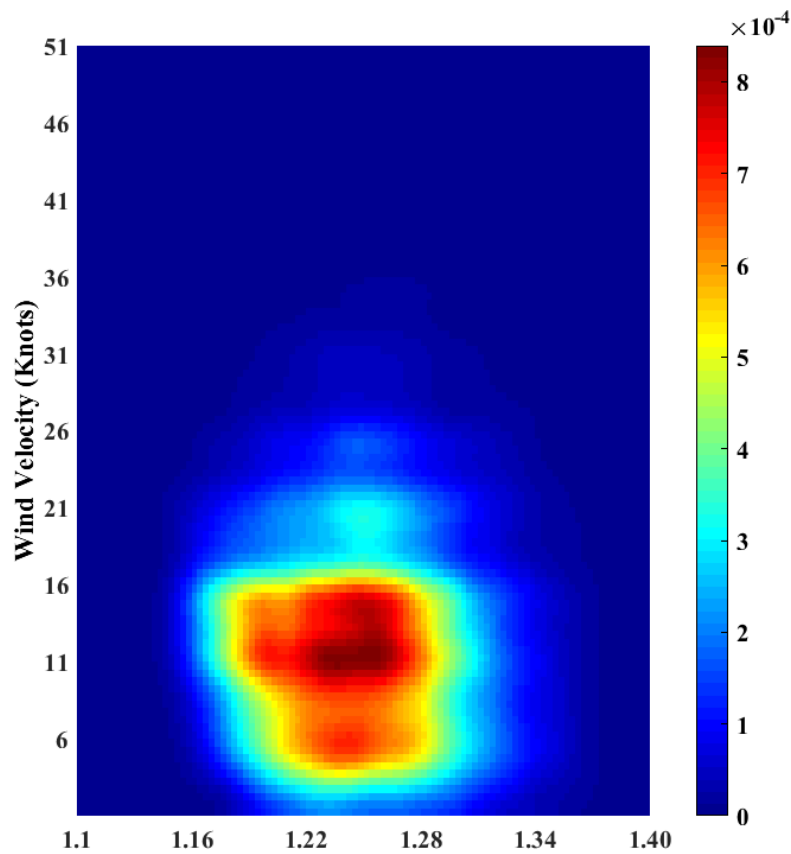


Figure 2.13: A Bivariate Probabilistic Wind/Density Model

2.7.2: A Time-Variant Bivariate Wind Resource Model

The bivariate environmental dataset $R_E(n)$ is passed through the nonstationary feature extraction algorithm. The previously identified periodic variance features, σ_1 and σ_2 , are extracted from the following bivariate environmental dataset,

$$R_{E\sigma_1\sigma_2} = \begin{bmatrix} \begin{bmatrix} V(1,1,1:m) \\ \rho(1,1,1:m) \\ \vdots \end{bmatrix} & \cdots & \begin{bmatrix} V(1,j,1:m) \\ \rho(1,j,1:m) \\ \vdots \end{bmatrix} \\ \begin{bmatrix} V(k,1,1:m) \\ \rho(k,1,1:m) \end{bmatrix} & \cdots & \begin{bmatrix} V(k,j,1:m) \\ \rho(k,j,1:m) \end{bmatrix} \end{bmatrix} \quad (35)$$

where $V(k,j,m)$ is a vector of wind velocity observations, $\rho(k,j,m)$ is a vector of air density observations and the plane (k,j) defines the observation phase with respect to σ_1 and σ_2 the diurnal and annual environmental variance. The bivariate case of (37-41) is applied to each planar point to define a KDE corresponding to the environmental conditions expected at that time. The resultant 5 dimensional model object is presented in (42):

$$F_{K\sigma_1\sigma_2} = \left[\begin{array}{ccc} \begin{pmatrix} F_K(1,1,V_1,\rho_1) & \cdots & F_K(1,1,V_{n_v},\rho_1) \\ \vdots & \ddots & \vdots \\ F_K(1,1,V_1,\rho_{n_\rho}) & \cdots & F_K(1,1,V_{n_v},\rho_{n_\rho}) \end{pmatrix} & \cdots & \begin{pmatrix} F_K(1,j,V_1,\rho_1) & \cdots & F_K(1,j,V_{n_v},\rho_1) \\ \vdots & \ddots & \vdots \\ F_K(1,j,V_1,\rho_{n_\rho}) & \cdots & F_K(1,j,V_{n_v},\rho_{n_\rho}) \end{pmatrix} \\ \begin{pmatrix} F_K(k,1,V_1,\rho_1) & \cdots & F_K(k,1,V_{n_v},\rho_1) \\ \vdots & \ddots & \vdots \\ F_K(k,1,V_1,\rho_{n_\rho}) & \cdots & F_K(k,1,V_{n_v},\rho_{n_\rho}) \end{pmatrix} & \cdots & \begin{pmatrix} F_K(k,j,V_1,\rho_1) & \cdots & F_K(k,j,V_{n_v},\rho_1) \\ \vdots & \ddots & \vdots \\ F_K(k,j,V_1,\rho_{n_\rho}) & \cdots & F_K(k,j,V_{n_v},\rho_{n_\rho}) \end{pmatrix} \end{array} \right] \quad (36)$$

For each planar point (k,j) , a bivariate KDE is generated and evaluated at points $(V_1:V_m)$ and $(\rho_1:\rho_m)$, with (n_v, n_ρ) being the respective size of the observation space. The model in (12) includes the effect of cross-correlation between wind velocity and air density, diurnal and seasonal phase, as well as any multimodal or parametric mixture evident in the probability distribution.

Due to the use of diurnal and seasonal feature patterns, the resulting probabilistic model corresponds to the expected wind velocity / air density regime organized according to the date and time of observation. Figure 2.14 displays sample probabilistic models corresponding to diametrically opposite annual and diurnal phases. The model data subsets are selected to display the extrema in the annual and diurnal phases, displaying the degree of time variance within the underlying environmental conditions. As observed, the wind-density model indicates a substantially greater overall wind resource during February, a function of the strong annual signal shifting both the wind velocity and air density distributions to higher values. During this period, the diurnal signal is relatively weak, but still has a slight effect on the shape and positioning of the joint probability distribution. During August, the opposite occurs. The diurnal signal (due to daytime heating) is much stronger, substantially shifting the wind/density distribution towards regions of lower air density (a function of temperature and barometric pressure) and higher wind velocity. The spatial extent of the wind/density models also varies with the annual and diurnal phase. The spatial extent of the model is a measure of the intermittency and variability of the wind resource. Essentially, during the winter months more wind power is available (due to a shift towards higher values of both variables); however, the range of possible conditions is

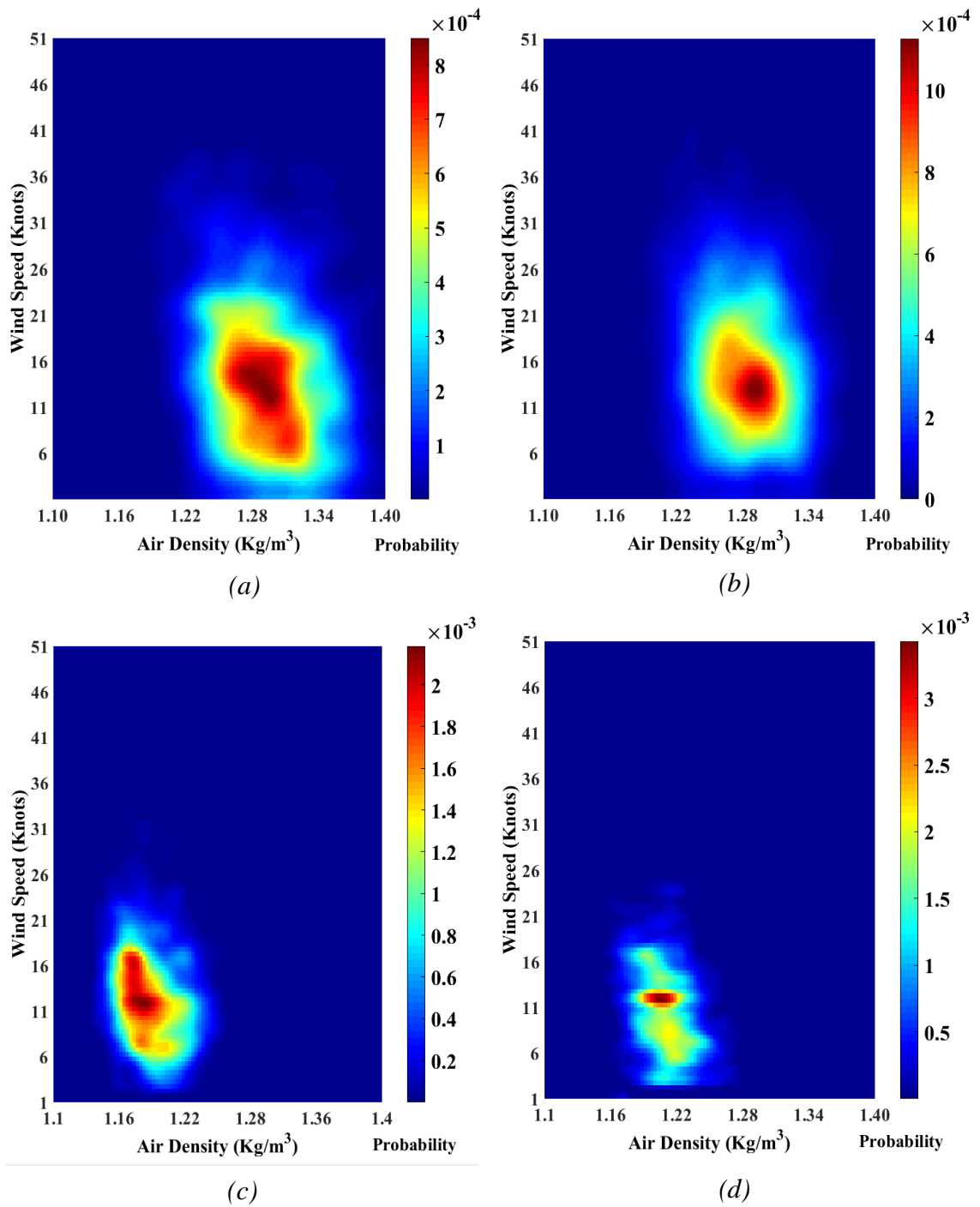


Figure 2.14: The Bivariate Wind Resource Model during (a) February at 5:00 a.m., (b) February at 5:00 p.m., (c) August at 5:00 a.m., and (d) August at 5:00 p.m.

larger. During the summer months (especially at night) the wind resource is less variable,

indicating lower (but more consistent) wind turbine output. The bivariate, time variant probabilistic model details this variance in environmental conditions, allowing complete seasonal/diurnal analysis of the site's wind resource.

Quantification of the site's wind resource is conducted by treating the probabilistic model as a discrete function. The mean wind power density is calculated at each seasonal/diurnal phase by substituting the appropriate probabilistic model into the fundamental wind power equation. The weighted summation across the probabilistic model allows an accurate determination of the mean wind power density, with normalization and unit conversions conducted as appropriate. Figure 2.15 displays the site wind power density

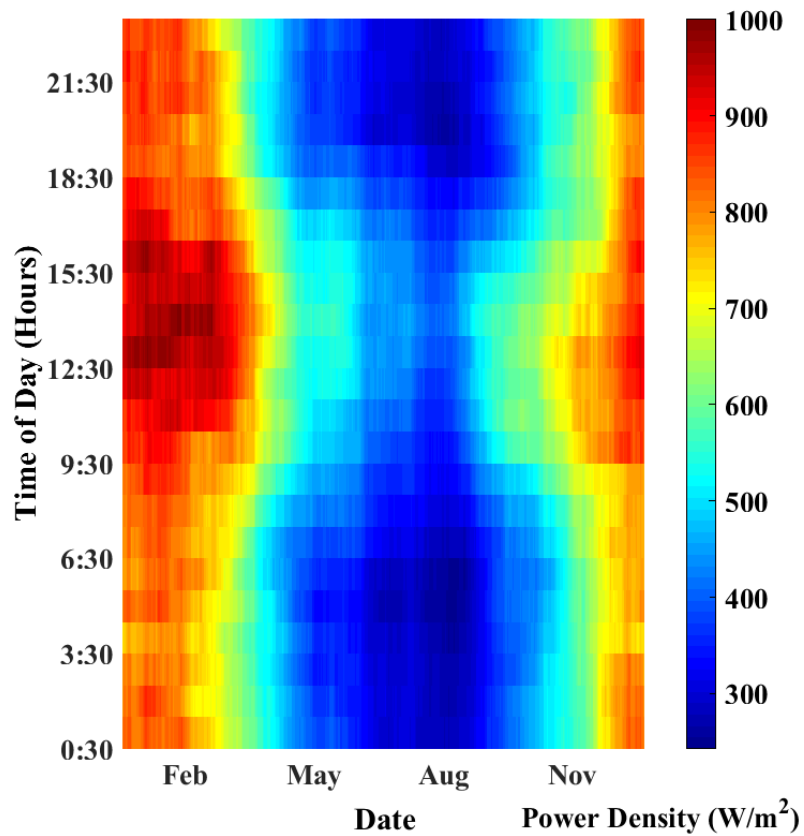


Figure 2.15: A time-variant model of site wind power density

obtained using the proposed time-variant multidimensional model. The mean wind power density shows significant variance as both a function of annual and diurnal phase, correlating with the observed variability in the underlying environment data. This probabilistic model of wind power density allows evaluation of wind system feasibility through comparison with the site electrical demand profile. In addition, site selection can be conducted with a higher degree of time-frequency resolution through the replacement of standard wind energy atlases with site-specific probabilistic wind power density models.

2.7.3: Model Validation

The performance of the proposed multidimensional modeling algorithm is evaluated through comparison with two existing methodologies: the bivariate single distribution model presented in [49] and [50], and the time-variate product of marginal distributions presented in Figure 2.10. The performance of the various models is evaluated through their correlation to the environmental data. For validation purposes, the models will be designed using an older 20 year dataset (taken from 1990-2009) and then tested against a more recent 5 year dataset (2010-2014). The performance of the proposed model is evaluated by calculating the correlation coefficient between each time-variant model object (corresponding to the annual and diurnal phase) and the empirically determined cumulative distribution function of the underlying data. The resulting value (R^2) measures the fit between the model distribution and the underlying wind/density dataset. The overall

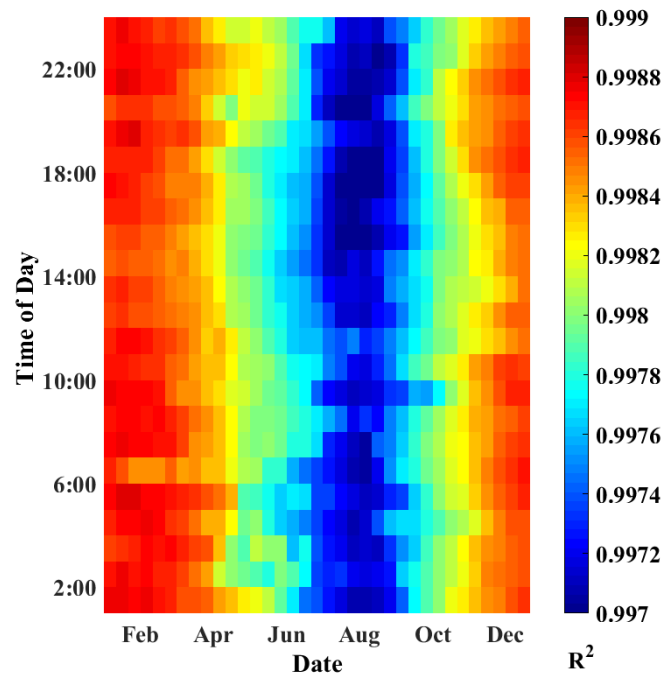
accuracy of the model is determined by averaging all time-variant R^2 samples to produce the mean model correlation. The correlation coefficient is computed in two dimensions, comparing the bivariate cumulative distribution function to the dataset empirical cumulative distribution [51]:

$$R^2(j, k) = \frac{\sum_{j=1}^n \sum_{i=1}^m [(ECDF(j, k, i_c, i_e) - \overline{ECDF(j, k)}) (CDF(j, k, i_c, i_e) - \overline{CDF(j, k)})]}{\sqrt{\{\sum_{j=1}^n \sum_{i=1}^m (ECDF(j, k, i_c, i_e) - \overline{ECDF(j, k)})^2\} \{\sum_{j=1}^n \sum_{i=1}^m (CDF(j, k, i_c, i_e) - \overline{CDF(j, k)})^2\}}} \quad (37)$$

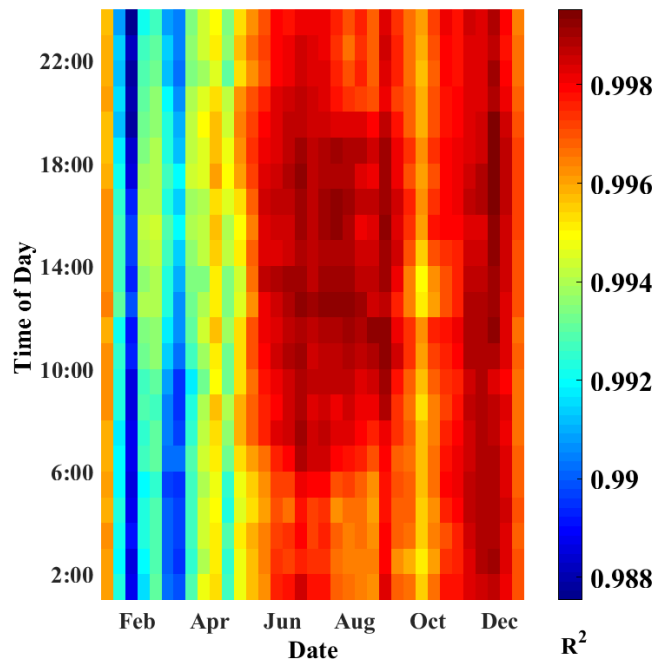
where (j, k) is the diurnal and seasonal phase of the cumulative distributions, (i_c, i_e) the position within the CDF/ECDF and the bar operator symbolizing the two-dimensional expected value. Figure 2.16(a) and (b) illustrate the proposed model's correlation within the design dataset and the validation dataset, respectively.

Within the design dataset, the proposed model fits the data with very high accuracy, with R^2 values ranging from 0.997 to 0.999. This is due to the convergence of the bivariate kernel smoothing algorithm. The degree of fit is slightly less during periods where the empirical distribution covers a small spatial area, with the best fit occurring with a wide underlying wind/density distribution. This behavior is no longer evident when using the validation set. The 5 year validation period has a slightly different underlying distribution due to the effects of (at this scale) random storm events, climate cycles and the general smaller size of the dataset. The correlation coefficient is therefore somewhat lower, ranging from 0.988 (during winter periods subject to random storm events disrupting the distribution) to 0.9985 for the majority of the remaining interval. The accuracy of the proposed model remains high using the validation dataset, verifying that the previously observed model performance can be expected when applying a designed model to future

observations. The relative performance of the proposed model is evaluated by comparing



(a)



(b)

Figure 2.16: Model Correlations using (a) the design datasets and (b) the validation dataset

the produced correlation values to equivalents generated using the pre-existing modeling methodologies. Figure 2.17 displays the correlation distributions of the three model types using the validation dataset. The mean correlation, the standard deviation stemming from time-variance and the 95% confidence bounds are tabulated to compare the performance of each model. Within both the design and validation datasets, the proposed model exhibits a superior correlation to the empirical data. The mean correlation of the proposed model is 0.9981 (design) and 0.9962 (validation) with the closest comparison the single bivariate distribution at 0.9592 (design) and 0.9604 (validation). This effectively corresponds to an error 10 times larger than the proposed model. The time-variant univariate distribution lags both models due to the lack of modeled wind/density correlation. The proposed model also

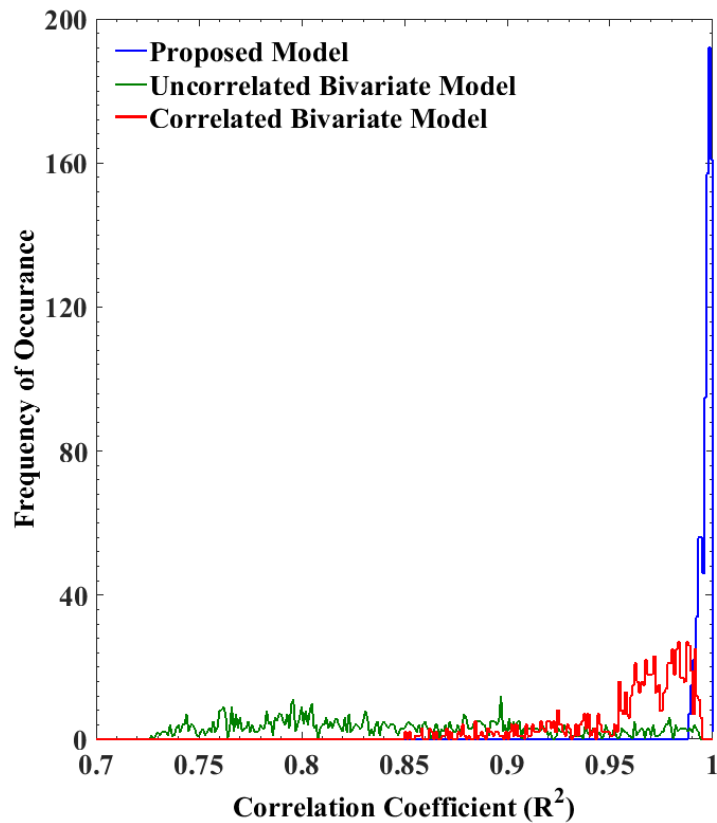


Figure 2.17: Distribution of Correlation Coefficients of Probabilistic Models

has a lower standard deviation, indicating more consistent time-variant performance. Using the validation dataset, the correlation coefficient of the proposed model is never lower than 0.98 and has a peak occurrence very close to 1. Both comparison models have periods of correlation under 0.9, with the univariate model ranging as low as 0.75. Additionally, there is no overlap between the respective 95% confidence bounds, indicating that the superior performance of the proposed model is not due to chance and represents an improvement in model accuracy. Overall, the proposed model is shown to be both valid for prediction of future probabilistic wind resource behavior, and superior to previously defined modeling methods under all observed conditions. The improvement in wind resource modeling can therefore be applied to wind turbine performance estimation, HWES design and the optimization of wind turbine design and installation.

2.8: Conclusions

A novel hybrid time/frequency analysis and modeling framework is developed to identify and model time-variance within a bivariate environmental dataset. Frequency domain analysis identifies and quantifies statistically significant time-variance in the nonstationary site wind velocity and air density statistics. A feature extraction algorithm is formulated to extract the nonstationary components from the environmental dataset. The refined dataset is organized to allow an optimized nonparametric kernel smoothing algorithm to produce a multi-dimensional probabilistic model that numerically characterizes the time-variant wind/density distribution. The modeling methodology accounts for bivariate cross- correlation as well as the identified nonstationary behavior.

The performance of the probabilistic model is validated by splitting the environmental dataset into design and validation segments, using 5 years of additional environmental data to validate the probabilistic model. This methodology ensures apriori as well as aposteriori model accuracy. The multidimensional, nonparametric probabilistic model provides improved time resolution in addition to a more accurate time-variant bivariate probability distribution, allowing high resolution probabilistic assessment of a site wind resource. The development and implementation of this novel modeling methodology advances the evaluation of a site's wind potential, turbine installation feasibility and allows probabilistic assessment of system contingencies, representing an improvement in the area of wind resource modeling.

Chapter 3: Probabilistic Assessment of Wind Reserves

3.1: Introduction

In this Chapter, the previously presented wind resource modeling methodology is augmented by advanced demand and wind turbine output modeling algorithms. The result is the presentation of a unified probabilistic approach for the assessment of wind reserves in islanded microgrids. The proposed model includes time-variant probabilistic wind resource modeling, probabilistic load modeling and an investigation into power system planning applications, including frequency regulation and demand response. Examples are provided using sample wind and demand data, with a full site case study left for presentation in a subsequent Chapter.

Recent advances in microgrid topologies have improved the feasibility of distributed generation. The continuing maturation of primary and secondary microgrid control algorithms leads to an emphasis on planning the implementation of distributed generation into existing microgrids. The installation of wind-based reserve generation provides flexibility to power system planners through its applications including: implementing peak-load demand response, its ability to provide secondary generation, as well as droop-based frequency regulation. Demand response (DR) [1]-[4] involves using fast-ramping generation (such as wind, solar or small hydro) to meet dynamic increases in electrical load during peaking periods. The energy supplied by DR units augments base-load and

secondary generation, reducing the reliance on slower thermal units during peak load periods. During periods of high energy availability, wind turbines can also provide secondary generation [5]-[6]. In microgrids, secondary generation (along with the base-load) is provided by the diesel generators – large thermal or nuclear plants are not available, especially during islanding periods. In standard power systems, frequency and voltage regulation is provided by dynamic stabilization systems embedded within conventional generation. Islanded microgrids cannot access these stabilization systems. In this case, wind generation can provide the required dynamic stabilization, including the regulation of microgrid frequency. The power inverter wind turbine / microgrid interface is sufficiently fast and stable to implement several methods of droop control, including P/f and the more complex configurations specific to various microgrid topologies [7]. The applications of wind generation for islanded microgrids justifies their installation wherever a significant amount of wind energy is available. Determining the feasibility of wind generation is a topic of ongoing investigation which is vital for the integration and management of renewable energy into microgrids [8]-[15].

Planning the integration of wind generation into an islanded microgrid requires algorithms that predict power system performance during any reasonable operating condition. The demand profile and wind energy availability must be modeled to allow optimization of system configuration. Current research in this field focuses on deterministic and probabilistic modeling, where techniques such as machine-learning algorithms and statistical tools are applied for demand and wind power forecasting to predict future system behavior [16]-[20]. These methods are best suited for short term planning of existing

systems as opposed to the assessment of long-term reserve capability. Machine learning is computationally expensive and unreliable during uncommon conditions that differ from previously extracted features. The drawbacks of deterministic modeling can be addressed by probabilistic approaches. Probabilistic power system planning estimates the probability of various system contingencies through analysis of the space of possible system behavior. Some preliminary research has been conducted in this area, including probabilistic demand forecasting [17] and studies on the effects of wind-based demand response on existing transmission systems [26], [20]. However, none of the previous studies focused on developing a probabilistic model combining demand profile and wind power availability for demand response and frequency regulation in islanded microgrids using wind reserves.

3.2: Probabilistic Demand Modeling

The previous Chapter has presented a probabilistic model of the site wind resource – allowing probabilistic estimation of wind turbine generation. A similar modeling methodology is required to model the electrical demand within a microgrid. During islanding conditions, the entirety of this demand must be supplied by local (distributed) generation, including any installed wind capacity when it is available. An advanced multidimensional probabilistic demand model is presented to form the basis of probabilistic wind reserve modeling, allowing probabilistic assessment of microgrid energy balance, demand response and the provision of secondary generation to be modelled using a unified methodology.

3.2.1: Overview of Electrical Demand

A unique characteristic of islanded microgrids is the reliance on local generation to supply electrical demand. Electrical demand is primarily the active power requirements of the microgrid, equating to the sum of all distributed loads and various transformer and line losses. The nature of electrical demand depends on the idiosyncratic characteristics of the microgrid, including the proportion of residential, commercial and industrial loads, the industries serviced, the site's climate and to some degree even the local culture. All of these factors influence the measured load profile. Figure 3.1 displays a sample of active power

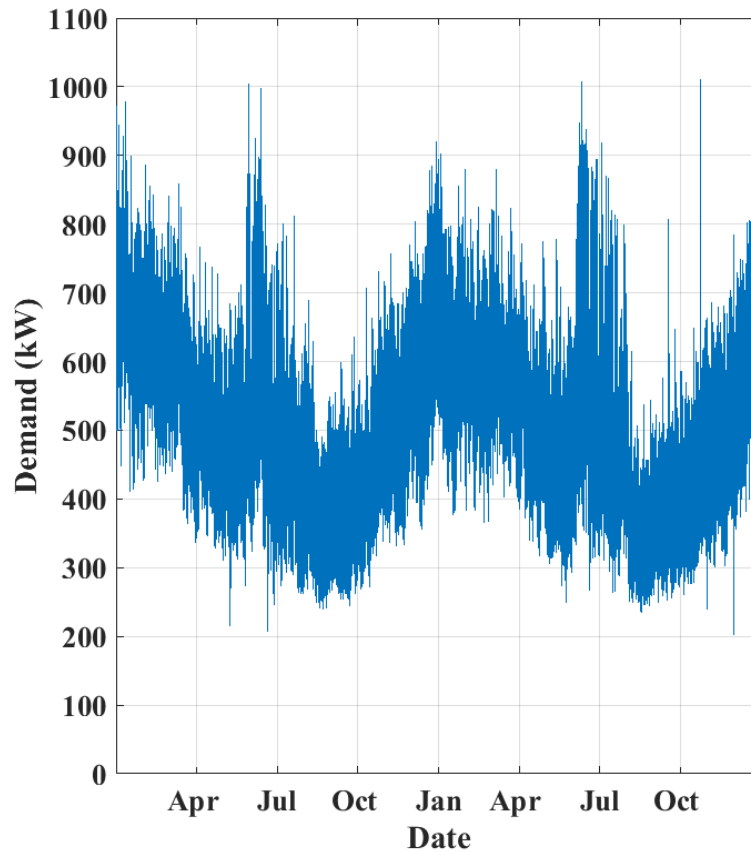


Figure 3.1: Sample Demand Data

demand, obtained over two years from an isolated microgrid. The load profile displays significant short and long term fluctuations, with short-period load minima ranging from 200 to 500 kW and maxima from 450 to 1000 kW. The mean microgrid demand is roughly 600 kW. Overall, the load data displays a high degree of variability at multiple timescales as well as complex non-sinusoidal periodic variance. The general statistical properties of the demand data are analyzed to perform an initial probabilistic assessment of the load profile. The load dataset is fitted to several probability distributions – the Gaussian, Gamma, Generalized Extreme Value, Lognormal and a nonparametric Kernel distribution. The parametric functional forms of the Gaussian, Lognormal and Kernel distributions are well known, and have been previously investigated in Chapter 2. The remaining probability distributions will be briefly overview before their fit to the load data is investigated.

The Gamma Distribution

The Gamma distribution is a two-parameter continuous probability distribution. The Gamma distribution family includes the exponential and chi-squared distributions – each is a special case. The general Gamma distribution has the following function form:

$$\gamma(x | \alpha, \beta) = \frac{\beta^\alpha}{\Gamma(\alpha)} x^{\alpha-1} e^{-\beta x} \quad (1)$$

where x is the variable of interest, α and β the positive, real distribution parameters and Γ the well-known Gamma function. The Gamma distribution has multiple applications, including signal processing, Bayesian statistics and climate modeling.

The Generalized Extreme Value Distribution

The Generalized Extreme Value distribution is a three-parameter, continuous probability distribution which includes the Gumbel, Frechet and Weibull distribution families. This distribution arises from extreme value theorem and has the following functional form:

$$G(x | \mu, \sigma, \xi) = \begin{cases} \frac{1}{\sigma} \left(1 + \xi \left(\frac{x - \mu}{\sigma}\right)\right)^{\frac{-1}{\xi}} e^{-(1 + \xi \left(\frac{x - \mu}{\sigma}\right))^{\frac{-1}{\xi}}} & \xi \neq 0 \\ \frac{1}{\sigma} e^{-\left(\frac{x - \mu}{\sigma}\right)} e^{-e^{-\left(\frac{x - \mu}{\sigma}\right)}} & \xi = 0 \end{cases} \quad (2)$$

where x is the variable of interest, μ the real-values location parameter, σ the positive real scale parameter and ξ the real-values shape parameter. The Generalized Extreme Value distribution is generally used in financial risk analysis. However, a risk exists when fitting this distribution, as the distribution moments (mean, variance, skewness and kurtosis) are undefined when the shape parameter is greater than 1, $\frac{1}{2}$, $\frac{1}{3}$ or $\frac{1}{4}$, respectively. Cursory statistical analysis using well-known techniques is often difficult when these criterion are encountered.

3.2.2: Stationary Probabilistic Load Modeling

Figure 3.2 displays the fitted probability distributions (Gaussian, Gamma, G.E.V, Lognormal and Kernel) of the 2-year load dataset. The electrical demand displays a reasonable continuous empirical distribution with minor multimodal behavior. Each of the parametric probability distributions overestimates the peak probability (occurring between 400 and 500 kW) while underestimating the probability of lower and higher demand near 300 and 750 kW. Essentially, the fitted parametric distributions have insufficient Kurtosis, however the mean, variance and skewness are reasonably accurate. The nonparametric

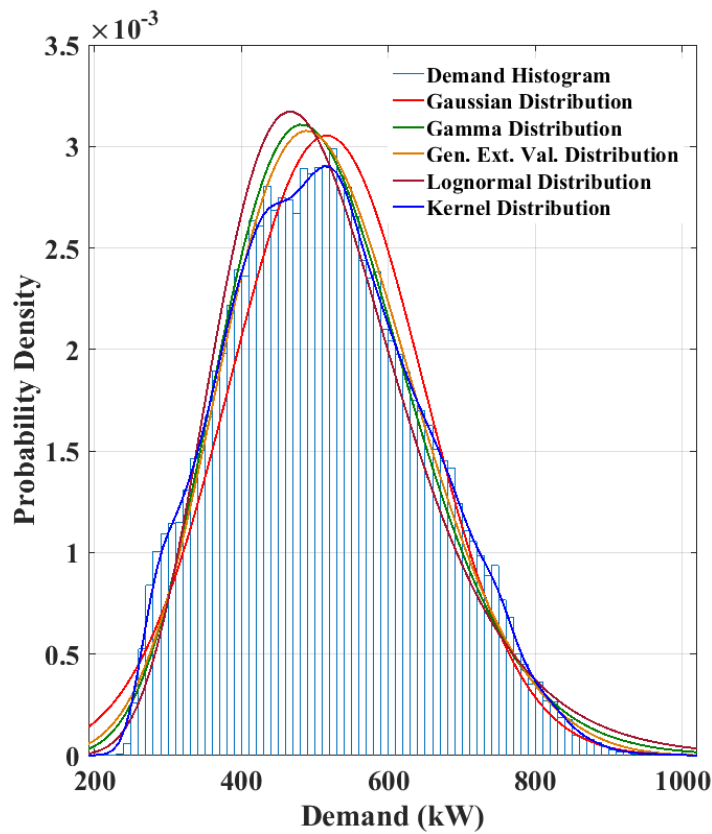


Figure 3.2: Demand Probability Distribution Models

Kernel smoothing distribution is more accurate – it successfully captures the multimodal nature of the empirical load distribution and exhibits correct tail weights. In addition, the nonparametric Kernel distribution captures the quick decline to zero probability at demand values under 250 kW or above 950 kW – regions where the parametric distributions still show significant probability mass. Overall, the nonparametric Kernel smoothing distribution displays the best visual fit to the load dataset.

The fitting accuracy of each probability distribution (quantified through the MAE, MAPE and RMSE) is displayed in Table 3.1. The visual assumption (that the Kernel smoothing distribution exhibits the best fit) is validated through all three prediction statistics – the Kernel distribution has a MAE, MAPE and RMSE of 0.000847, 0.1823 and 0.0011, respectively. For all prediction metrics, these errors are considerably smaller than the nearest competitors (values of 0.0062, 0.8074 and 0.0079 from the G.E.V, Lognormal and G.E.V distributions, respectively). The overall fitting accuracy of the nonparametric Kernel smoothing distribution indicates that it (similar to the wind velocity analysis) is the optimal fitting algorithm for probabilistic assessment of electrical demand.

Table 3.1: Stationary Probabilistic Load Model Prediction Errors

Distribution	MAE	MAPE	RMSE
Gamma	0.0078	2.0068	0.0093
G.E.V	0.0062	3.1016	0.0079
Lognormal	0.0117	0.8074	0.0148
Gaussian	0.0105	6.5891	0.0144
Kernel	0.000847	0.1823	0.0011

3.2.3: Nonstationary Behavior of Load Profiles

The analysis conducted in the previous system assumes that the load dataset is a stationary signal. Similar to the wind velocity analysis in the previous Chapter, this assumption significantly simplifies the probabilistic analysis, reducing the electrical demand model to a single probability distribution. The assumption of stationarity (or nonstationarity) must again be investigated to ensure its validity for the new dataset – otherwise important information is lost during the probabilistic modeling process. The well-known relationship between electrical demand and climate suggests the existence of nonstationary behavior. To validate, small subsets are drawn corresponding to measurement periods at diametrically opposite seasonal and diurnal phases. The previously defined nonparametric kernel distribution is fitted to four 124-element electrical demand subsets, with the resulting distribution compared to that of the entire 70179-element

demand dataset. The first four empirically determined distribution moments (mean, standard deviation, skewness and kurtosis) are compared across each subset. Any variation among these parameters indicates non-stationary behavior.

Figure 3.3 displays the fitted Kernel distributions of each data subset, along with that of the entire dataset. Significant and fundamental differences in the type and location of each probability distribution is evident. The modality, mean and variance of each distribution leads to a situation where there is little overlap between each subset, with the overall distribution reflecting a mixture model created by summation of the individual displaced subset distributions. This strongly suggests nonstationary characteristics in the demand

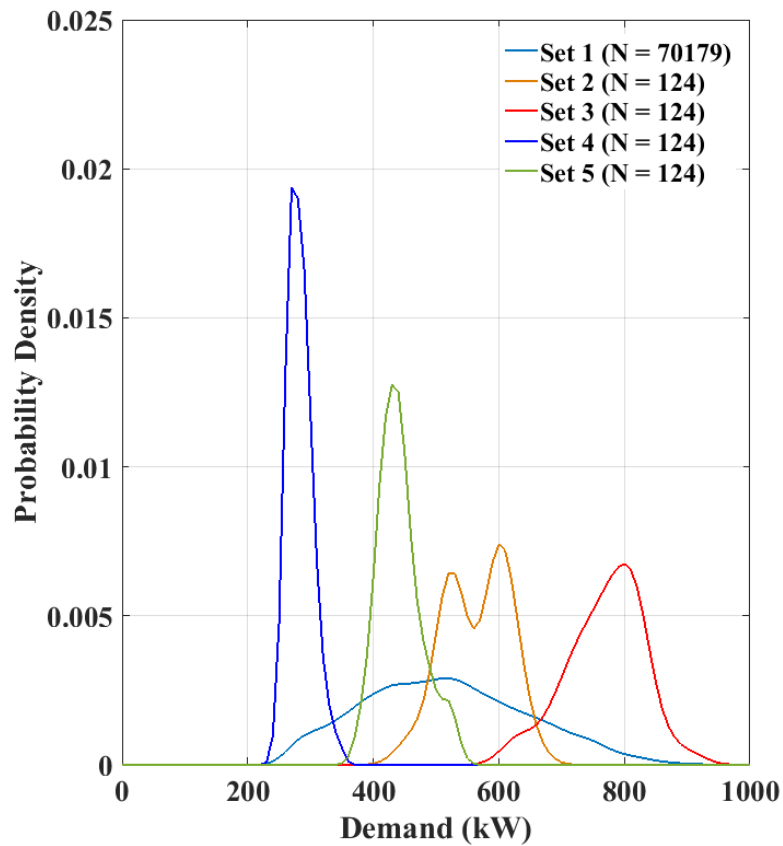


Figure 3.3: Probability Distributions of Demand Subsets

dataset. Table 3.2 displays the distribution moments associated with these subset (and the complete) probabilistic models. The mean demand varies from 283.3 kW to 768.9 kW – essentially a tripling in demand. The standard deviation varies from 19.1 to 60.4 kW – also a 3 to 1 variability. As a ratio of the mean, the standard deviation remains relatively constant. However, the distribution skewness also displays significant variance, with two datasets showing negative skewness and the remaining positive skewness. In addition, both platykurtic and leptokurtic behavior is evident. Essentially, the shape and location of the subset distributions are fundamentally different, lending credibility to the assumption of a nonstationary load dataset and invalidating single-distribution probabilistic modeling.

Table 3.2: Distribution Moments of Load Subsets

Dataset	Mean	Std. Deviation	Skewness	Kurtosis
Set 1 (N = 70179)	515.7676	130.6324	0.2861	2.5695
Set 2 (N = 124)	564.2089	49.5666	-0.2486	2.1159
Set 3 (N = 124)	768.9136	60.3940	-0.4488	3.0874
Set 4 (N = 124)	283.2813	19.0908	0.7636	3.4951
Set 5 (N = 124)	441.9026	33.8822	0.7042	3.1981

3.2.4: Frequency Domain Analysis

The identified nonstationary behavior of the electrical demand indicates that the augmented time-variant probabilistic modeling algorithms from the previous Chapter are also applicable. The demand dataset is modeled as a general discrete nonstationary dataset, $x(n)$, comprised of a stationary base dataset, $x_s(n)$, with nonstationary behavior modeled as superimposed periodic features, $x_{\sigma_1 \dots \sigma_n}$. The nonstationary variance periods, $\sigma_1 \dots \sigma_n$ which exist within $x(n)$ are identified (in a similar vein to the wind velocity data) to allow probabilistic modeling algorithms to accurately reflect this nonstationary behavior. The analysis framework detailed in Chapter 2 (based around wide-band frequency domain study) is capable of identifying and quantifying any periodic variance contributors within the demand data, allowing more advanced time-variant probabilistic analysis of the nonstationary microgrid electrical load profile. The highly nonstationary behavior evident from the previous section suggests that multiple variance contributors exist – their identification is vital to the development of an accurate, time-variant probabilistic demand model.

The frequency domain analysis algorithm presented in Chapter 2 was applied to the electrical demand dataset to isolate any statistically significant variance contributors. Figure 3.4 displays the Fourier amplitude spectrum, the logarithmic moving average as well as the corrected moving average obtained using the recursive removal of statistically significant variance periods. The demand spectrum includes the individual magnitudes of the sinusoidal frequency components, indicating the amount of variability expected at a

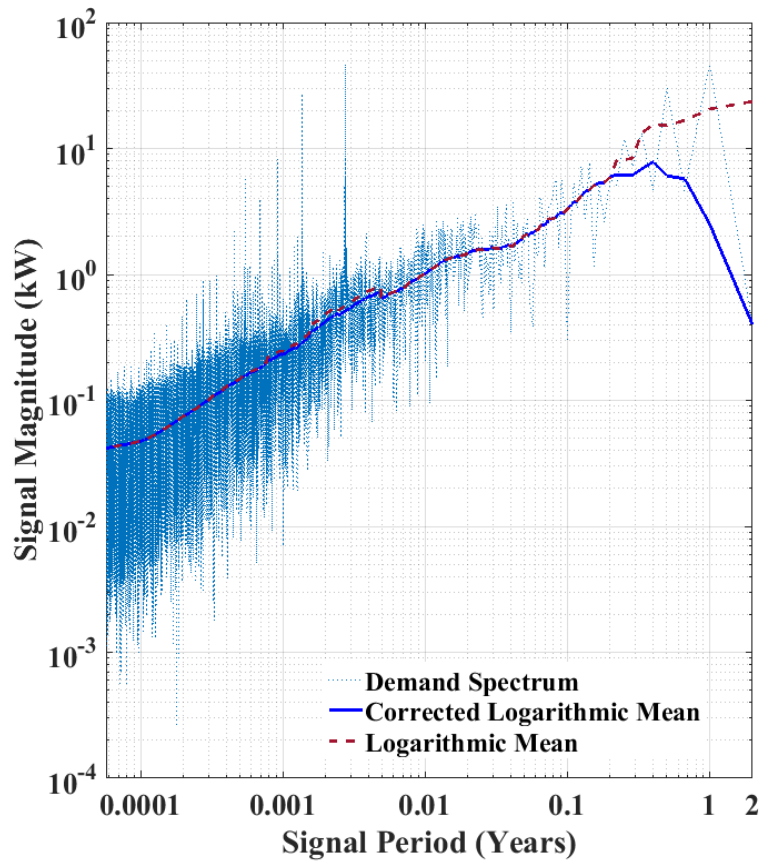


Figure 3.4: Demand Amplitude Spectrum

particular frequency. It is more complex than the wind spectrum, with an annual signal visible with a 2nd harmonic present, indicating a non-sinusoidal seasonal-cycle load variance. The dataset length makes precise identification of seasonal trends difficult, however the absolute magnitude of the signal verifies its presence. At timescales of less than 3 months, the overall demand variance is modelled as slightly pink ($f^{-1/2}$) noise, with progressively larger load variation observed at longer observation periods. This trend has a significant diurnal signal superimposed – this diurnal signal has multiple harmonics and is amplitude modulated (due to the presence of near-symmetrical sidebands) indicating a non-sinusoidal signal which varies over the course of a year. The complexity of this signal

indicates that a full multidimensional probabilistic model is needed which is capable of not only modeling each trend individually, but also their interactions.

Figure 3.5 displays the mean seasonal and diurnal demand variance signals extracted from the frequency spectrum, with the long period mean also removed for clarity. This causes negative values to indicate below-average demand while positive variance values reflect above-average demand. The seasonal signal is observed to be somewhat stronger than the diurnal signal, with an amplitude of 130 kW in comparison to 105 kW. The seasonal signal is sinusoidal with a superimposed second harmonic, with the peak occurring during January, the harmonic peak during June and the minimum during September. The diurnal signal is more complex, being composed of multiple harmonics of varying

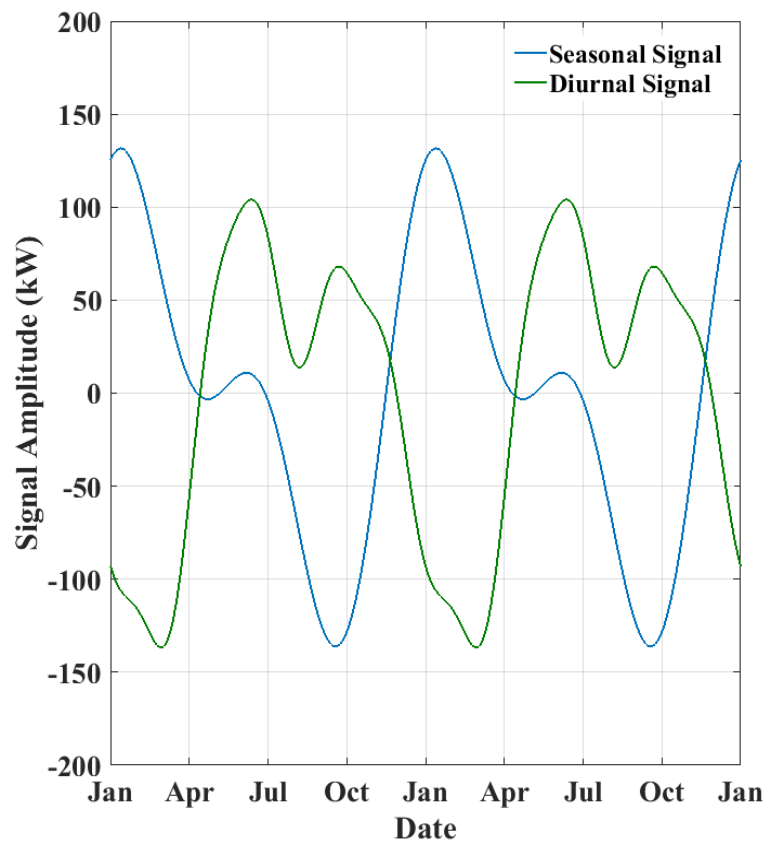


Figure 3.5: Seasonal and Diurnal Demand Variance

amplitude and phases. This signal has a peak of 105 kW shortly before noon, a secondary peak of 65 kW near 5:00pm and a single minimum at -135 kW near 3:00 a.m. However, the existence of amplitude modulation indicates that this diurnal signal is not constant throughout the year – however the general behavior is as described. The presence of these significant seasonal and diurnal variance features validates nonstationary load behavior, and their identification and quantization allows appropriate time-variant probabilistic modeling algorithms to be implemented, generating a more accurate probabilistic demand model.

3.2.5: Time-Variant Probabilistic Load Modeling

The nonstationary demand dataset is modelled using a time-variant, univariate Kernel smoothing algorithm (as described in Chapter 2). The development of the load model requires feature extraction (to model the identified seasonal and diurnal variance signals), bandwidth-optimized Kernel distribution algorithms and a fine numerical mesh covering the entire space of potential demand values. The resultant time-variant probabilistic load model contains information regarding the general load profile, the relationship between the base, secondary and peak load conditions and also provides vital information with respect to time-variant behavior, including cross-frequency interactions and their effects on various statistical properties.

Feature Extraction

The electrical demand dataset is expressed as a discrete, nonstationary pseudorandom variable, $L(n)$, with time-variant probability distribution, $p_L(x,t)$. Assuming a sufficient dataset of length N to model annual-scale nonstationary behavior of $k*n$ and data measurement spacing tight enough to allow detection of diurnal variance of length $j*n$, the annual and diurnal nonstationary variance features are extracted from $L(n)$,

$$L_{\sigma_1\sigma_2} = \left[\begin{array}{ccc} L(1,1,1:m) & \cdots & L(1,j,1:m) \\ \vdots & \ddots & \vdots \\ L(k,1,1:m) & \cdots & L(k,j,1:m) \end{array} \right] \quad (3)$$

where each matrix element (j,k) is a vector of length m consisting of appropriate dataset samples. These data vectors contain information including the underlying load PDF for the time specified by (j,k) . The multiscale time-variant load PDF, $p_L(j,k,x)$, is approximated by applying the optimized Kernel smoothing algorithm (Chapter 2) to each data vector, producing the following multivariate load model:

$$F_{L\sigma_1\sigma_2} = \left[\begin{array}{ccc} F_L(1,1,p_1:p_n) & \cdots & F_L(1,j,p_1:p_n) \\ \vdots & \ddots & \vdots \\ F_L(k,1,p_1:p_n) & \cdots & F_L(k,j,p_1:p_n) \end{array} \right] \quad (4)$$

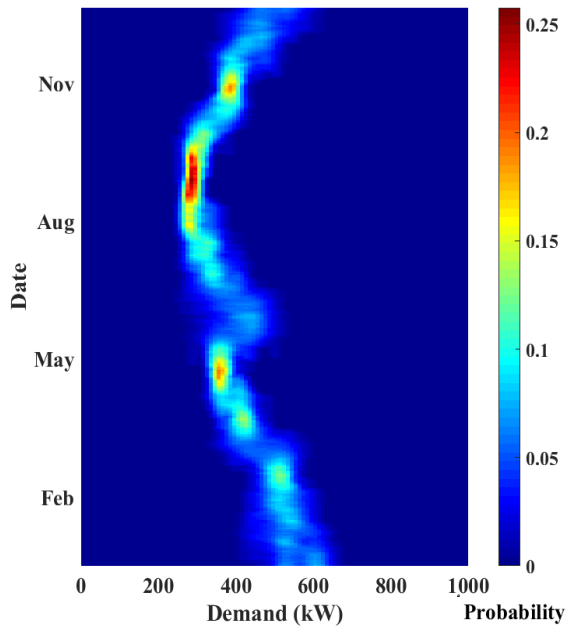
where each vector, $F_L(j,k)$, is comprised of a KDE evaluated at points $p_1:p_n$. The KDE bandwidth is selected to minimize AMISE, ensuring the correct fit to the load profile.

The Probabilistic Load Model

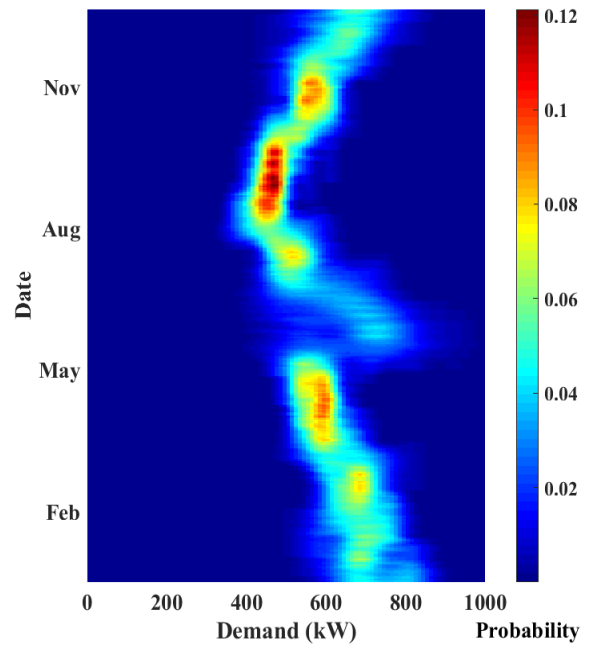
Figures 3.6(a-d) display samples of the resulting time-variant probabilistic load model. The displayed distributions correspond to (a) 3 a.m., (b) 9 a.m., (c) August 28th at 3 p.m. and (d) 9 p.m. These samples display the seasonal load profile variation at different parts of the diurnal cycle. The selection of distribution samples emphasizes the nonstationary nature of the probabilistic demand profile. The lowest, least variable probabilistic load profile is observed at 3 a.m. This is during the diurnal load minimum – most commercial and industrial customers are quiescent along with a significant proportion of residential demand. A seasonal cycle is evident, with the most likely demand value ranging from 550 kW in January to a minimum of 300 kW during August and September. A small secondary peak is evident during May and June, where the demand becomes less concentrated and increases to roughly 450 kW after previously declining to the 375 kW range. The load profile itself is dense, with demand rarely varying by more than 50 kW from the associated probabilistic mode.

The demand distribution is significant different at 9 a.m., with the probabilistic modes increasing to a maximum of 700 kW during January and 450 kW during August and September. In addition, the secondary peak during June is more evident, with the most likely load increasing from 600 to 750 kW. The demand distribution is also wider throughout – the load frequently varies by up to 100 kW on either side of the probabilistic peak. Essentially, the load displays a higher mean value with greater variance as commercial and industrial customers are coming online. By 3 p.m., the demand profile has

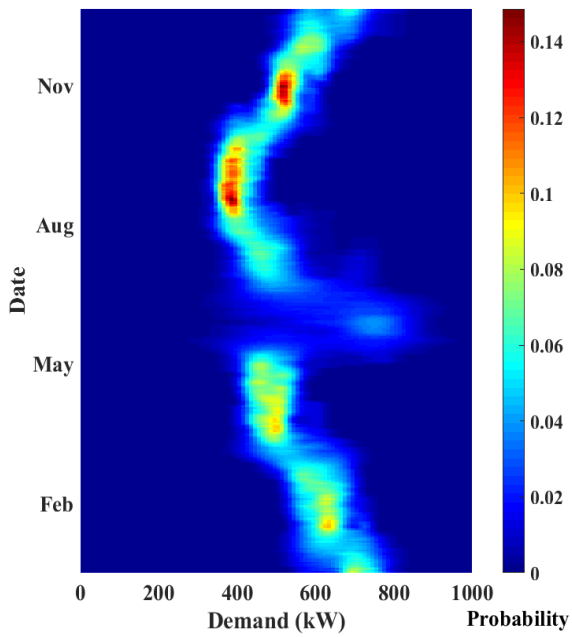
become more concentrated. The general range of probabilistic modes remains 450 to 700 kW with a secondary peak near 750kW. However, the demand variance is less during most times of the year, with the distribution width decreasing to roughly 75 kW. At 3 p.m., most commercial and industrial customers are in steady-state daytime operation, leading to the decreased variability in the load profile. The load profile is similar at 9 p.m. – it is slightly more concentrated due to residential loads (the majority of commercial and industrial customers are now offline). The secondary peak is weaker, suggesting that it stems from commercial or industrial customers. In general, significant variability is observed in the load profile due to the diurnal and seasonal cycles. Probabilistic wind reserve modeling requires this information to accurately assess the relative performance of wind generation when applied to a microgrid.



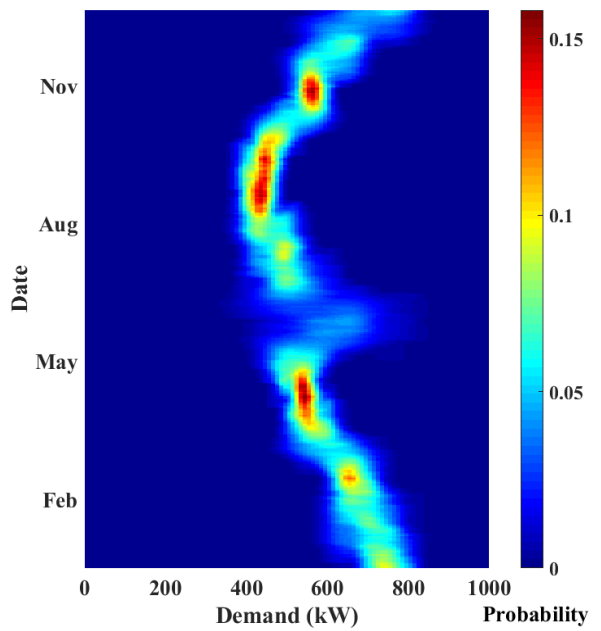
(a)



(b)



(c)



(d)

Figure 3.6: Probabilistic Demand Distribution at (a) 3 a.m., (b) 9 a.m., (c) 3 p.m. and (d) 9 p.m.

The developed time-variant probabilistic electrical load model is evaluated through several prediction statistics. The MAE, MAPE and RMSE of each individual probability distribution (corresponding to a time and date, respectively) is calculated by comparing the model probability distribution to the empirical distribution of the sample data. Table 3.3 displays general prediction statistics applied to the demand dataset. The MAE, MAPE and RMSE have mean values of 0.0045, 0.0415 and 0.0100, respectively. This indicates that the probabilistic modeling algorithm is capable of accurately modeling the true demand distribution. However, significant variance does exist across the range of probabilistic models, with the MAE ranging from 0.000781 to 0.0264, the MAPE from 0.0017 to 0.4184 (likely an artifact of a near-zero empirical value) and the RMSE ranging from 0.0032 to 0.0366. Essentially, the nonstationary behavior of the load dataset influences the accuracy of the probabilistic model.

Table 3.3: General Demand Data Probabilistic Prediction Statistics

Statistic	MAE	MAPE	RMSE
Minimum	0.000781	0.0017	0.0032
Mean	0.0045	0.0415	0.0100
Maximum	0.0264	0.4184	0.0366

Table 3.4 displays the prediction statistics for the demand subsets modeled when identifying nonstationary dataset behavior. The relative accuracy of the probabilistic model is seen to be highest during the seasonal load minimum (Set 4 and Set 5), with MAE, MAPE

and RMSE values as low as 0.0016, 0.0128 and 0.0067, respectively. The prediction errors are highest during the winter load maximum (Set 2 and Set 3) with MAE, MAPS and RMSE values as high as 0.0066, 0.0319 and 0.0169, respectively. However, despite the increased prediction errors, the overall correlation coefficient between the empirical and model distributions remains above 0.999, indicating a strong in-sample fit to the actual demand distribution. Figure 3.7 displays the probability distribution of the prediction statistics. The MAE and RMSE both resemble an extreme value distribution, with a pronounced mode near their mean value and a slightly extended right tail. The MAPE is similar, however it is stretched in the x-axis due to the normalization inherent in the MAPE calculation.

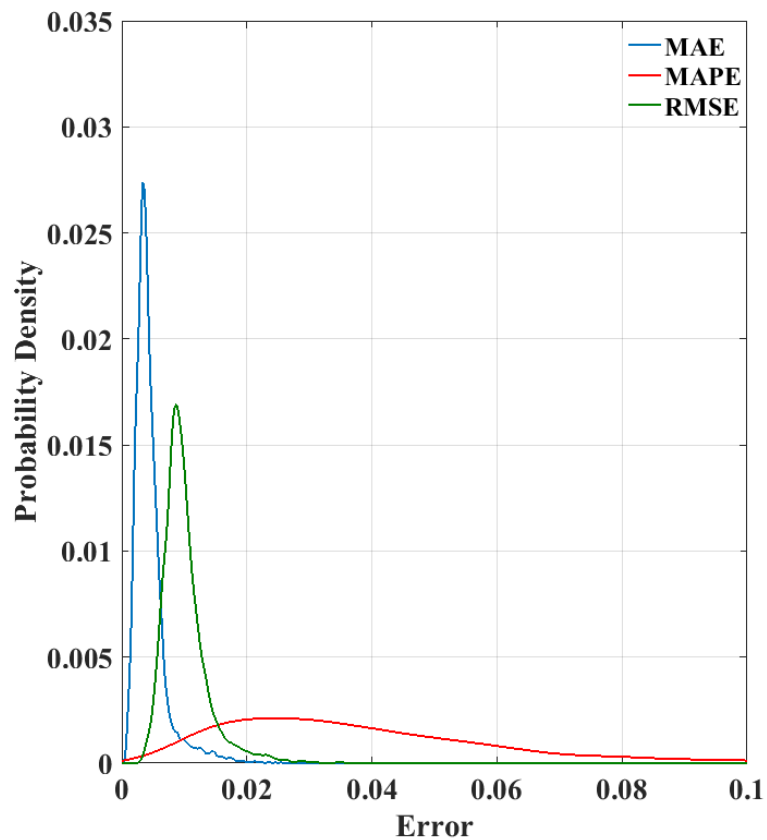


Figure 3.7: Probability Distribution of Prediction Statistics

However, in all cases the prediction errors are low, indicating the ability of the probabilistic modeling algorithm to match the empirical demand distribution.

Table 3.4: Demand Subset Probabilistic Prediction Statistics

Dataset	MAE	MAPE	RMSE	Correlation
Set 1 (N = 70179)	0.0045	0.0415	0.0100	0.9998
Set 2 (N = 124)	0.0066	0.0319	0.0169	0.9994
Set 3 (N = 124)	0.0050	0.0233	0.0123	0.9995
Set 4 (N = 124)	0.0016	0.0128	0.0067	0.9999
Set 5 (N = 124)	0.0024	0.0161	0.0070	0.9999

3.2.6: Probabilistic Assessment of Load Profiles

Probabilistic assessment of microgrid load profiles requires knowledge of the cumulative probability of demand values. The previously obtained probabilistic load profile is integrated to produce multidimensional cumulative distribution function (CDF):

$$C_{L\sigma_1\sigma_2}(j, k, p_n) = \int_{p=0}^{p_n} F_{L\sigma_1\sigma_2}(j, k) dp \quad (5)$$

$$C_{L\sigma_1\sigma_2} = \left[\begin{array}{ccc} C_L(1, 1, p_1:p_n) & \cdots & C_L(1, j, p_1:p_n) \\ \vdots & \ddots & \vdots \\ C_L(k, 1, p_1:p_n) & \cdots & C_L(k, j, p_1:p_n) \end{array} \right] \quad (6)$$

where each matrix element (k,j) contains a CDF model of the corresponding electrical load. Figure 3.8 displays a sample CDF, displaying the seasonal demand variance at 5pm. The cumulative load distribution displays the minimum and maximum expected demand values. The lowest non-zero CDF value ranges from 400 to 600 kW, representing the absolute base load which must always be available. The point at which the CDF converges to unity represents the greatest possible demand – this value ranges from 650 to 900 kW. This amount of generation must be available in reserve to avoid loss of load contingencies. The intermediate values reflect the underlying probability distribution, with the median load value roughly matching the previously defined probabilistic modes.

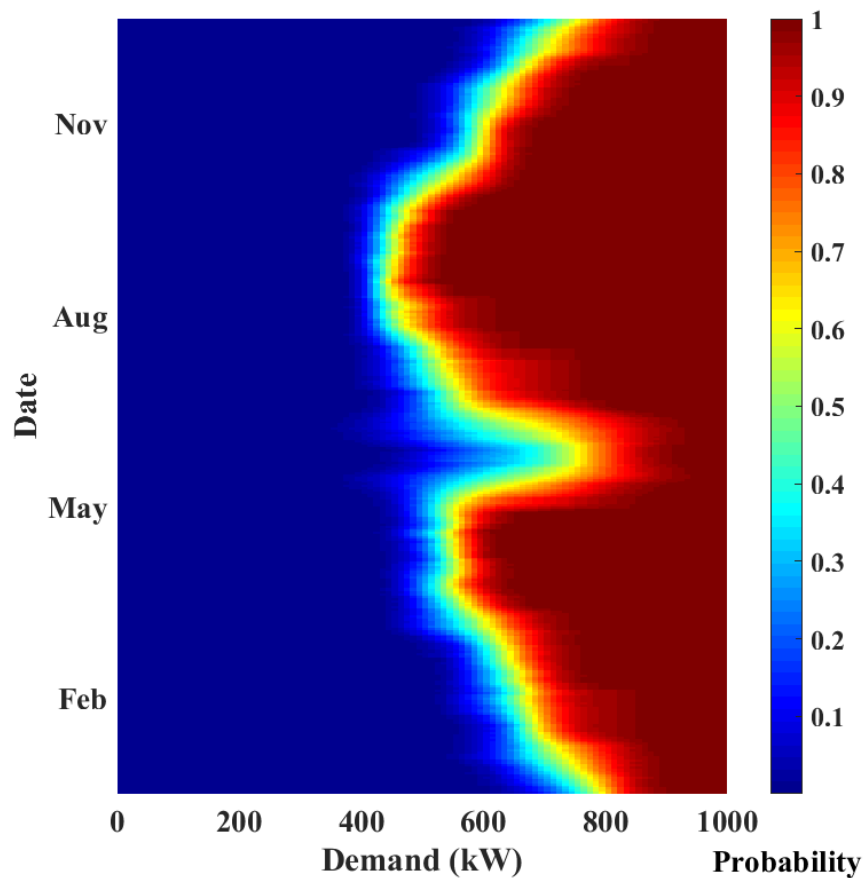


Figure 3.8: An Example Demand CDF

Microgrid load profiles are divided into peak, secondary and base load components. Figure 3.9 displays an example of this division. The base load represents the constant demand which must always be available. This varies according to the seasonal cycle, and is (in large transmission grids) often supplied by slow-ramping coal or nuclear generation. The secondary load includes most of the diurnal-cycle variability, and is supplied by faster units. The peak load is comprised of the highest load values during diurnal-cycle peaks, in addition to any transient load increases due to cold-load pickup or other contingencies. In the example system, the base load is roughly 450 kW, the secondary load 700 kW and the peak load as high as 950 kW. In a microgrid, a slightly different probabilistic assessment of these load criterion is needed. The distributed generating units are grid forming – they

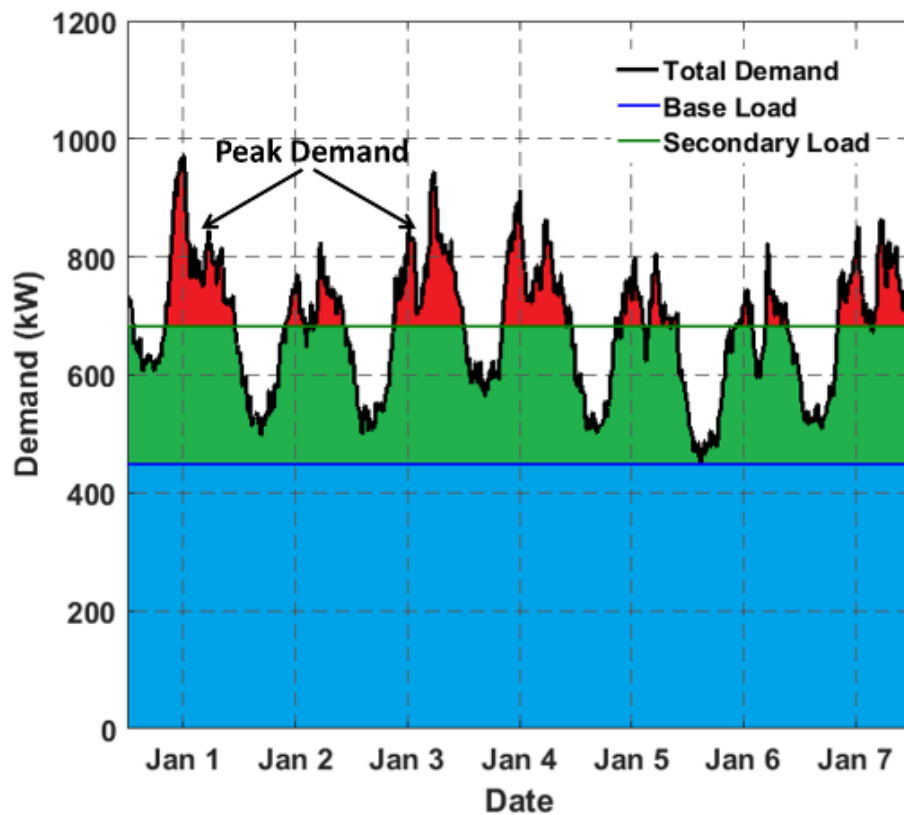


Figure 3.9: Microgrid Load Profiles

can ramp quickly enough to follow hourly load fluctuations. The secondary and peak loads can also be supplied by these generators – as the only energy source in the grid, an engineering decision must be made to select generators with the ramping capability to match the microgrid peaking profile. When intending to use wind generation as reserve capacity, probabilistic load profile assessments are more valuable in predicting the system state during load variation.

The multidimensional, cumulative probabilistic load model is used to determine probabilistic estimates of the base load, secondary load and peak load corresponding to the seasonal and diurnal phase. The base load represents constant demand which is nearly always exceeded and is defined as the 5th percentile of the CDF. The secondary load represents the median electrical demand, defined as the 50th percentile of the CDF. Finally, the peak load represents demand levels which are present but rarely exceeded (the 95th percentile of the CDF). This type of probabilistic assessment moves the application of reserve generation into the shorter timescales more appropriate for islanded microgrids. The reserve generation requirement can be probabilistically assessed by subtracting the base load from the probabilistic load model. Figures 3.10 (a), (b) and (c) display the expected base, secondary and peak demand values for each date and time. The base load profile shows significant seasonal and diurnal variability, ranging from a minimum of 250 kW (at 4 a.m. during August) to 700 kW (at 1 p.m. and 7 p.m. during January). In general, the seasonal base load variation is unimodal, with a single winter peak and a summer minima. A slight secondary peak is evident during the diurnal peak periods, however it is small compared to the overall variability present. The secondary load does not follow this

unimodal behavior. While the minimum and maximum load values (in this case 300 and 800 kW, respectively) occur at the same date and time, a pronounced secondary peak is evident between 7 a.m. and 9 p.m. during May and June. This is likely due to a single, large industrial customer within the microgrid which has a seasonal operation schedule. The load during this secondary peak reaches values comparable to the winter maxima, representing a significant requirement for reserve generation. The peak load profile is similar to the secondary load, ranging from 350 to 950 kW and following the same seasonal and diurnal load pattern. The high amplitude variability in the secondary and peak load profiles indicate a substantial requirement for reserve generation – the base load often accounts for barely half of the total demand.

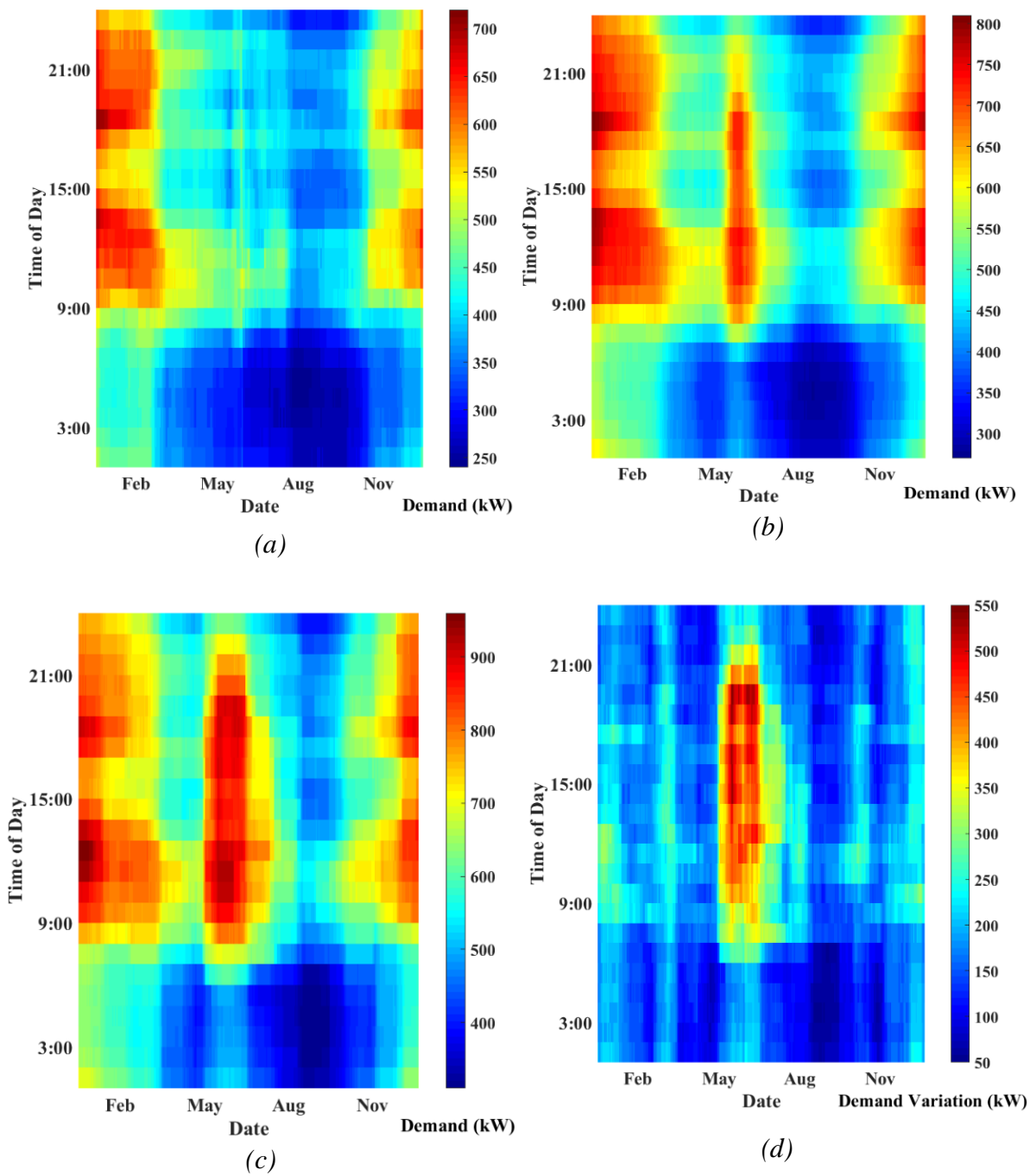
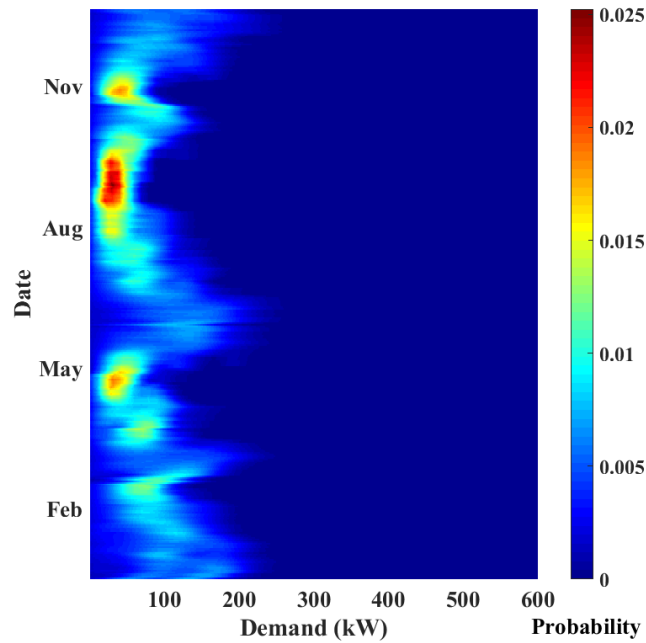


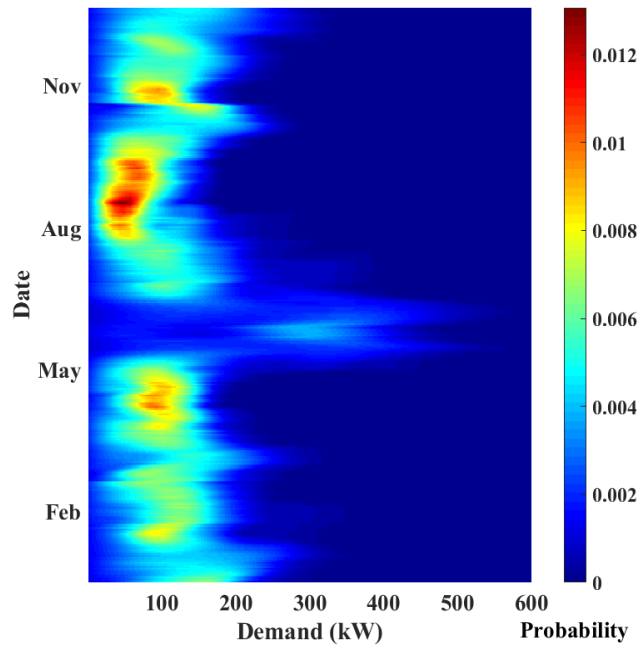
Figure 3.10: Expected Values of (a) The Base Load, (b) The Secondary Load, (c) The Peak Load and (d) the spread between the Base and Peak Demand.

Figure 3.10(d) displays the difference between the expected peak and base demand values – indicating the amount of reserve capacity required to meet short-period load fluctuations. The effect of the industrial customer is clearly evident – the demand becomes much more volatile, with a difference of nearly 500 kW between the base load and peak demand. Essentially, this customer only intermittently consumes energy, requiring reserve units to be available. The remainder of the time, the previously defined seasonal and diurnal variability is evident, with the demand variability peaking during the winter and during working hours, with a minimal load spread occurring during summer nights. The variability in the peak demand in relation to the base load indicates a time-variant wind reserve requirement which must be further investigated using probabilistic modeling.

Figures 3.11(a) and 3.11(b) display the seasonal probability distribution (at 3 a.m. and 5pm) of the electrical demand with the base load subtracted. Essentially, this produces a probabilistic model of the secondary generation requirement. While the peak load profile displays the 95% percentile of electrical demand, the presented probabilistic model provides additional statistical information, including the expected value, variance and other statistical properties of the secondary demand. The general pattern of demand variability is similar to the previously defined peak and secondary demand variance, with a maximum during the winter months and when the industrial customer is active. However, the probabilistic model also displays the change in demand distribution which occurs in addition to this variability. In this case, the diurnal cycle is dominant. During the diurnal



(a)



(b)

Figure 3.11: Probabilistic Demand Models at (a) 3 a.m. and (b) 5pm

peak, the distribution of secondary demand becomes much wider, indicating greater short-period variability in electrical demand. The expected secondary demand requirement is

near 100 kW for most of the year. However, the industrial customer increases this value to 300 kW. In addition, the diurnal minimum at night has demand variability as low as 50kW, especially during the summer months. The majority of the seasonal cycle is filtered out by removal of the base demand – providing the insight that the diurnal cycle dominates load variability while the seasonal cycle primarily influences the base load quantity.

Figure 3.12 displays the expected value of the probabilistic secondary demand for each date and time. It is similar in shape to the peak load profile, however as a formally calculated expected value it represents the long period statistical mean reserve requirement. Assuming the presence of energy storage or a transmission grid interconnection, the

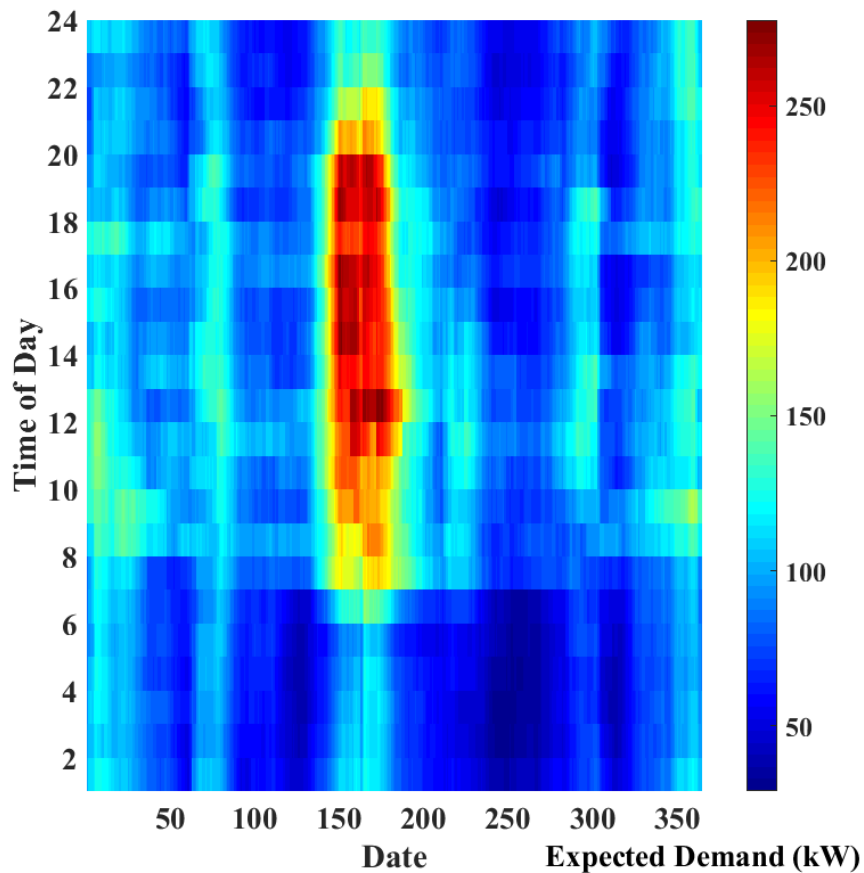


Figure 3.12: Expected Value of Secondary Demand

expected value can be used to size reserve generation for net-neutral microgrid energy balance. For islanded systems, the peak demand profile must be used to size generation capacity – the expected value now has applications in reliability, scheduling and economic analysis. The expected secondary demand varies from 50 to 250 kW, indicating that any secondary generation must be significantly oversized for many seasonal and diurnal phases in order to meet the peak demand. The significant and fundamental variability in demand profiles indicates that wind reserve assessment requires a joint probabilistic analysis of available wind energy and its temporal relation to probabilistic demand variance.

3.3: Probabilistic Wind Reserve Assessment

The wind reserve is the quantity of wind power available to meet reserve applications such as demand response or frequency regulation. It is a function of the site's wind resource, load profile and system architecture. The high fluctuation in wind power availability and electrical demand suggest that probabilistic (as opposed to deterministic) analysis is an optimum method of wind reserve assessment [17]-[18]. The advantages of probabilistic models are amplified in islanded microgrids, where fluctuations in any factor have a significant effect on system behavior and long-distance energy dispatch is not possible. This section presents a probabilistic wind reserve assessment algorithm involving probabilistic modeling of wind turbine power output and its combination with the previously defined demand model, producing an energy balance model applicable to wind reserve applications.

3.3.1: Wind Turbine Power Output Modeling

The probabilistic wind turbine output is modelled by a complex recursive algorithm which combines the wind turbine power curve, $P_t(V)$, (obtained from the manufacturer) with each bivariate dataset element. Initially, the space of potential wind turbine outputs is produced:

$$P_t(V_{set}, \rho_{set}) = P_t(V_{set}) \times \frac{\rho_{set}}{\rho_{base}} \quad (7)$$

where V_{set} and ρ_{set} are the discrete vectors of possible environmental conditions contained within the bivariate wind resource model $F_{K\sigma 1\sigma 2}$ and ρ_{base} the base air density used to calculate the wind turbine power curve. The vector multiplication results in a matrix of wind turbine power output values filling the bivariate model space. The resolution of the bivariate model is limited by the source data and the available computational resource – in this case wind velocity is discretized to 0.5 knot values and air density to 0.003 kg/m³.

A probabilistic extension of the wind turbine output matrix is produced by the substitution of the time-variant bivariate probabilities:

$$F_t(k, j, V_{set}, \rho_{set}, 1) = P_t(V_{set}, \rho_{set}) \quad (8)$$

$$F_t(k, j, V_{set}, \rho_{set}, 2) = F_{K\sigma 1\sigma 2}(k, j, v, \rho) \quad (9)$$

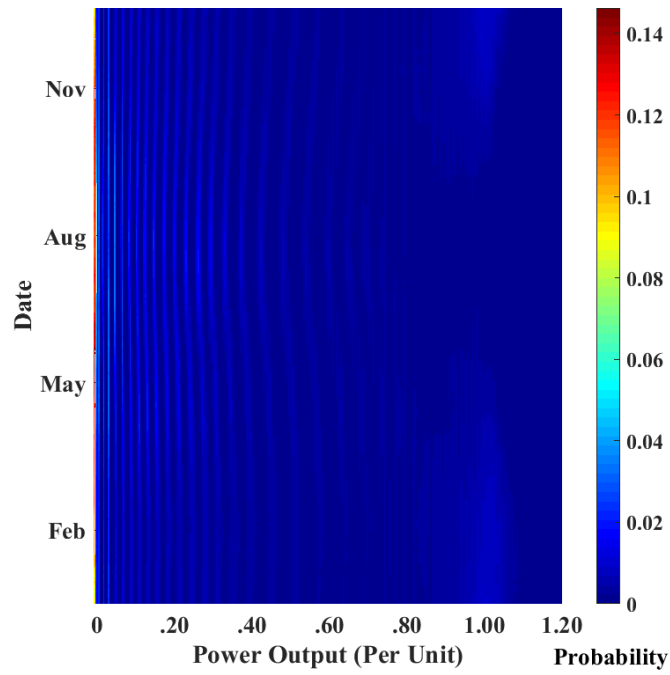
This model contains every time-variant environmental condition, its probability of occurrence and the associated wind turbine output power. A time-variant probabilistic model of the wind turbine output power is produced by compressing the model according to discrete ranges of wind turbine output:

$$F_{Pt}(k, j, P_o) = \sum_{j=1}^m \sum_{i=1}^n \begin{cases} F_{K\sigma 1\sigma 2}(k, j, V_m, \rho_n), & P_o - \epsilon \leq P_t(V_m, \rho_n) < P_o + \epsilon \\ 0 & else \end{cases} \quad (10)$$

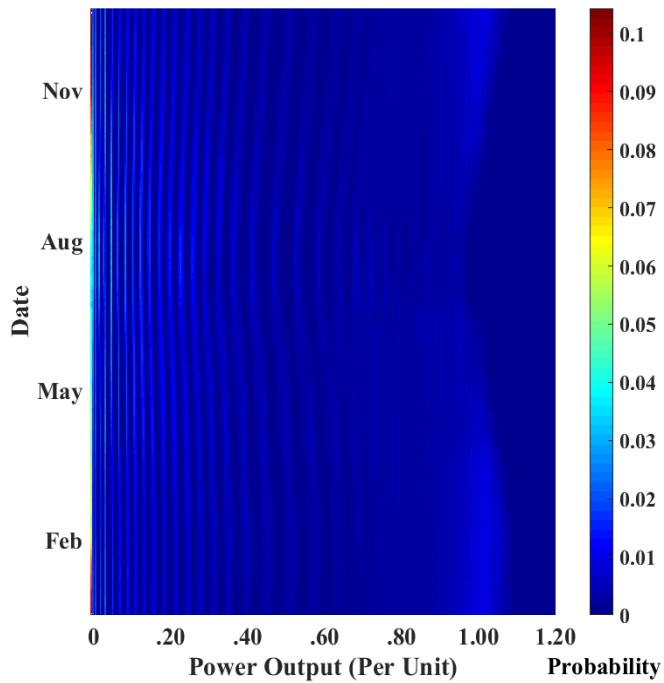
where P_o is the discrete output power and ϵ a parameter representing the effective “bin width” of the wind turbine power output. The result is to remove the dimensions corresponding to V and ρ , resulting in a model which contains the total probability of each

potential wind turbine power output as a function of the seasonal and diurnal phase – the environmental condition probabilities are embedded within this sum probability. The nature of this probabilistic model is dependent on both the shape of the wind turbine power curve and the bivariate wind resource model, and provides a probabilistic estimate of the power output of any particular wind turbine when installed under a known environmental regime.

Figures 3.13(a) and 3.13(b) display samples of the probabilistic wind turbine output model, corresponding to the seasonal cycle at 3 a.m. and 5pm. The power output is normalized by the turbine rating – in this case a Northern Power Systems 100C-24 wind turbine [21] was selected. Discretization artifacts are visible in the intermediate power output ranges – this is due to the sharp slope of the power curve in this area in combination with the unavoidable limit to the wind data resolution. A significant seasonal trend is evident, especially near the rated output region. At 3 a.m. during the winter months (November to April) significant probability mass exists near an output of 1 Per-Unit, representing full-capacity operation at variable air densities. However, this operating condition does not occur during the summer months – the probability of sufficient wind is low enough that it was not observed during the multi-year sample dataset. During this period, the probability of quiescent operation (power outputs near 0) is significantly higher, indicating an inferior wind resource and a general lack of available energy. Diurnal variability is also evident. While at 3 a.m. the summer months see essentially no rated operation, at 5pm there is probability mass near full-load. The maximum observed output power varies according to the environmental air density – during the winter months, values



(a)



(b)

Figure 3.13: Normalized Probabilistic Wind Turbine Output at (a) 3 a.m. and (b) 5pm

of up to 1.1 Per-Unit are possible assuming a passive stall-controlled wind turbine. At all

times of the year, the diurnal signal places more probability mass near rated power output during the early evening. Quiescent operation is also less likely, with at least some wind power generally available. This is likely due to daytime heating increasing the local wind velocity through various mesoscale airmass circulations. In general, the probabilistic wind turbine output model provides vital information regarding wind turbine performance, including variability due to time-variant environmental conditions and the precise behavior of the installed wind turbine.

The expected wind turbine output power can be obtained by integration of the general probability distribution:

$$E_{Pt}(k, j) = \int_{P_{min}}^{P_{max}} P F_{Pt}(k, j, P) dP \quad (11)$$

where the bounds of integration are the minimum and maximum values of the power output function. The precise boundaries depend on the wind turbine power curve and the choice of discretization – in general they range from just below zero to slightly above the manufacturer’s rated power (for smaller turbines) to the maximum rated power (for larger pitch or speed controlled wind turbines). The wind turbine capacity factor is calculated by normalizing the power output by the turbine rating. Figure 3.14 displays the expected wind turbine capacity factor. A significant seasonal and diurnal trend is evident, with the capacity factor ranging from 0.25 during summer nights to 0.55 during winter days. The maximum capacity factor is observed during February at about 1 p.m., with dual minima evident at 9 p.m. and 5 a.m. during August. The capacity factor is an expected value which gives a general, long-period estimate of wind turbine performance. However, a more detailed

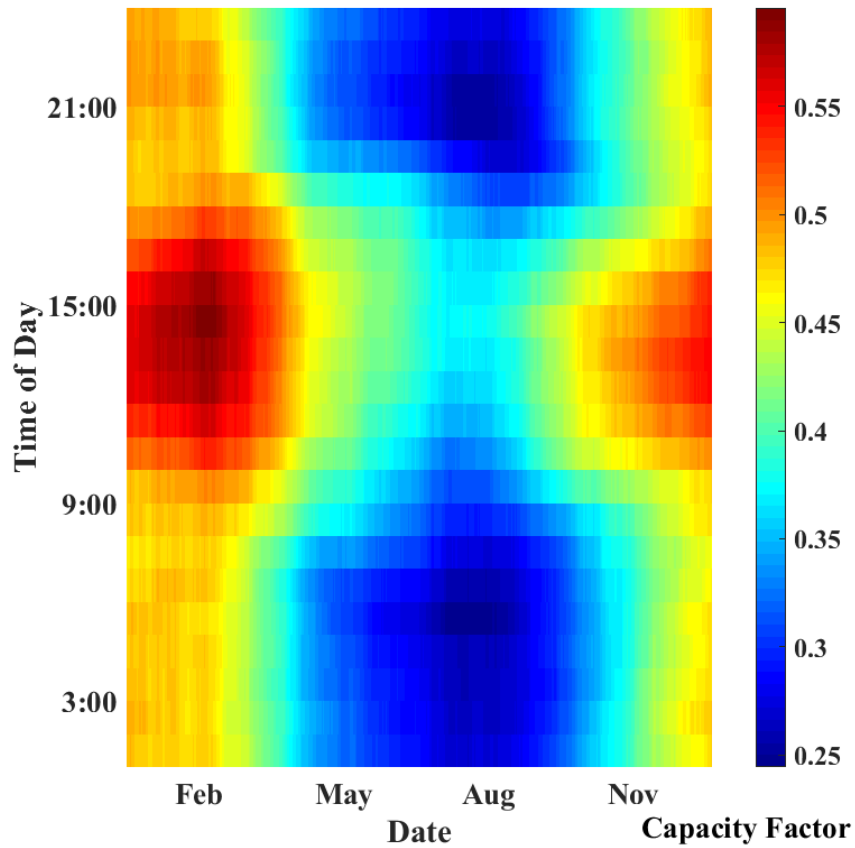


Figure 3.14: Expected Wind Turbine Capacity Factor

probabilistic analysis involving both the wind turbine and electrical demand models is needed to assess the effectiveness of wind turbines in providing dynamic reserve generation.

3.3.2: Probabilistic Load Pickup

One method for evaluating the effectiveness of supplementary wind generation is probabilistically modeling its ability to meet the secondary demand. In this situation, the secondary demand is modelled as what remains after subtracting the base load (the 5th percentile of probabilistic demand). The result is a set of probability distributions which

were detailed in the previous section. The available wind generation is modelled in a similar vein, using a wind turbine power curve, a set of environmental data and the defined annual-diurnal feature extraction and probabilistic modeling algorithms. The probabilistic wind turbine power output model is a proxy for available wind generation, and can be superimposed on the appropriate (at the same seasonal and diurnal phase) secondary demand distribution to begin the process of modeling probabilistic load pickup.

Figures 3.15(a-d) display such superimposed distribution, measured at (respectively) 3 a.m. on January 1st, 5pm on January 1st, 3 a.m. on August 28th and 5pm on August 28th. These sample points roughly represent the extrema of the observed seasonal and diurnal demand and wind resource variability, providing the most visually evident bases for observing time-variance in probabilistic load pickup. In Figure 3.15(a), the wind turbine power output distribution displays the dual-peaking pattern expected when the wind regime includes periods of high wind velocity. While the majority of probability mass is at or near the quiescent state, a secondary peak exists at rated power output – in this case 250kW, representing the size of the wind generation exemplar. For easier visual presentation, the wind turbine output distribution was smoothed to minimize the effects of the discretized environmental data – further calculations use the original datasets to avoid introducing fitting error. The probabilistic secondary demand model is naturally smoother, therefore visual processing was not required. The demand distribution is bimodal, with dual peaks at 55 and 130 kW above the base load. The distribution has a high variance – significant probability mass exists from 0 kW (representing base load demand) to 200 kW. In this situation, the wind turbine power output has probability mass above any particular demand

value, visually suggesting that the wind turbine can meet this demand value at least some of the time. Figure 3.15(b) displays a similar wind turbine output profile, with a slightly greater probability of rated power output due to the diurnal wind resource cycle. However, during this period the demand distribution is substantially different. Due to the diurnal load cycle, the distribution is unimodal and shifted to higher values, with the most likely secondary demand increasing to 135 kW and raging as high as 300 kW in exceptional circumstances. There is substantially less probability mass near the base load. The interplay between these probability distributions suggests that at this point of the diurnal cycle, wind generation would be less effective at meeting the secondary demand.

Figure 3.15(c) displays the substantially different demand and wind turbine output distributions observed during the summer load and wind resource minima. The wind turbine output is now significantly shifted towards quiescent operation, with less probability mass near rated output. This is due to the wind regime shifting towards calmer conditions. The demand distribution is also significantly shifted – as this is during the seasonal and diurnal minima, the distribution peaks at 25 kW above the base load. Very little probability mass exists above 100 kW, indicating the rarity of significant increases in demand during this seasonal and diurnal phase. Figure 3.15(d) displays the distributions later in the day, during the diurnal wind resource and load maximum. The wind turbine output distribution is slightly shifted towards higher power output, with daytime heating driving higher wind velocities, leading to a higher probability of rated-power operation. However, the demand distribution is also shifted, with the highest probability secondary demand increasing to 50 kW above the base load, with significant probability mass existing

at up to 150 kW. The dual variance apparent in both the available wind energy (from the turbine output distribution) and the demand indicates that modeling probabilistic load pickup requires a rigorous mathematical analysis of the probability distributions observed at each seasonal and diurnal phase.

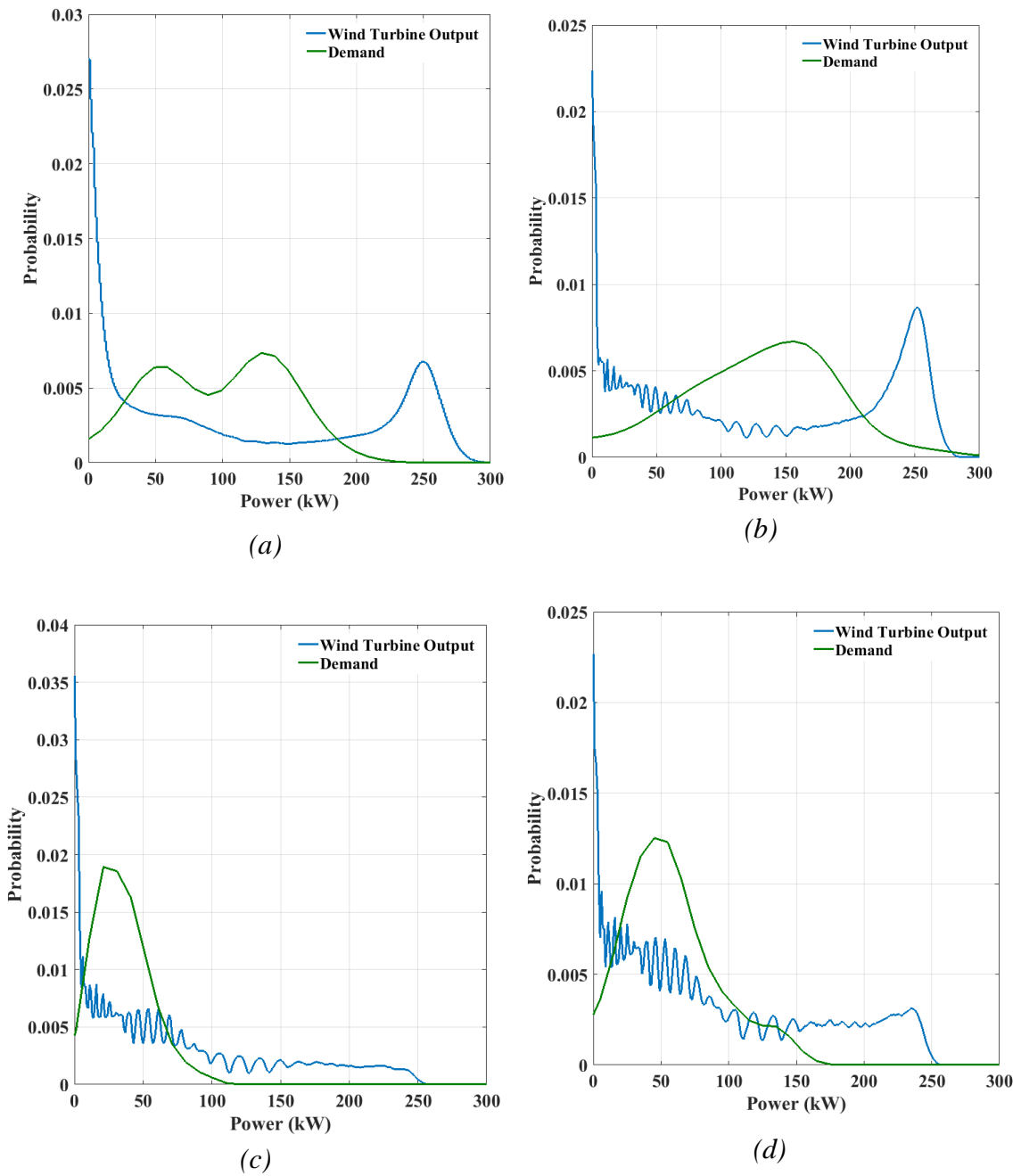


Figure 3.15: Probabilistic Comparisons of Demand and Wind Generation on (a) January 1st at 3 a.m., (b) January 1st at 5pm, (c) August 28th at 3 a.m., and (d) August 28th at 5pm

The developed probabilistic wind turbine output and electrical demand models allow a determination of the probabilistic energy balance. Essentially, assuming a demand distribution and wind turbine installation, the probability of any given power surplus or deficit can be expressed. This results in a probabilistic load pickup distribution, allowing determination of loss of load probability, secondary regulation requirements and to provide a general picture of wind reserve feasibility. The probabilistic power balance model is developed by first defining the space of potential power balance conditions:

$$P_{bal}(k) = P_{TO}(i) - P_{LO}(j), \quad k = (ji) + j \quad (12)$$

where P_{TO} is the vector of discrete wind turbine output values and P_{LO} is the discrete electrical demand values used in their respective probabilistic models. This defines every possible power balance condition allowable under the modeling regime. The likelihood of each balance condition is evaluated by multiplying the two marginal (output and demand) distributions taken at a single seasonal and diurnal phase:

$$Pr_{bal}(n, m, k) = F_{pt}(n, m, i) * F_{L\sigma_1\sigma_2}(n, m, j), \quad k = (ji) + j \quad (13)$$

where F_{pt} is the appropriate wind turbine output model and $F_{L\sigma_1\sigma_2}$ the demand model. The resulting probability object contains a matrix (corresponding to the seasonal and diurnal phase) for each potential power balance value defined in (12). This model is sorted according to the power balance value, with duplicate entries (representing more than one way to get to a particular power balance) having their probability values added to represent the combined likelihood of encountering that situation. The final model determines the

probabilistic energy balance according to the seasonal and diurnal phase, allowing a more detailed investigation into wind reserve performance.

Figure 3.16 displays four samples of the probabilistic power balance model (16), corresponding to 3 a.m. on January 1st, 5pm on January 1st, 3 a.m. on August 28th and 5pm on August 28th. These sample times represent the extrema in wind resource and demand distributions. In this case, the wind turbine output model was developed using the Northwind 100c_24 wind turbine, scaled up to assume 250 kW of generation capacity. The probabilistic models are multimodal and time-variant, displaying the complex interplay between the wind turbine output and the electrical demand. During January, the probability distribution is fairly symmetric about 0. At 3 a.m., the distribution is bimodal in the deficit region, with dual peaks at a power shortage of 120 and 50 kW. This is due to the fairly dense demand distribution at this time. The surplus region has a similar probability, albeit shifted by the rated wind turbine output and slightly diminished due to the somewhat lower probability of rated generation as opposed to quiescent wind turbine operation. At 5pm, the entire distribution is shifted towards a power deficit, as the demand increases without a significant change in the wind turbine output distribution. During August, the probabilistic behavior is significantly different. A significant probability peak occurs at a small deficit, representing quiescent wind turbine operation combined with near-base load demand. This is most significant at 3 a.m., when the demand distribution is clustered at low values. The surplus region is essentially a shifted version of the wind turbine output distribution, as during this period the secondary demand is usually small compared to the rated capacity of the wind generation. At 5pm, the distribution shifts slightly toward an energy deficit and

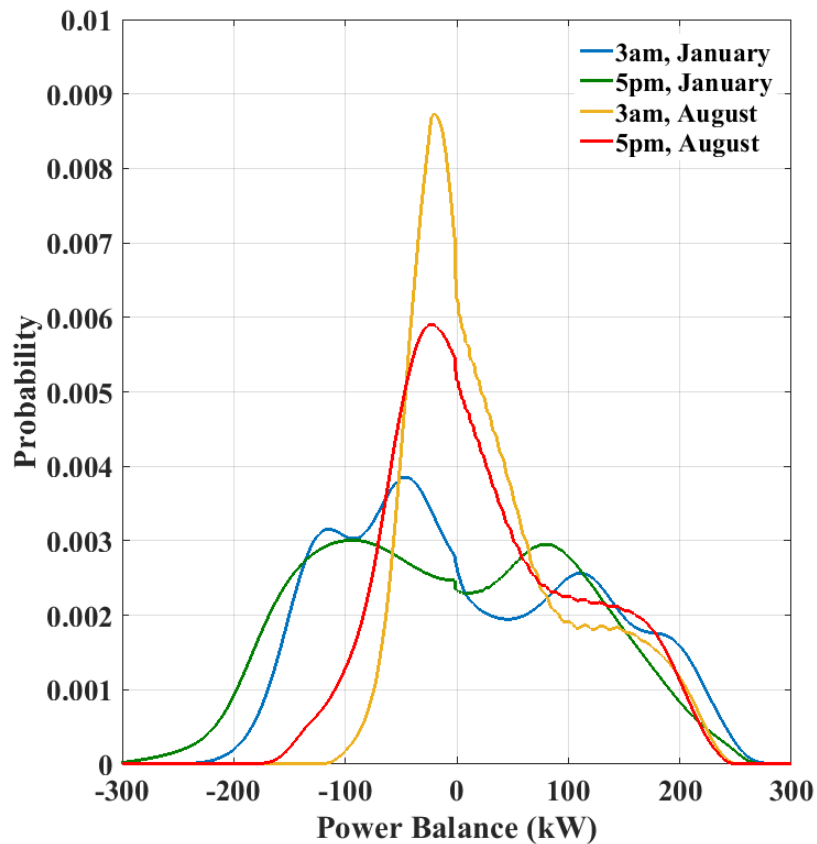


Figure 3.16: Energy Balance Distribution (250 kW Generation)

spreads out, representing the change in demand distribution detailed in the previous section. Overall, a significant probability of energy surplus exists at all times, detailing the ability of wind to act as reserve generation. However, the nature of the probability distribution implies that wind alone is not callable of always meeting the energy demand – additional action by conventional generation is required.

Figure 3.17 displays a similar probabilistic power balance model developed using the Northwind 100c_24 wind turbine scaled up to 500 kW of rated generation capacity. The increased wind generation significantly influences the probabilistic power balance. With more wind energy available, the majority of the probability mass occurs within the energy

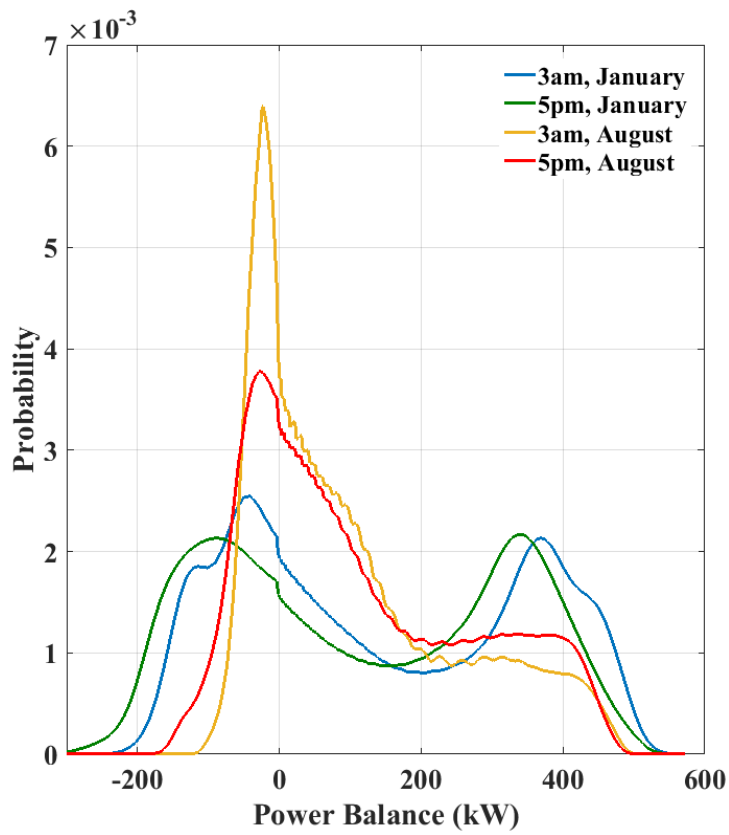


Figure 3.17: Energy Balance Distribution (500 kW Generation)

surplus region. However, there is still a significant probability of an energy deficit due to quiescent wind turbine operation. The relative probability of quiescent operation shows the seasonal variability detailed in the Figure 16, with a greater likelihood of a small energy deficit during August, with a more dispersed deficit distribution during January. The diurnal cycle also has an effect – the wider demand distribution at 5pm shifts the majority of the distribution towards a greater energy deficit while also spreading out the distribution peaks. However, the greater wind resource during this time of day is capable of increasing the probability of a significant energy surplus (> 200 kW) due to the higher likelihood of rated-power wind turbine operation. Overall, the higher wind capacity does lead to a greater

probability of an energy surplus, however it is still unable to reliably meet secondary demand due to the intermittent nature of wind generation.

3.4: Applications of Wind Reserves

The previously presented probabilistic electrical demand, wind turbine output and power balance models form the basis of wind reserve modelling. The installed wind generation is considered for three applications. The first is secondary / peak load demand response, where the wind power supplements base load generation to meet the peak demand. The second wind generation application is peak-load demand response, where wind power is primarily used to smooth peaking periods while the base and secondary loads are maintained by conventional power generation. In this case, the secondary load is supplied by conventional generation, reducing the amount of wind reserve required. In either situation, the probabilistic wind generation requirement is calculated by

$$G_R(j, k) = C_{L\sigma_1\sigma_2}(j, k, 0.95) - C_{L\sigma_1\sigma_2}(j, k, P_c) \quad (14)$$

where G_R is the generation reserve requirement and P_c is the case-specific baseline generation profile (0.05 or 0.5, respectively). The probability of sufficient wind generation can be calculated by

$$P_R(j, k) = \int_{p=G_R}^{p=\infty} F_{PT}(k, j, P) dP \quad (15)$$

where P_R is the probability of sufficient wind generation, G_R forms the lower bound of integration and F_{PT} is the wind turbine output probability distribution calculated in (10).

The final P_R matrix is a probabilistic model to determine the ability of wind power to augment conventional generation during peak load.

The final application of wind generation is microgrid frequency regulation. Using the probabilistic wind turbine output power calculated in (10), the equivalent frequency droop coefficient can be substituted to determine the probabilistic frequency regulation capability of wind generation:

$$P_{FW}(j, k, F) = \int_{p=FK_F}^{p=\infty} F_{Pt}(k, j, P) dP \quad (16)$$

where $P_{fw}(j, k, F)$ is a probabilistic model predicting the likelihood of wind generation being capable of providing a specific amount of frequency regulation. This model presents a seasonal / diurnal probabilistic analysis of wind's frequency regulation capability during moderate to large dynamic load excursions. The performance of this probabilistic modeling methodology will be examined by a case study in Chapters 5 and 6.

3.5: Conclusions

In this Chapter, a detailed methodology has been developed to enable the probabilistic modeling of wind reserves. The modeling techniques used have been designed to produce strong results with respect to the feasibility, performance and dynamic behavior of islanded microgrids using wind power generation to augment base-load conventional sources. The proposed time-variant, multivariate probabilistic modeling algorithms successfully compensates for nonstationary behavior in the environmental and electrical demand datasets, providing an accurate assessment of the wind regime and demand profile, and its probabilistic transient variability. In addition, a probabilistic power-balance model is developed to evaluate the feasibility and general performance of wind generation when acting as a power reserve. The use of advanced multidimensional kernel density estimators with optimized bandwidth selection improves the ability of the new model to capture multimodal probabilistic behavior, which is an improvement on unimodal parametric distributions, providing improved accuracy compared to standard mixture models.

Chapter 4: Modeling, Simulation and Control of Islanded Microgrids

4.1: Introduction

The implementation of wind-based reserve generation in islanded microgrids requires an analytical and numerical framework which can be used to model, simulate and control the dynamic behavior of the system. This Chapter presents an overview of microgrid topologies, including techniques for grid forming using conventional generation. Grid synchronization of distributed generation is reviewed, with recently developed techniques exhibiting the robustness and stability required for use in islanded microgrids. Subsequently, microgrid interconnection architectures are reviewed, including a brief study of an LCL power filter, droop-based voltage-source inverter control and stationary-frame reference generation using the instantaneous power theory. With the successful development of control techniques suitable for interfacing distributed generation into a microgrid, their application to wind turbines is studied. The main types of wind turbine generators are briefly presented, with the direct-drive PMSG design considered for further study. The steady-state and dynamic behavior of a PMSG wind turbine is investigated, including rotating-frame stator current control, back-to-back power electronic converter topologies and DC-link maintenance by current reference synthesis. The overall result is a microgrid topology implemented in the PLEXIM simulation environment suitable for use

in validating the wind reserve applications investigated and presented in the Chapters 2 and 3.

4.2: Microgrid Topology

A unique characteristic of Microgrids is their reliance on distributed generation and demand units. Both sources and sinks of active and reactive power can exist anywhere within the microgrid architecture, resulting in complex interactions between grid components. The fundamental components of the microgrid topology are distributed generation – generators located within distribution infrastructure as opposed to large transmission systems, power electronic converters for grid integration and control, and the potential for islanding, where the microgrid is isolated from the larger transmission grid. Microgrids can also be implemented as either AC or DC, influencing the control and distribution technology required for the practical implementation of microgrid generation and demand.

4.2.1: Overview of Distributed Generation

Distributed generation (DG) refers to generation infrastructure connected within a microgrid [1, 2], using distribution level (25 kV or below) equipment for the implementation of power delivery. It is located at the point of consumption from the viewpoint of a large transmission system. Figure 4.1 [3] displays a common distributed

generation architecture. An energy source (in this case PV) is connected to local loads through power converters. These converters are bidirectional in design, allowing power to flow from the distributed generation to the grid as well as from the distribution line to the local load. Distributed generation can be implemented using a variety of energy sources and power management strategies, including conventional generators, wind turbines, photovoltaics and local energy storage, among others [1],[2],[4],[5].

The implementation of distributed generation into microgrids presents additional engineering challenges. The inclusion of multiple localized generation units introduces stability and power flow problems [6], especially considering traditional supplementary generators which exhibit a low degree of controllability from the viewpoint of distribution system controllers [6]. These issues are currently addressed by the development of improved generation control algorithms as well as the adoption of renewable energy. Model microgrids include distributed generation in the form of multiple thermal (typically diesel) generators, wind or solar generation interfaced using power electronic converters and potentially energy storage [11]. The renewable generation is interfaced using individual,

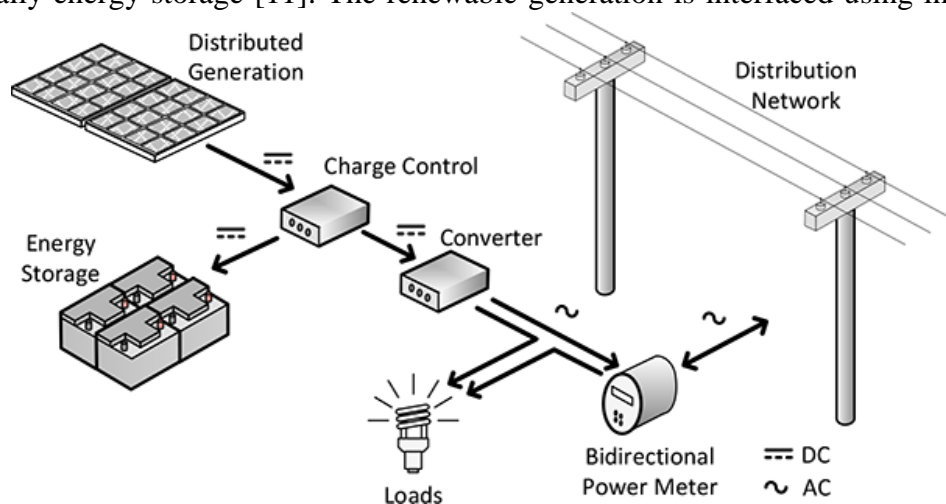


Figure 4.1: Distributed Generation [Bernadon, 2014]

parallel-connected PWM inverters [6] and implements grid-supporting algorithms such as droop control [15]-[16] and demand response (DR) [16]-[19]. Advances in islanding operation [6], [12], [21]-[23], grid synchronization [6],[14], [24]-[25], and frequency regulation [6], [13]-[15], including DSOGI-FLL based resonant synchronization algorithms [6], [24]-[25], in combination with virtual-impedance based droop controllers [22]-[23] are now capable of reliably interfacing intermittent distributed generation to weak or islanded microgrid systems. With these advances, distributed generation is evolving into a viable component of power systems, allowing the continued adoption of renewable energy into both transmission networks and microgrids.

4.2.2: Microgrid Implementation – AC and DC

The physical implementation of microgrids follows several overarching strategies. The most common topologies are AC microgrids [6], where distribution generation is interacted with a common AC bus (often the distribution network itself), DC microgrids, where DG units are connected to a DC bus when is then interfaced with the distribution grid through a power electronic converter [7], and hybrid microgrids [8], where both an AC and DC bus are present. Each topology has unique characteristics which influence their control, operation and performance. Figure 4.2 [9] displays a comparison between AC and DC microgrids. The AC microgrid is dominated by DC/AC and AC/AC converters. Storage and PV sources generate DC power, which is inverted to AC and interconnected to the AC

bus. Wind turbines generate variable-frequency AC (depending on the generator type) and therefore require a more complex AC/AC converter topology. In an AC microgrid, the common residential, commercial and industrial AC loads can often be directly connected to the AC bus through a standard distribution transformer. Any DC loads are connected through a power rectifier and filter. The DC microgrid uses a DC bus to interconnect the distributed generation units. In this situation, PV and energy storage are interfaced using DC-DC converters – generally of the boost type to maintain a high DC-bus voltage. Wind turbines and conventional generation are connected to the DC bus using controlled boost rectifiers. A single large power inverter is then used to interface the DC bus with the grid.

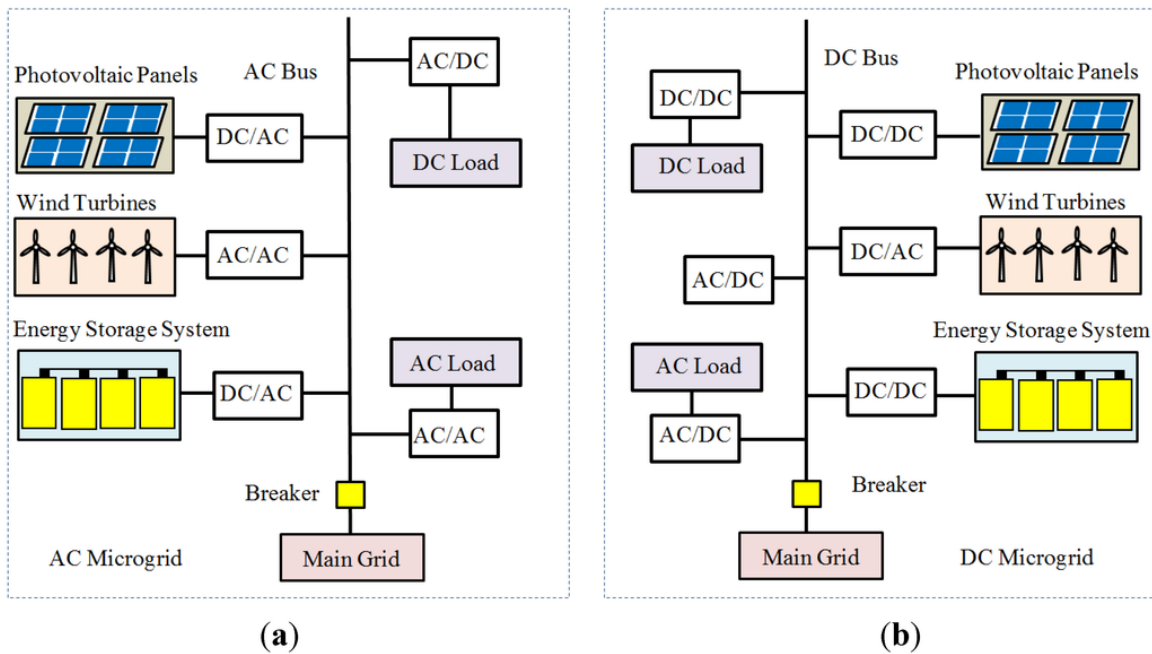


Figure 4.2: (a) AC and (b) DC Microgrid Topologies [Backhaus, 2013]

4.2.3: Islanding

Microgrids often exist within areas normally covered by transmission infrastructure. The microgrid's AC bus can be connected to the transmission infrastructure. These grid-connected microgrids can act as a single distributed generator, perform reactive power support and assist with transmission grid frequency regulation. The reverse is also true – the transmission grid can be used by the microgrid for voltage and frequency regulation and for transient demand response [16-19]. The large inertia of the transmission grid acts as a stabilizing influence, allowing the microgrid to be robust against disturbances, power flow contingencies or generation intermittency. The advantages of grid interconnection are significant with respect to microgrid operation and stability. However, the possibility of isolation from the transmission grid requires Microgrids to be operable without transmission-grid interconnection. This condition is referred to as islanding. Islanded microgrids are networks containing distributed generation which are either temporarily or permanently isolated from transmission infrastructure.

Figure 4.3 [10] displays a diagram of a grid-connected versus an islanded microgrid topology. Figure 4.3(a) displays a grid connected microgrid. This type microgrid is easier to operate – active and reactive power can be shared with the larger transmission grid, with it acting as an infinite bus to stabilize the system against transient disturbances. Assuming the distributed generation is small compared to the transmission grid size, the distributed generators can be operated for optimal economic performance, maximizing the returns from renewable sources such as PV or wind turbines. Figure 4.3(b) displays an islanded

microgrid. Whether due to a relay trip at the coupling point or absolute isolation, the transmission grid is not accessible. In this situation, the active and reactive power demand of all connected loads must be met locally by the distributed generation. Grid forming [6] must be accomplished by the largest, highest-inertia generators, with grid support and stabilization the province of the remaining distributed generation. Islanded microgrids are therefore more difficult to control and less stable, lacking the electrical and mechanical inertia of larger systems. Intermittency in renewable supply has a larger effect on grid behavior, in addition to load variability, any transient contingencies as well as the presence of unbalanced or non-linear demand [23, 26]. Due to the requirement for contingency response, microgrids must be capable of operating under islanded conditions. Therefore, the focus of this Chapter is mainly on the modelling and control of these islanded microgrids. Transmission-grid interconnection, synchronous islanding and economic optimization [28] are less significant for isolated microgrids and are beyond the scope of this investigation.

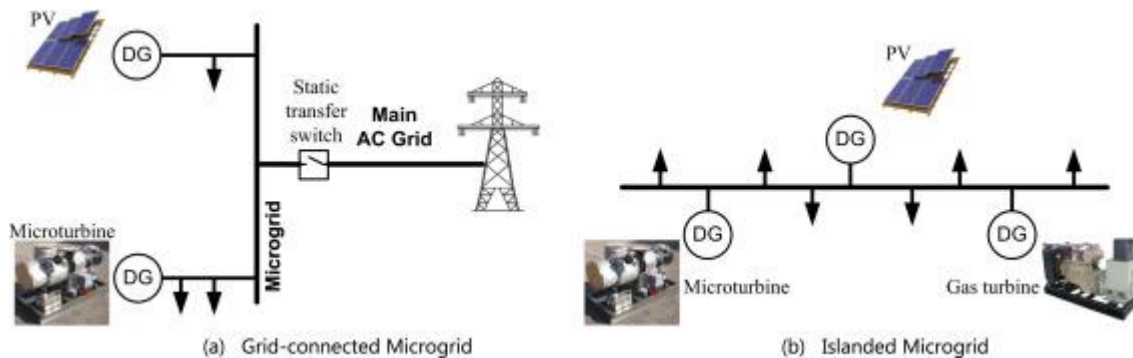


Figure 4.3: (a) Grid Connected vs. (b) Islanded Microgrids [Tayab, 2017]

4.3: Analysis, Modeling and Control of Microgrids

The investigation of wind reserves in Islanded microgrids requires an analytical and numerical framework for validating microgrid operation. The simulated microgrid must include a grid-forming generator, wind generation, multiple loads and the associated unit and distribution transformers. The modeling and control methodology must be validated using this simulation infrastructure to ensure accurate results when evaluating wind reserves. Figure 4.4 displays the microgrid topology developed for wind reserve simulation. In islanded microgrids, diesel generators are normally used for grid forming, with secondary units operating isochronously (directly coupled) with the primary [29-31]. A delta-wye unit transformer connects the diesel generators to the AC distribution grid. The grid voltage level is adjustable by changing the transformer model used – common values such as 4.16 kV, 12.5 kV and 13.8 kV can be simulated to match client microgrid configurations. A point of common coupling connects wind generation, the diesel generators and the primary distribution transformer. Voltage and current values are measured at this point for the grid synchronization and control of connected inverters. The electrical demand is simulated using constant-impedance loads, sized to consume realistic amounts of active or reactive power depending on the size of the client microgrid. The detailed control configuration of this microgrid will be investigated in this section, validating the simulation environment which is used in a subsequent Chapter to perform a case study assessing wind reserves in a client microgrid.

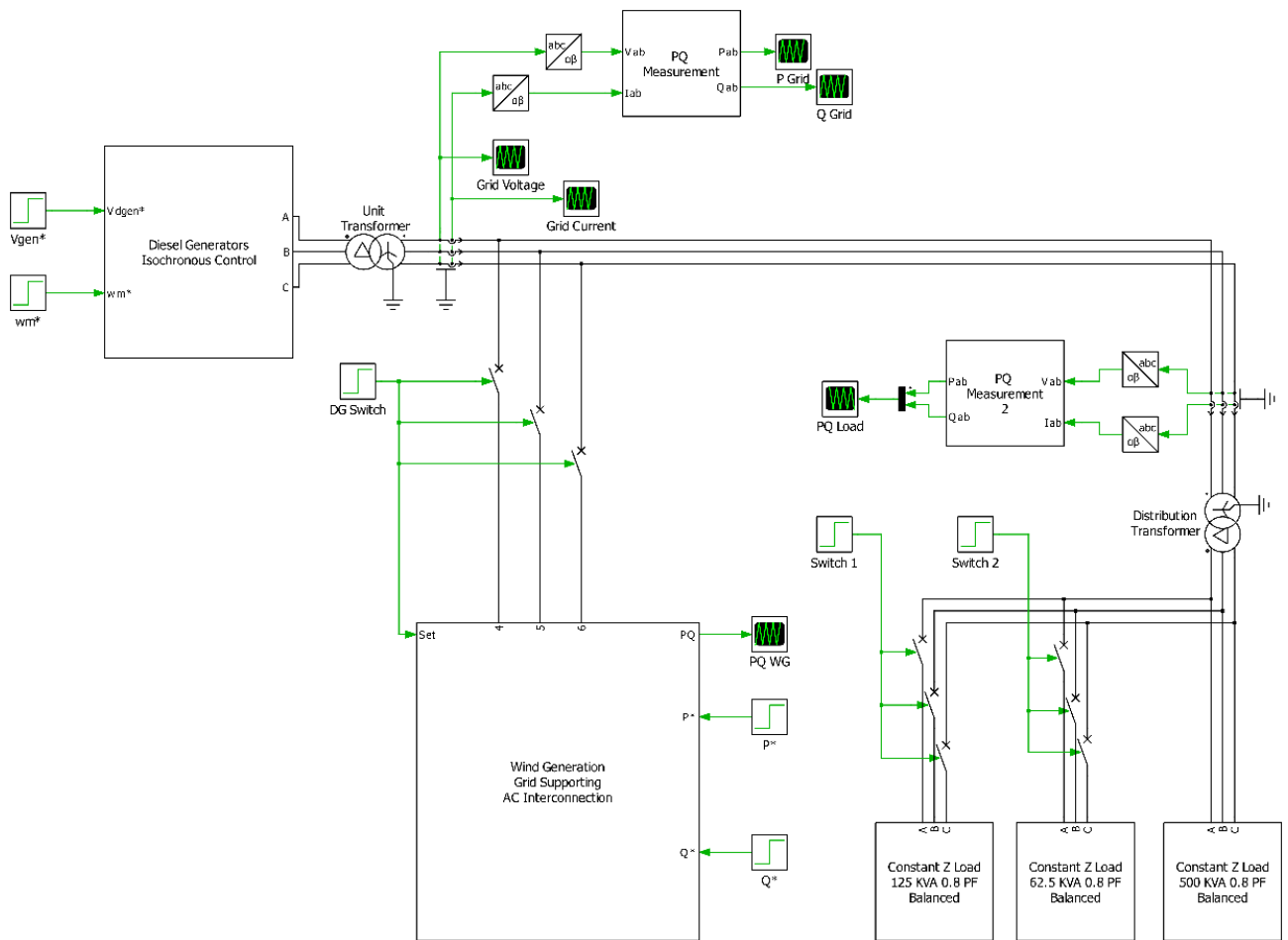


Figure 4.4: Microgrid Simulation Topology in PLEXIM

4.3.1: Grid Forming in Microgrids

Grid forming in an islanded microgrid is performed by the largest active diesel generator, maximizing microgrid inertia and stability. Diesel generators use an internal combustion engine to drive a prime mover connected to a synchronous generator. As diesel engines operate at high speeds, a two or four pole machine is often used. Within the

simulation environment, the synchronous machine is modelled using the rotor reference frame – a rotating frame generated using the well-known Park transformation. A detailed analytical model of a synchronous machine is presented in [32], and is used within the PLEXIM simulation environment. The behavior of a synchronous machine under non-saturated operation is well-known, as is the control architecture required for grid forming operation. Figure 4.5 displays the simulation topology used to implement the grid-forming diesel generator. The synchronous generator model presented in [32] is implemented by PLEXIM, with generator parameters selected to match commonly available 100 kW to 1 MW diesel generators. The selected generator is a salient-pole design, requiring the more complex numerical model with separate direct and quadrature-axis inductance values. The field winding of the synchronous generator is excited by an IEEE standard [33] exciter, in this case modelled as a first order feedback transfer function. The command excitation voltage is supplied by a PI excitation controller. The generator terminal voltage is the variable of interest – it is converted into a rotating reference frame using the Park transformation and a 3-phase PLL connected to the stator terminals. The control action maintains the generator terminal voltage through changes in stator current induced by demand variation. The prime mover is controlled by a PI engine governor in series with a transfer function implementing a first order time-constant. The engine governor sets the grid frequency through controlling the rotor speed of the synchronous generator. Assuming that a speed sensor is included within the diesel generator, the controller can directly compare with a reference value to implement reliable grid frequency control. If a speed sensor is absent, a PLL [34, 35], EPLL [36] or FLL [37] can be used to obtain the grid

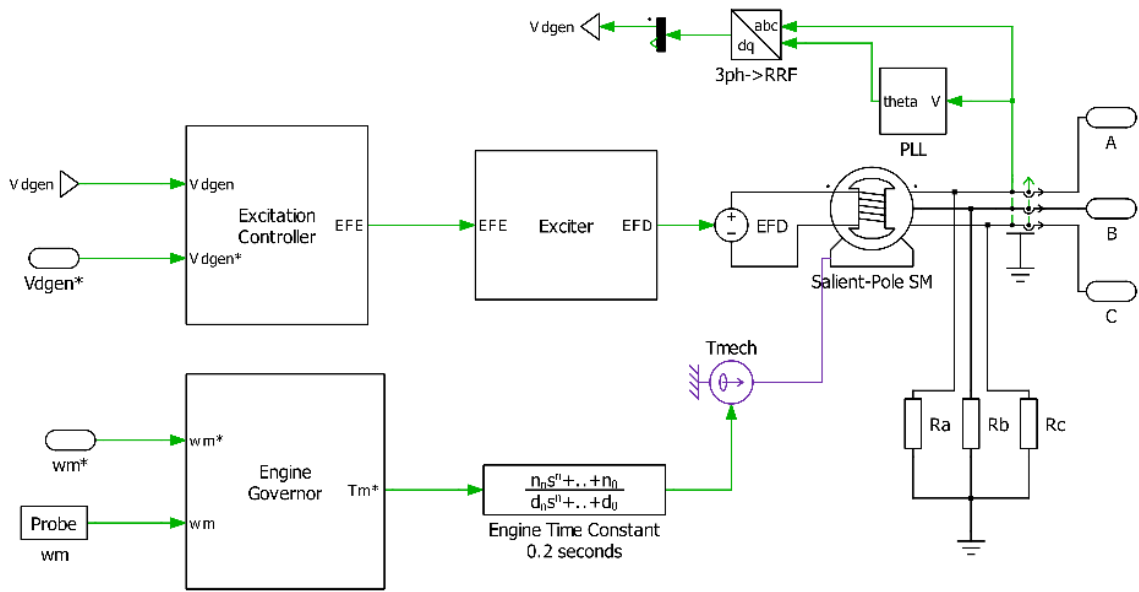


Figure 4.5: Grid Forming Diesel Generator

frequency using the stator terminal voltage, with the rotor speed then obtained and fed to the governor.

Figure 4.6 displays the detailed controller diagram of the generator excitation system. The exciter is modelled as an integrator with feedback. The transfer function of this system is as follows:

$$E(s) = \frac{G(s)H(s)}{1 + G(s)H(s)} \quad (1)$$

where

$$G(s) = \frac{K_{Ie}}{s} \quad (2)$$

and $H(s)$ is the exciter feedback gain K_E . The value of K_{Ie} determines the response speed of the exciter. Substituting the selected gain values, the net feedback transfer function is a first order time constant:

$$E(s) = \frac{50/s}{1 + 50/s} \quad (3)$$

which is simplified to:

$$E(s) = \frac{50}{s + 50} \quad (4)$$

This produces a fast exciter (with a time constant of 0.02 seconds) – a reasonable assumption given that the excitation system is often comprised of a smaller machine connected to the prime mover shaft. For simulation purposes, the exciter is assumed to be 10 times faster than the diesel engine in responding to command changes.

The excitation controller implements a standard parallel PI transfer function:

$$C(s) = \left(K_p + \frac{K_i}{s} \right) (V^* - V) \quad (5)$$

Where V^* is the direct-axis terminal reference voltage in the rotating reference frame and V the measured direct axis terminal voltage. A saturation block is added to prevent over excitation during initial start-up - the generator is non-linear across large rotational speed changes and is difficult to control using gains optimized for full-speed operation. Saturation addresses this issue and also ensures that practical limits are followed with respect to the generator field voltage. Combining (5) with (4) and assuming non-saturated behavior, the controller transfer function is expressed as:

$$C_E(s) = \left(K_p + \frac{K_i}{s} \right) (50/(s + 50)) \quad (6)$$

During steady-state operation, the relationship between the excitation voltage and the generator terminal voltage can be simply modelled as a first order transfer function [32]:

$$T(s) = \frac{T_e}{s + T_e} \quad (7)$$

where T_e is the generator's electrical time constant, included on most manufacturer datasheets. In general, this value should be at least 10 times larger than the exciter to prevent controller oscillation. Combining this time constant with the controller model and accounting for the voltage feedback, the excitation controller has the following behavior:

$$\frac{V}{V^*} = \frac{(K_p + K_i/s) (50/(s + 50)) \frac{T_e}{s + T_e}}{1 + (K_p + K_i/s) (50/(s + 50)) \frac{T_e}{s + T_e}} \quad (8)$$

Simplifying, the excitation system can be modelled as follows:

$$\frac{V}{V^*} = \frac{50K_pT_e s + 50K_iT_e}{s^3 + (T_e + 50)s^2 + 50T_e(1 + K_p)s + 50K_iT_e} \quad (9)$$

The transfer function defined by (9) has uniquely positive coefficients using negative-feedback control. Using the well-known Routh-Hurwitz criterion, the closed-loop controller is stable when the following condition is met:

$$(T_e + 50) > \frac{K_i}{(1 + K_p)} \quad (10)$$

Under practical conditions, K_i is less than or equal to K_p , therefore the excitation controller (within the bounds of nominal generator operation) will correctly converge to the reference terminal voltage.

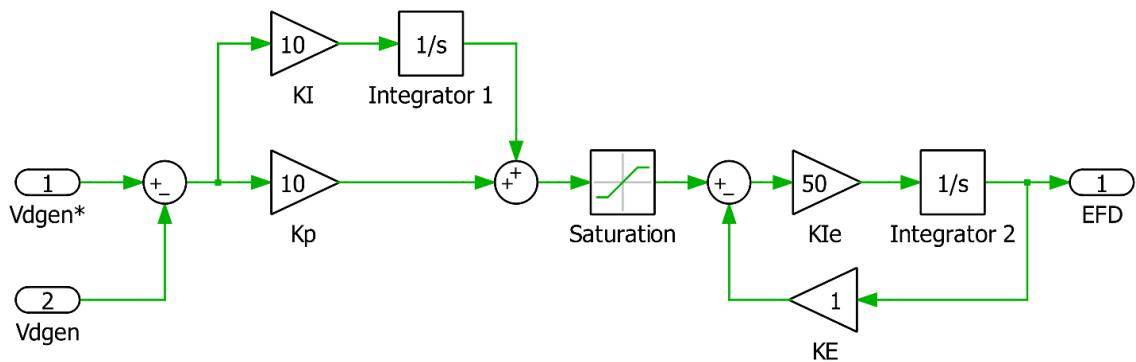


Figure 4.6: Diesel Generator Excitation Controller

Figure 4.7 presents the control architecture of the speed governor. The mechanical behavior of the diesel engine is modelled as a first-order time constant, in this case set to 0.2 seconds for small changes in engine torque expected from the controller. The transfer function of this controller is similar to the excitation system – the repeated derivation of the PI feedback transfer function is therefore left as an exercise. The mechanical behavior of the synchronous generator (from the viewpoint of the prime mover) follows an inherently stable first-order behavior assuming a constant electrical load and a small deviation in operating speed – therefore the governor will also be stable assuming realistic controller gains. The response of the governor system approximates a first-order time constant, with the response speed proportional to the magnitude of the controller gains. An excessively high gain may cause oscillation or torsional vibration. In the proposed simulation environment, the controller gains have been tuned to produce a controller response with a time constant significantly slower than the generator’s electrical response, reducing the probability of generator damage. The slow operation of mechanical governors leads to the

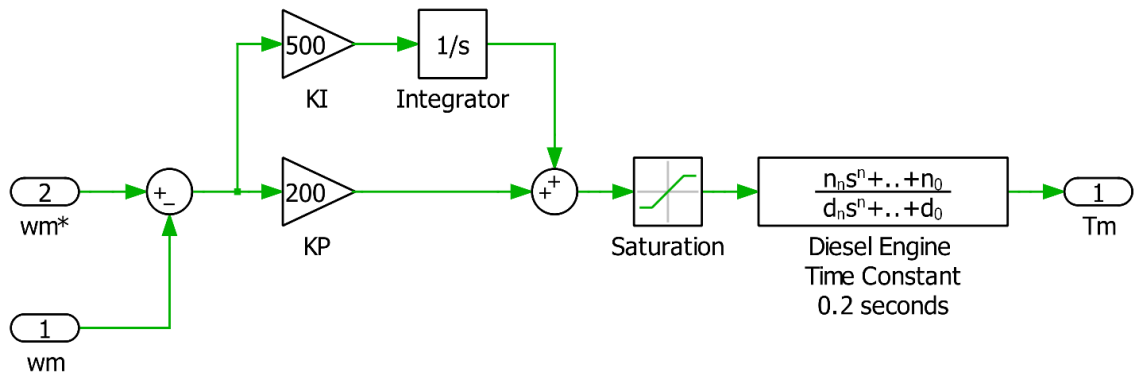


Figure 4.7: Diesel Engine Governor

use of grid-supporting control and provides the need for wind reserves to maintain grid frequency during demand variation or other transient contingencies.

4.3.2: Grid Synchronization and Interconnection of Distributed Generation

Grid Synchronization

The interconnection of distributed generation with the utility grid requires fast, accurate synchronization algorithms. In islanded microgrids, additional issues occur due to the relatively weak grid being vulnerable to disturbances created by imperfect interconnection. Essentially, to connect a distributed generator (such as a wind turbine or PV array) to a microgrid, the synchronization system must be able to match a potentially unbalanced or distorted grid in such a way as to minimize switching-induced disturbances. To compensate for unbalanced or distorted grids, the synchronization algorithm should be able to quickly and accurately identify the positive and negative sequence components of the grid voltage

[37]. Conventional techniques such as a PLL or SRF-PLL [34] are not capable of this. Newer techniques such as DSRF-PLL [35] or EPLL [36] exhibit better performance. The latest and most reliable method for grid synchronization is the “Dual Second Order Generalized Integrator Frequency Locked Loop” (DSOGI-FLL), presented in [37]. The underlying behavior and performance of the DSOGI-FLL will be briefly reviewed and its implementation in the simulation environment demonstrated to validate its application in the grid synchronization of distributed generation.

Figure 4.8 displays the second order generalized integrator. The SOGI has the following transfer function [37]:

$$S(s) = \frac{s\omega'}{s^2 + \omega'^2} \quad (11)$$

(11) shows that the SOGI is resonant at the frequency ω' , acting as an infinite-gain integrator [37] for any sinusoidal signal at an equivalent frequency. Augmenting the SOGI with a quadrature signals generator (QSG), the following tracking behavior emerges [37]:

$$D(s) = \frac{k\omega's}{s^2 + k\omega's + \omega'^2} \quad (12)$$

$$Q(s) = \frac{k\omega'^2}{s^2 + k\omega's + \omega'^2} \quad (13)$$

The resonance frequency ω' and damping factor k is set externally. The transfer functions presented in (12) and (13) indicate band-pass and low-pass filter behavior, respectively. Figure 4.9 displays the SOGI-QSG, where v' is connected to D and qv' to Q , representing

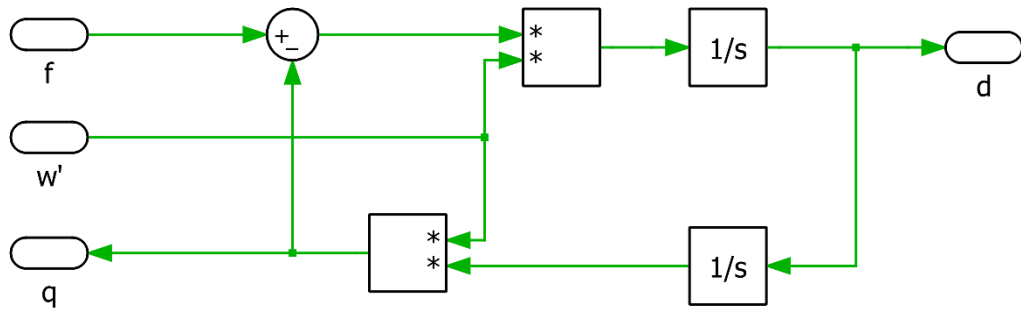


Figure 8: SOGI Configuration

the direct and quadrature components of the input voltage waveform v . The SOGI gain k is tunable to influence the response speed and sensitivity of the SOGI-QSG.

The SOGI-QSG is not in itself frequency-adaptive, being restricted to the natural resonance frequency ω' input into the SOGI. A frequency locked loop (FLL) can be inserted into the SOGI-QSG as in [37] to augment the system's frequency adaptability. Figure 4.10 presents the FLL configuration in PLEXIM. The FLL uses the error signal from the SOGI-QSG as an input, multiplying it with the identified quadrature voltage waveform to complete the initial PLL architecture. An integrator controller with an initial guess frequency (in this case 377 rad/s) is used to track the frequency of the voltage waveform, returning this to the SOGI to ensure that it continuously adapts to changes in grid frequency. The gain of the FLL is normalized using an algorithm presented in [24], resulting in the

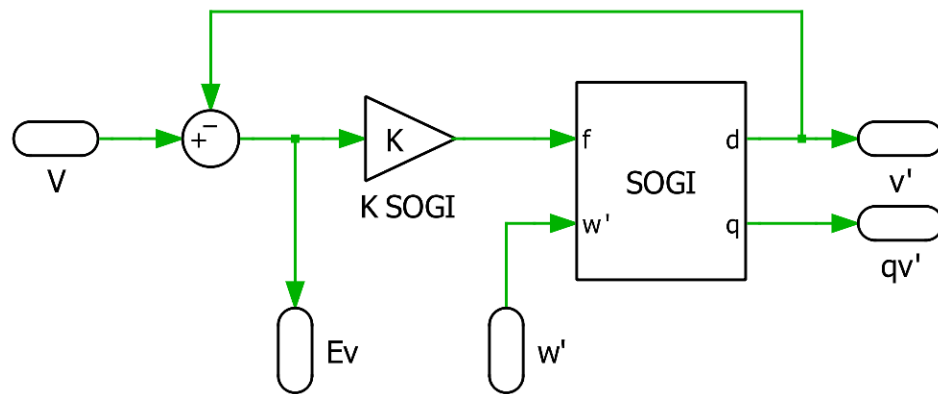


Figure 4.9: The SOGI-QSG

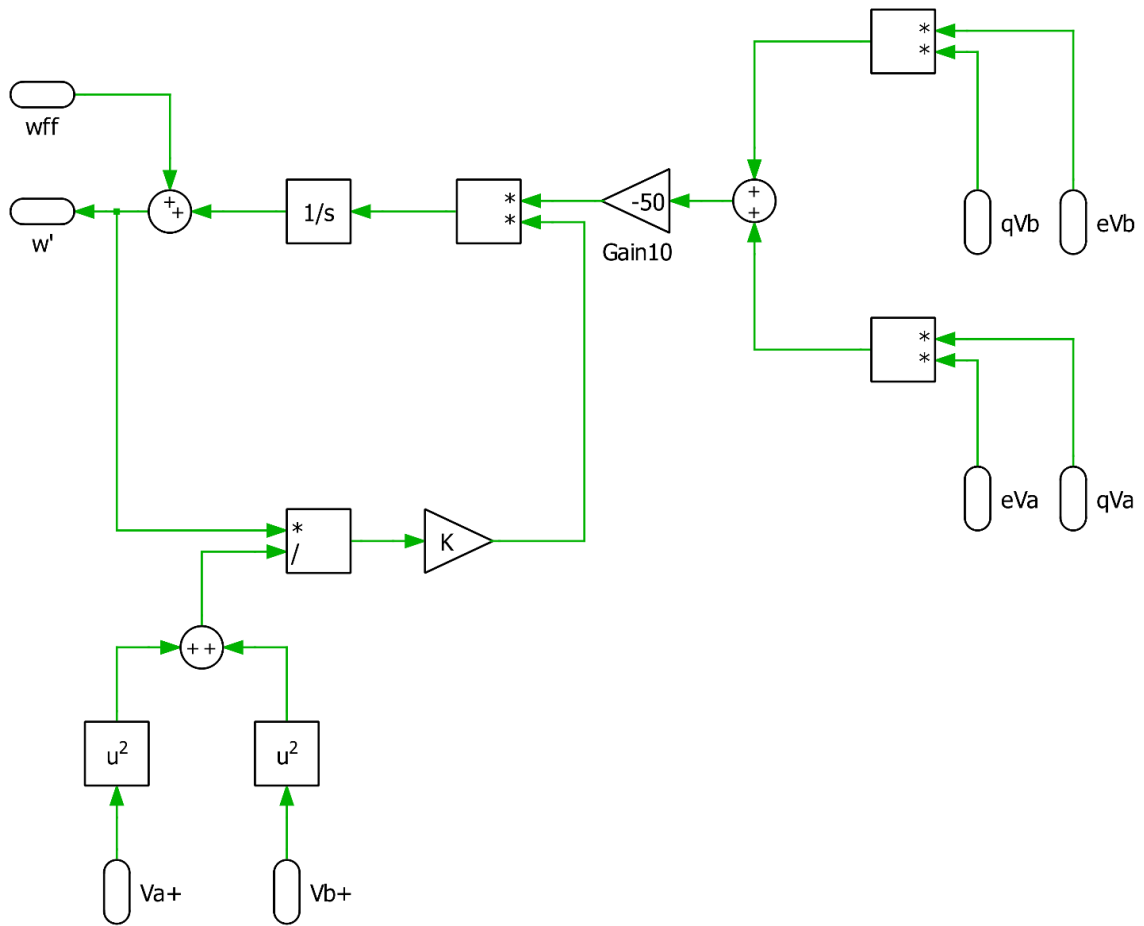


Figure 4.10: Gain-Normalized FLL Configuration in PLEXIM

FLL response approximating first-order behavior with a tunable time constant. Setting the FLL gain to 50 and applying normalization, the DSOGI-FLL has a time constant of ~ 0.02 seconds, roughly equivalent to the grid-forming exciter and ensuring a fast response to grid frequency deviations. The result is a robust, stable combination of the SOGI and FLL which implements grid synchronization.

To allow the determination of both positive and negative sequence grid components, dual SOGI-QSGs are implemented, both using the gain-normalized FLL to perform frequency synchronization. This topology is the DSOGI-FLL, as presented in [24-25, 37]. Figure 4.11 presents the DSOGI-FLL as implemented. The grid voltage is transformed into the stationary frame, with each component then sent separately to one of the two SOGI-QSGs. The gain-normalized FLL uses the SOGI-QSG error signals to isolate the fundamental grid frequency ω' , which is then fed back to the SOGIs, adapting them to any changes in grid frequency. The SOGI-QSG outputs are the direct and quadrature components of the stationary-frame grid voltages, when are then transformed into the stationary positive and negative sequence components as follows [24-25, 37]:

$$V_{\alpha+} = V_{\alpha} - qV_{\beta} \quad (14)$$

$$V_{\beta+} = qV_{\alpha} + V_{\beta} \quad (15)$$

$$V_{\alpha-} = V_{\alpha} + qV_{\beta} \quad (16)$$

$$V_{\beta-} = -qV_{\alpha} + V_{\beta} \quad (17)$$

with the initial gain of $\frac{1}{2}$ applied before the signals reach the DSOGI-FLL. The final result is the identification of the stationary-frame positive and negative sequence grid voltages, in addition to the instantaneous grid frequency. This information allows the synchronization of distributed generation to unbalanced or distorted microgrids, with the precise matching of sequence components minimizing disturbances inherent during interconnection.

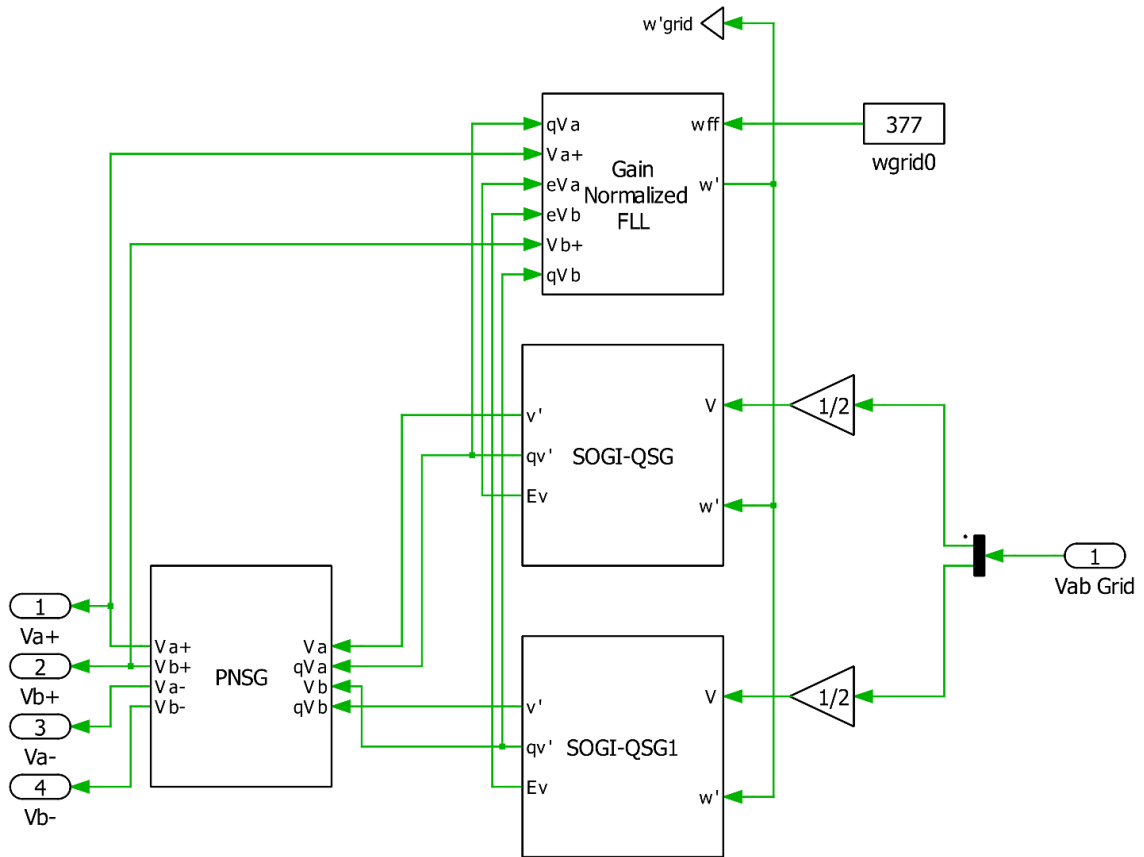


Figure 4.11: DSOGI-FLL with PNSG in PLEXIM

Grid Interconnection

The control of an inverter generally centers around the active and reactive power sent into or out of the utility grid [6]. However, the inverter itself is a PWM-switched device using either SPWM [38], space vector control [38] or another scheme to control the AC terminal voltages. A control algorithm is required which converts active and reactive power (P and Q) reference signals into terminal voltage specifications. Two methods are commonly used – the voltage source inverter (VSI) topology, where the inverter tracks a

current reference by varying the terminal voltage [38] with a constant supporting DC link voltage, and the current source inverter (CSI) topology, where the inverter current is constant, with the terminal voltage reference being met by varying either the duty cycle or DC link voltage. For hybrid AC/DC and DC microgrids, the DC link voltage is low-impedance and nearly constant. Therefore, the VSI topology is used. The first step in VSI control is developing the current references required to meet the requested P and Q values. When the grid conditions are balanced (or nearly so), the extraction of positive and negative sequence components allows the calculation of inverter current references through the instantaneous power theory [39]:

$$\begin{bmatrix} I_\alpha \\ I_\beta \end{bmatrix} = \frac{1}{V_\alpha^2 + V_\beta^2} \begin{bmatrix} V_\alpha & V_\beta \\ V_\beta & -V_\alpha \end{bmatrix} \begin{bmatrix} P \\ Q \end{bmatrix} \quad (18)$$

Figure 4.12 displays the implementation of instantaneous power theory. The stationary frame components isolated from the DSOGI-FLL are applied to the appropriate mathematical operations (18), converting the P and Q reference values into stationary-frame current reference signals. These current references are then used to implement VSI control. Figures 4.13 and 4.14 displays the control architecture of the VSI. Each stationary-frame current reference is fed through a proportional-resonant (PR) controller [6. 40-41]. PR controllers exhibit superior performance in tracking sinusoidal signals [40-41] of a known frequency. As the DSOGI-FLL identified this frequency, the PR controllers can be easily adapted to maintain resonance and therefore tracking performance. The PR controller has the following transfer function [40-41]:

$$G_{PR}(s) = K_P + \frac{K_R s}{s^2 + \omega_0^2} \quad (19)$$

where K_P and K_R are the tunable controller gains and ω_0 the resonant frequency. The resultant VSI control law is as follows:

$$V_{\alpha T}^* = V_\alpha + \left(K_P + \frac{K_R s}{s^2 + \omega_0^2} \right) (I_\alpha^* - I_\alpha) \quad (20)$$

$$V_{\beta T}^* = V_\beta + \left(K_P + \frac{K_R s}{s^2 + \omega_0^2} \right) (I_\beta^* - I_\beta) \quad (21)$$

where $V_{\alpha T}$ and $V_{\beta T}$ are the stationary-frame inverter terminal voltage references. V_α and V_β are the stationary-frame grid voltages measured at the point of common coupling (on the low side of transformer). I_α and I_β are the grid interconnection currents, measured again at the point of common coupling.

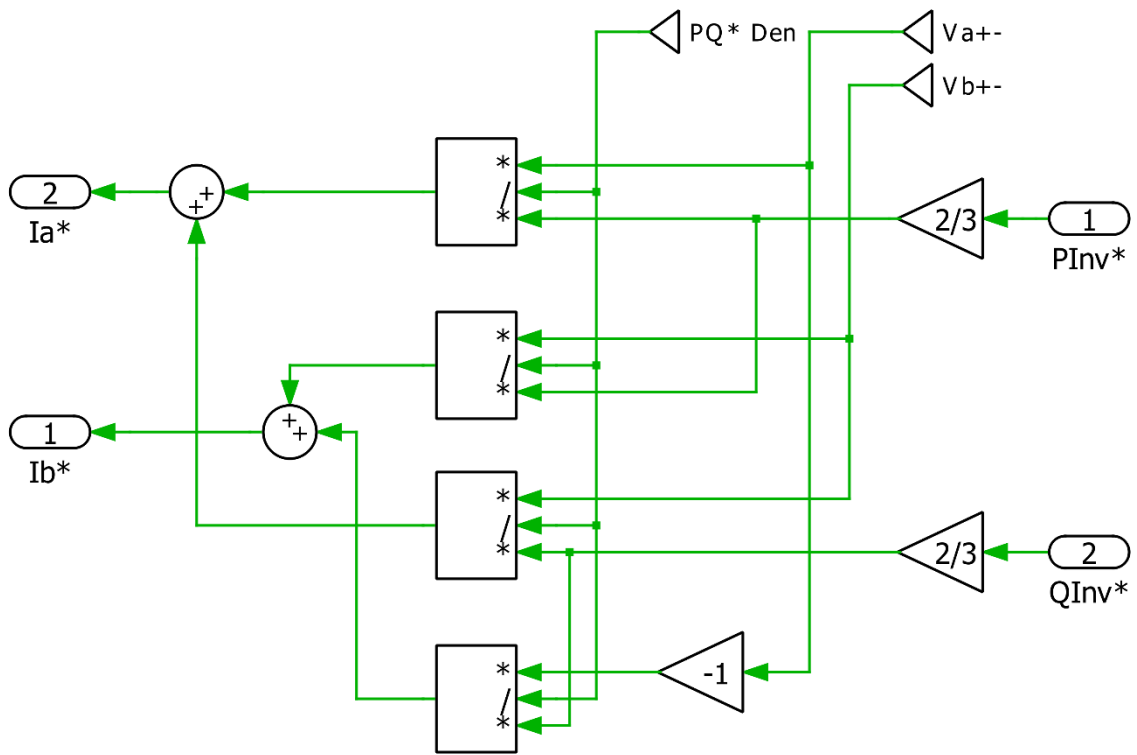


Figure 4.12: PLEXIM Implementation of the Instantaneous Power Theory

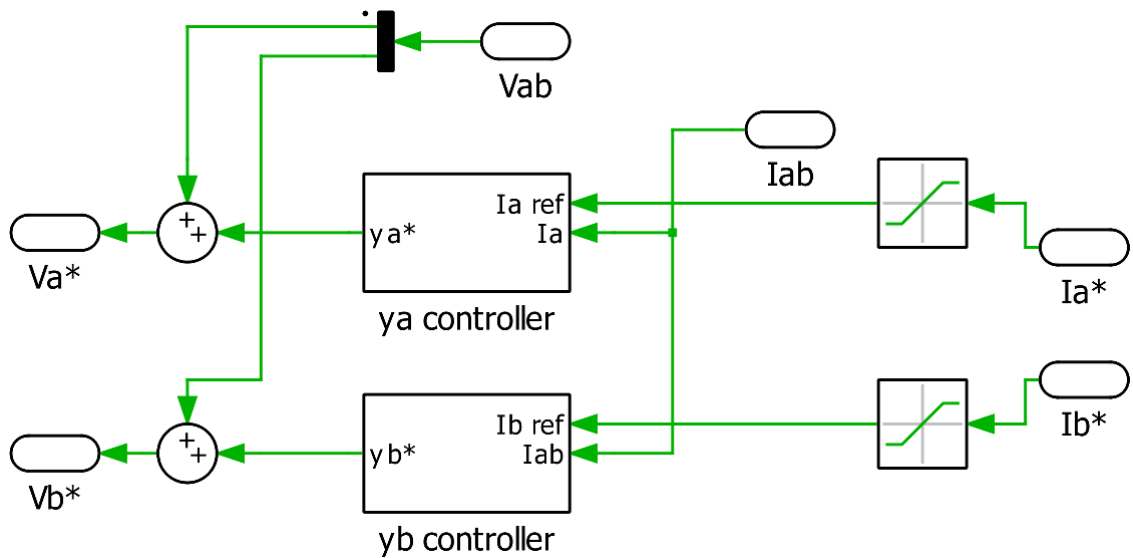


Figure 4.13: VSI Controller Architecture

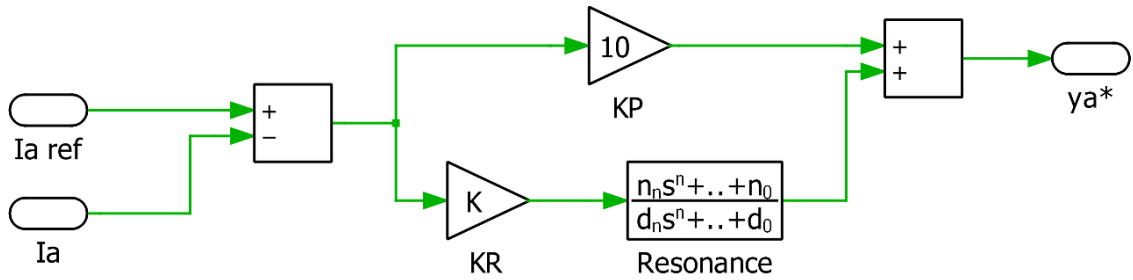


Figure 4.14: VSI Current Controller

The performance of the PR-VSI controller is dependent on the line impedance, power filter behavior as well as inverter dynamics. Figure 4.15 displays the grid interconnection topology used in the PLEXIM simulation environment. A VSI is connected through a damped LCL power filter and a unit transformer (required to increase the inverter output voltage to match the power system voltage level) to the point of common coupling (PCC). For control purposes, the PCC is assumed to be at the primary (low voltage) side of the unit transformer – transformer core and copper losses should not be significant (< 5%) under reasonable load conditions. Additionally, the inverter dynamics are assumed to be much faster than the microgrid dynamics - a 2 or 3-level SVPWM VSI operating at a switching frequency of greater than 5 kHz has a response time of less than 1ms. Therefore, the inverter terminal voltage is assumed to equal its reference value:

$$V_{\alpha\beta T}^* = V_{\alpha\beta T} \quad (22)$$

where $V_{\alpha\beta}$ represents the stationary-frame inverter terminal voltages and $V_{\alpha\beta}^*$ the controller references. This simplifies the grid interconnection analysis by removing inverter dynamics.

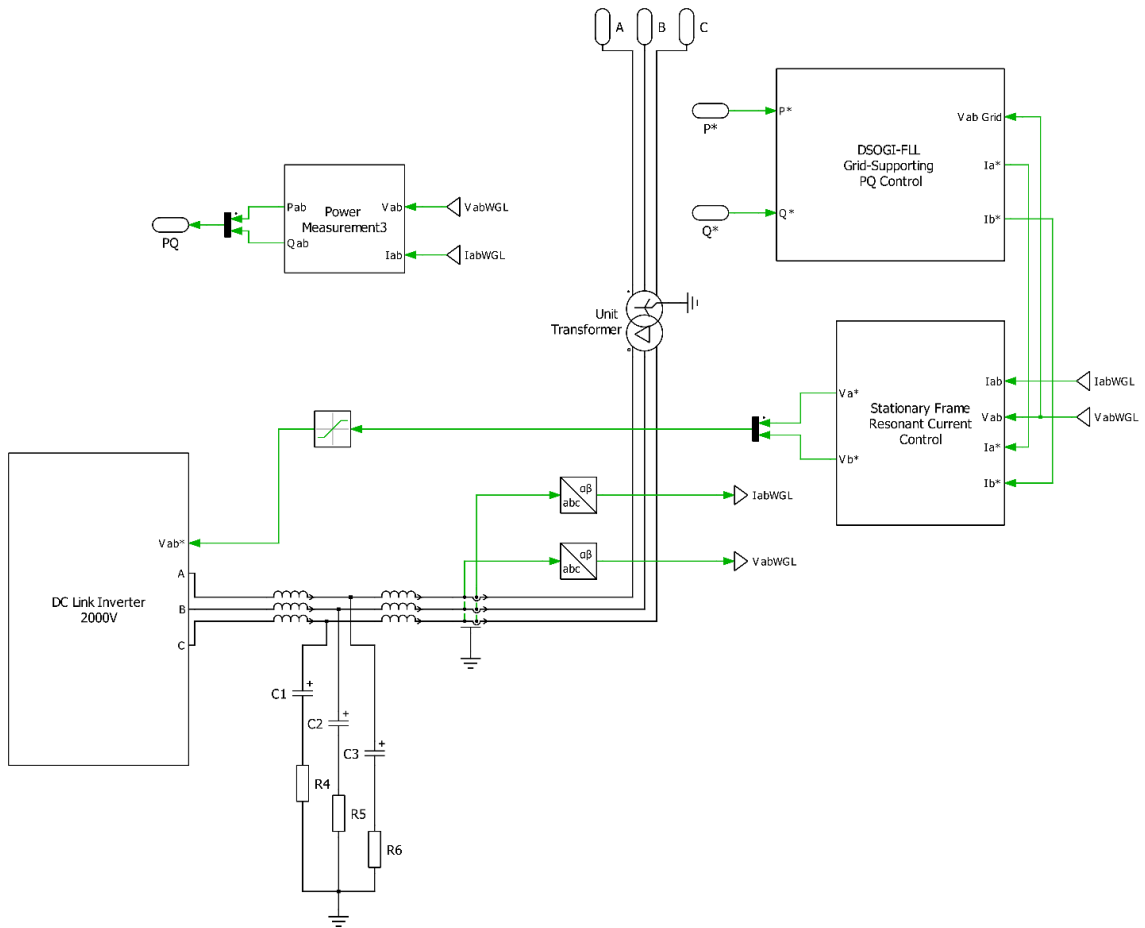


Figure 4.15: Distributed Generation Interconnection Topology

The damped LCL power filter's stationary-frame dynamics are derived by first identifying the relation between the LCL node voltage ($V_{\alpha\beta 1}$) and the inverter terminal voltage:

$$V_{\alpha\beta T} = V_{\alpha\beta 1} + sL_1 I_{\alpha\beta T} \quad (23)$$

Where L_1 is the leftmost inductance and $I_{\alpha\beta T}$ the stationary-frame inverter terminal current. Assuming balanced three-phase resistance and capacitance in the shunt branch, the follow relation arises:

$$I_{\alpha\beta s} = \frac{V_{\alpha\beta 1}}{(R + \frac{1}{sC})} \quad (24)$$

Where R and C are the resistance and capacitance values, and $I_{\alpha\beta s}$ the shunt branch current. Assuming that the line inductance between the LCL filter and the PCC is included within the rightmost inductance L_2 , and by performing nodal analysis, the following emerges:

$$V_{\alpha\beta 1} = V_{\alpha\beta} + sL_2 I_{\alpha\beta} \quad (25)$$

$$I_{\alpha\beta T} = I_{\alpha\beta} + I_{\alpha\beta s} \quad (26)$$

In this situation, the derivation seeks to determine the relationship between the stationary frame LCL terminal voltages and the resultant PCC output current. Substituting (26) and (25) into (23):

$$V_{\alpha\beta T} = V_{\alpha\beta} + sL_2 I_{\alpha\beta} + sL_1 (I_{\alpha\beta} + I_{\alpha\beta s}) \quad (27)$$

the inverter terminal voltage is expressed as a function of the PCC voltage, PCC current and the LCL shunt current. Substituting (24) into (27), the shunt current is replaced as follows:

$$V_{\alpha\beta T} = V_{\alpha\beta} + sL_2 I_{\alpha\beta} + sL_1 (I_{\alpha\beta} + \frac{V_{\alpha\beta 1}}{(R + \frac{1}{sC})}) \quad (28)$$

By substituting (25) into (28), the node voltage can be removed from the equation:

$$V_{\alpha\beta T} = V_{\alpha\beta} + sL_2 I_{\alpha\beta} + sL_1 (I_{\alpha\beta} + \frac{V_{\alpha\beta} + sL_2 I_{\alpha\beta}}{(R + \frac{1}{sC})}) \quad (29)$$

Collecting terms and simplifying, the inverter terminal voltage is shown to be a function of both the PCC voltage and the PCC current:

$$V_{\alpha\beta T} = V_{\alpha\beta} \left(1 + \frac{sL_1}{R + \frac{1}{sC}} \right) + I_{\alpha\beta} \left(s(L_1 + L_2) + \frac{s^2 L_1 L_2}{(R + \frac{1}{sC})} \right) \quad (30)$$

Further simplifying:

$$V_{\alpha\beta T} = V_{\alpha\beta} \left(1 + \frac{s^2 CL_1}{sRC + 1} \right) + I_{\alpha\beta} \left(s(L_1 + L_2) + \frac{s^3 CL_1 L_2}{(sRC + 1)} \right) \quad (31)$$

$$V_{\alpha\beta T} = V_{\alpha\beta} \left(1 + \frac{s^2 CL_1}{sRC + 1} \right) + I_{\alpha\beta} \left(\frac{s^3 CL_1 L_2 + s^2 RC(L_1 + L_2) + s(L_1 + L_2)}{(sRC + 1)} \right) \quad (32)$$

The final transfer function developed in (32) displays the dynamic behavior of the PCC current in terms of the inverter terminal voltage and the PCC voltage. The feed-forward path in the PR controller architecture (Figure 4.12) is clearly justified – it cancels part of the disturbance transfer function $V_{\alpha\beta T}/V_{\alpha\beta}$ and improves the transient behavior of the PR controller. The closed loop performance of the PR controller is calculated by neglecting the disturbance caused by the PCC voltage, which in either case is attenuated by the feed forward. The control laws expressed in (20) and (21) (with the feedforward term removed) can be combined with the plant dynamics in (32) to get the open-loop transfer function of the controller:

$$\frac{I_{\alpha\beta}}{I_{\alpha\beta E}} = \left(K_P + \frac{K_R s}{s^2 + \omega_0^2} \right) \left(\frac{(sRC + 1)}{s^3 CL_1 L_2 + s^2 RC(L_1 + L_2) + s(L_1 + L_2)} \right) \quad (33)$$

where $I_{\alpha\beta}E$ is the reference tracking error. Using the relation described in (1), the closed-loop transfer function (after simplification and the use of symbolic variables) is:

$$\frac{I_{\alpha\beta}}{I_{\alpha\beta}^*} = \frac{\alpha s^3 + \beta + \gamma s + \delta}{As^5 + Bs^4 + Ds^3 + Es^2 + Fs + \delta} \quad (34)$$

$$\alpha = K_p CR \quad (35)$$

$$\beta = (K_p + K_R CR) \quad (36)$$

$$\gamma = (\omega_0^2 K_p CR + K_R) \quad (37)$$

$$\delta = K_p \omega_0^2 \quad (38)$$

$$A = CL_1 L_2 \quad (39)$$

$$B = CR((L_1 + L_2)) \quad (40)$$

$$D = (CL_1 L_2 \omega_0^2 + L_1 + L_2 + K_p CR) \quad (41)$$

$$E = (K_p + K_R CR + CR \omega_0^2 (L_1 + L_2)) \quad (42)$$

$$F = K_R + \omega_0^2 (L_1 + L_2 + K_p CR) \quad (43)$$

The closed loop behavior in (34) is shown to be stable under a variety of configurations [40-41], with a specific emphasis on stability when the resonant frequency is properly tuned to match the observed grid frequency. The tuning of the resonant gains is detailed in [40-41], and is highly dependent on the microgrid configuration and the design of the converter, power filter and the effects of the grid and transformer losses (when significant). A full analytical model of the islanded microgrid is a MIMO system with complex non-linear

behavior depending on the grid voltage, power flow and generator and DC-link dynamics. While the latter will be investigated in a later section, a unified analytical framework is not required for the numerical validation of wind reserves and is therefore beyond the scope of this thesis.

4.3.4: Microgrid Support using Distributed Generation

In standard power systems, frequency and voltage regulation is provided by dynamic stabilization systems embedded within conventional generation. Islanded microgrids cannot access these stabilization systems. In this case, wind generation can provide the required dynamic stabilization, including the regulation of microgrid frequency. The power inverter wind turbine / microgrid interface is sufficiently fast and stable to implement several methods of droop control. Droop control implements inverter control algorithms to simulate the functionality of a synchronous generator [6, 42]. The basic functionality is described by P/f and Q/V droop control [6, 42]:

$$P_{Inv} = k_{DP}(f - f^*) \quad (44)$$

$$Q_{Inv} = k_{DQ}(V - V^*) \quad (45)$$

Where P_{inv} and Q_{inv} are the resulting inverter reference active and reactive commands and K_{dp} and K_{dq} the droop coefficients. The droop coefficients are related to the microgrid system, including the feeder line impedance and generator inertia. The relations in (44) and (45) assume a grid which is primarily inductive. In situations where resistive behavior is

expected, Q/f and P/V droops are more appropriate [6, 42-43]. Most microgrids fall between these two extremes, leading to more advanced droop control techniques such as virtual impedance [6, 44-45], virtual admittance [46], adaptive droop coefficients [43] or nonlinear droop control [47].

Within the simulation environment, conventional droop control is sufficient to investigate the behavior of wind reserves. Figure 4.16 displays the developed droop control architecture. The conventional linear droop control is augmented with an integral frequency restoration term, allowing the VSI to act as a virtual governor. This assists the grid-forming generator in frequency restoration by instituting permanent power sharing during demand increases. The droop coefficients are adjustable depending on the size of the simulated microgrid – generally they are set to between 0.01 and 0.04 per-unit reflecting the behavior of synchronous generator governors during load changes. The voltage regulation loop implements linear Q/V droop control. The grid-forming generator's excitation controller is fast enough to quickly restore the grid voltage during sags. Therefore, the primary purpose of the voltage droop controller is to share the reactive power requirement among the distributed generation. In both frequency and voltage droop regulation, the ratio of the droop coefficients determines the power sharing between inverters and generators. Scaling these coefficients based on the inverter (and distributed generator) ratings ensures fast and robust uptake of active and reactive power demand.

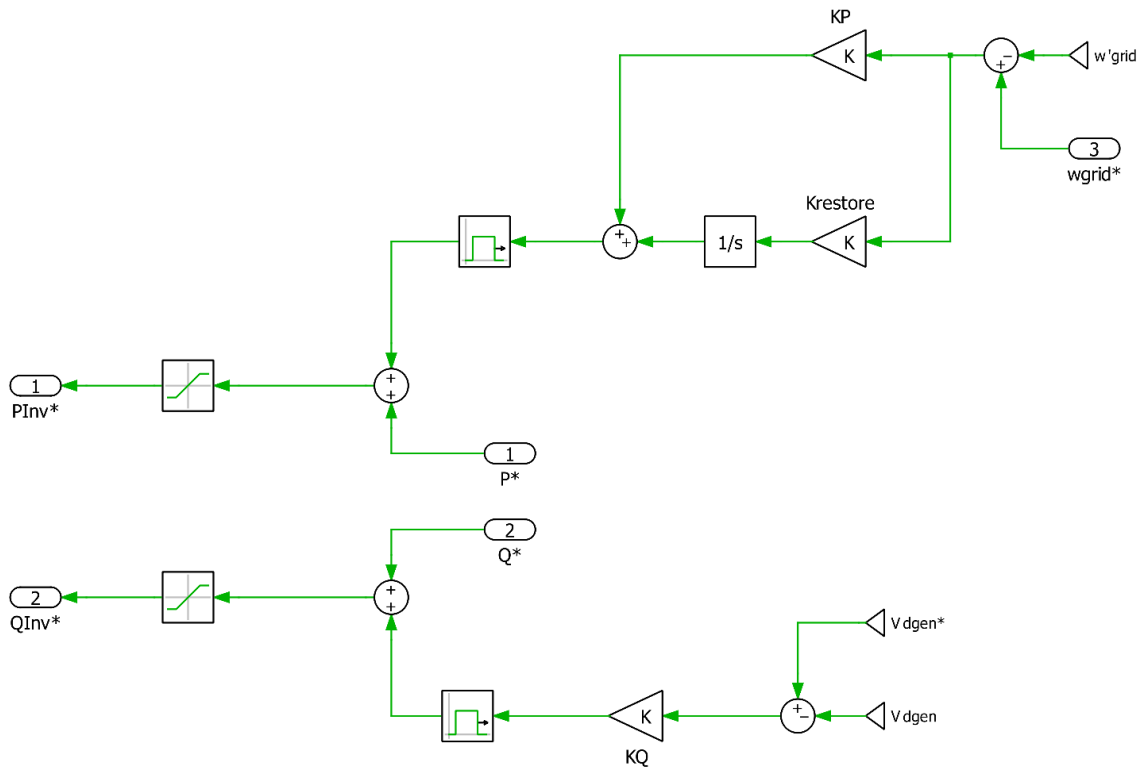


Figure 4.16: Voltage and Frequency Droop Regulation in PLEXIM

In addition to frequency and voltage regulation, distributed generation can also be dispatched by supervisory control to feed active and reactive power into the grid. This grid-feeding operation allows wind farms or PV arrays to supply all available energy to the microgrid, with the conventional generators shifting to a reserve role. Grid feeding inverter operation is accomplished by directly supplying the P and Q references to the primary controller, with the resultant inverter terminal voltage acting as a source for the microgrid. The determination of these references is accomplished by higher level control algorithms or direct dispatch by grid operators. In islanded microgrids, the rate of reference change is limited to that of the grid-forming synchronous generator's power output, otherwise voltage and frequency disturbances would result. Finally, distributed generation can be used to

directly from the grid. Grid forming control replaces the inverter P and Q references with voltage and frequency references [6]. This control technique is not as common for intermittent sources in islanded microgrids, however during periods of high wind energy a wind reserve can be used in this manner when the amount of injected power becomes the majority of the microgrid demand. The inverter creates virtual inertia by the controller action – very little voltage or frequency regulation is required during load changes as long as the DC link voltage behind the inverter can be maintained by the wind turbine, PV array or other energy source.

4.4: Integration of Wind Generation into Islanded Microgrids

Wind generation is a constantly growing source of renewable energy. Advances in wind turbine materials, power electronics, generators and control techniques are continuously decreasing the capital and maintenance costs of wind generation. The improved performance of wind generation has made it increasingly viable for installation in isolated microgrids. Many islanded and isolated microgrids exist in Nordic or coastal areas where the average solar insolation is low and the cost of transporting fuel is high – these locations are ideal for wind generation. The specific requirements of islanded microgrids (as described in the previous sections) require advanced control and grid interconnection equipment to interface wind turbines with the microgrid. The precise equipment required depends on the type of wind turbine, with each having advantages and disadvantages with respect to performance within a microgrid.

4.4.1: Overview of Wind Turbine Generators

Wind turbines are generally constructed in one of four types (Type A, B, C or D). [48] presents a comprehensive review of the types of wind turbines and their behavior. Figure 4.17 [48] displays the general architecture of each wind turbine type. Type A wind turbines use squirrel-cage induction generators, connected to the grid through a soft-starter. A capacitor bank is included to provide excitation to the generator, improving the power

factor and start-up performance. Using this configuration, the wind turbine must operate at a near-fixed speed very slightly above synchronous speed, with the power generated by the induction generator a function of the resulting slip value [49]. Advantages of this design include its simplicity and cost. However, it is not appropriate for weaker grids, as any output power fluctuations are directly transmitted to the grid without the possibility of attenuation through control action. Therefore, type A wind turbines are not appropriate for islanded microgrids. Type B wind turbines use wound-rotor induction generators (WRIG) [50]. The WRIG allows slight speed variation (up to 10%) [48] by varying the rotor resistance, changing the slip/power curve and allowing some control of the output power. This design also requires a soft starter (as induction generators draw very high current upon starting) [50] as well as a capacitor bank for reactive power compensation. The Type B wind turbine is also directly connected to the grid – therefore it is also inappropriate for use in islanded microgrids. Wind turbines must be at least partially isolated from the microgrid to allow

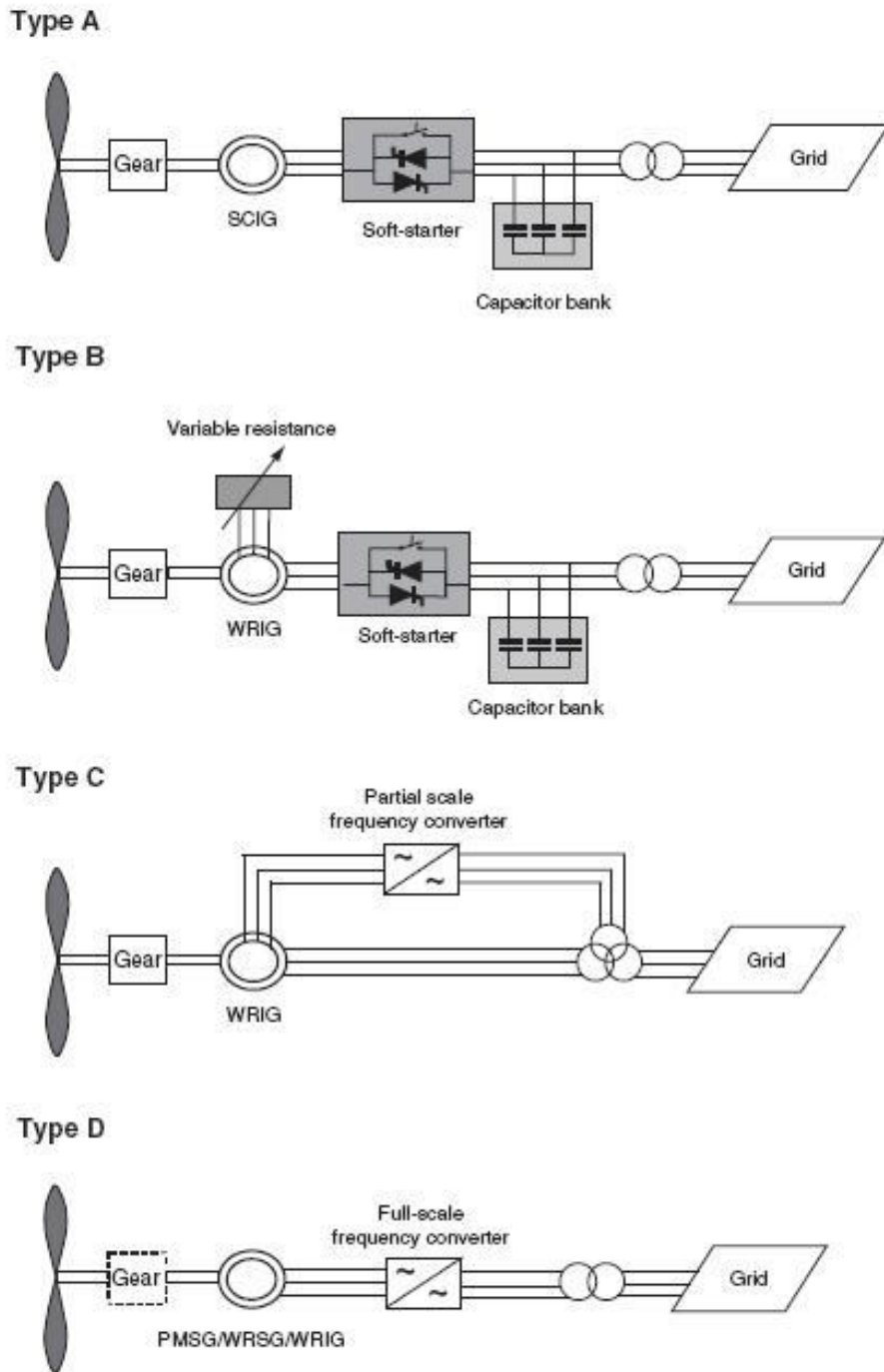


Figure 4.17: Wind Turbine Types [Ackermann, 2012]

for control of active and reactive power transfer – otherwise microgrid stability is threatened during wind velocity changes.

Type C wind turbines are common in very large installations [51]. This type uses a doubly-fed induction generator (DFIG) [52, 53] in combination with a partially-scaled AC/AC frequency converter. The converter controls the rotor currents, allowing the stator currents to be modified to provide some control over active and reactive power. The DFIG wind turbine can vary by up to ~30% from synchronous speed [52, 53], allowing the use of speed-control MPPT to increase wind turbine efficiency. However, DFIGs have poor fault ride-through capability – a grid disturbance will affect their excitation in addition to their stator-grid connection. In addition, the DFIG requires two connections to the grid (the direct stator-grid connection and the rotor-grid using the converter) which must each have protection and control sensors. The poor fault tolerance, complexity and limited controllability of DFIG wind turbines makes them less suitable for use in islanded microgrids. Type D wind turbines are replacing Type C in progressively larger installations. Type D wind turbines most often use a permanent-magnet synchronous generator (PMSG) [54] connected through a full-scale AC/AC converter. The PMSG output frequency is directly proportional to the rotor speed and the number of pole pairs. It is possible to directly connect the wind turbine shaft to the PMSG without requiring a gearbox, using a multipole PMSG design to produce a sufficiently high-frequency stator voltage. The Type D PMSG wind turbine is best suited for islanded microgrids. The AC/AC converter insulated the PMSG from the grid, allowing disturbances on either side to be damped by control action and preventing grid faults or mechanical disturbances from propagating. In addition, the PMSG has constant internal excitation – the generator power factor can be completely controlled using the AC/AC converter. The disadvantages of the PMSG are primarily cost and controller based – active power converter controllers are required to ensure correct

PMSG operation, in addition to the costs of the full scale frequency converter and the magnets (often rare-earth) within the PMSG. However, these disadvantages are mitigated by the degree of controllability provided, in addition to continual decreases in cost. Therefore, it will be assumed (for investigation and analysis) that a Type D direct-drive PMSG wind turbine will be used for implementation of wind reserves in an islanded microgrid.

4.4.2: Modeling and Control of Direct-Drive PMSG Wind Turbines

The modeling and control of a permanent-magnet synchronous generator is vital to the successful integration of a PMSG wind turbine into an islanded microgrid. Figure 4.18 displays the general control architecture of a direct-drive PMSG wind turbine implemented in the PLEXIM simulation environment. The PMSG stator terminals are connected to a controlled rectifier, allowing the terminal voltages to be adjusted as required to implement the stator current references. The stator currents are controlled using the power converter voltage references – these are generated using a decoupled D-Q PI controller. The stator current references are generated depending on the overarching control law. In this case, zero-direct-axis current control is implemented to ensure the PMSG operated at unity power factor. The quadrature-axis current references is generated by a DC-link controller which balances the power flow across the power converter. This controller can also be replaced by a power reference synthesizer [54] or a PMSG speed controller, depending on

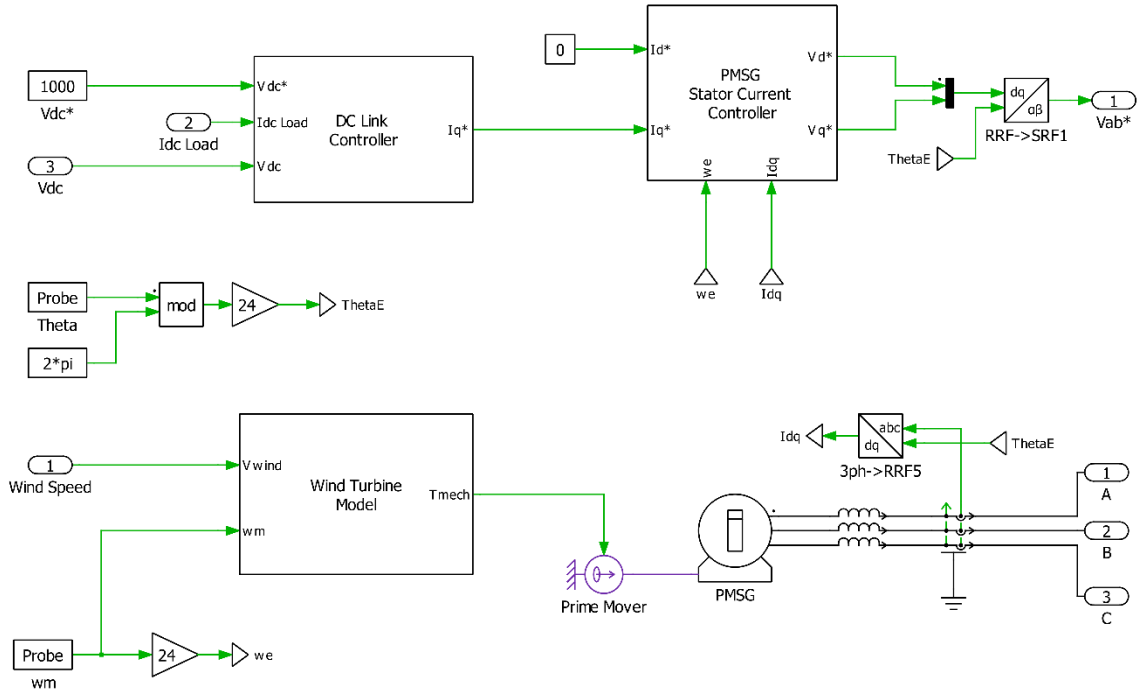


Figure 4.18: PMSG Control and Modeling Topology in PLEXIM

the application. The aerodynamic behavior of the wind turbine is simulated in real-time to provide the prime-move torque of the PMSG, allowing the interconnected mechanical and electrical systems to be modelled and controlled. The core of this simulation environment is the PMSG model, implemented as voltage-behind reactance in a rotating reference frame [55]-[57].

The PMSG is a constant-excitation generator which produces a variable-frequency output proportional to the rotor speed. The PMSG is most commonly modelled in the D-Q frame (the Park transformation) [55]. Further transformed into the s-domain, this results in the following stator relations [54]:

$$v_{sd} = L_{sq}i_{sq}\omega_e - sL_{sd}i_{sd} - R_s i_{sd} \quad (46)$$

$$v_{sq} = (\varphi_m - L_{sd}i_{sd})\omega_e - sL_{sq}i_{sq} - R_s i_{sq} \quad (47)$$

where v_{sd} and v_{sq} are the d and q-axis stator terminal voltages, L_{sd} and L_{sq} the stator inductances, ω_e the electrical angular velocity, R_s the stator winding resistance, i_{sd} and i_{sq} the d-q axis stator currents and φ_m the flux supplied by the permanent magnets. In the rotating reference frame, cross coupling is observed between the direct and quadrature axes. These axes can be decoupled by substitution of an alternate set of control variables [54]:

$$y_{sd} = v_{sd} - L_{sq}i_{sq}\omega_e \quad (48)$$

$$y_{sq} = v_{sq} - (\varphi_m - L_{sd}i_{sd})\omega_e \quad (49)$$

This decoupling improves the transient response of a current controller by removing the disturbances created by the inherent cross-coupling. The decoupling term should also include any line inductance present between the PMSG stator terminals and the converter terminals. Figure 4.19 displays the q-axis control architecture implemented in the PLEXIM simulation environment. A standard PI controller is used, with the decoupling terms added as feed-forward compensation. The result is the q-axis voltage reference supplied to the PMSG-side power converter. A similar process is used to produce the d-axis voltage reference. However, the d-axis current reference is usually set to zero [54], resulting in unity power factor PMSG operation. In this situation, only the q-axis current reference is used to control the PMSG output power.

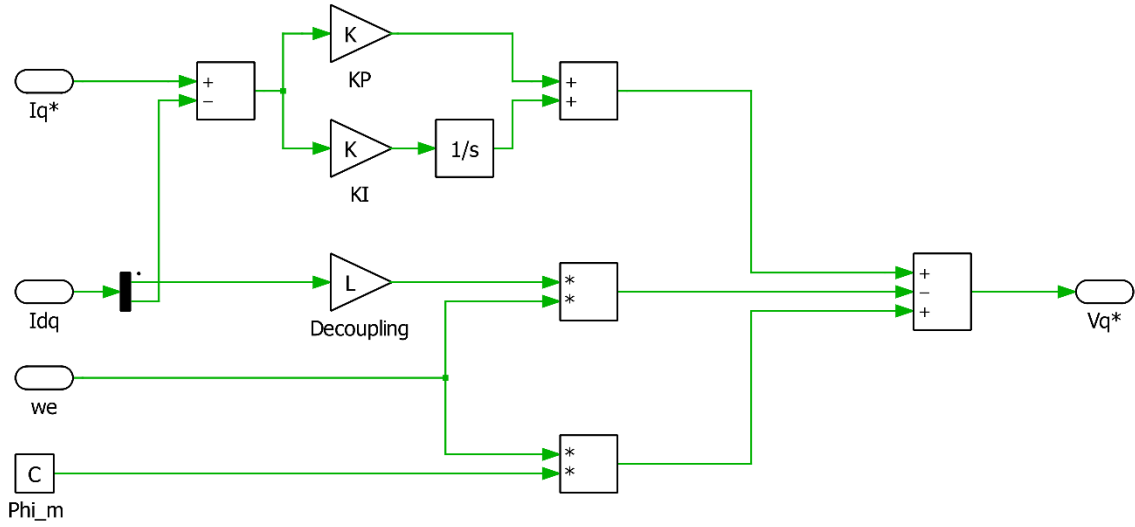


Figure 4.19: Q-axis stator current controller in PLEXIM

The PMSG controller presented above has been shown [54] to reliably implement direct and quadrature-axis current references by controlling the power converter terminal voltage reference. The generation of the current references is dependent on the control strategy of the PMSG wind turbine. Fundamentally, the interaction between the PMSG and the wind turbine is modelled by equating the PMSG electromagnetic torque with the wind turbine's mechanical and aerodynamic behavior. The PMSG electromagnetic torque (in the D-Q reference frame) is expressed as follows [54]:

$$T_e = \frac{3}{2}p(\varphi_m i_{sq} - (L_{sd} - L_{sq})i_{sd}i_{sq}) \quad (50)$$

where p is the number of pole pairs in the PMSG rotor. For surface-mount PMSG designs, L_{sd} can equal L_{sq} [55], resulting in the secondary term disappearing from (50). This linearizes the electromagnetic torque relation and makes control easier. This behavior also appears when the d-axis current is zero (or nearly so) during unity power factor operation.

Otherwise, (50) is non-linear, introducing additional control difficulties. The use of this zero-d-axis current control method is assumed for simplicity of future analysis.

The s-domain mechanical behavior of the directly coupled PMSG-wind turbine system is modelled as follows [53]:

$$Js\omega_m = T_{tur} - T_e - T_{friction} \quad (51)$$

where T_{tur} is the wind turbine mechanical torque produced by the blades, T_e the PMSG electromagnetic torque and $T_{friction}$ the torque losses due to friction within the lumped mechanical system. J is the lumped moment of inertia, and ω_m the mechanical speed of the rotating system. The electrical angular speed we can be obtained simply by multiplying ω_m by the number of pole pairs in the PMSG. The aerodynamic torque of the wind turbine is expressed as follows [53]:

$$T_{tur} = \frac{1}{2} \rho \pi r^3 V_{wind}^2 C_t(\lambda, \beta) \quad (52)$$

Where ρ is the air density, r the blade radius, V_{wind} the free-stream wind velocity and C_t the wind turbine's torque coefficient [53, 58]. The torque coefficient is a non-linear function of the blade pitch angle β and tip-speed ratio λ . It is related to the power coefficient C_p through division by the mechanical angular velocity. The power coefficient has a commonly-used exponential approximation [59]:

$$C_p(\lambda, \beta) = 0.5176 \left(\frac{116}{\kappa} - 0.4\beta - 5 \right) e^{-\frac{21}{\kappa}} + 0.0068\lambda \quad (53)$$

where the intermediate value κ is used to simplify the final equation based on β and λ .

$$\kappa = \frac{1}{\frac{1}{\lambda + 0.08\beta} - \frac{0.035}{\lambda^3 + 1}} \quad (54)$$

Figure 4.20 presents the PLEXIM implementation of this wind turbine model where equations (53) and (54) are implemented within an aerodynamic model subsystem. In this case, the blade pitch is assumed to be zero, wind turbines of the size used for islanded microgrids generally use passive stall or speed control. The wind velocity and mechanical rotational velocity are inputs to the system, with the resulting tip-speed ratio and mechanical torque calculated mathematically. The mechanical torque is then output to the prime mover of the PMSG, which closes the loop by changing speed based on the dynamic balance between the mechanical and electromagnetic torques. The non-linear behavior of the wind turbine requires algorithms such as MPPT or gain scheduling to optimize performance. However, the high inertia of the wind turbine leads to the mechanical time constant of the system being substantially slower than the PMSG's electrical time constant, allowing supervisory control to prevent mechanical instabilities using the PMSG control references.

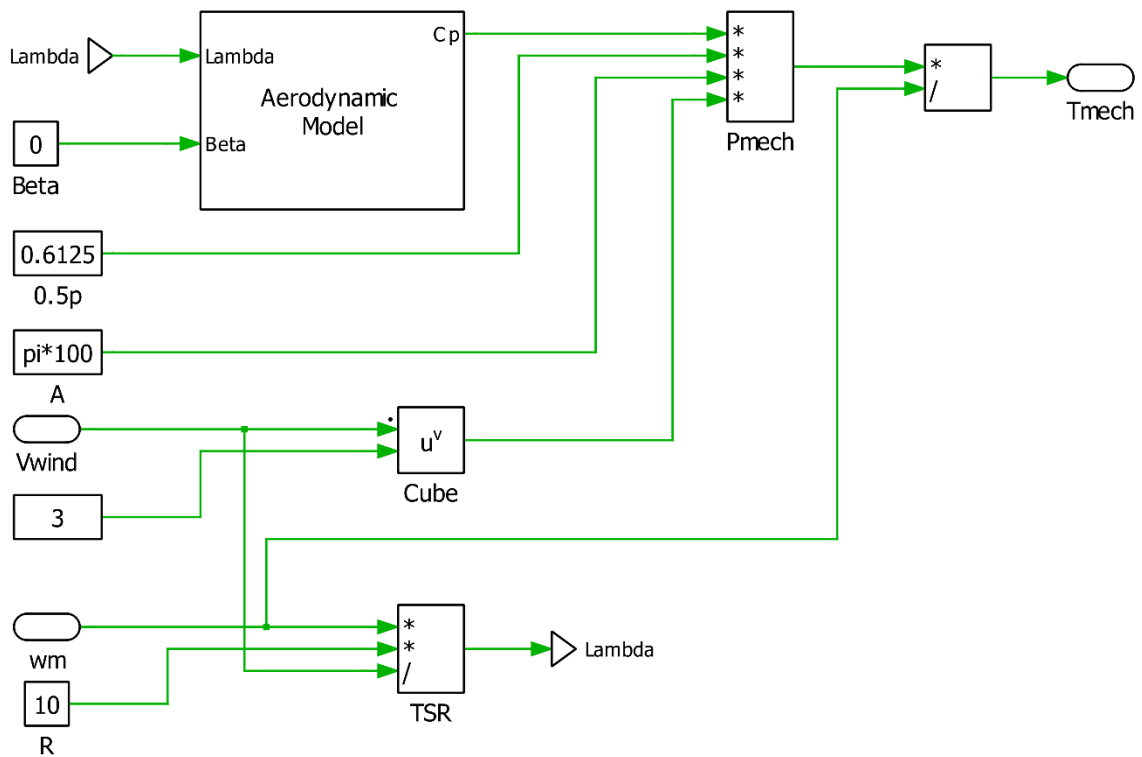


Figure 4.20: Dynamic Wind Turbine Model in PLEXIM

4.4.3: Grid Interconnection using Back to Back Power Converters

The grid interconnection of a PMSG wind turbine requires an AC/AC frequency converter [60]. The variable speed of the wind turbine rotor results in the PMSG's electrical output frequency varying across a wide range – direct grid interconnection is not possible due to this forced frequency mismatch. The most commonly used grid interconnection topology for a PMSG wind turbine is the back-to-back AC/AC converter topology [60]. Figure 4.21 presents the PLEXIM implementation of this converter. The PMSG terminal voltages are fed into a 6-pulse, 2 level Insulated Gate Bipolar Transistor (IGBT) converter

which operates as a controlled rectifier [60]. The IGBT converter uses Space Vector Pulse-Width Modulation [38] (SVPWM) to convert the variable-frequency AC input into a DC voltage across the DC-link capacitor. The DC-link capacitor filters out the PWM commutation, producing a steady DC voltage for use in either DC interconnections or (in this case) to isolate the AC PMSG terminals from the distribution grid. The DC-link voltage is then supplied to a SVPWM inverter, again a 6-pulse, 2 level IGBT converter [38]. The inverter supplies the AC terminal voltages requested by the grid synchronization and interconnection controllers described in the previous section.

The control topology described in the PLEXIM simulation environment does not have grid-side control of the DC-link voltage. To maintain DC-link stability, the PMSG control architecture must set the terminal voltage references to match the PMSG electrical output power to the inverter demand across the DC-link. The DC-link dynamics are as follows:

$$V_{dc} = \frac{I_{rect} - I_{inv}}{sC_{Link}} \quad (55)$$

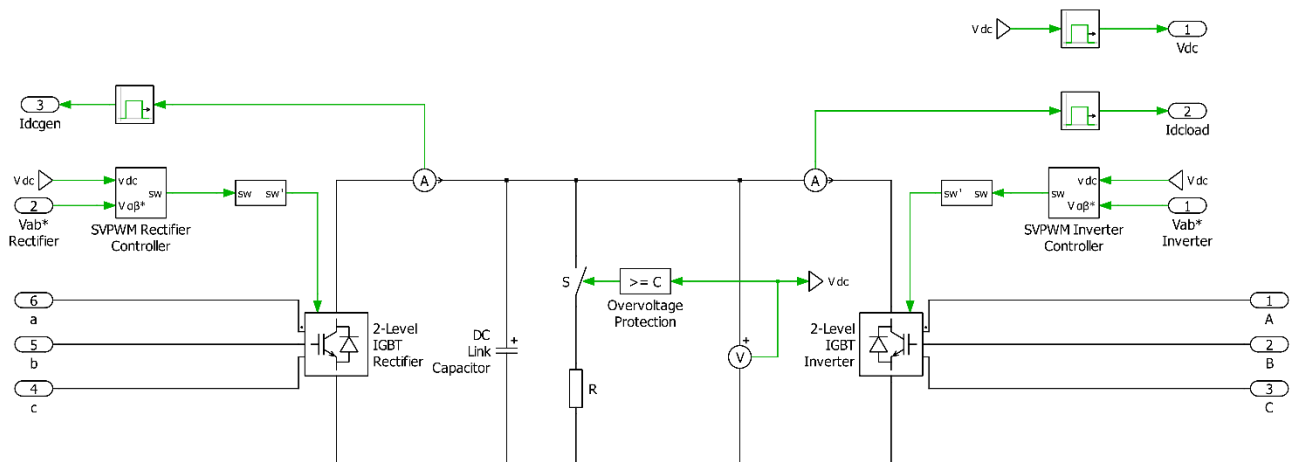


Figure 4.21: Back-to-Back Converter Architecture in PLEXIM

Where V_{dc} is the DC-link voltage, I_{rect} the current supplied by the rectifier, I_{inv} the current drawn by the inverter and C_{Link} the DC-link capacitance. Inverter dynamics are neglected due to their fast time constants relative to the overarching controller behavior. The relationship between the DC-link current and the PMSG terminals is derived by equating power flow across the IGBT rectifier. The terminal power supplied by the PMSG can be expressed in the rotating frame as follows:

$$P_G = \frac{3}{2}(v_{sd}i_{sd} + v_{sq}i_{sq}) \quad (56)$$

The rectifier output power is simply:

$$P_R = V_{dc}I_{rect} \quad (57)$$

Substituting (55) into (57), the relationship between the DC-link current and rectifier power is obtained:

$$P_R = \frac{I_{rect} - I_{inv}}{sC}I_{rect} \quad (58)$$

Equating (56) and (58), simplifying, and assuming zero d-axis PMSG stator current, the following emerges:

$$\frac{I_{rect}^2 - I_{inv}I_{rect}}{sC} = \frac{3}{2}(v_{sq}i_{sq}) \quad (59)$$

The relationship in (59) indicates that the q-axis current reference required for power balance is as follows:

$$\frac{2}{3}\left(\frac{I_{rect}^2 - I_{inv}I_{rect}}{sCv_{sq}}\right) = i_{sq} \quad (60)$$

Returning to (56) and (57), the rectifier current is expressed as a function of the q-axis stator current:

$$I_{rect} = \frac{3v_{sq}}{2V_{dc}} i_{sq} \quad (61)$$

Substituting (61) into (60) and simplifying, the current reference requirement emerges:

$$\frac{3}{2} \left(\frac{v_{sq} i_{sq}^2}{sCV_{dc}^2} - \frac{I_{inv} i_{sq}}{sCV_{dc}} \right) = i_{sq} \quad (62)$$

This equation is non-linear with respect to the DC-link voltage. However, assuming control action to maintain a steady DC-link voltage value, (62) can be linearized and used to tune a controller. The complete derivation of controller behavior and the resultant PMSG and DC link dynamics is beyond the scope of this thesis - further analysis in this area can be found in [53].

Figure 4.22 displays the DC-link controller. A conventional PI controller format is used, with a feed-forward of the inverter current demand. As seen in (62), this compensates for the effect of changing inverter current on the DC-link dynamics, improving the transient performance of the controller. The DC-link controller provides the Q-axis current reference to the PMSG controller. This control format is best suited for standard zero d-axis current control methodology. The results of the presented control approach is best suited for grid-forming and grid-supporting interconnection topologies, where the power transfer between the grid and DC-link is regulated by grid-side controller action. Grid-feeding operation would result in the power references being produced by a wind turbine controller, with these references then implemented using the existing PMSG control architecture. Grid-

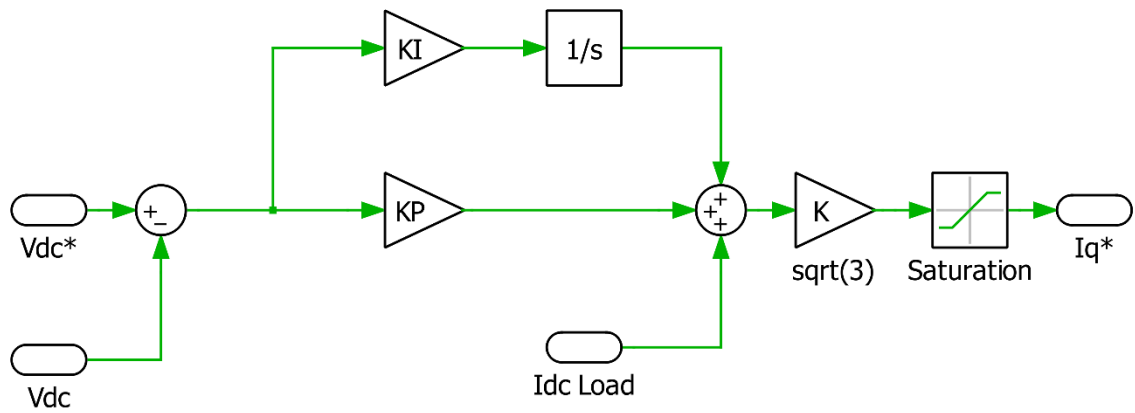


Figure 4.22: DC-Link Voltage Controller in PLEXIM

feeding operation is unlikely in islanded microgrids with significant wind penetration, as variations in wind speed would result in microgrid instability due to the lack of electrical inertia. The use of wind generation as a reserve for microgrid support and regulation (as presented in Chapter 3) required the control architecture presented in this Chapter, optimized for grid-supporting operation.

4.5: Conclusions

In this chapter, an overview of various aspects of analysis, modeling and control of islanded microgrids was presented. An analytical and numerical framework for the implementation of wind-based reserve generation in islanded microgrids was developed within the PLEXIM simulation environment. The PLEXIM environment allows for case-study analysis of wind reserve applications based on field data and microgrid topologies. Aspects of microgrid operation and modeling were reviewed, including grid forming techniques, grid synchronization of distributed generation and various droop-based grid interconnection schemes. These control techniques are applicable to wind turbine installation. Wind turbine generators were briefly reviewed, with direct-drive PMSG designed explored in greater detail. Their steady-state and dynamic behavior was reviewed, with decoupled rotating-frame control topologies implemented and analytically modeled to allow for interconnection with islanded microgrids. The grid interconnection topology was also reviewed, with the behavior of a back-to-back power converter modeled with respect to DC-link voltage regulation.

Chapter 5: Cartwright – A Case Study: Resource Modeling

5.1: Introduction

This Chapter presents a case study, conducted to validate the wind resource modeling, probabilistic demand analysis and wind reserve assessment algorithms. A remote community is selected where future integration of wind generation is planned. The amount of required wind generation, the performance of the created wind reserve and the general behavior of the augmented distribution grid is investigated, producing a probabilistic assessment of dynamic electricity reserves created by the installation of wind generation. Multiple wind turbine types and generation amounts are investigated, allowing engineering decisions to be made based on the information provided by the previously presented probabilistic wind reserve assessment algorithm. Due to the availability of generation and environmental data, the community of Cartwright, Newfoundland and Labrador is selected as the subject community of the subsequent case study.

Cartwright is a small community on the eastern coast of Labrador, Canada. The local electrical infrastructure forms an islanded microgrid - Cartwright is isolated from the transmission grid and relies entirely on local generation resources. Figure 5.1 illustrates Cartwright's microgrid architecture. It is an islanded microgrid relying on four diesel

generators (rated 800, 600, 500 and 400 kW respectively) to provide electricity to residential, commercial and industrial customers. The residential and commercial customers have a peak demand of roughly 800 kW, with a large industrial load (a shrimp processing plant) consuming up to an additional 400 kW during periods of operation. The reliance on diesel generation and isolated nature of Cartwright's microgrid leads to its suitability for the inclusion of wind power generation. The performance of wind generation at Cartwright is investigated using the wind probabilistic wind reserve assessment algorithm detailed in the previous two Chapters.

The case study is conducted using five years (2010-2014) of hourly wind and other environmental data, obtained from Environment Canada. This data is used to generate the site wind resource model by utilizing the multidimensional probabilistic modeling algorithm detailed in Chapter 2. Electrical demand data is available for the years 2015 and 2016 with 15-minute resolution. The probabilistic electrical demand profile is modelled using the algorithm detailed in Chapter 3. The combined probabilistic wind resource and demand models will be used for wind reserve assessment, investigating the performance of potential wind installations and the probabilistic viability of implementing a dynamic wind reserve.

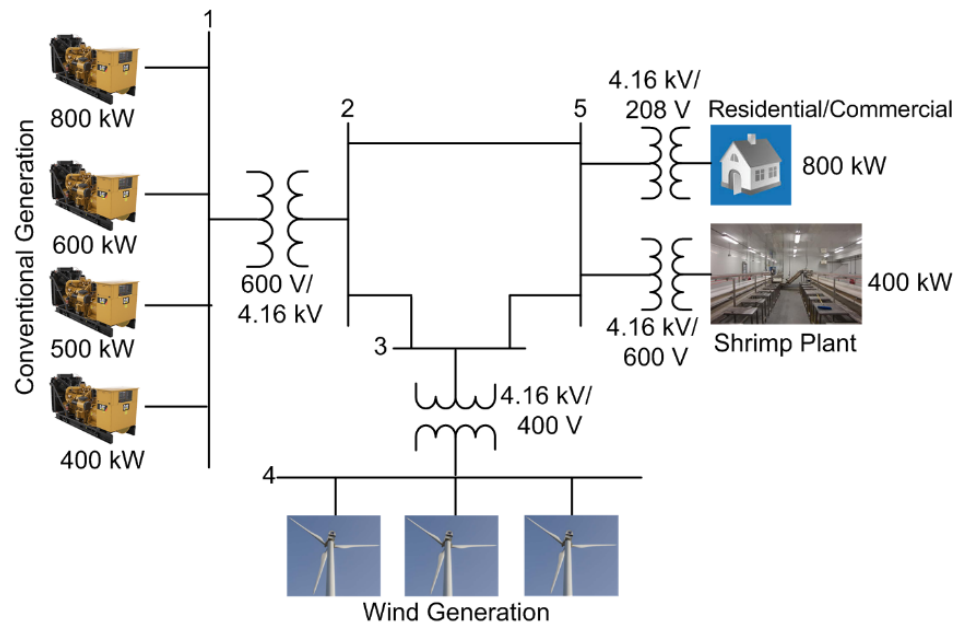


Figure 5.1: Cartwright Microgrid Architecture

5.2: The Wind Resource Model

The evaluation of Cartwright’s wind resource is conducted using the bivariate, multidimensional modeling algorithm presented in Chapter 2. Five years of hourly wind velocity data (2010-2014) was obtained from Environment Canada. At the same sample times, the air temperature, barometric pressure and relative humidity were also acquired. Using the ideal gas law, hourly samples of air density data were generated. The two data sample vectors were combined to create a bivariate environmental dataset for use in wind resource modeling. As the two environmental variables are not completely independent, the bivariate Kernel smoothing algorithm is required to accurately model the joint distribution of the two environmental variables. The environmental dataset is also

nonstationary – seasonal and diurnal variance contributors were previously identified to exist within the sample observations. To account for all these factors, the bivariate, multidimensional wind resource model was created by fitting the optimized two-dimensional Kernel distribution algorithm to appropriate phase-organized subsets of environmental data.

Figure 5.2 (a-d) presents the resulting wind/density probability distributions, sampled at 3 a.m. and 5pm on January 1st and August 28th. These sample times represent the extrema in the identified seasonal and diurnal wind/density variance, displaying the nonstationary character of the environmental dataset. Figure 5.2(a) presents the wind/density distribution at 3 a.m. on January 1st. The distribution is bimodal, with a primary peak probability at a wind velocity of 12 knots and an air density of 1.36 kg/m³. A secondary peak exists at an air density of 1.33 kg/m³ with calm winds. In general, the distribution is fairly continuous, smoothly varying across the environmental condition space. A slight correlation exists between wind velocity and air density – higher wind speeds are associated with lower mean air density. Overall, wind velocity values of greater than 20 knots are uncommon, with the air density rarely exceeding the range bounded by 1.25 and 1.42 kg/m³. Figure 5.2(b) presents the wind/density distribution at 5pm on January 1st. The distribution remains bimodal – the peak wind velocity is at 13 knots with the peak air density near 1.36 kg/m³. The secondary peak is more amplified, representing calm conditions with an air density between 1.28 and 1.36 kg/m³. The highest wind velocity values again tend to occur at lower air densities, representing a slight negative correlation between the environmental variables. The overall distribution is smooth, with the probability mass concentrated

between wind velocities of 0 and 30 knots and the air density ranging between 1.25 and 1.42 kg/m³. The diurnal cycle is not that strong during January – the weak solar heating and prevailing synoptic pattern at Cartwright is dominated by the seasonal variability in climate conditions.

The diurnal cycle has a substantially stronger effect on the observed wind/density regime. Figure 5.2(c) presents the probability distribution at 3 a.m. on August 28th. At this time, calm conditions dominate, with the majority of probability mass concentrated at low wind speeds (under 5 knots) with an air density of near 1.25 kg/m³. Periods of higher wind velocity do exist, however no significant probability exists supporting a velocity above 20 knots. During this period, the air density varies between 1.20 and 1.30 kg/m³, tightly clustered around the most likely value of 1.25 kg/m³. The wind resource is very poor at this seasonal and diurnal phase – a wind turbine is unlikely to produce significant energy when the wind velocity distribution is heavily biased towards calm conditions. Figure 5.2(d) displays the wind/density distribution at 5 p.m. on August 28th. At this time of year, diurnal cycles are significant. Mesoscale climate phenomena driven by daytime heating has shifted the most likely wind velocity to 8 knots, with the associated air density at approximately 1.22 kg/m³. During this period, calm conditions still exist. However, they are now dominated by the probability mass at a higher wind speed. Overall, the wind velocity distribution has significant probability at wind velocities ranging from calm to 20 knots, with the air density varying between 1.17 and 1.27 kg/m³.

The generated wind resource model indicates significant seasonal and diurnal variability in the underlying statistical behavior of the environmental variables. The wind/density

probability distribution is substantially more favorable during the winter months, with more probability mass at higher values of both wind velocity and air density. In addition, a diurnal cycle is observed, where the late afternoon consistently has a wind regime shifted towards higher velocities. This effect is strongest during the summer months. The air density regime shifts lower due to this cycle, however the net benefit is greater wind power availability due to the larger relative effect wind velocity has on the power contained within the wind. 8756 additional wind/density distributions exist within the generated model, allowing an assessment to be made for any time of day or day of the year. In most cases, the distributions smoothly transition between the extrema presented previously – some exceptions exist due to the relatively small dataset size and the chaotic behavior of environmental conditions. For further wind resource analysis, studies of the available wind power density and theoretical wind turbine power output are conducted and presented.

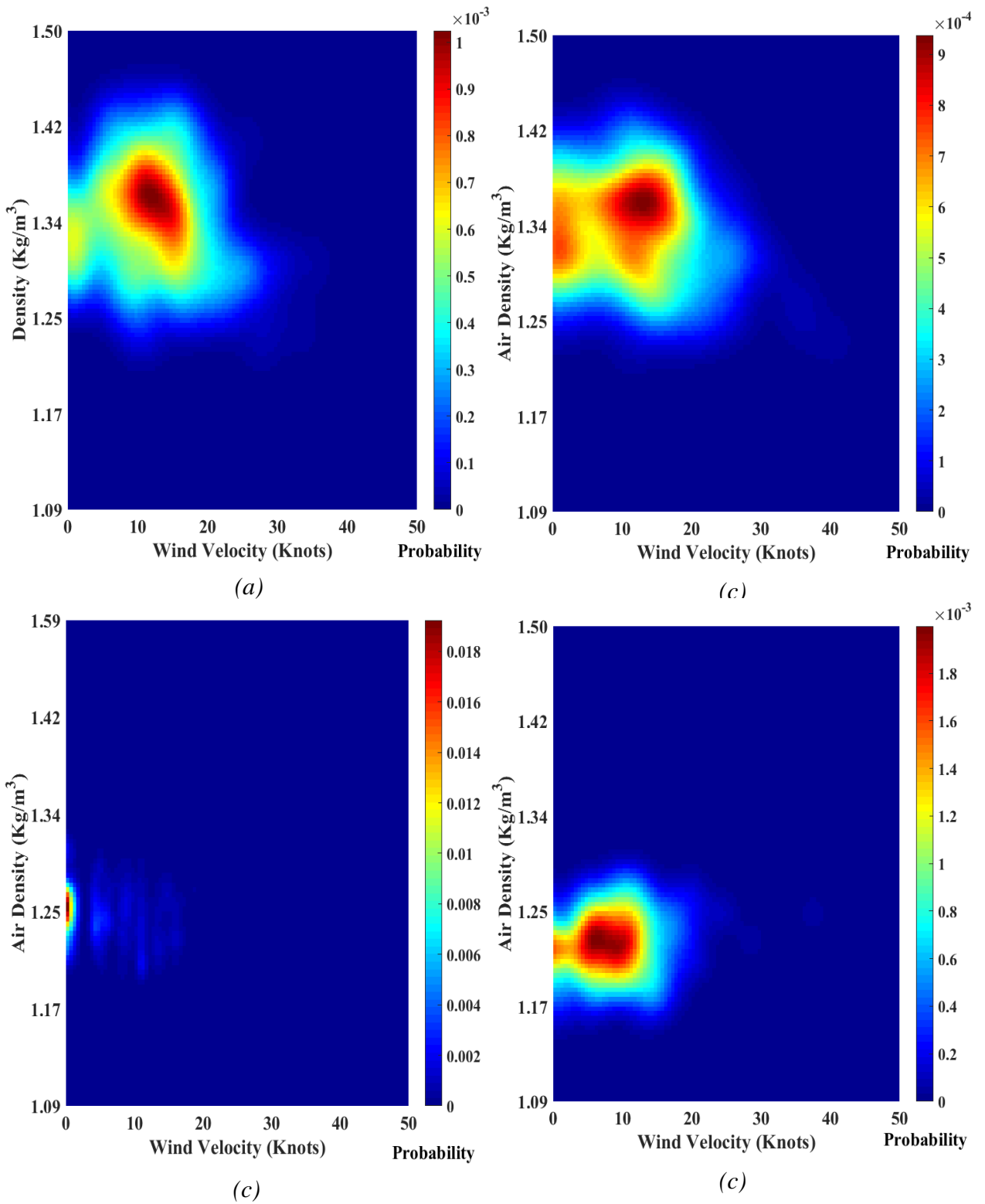


Figure 5.2: Probabilistic Wind Resource Model for Cartwright during (a) January at 3:00 a.m., (b) January at 5:00 p.m., (c) August at 3:00 a.m., and (d) August at 5:00 p.m.

The wind power density is calculated by a weighted sum of the wind velocity and air density values encountered within the multidimensional model. For each time and date, the wind power equation (Chapter 2) is used to calculate the wind power density inherent at each point of the bivariate distribution space. These values are then weighted by their probability of occurrence and summed to produce a single value – the expected wind power density. The result is a 24·365 matrix of wind power density predictions representing the seasonal and diurnal variability observed in the wind velocity and air density regimes. Figure 5.3 presents the calculated wind power density values. The wind power density at Cartwright varies from 50 to 500 w/m², with a minimum during August between 9 p.m. and 3 a.m. The maximum wind power density is during January between 9 a.m. and 3 p.m. In general, wind energy is only consistently available from November to March, with October and April also having a significant wind resource during the diurnal peak. The degree of variation due to annual and diurnal cycles is much larger than at a site such as St. John's (Investigated in Chapter 2) – there is essentially an order of magnitude variation in the available wind energy. Any wind installation must expect quiescent operation during much of the year, with the majority of energy being produced over a shorter period during the winter months. The overall wind reserve feasibility and availability will depend on the interaction of this variability with the demand profile and wind turbine design.

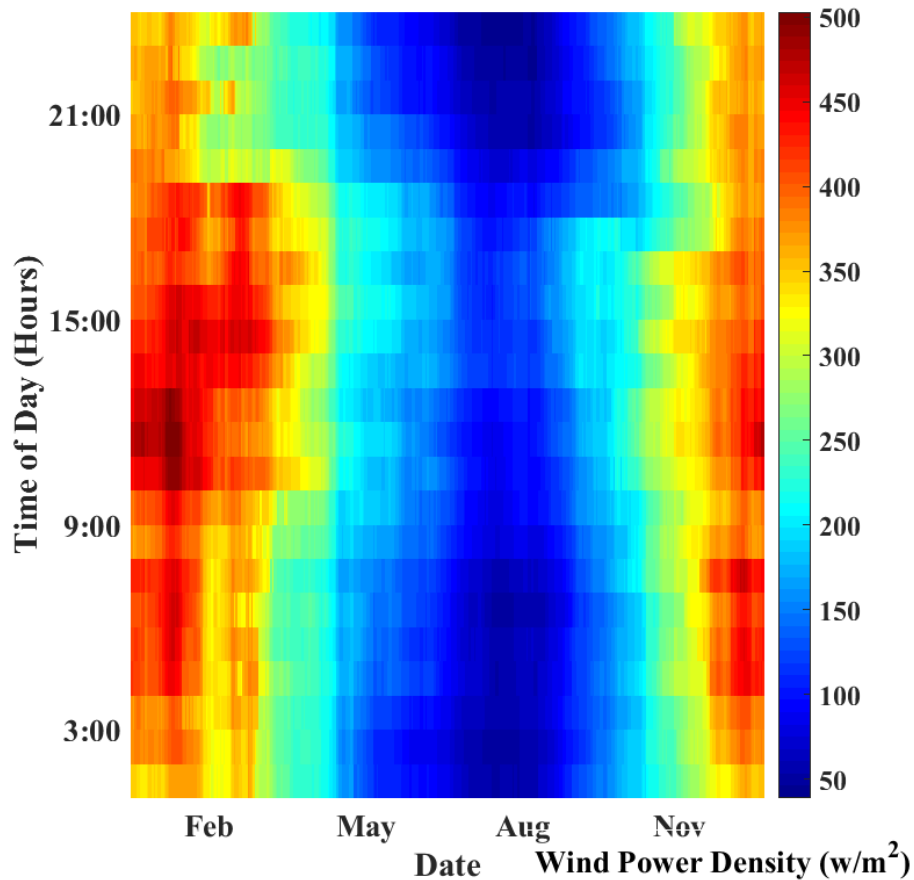


Figure 5.3: Cartwright's Wind Power Density

The generation of an accurate probabilistic wind/density model allows the prediction of the performance of a wind turbine installation. Two wind turbine designs are selected – the Northern Power Systems 100c-21 and Northern Power Systems 100c-24. The NPS 100C-21 is a 100 kW rated wind turbine optimized for higher wind speed operation. It has a cut-in wind speed of 3 m/s, a rated wind speed of 15 m/s and cuts out at a wind velocity of 25 m/s. The NPS 100c-24 is a similar wind turbine, also with a 100 kW rated output. It has a cut-in wind velocity of 3 m/s, a rated wind velocity of 12 m/s and a cut-out wind speed of 25 m/s. The NPS 100c-24 is designed for lower-velocity wind regimes. Both wind turbines

are direct-drive, permanent magnet generator designs that use a power electronic converter system to interconnect with the grid. The power curve of each wind turbine is available from the manufacturer. It is interpolated to match the discrete wind velocity values within the probabilistic model, then expanded to accommodate for the variations in air density. The result is a matrix of potential power outputs defining the behavior of each wind turbine within the model design space. Using the methodology described in Chapter 3, the probabilistic power output of the wind turbine is developed using the appropriate wind resource model. This process is repeated for each wind turbine, allowing a comparison of the probabilistic output of each design. Given the manufacturer power curve and limiting criterion, any wind turbine design can be investigated in this manner. To more easily account for the use of multiple turbines, the power output was normalized by the turbine rating (100 kW for each case) and is therefore displayed in per-unit values. The probability of quiescent operation (wind speeds below the cut-in value) is removed from the distribution for ease of visual analysis and displayed separately.

Figures 5.4(a-d) display the probabilistic power output of the NPS 100c-21 when installed in Cartwright. Figure 5.4(a) displays the output distribution at 3 a.m., varying across the seasonal cycle. Throughout the year, the majority of probability mass exists at less than 10% of the rated output, representing near quiescent operation during wind speeds in the range of 3 to 7 m/s. The probability of rated power output is expressed by integrating the probability mass near 1.00 per-unit – a spread distribution is formed here due to the variation in air density affecting the actual captured power. At this time, rated operation is only observed to occur between November and April, however with a low probability.

During the remainder of the year, the wind velocity and air density distributions do not permit full-load operation, indicating that it would be an extremely rare occurrence. Figure 5.4(b) displays the power output distribution at 9 a.m. At this time, similar behavior is observed. However, the change in wind regime due to the diurnal cycle has shifted more probability mass towards rated power output (during the winter months). During the remainder of the year, operation is primarily near quiescence (under 0.1 per-unit) with a slight secondary peak at roughly 20% of the rated power output, likely driven by the beginning of daytime heating. Note that Cartwright is a fairly high-latitude site, therefore 9 a.m. is well after sunrise from May to August where this effect is most evident.

Figure 5.4(c) displays the wind turbine behavior at 3 p.m. At this point, the wind resource is near its overall maximum due to the diurnal cycle. The probability of rated operation is at its highest, with some probability mass existing during all periods except for July and August. There is also a reduced probability of quiescent operation, with significant output in the range of 0.2 per-unit evident from April to October. However, the seasonal cycle still dominates the variability in wind turbine power output. Figure 5.4(d) displays the power output distribution at 9 p.m. As in Figure 5.4(a), quiescent operation is now more common, with little probability mass above 0.1 per-unit except for during the winter months. Rated operation is still observed during the winter, however it is less common due to the diurnal cycle partially suppressing the wind velocity regime. Essentially, the NPS 100c-21 will not be active at rated power a significant proportion of the time when installed in Cartwright's wind regime.

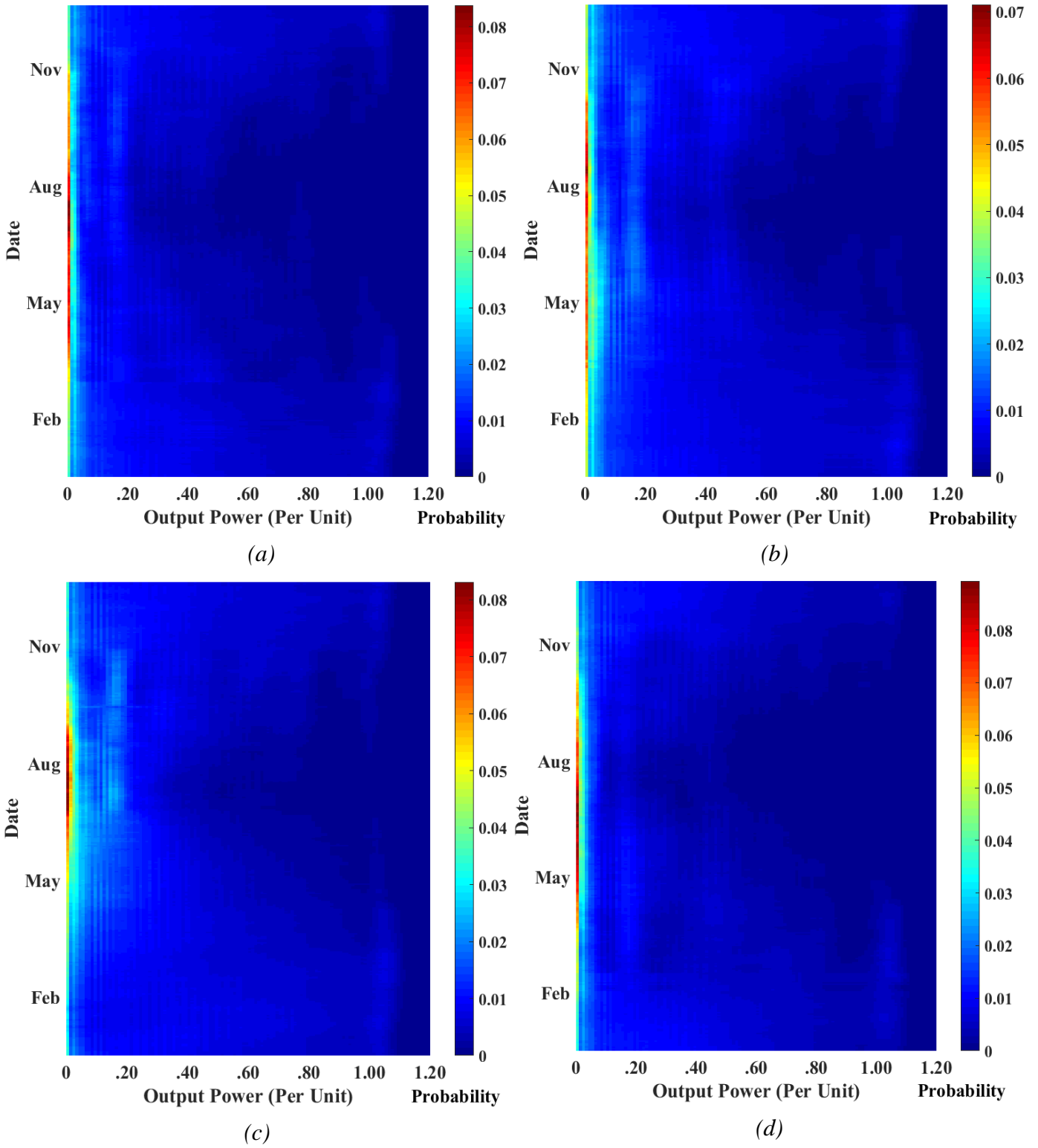


Figure 5.4: Probabilistic Power Output of the NPS-100c-21 in Cartwright at (a) 3:00 a.m., (b) 9:00 a.m., (c) 3:00 p.m. and (d) 9:00 p.m.

Figure 5.5 presents the probability of quiescent operation (no power output) for the NPS-100c-21 wind turbine, observed at 3 a.m., 9 a.m., 3 p.m. and 9 p.m. throughout the seasonal cycle. Due to the design of the wind turbine in combination with Cartwright's wind regime, this probability can be as high as 63% at 9:00 p.m. during August. From 9 p.m. to 9 am, a significant seasonal cycle is evident in the probability of quiescence, with a winter minimum (near 15%) observed during January for all 3 observation times. The overall probability of quiescent operation is highest at 9:00 p.m. during most of the year, except for near the summer solstice (May and June) where 3:00 a.m. exhibits a greater likelihood. Sunset is later than 9:00pm at Cartwright during this period due to the latitude of the site, explaining this variability. At 3:00 p.m., quiescent behavior is relatively unlikely throughout the year, peaking at 25% in August and reaching a minimum value of 15% during April. In general, the NPS-100c-21 wind turbine will only produce power between 35 and 85% of the time, with the most reliable operation during the afternoon and during the winter months.

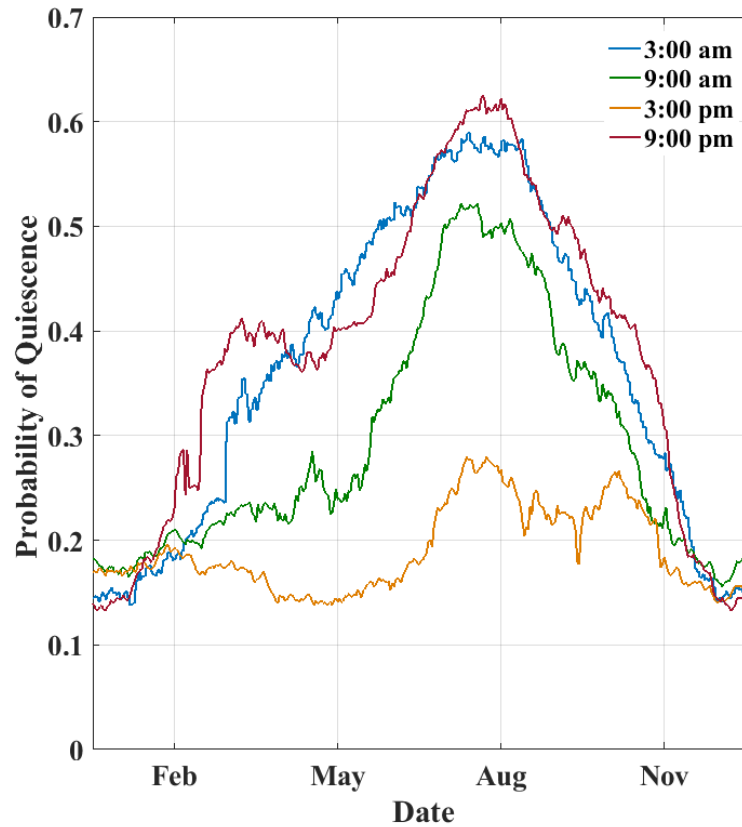


Figure 5.5: Probability of Quiescent Operation – NPS-100c-21 at Cartwright

Figure 5.6(a-d) displays the probabilistic power output of the NPS 100c-24 wind turbine, again observed 3 a.m., 9 a.m., 3 p.m. and 9 p.m., respectively. Figure 5.6(a) displays the wind turbine behavior at 3:00 a.m., throughout the seasonal cycle. Compared to the NPS 100c-21, significantly more probability mass exists at higher per-unit power outputs. Rated operation is more common, and is observed throughout the year (albeit with the same emphasis towards the winter months). In addition, probability mass is observed at outputs between 0.2 and 0.35 per-unit throughout the year, indicating a more reliable energy supply. This is due to the NPS-100c-24 being optimized for performance at lower wind speeds,

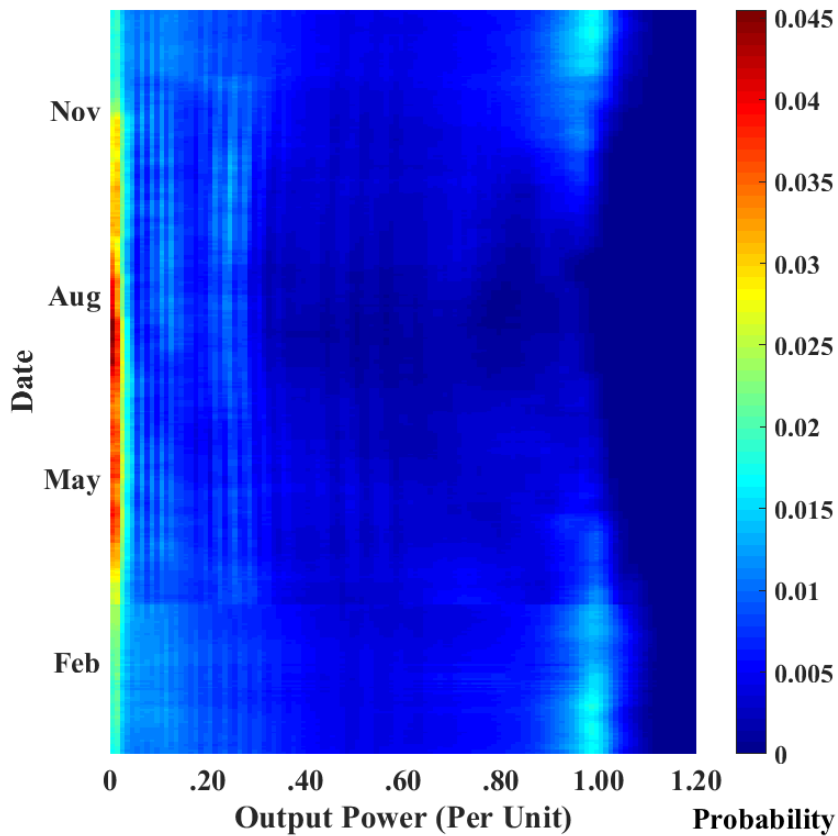


Figure 5.6(a) – Probabilistic Power Output of the NPS-100c-24 in Cartwright at 3:00 a.m.

which better matches Cartwright’s wind regime at this time. Figure 5.6(b) displays the wind turbine’s probabilistic output at 9 a.m. The effect of daytime heating has increased the probability of non-quiescent behavior during April to October, with probability mass now

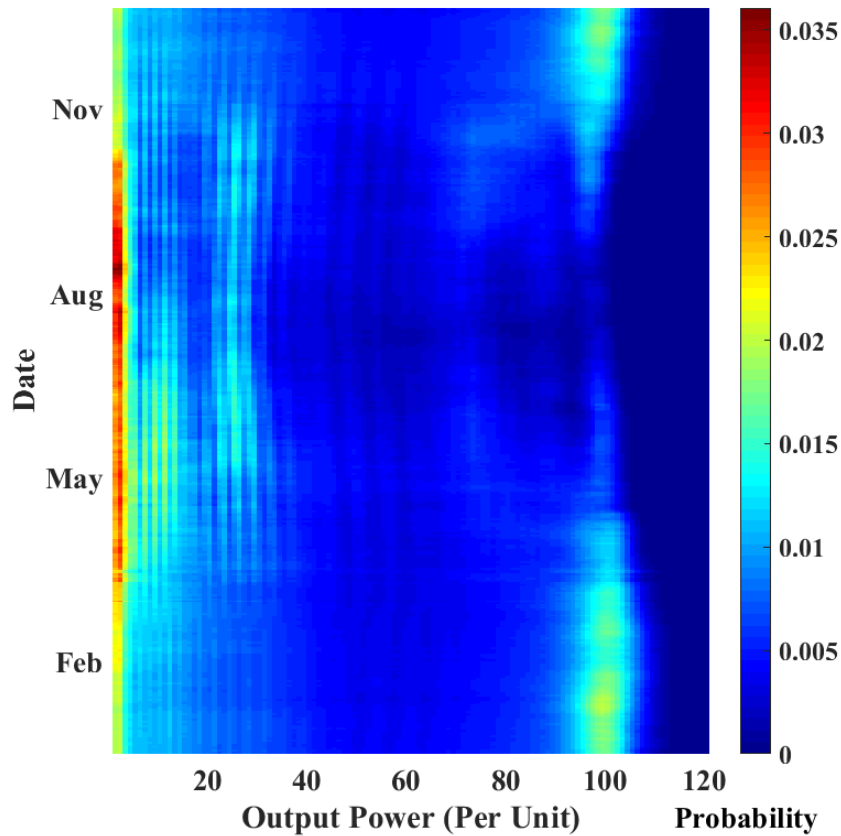


Figure 5.6(b) – Probabilistic Power Output of the NPS-100c-24 in Cartwright at 9:00 a.m.

existing near 0.30 per-unit during these periods. In addition, rated power operation continues to become more common during November to March, with full-load operation now representing a significant proportion of the total probability distribution. The overall proportion of non-quiescent behavior remains significantly larger than that exhibited by the NPS 100c-21, reflecting the wind turbine design’s suitability for Cartwright’s wind regime.

The diurnal trend towards increased wind energy production continues through 3 p.m. Figure 5.6(c) displays the probabilistic wind turbine power output at this time, varying across the seasonal cycle. The effect of the diurnal cycle is to shift a significant amount of

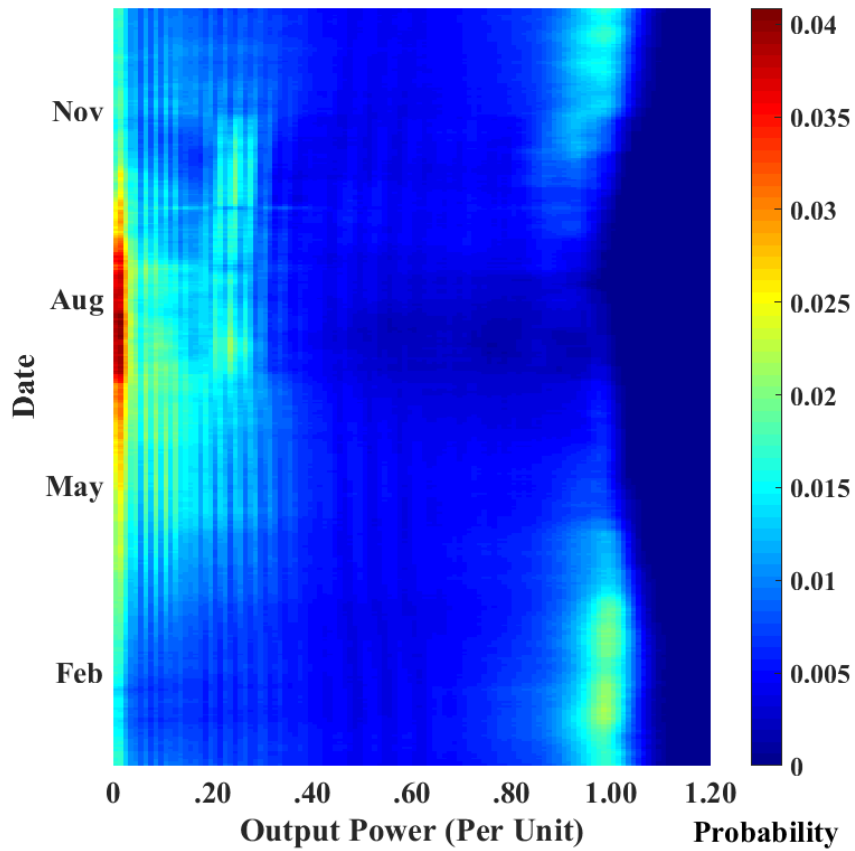


Figure 6(c) – Probabilistic Power Output of the NPS-100c-24 in Cartwright at 3:00 p.m.

probability mass from quiescent operation to partial-load (0.1 to 0.4 per-unit) output, with this effect most evident during May to October. During the remainder of the year, the diurnal cycle shifts probability to rated-output operation, reflecting the increased probability of higher wind velocities observed in Figure 5.2(b) and Figure 5.2(c). The overall effect is more reliable and consistent wind turbine operation due to a diurnally-enhanced wind regime. Figure 5.6(d) displays the NPS-100c-24’s probabilistic power output at 9 p.m. The loss of diurnal enhancement has shifted probability mass towards quiescent operation, producing a distribution similar to that in Figure 5.6(a). However, in

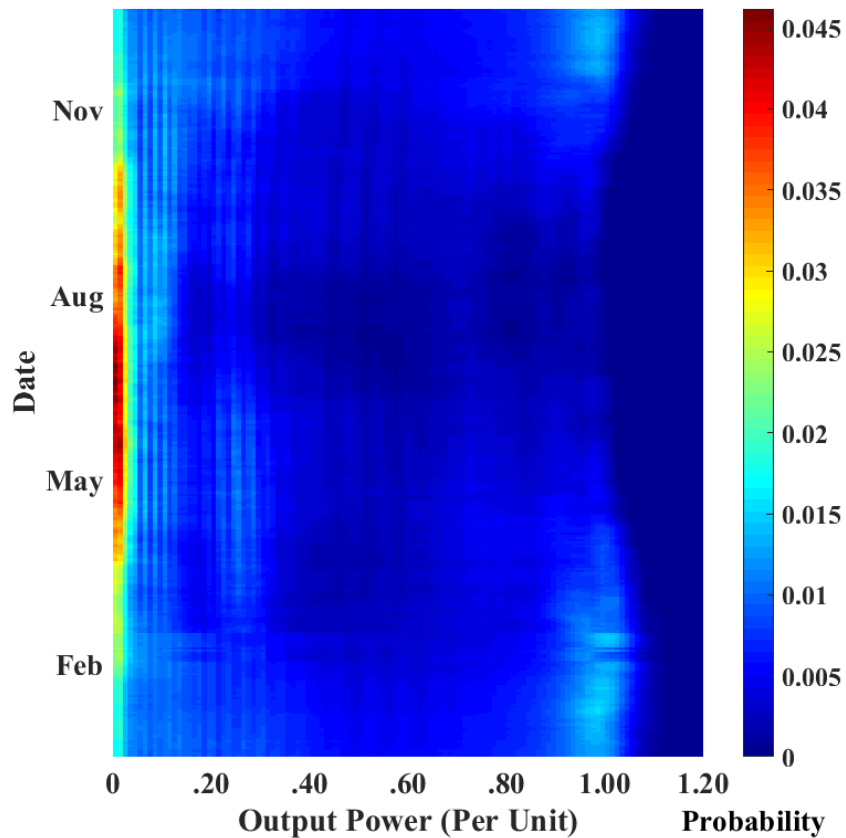


Figure 5.6(d) – Probabilistic Power Output of the NPS-100c-24 in Cartwright at 9:00 p.m.

comparison to the NPS 100c-21 (Figures 5.4(a) and 5.4(d)) significantly superior performance is observed, with a greater proportion of rated output operation and a generally greater probability of power outputs equal to or greater than 0.1 per-unit. Overall, a visual comparison of the probabilistic wind turbine output suggests that the NPS 100c-24 is a superior choice for Cartwright.

Figure 5.7 presents the probability of quiescent operation (no power output at all) for the NPS-100c-24 wind turbine. Similar to Figure 5.5, the probability is observed at 3 a.m., 9 a.m., 3 p.m. and 9 p.m. throughout the seasonal cycle. The plot is essentially identical to that of the NPS-100c-21 (Figure 5.5) – each turbine has very similar low wind-speed

performance, cutting in a 3 m/s. The design of the NPS-100c-24 wind turbine in combination with Cartwright's wind regime results in a probability of Quiescence as high as 62% at 9:00 p.m. during August. A significant seasonal cycle is evident between 9:00 p.m. and 9:00 a.m., with a winter minimum (near 15%) observed during January for all 3 observation times within this range. The overall probability of quiescent operation is highest at 9:00 p.m. from July to April, During May and June (near the Summer Solstice) the highest probability of quiescence shifts to 3:00 a.m. Sunset is later than 9:00pm at Cartwright during this period due to the high latitude of the Cartwright, explaining this variability. At 3:00 p.m., quiescent behavior is relatively unlikely throughout the year, peaking at 25% in August and reaching a minimum value of 15% during April. In general, the NPS-100c-24 wind turbine (similarly to the NPS-100c-21) will only produce power between 35 and 85% of the time, with the most reliable operation during the afternoon and during the winter months. However, the analysis conducted previously indicates that it exhibits superior performance during non-quiescent operation.

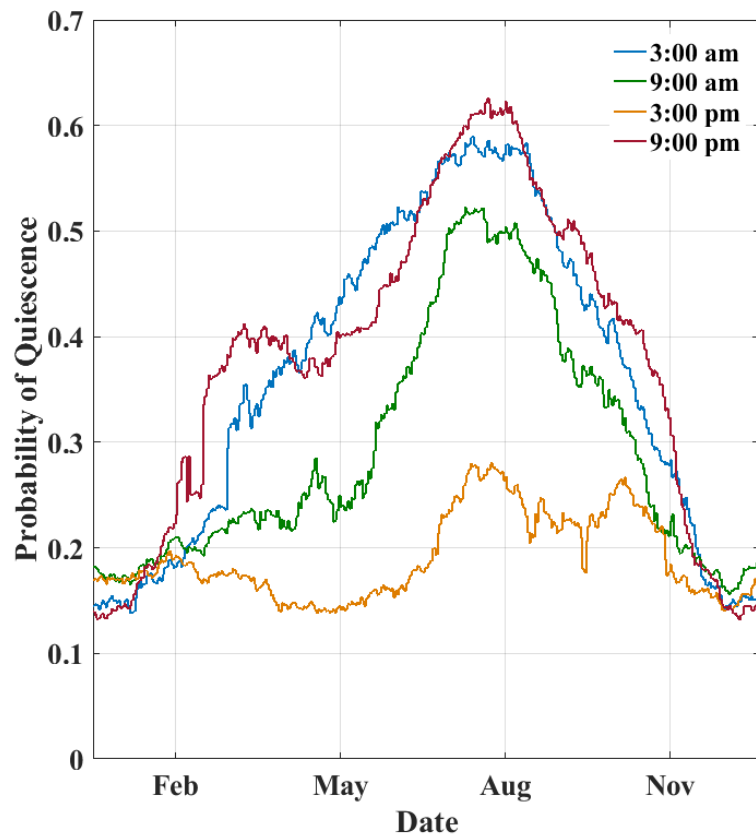


Figure 5.7: Probability of Quiescent Operation – NPS-100c-24 at Cartwright

Visual inspection of the probabilistic wind turbine output plots grants valuable information regarding the absolute and relative performance of each turbine design. However, the quantitative performance of the wind turbines is better estimated by integrating under each distribution to produce the predicted wind turbine capacity factor. Using the algorithms presented in Chapter 3, the expected value of the wind turbine output is calculated, then normalized by the rated power value (100 kW for both turbine designs). The seasonal and diurnal variability in the wind turbine capacity factor is revealed by this analysis, allowing for the continuation of the investigation into the wind reserves generated by their installation. Figure 5.8(a) displays the expected capacity factor of the NPS-100c-21 wind turbine when installed at Cartwright. The seasonal and diurnal-cycle variability is

easily observed, supporting the assertions made when examining the probabilistic wind turbine power output. The expected capacity factor reaches a maximum of 0.38 between 10:00 a.m. and 4:00 p.m. during January. A capacity factor value in excess of 0.3 is observed throughout the day during December, January and early February, with the diurnal cycle extending this behavior into March and November during the 10:00 a.m. to 4:00 p.m. peak wind velocity period. During these periods, Cartwright’s wind regime is sufficient for wind turbine operation at an acceptably high capacity factor. However, the minimum expected capacity factor is only 0.04, and occurs during August at approximately 11:00 p.m. Low capacity factors of less than 0.10 are observed during July, August and September between 8:00 p.m. and 9:00 a.m. The diurnal cycle increases the minimum

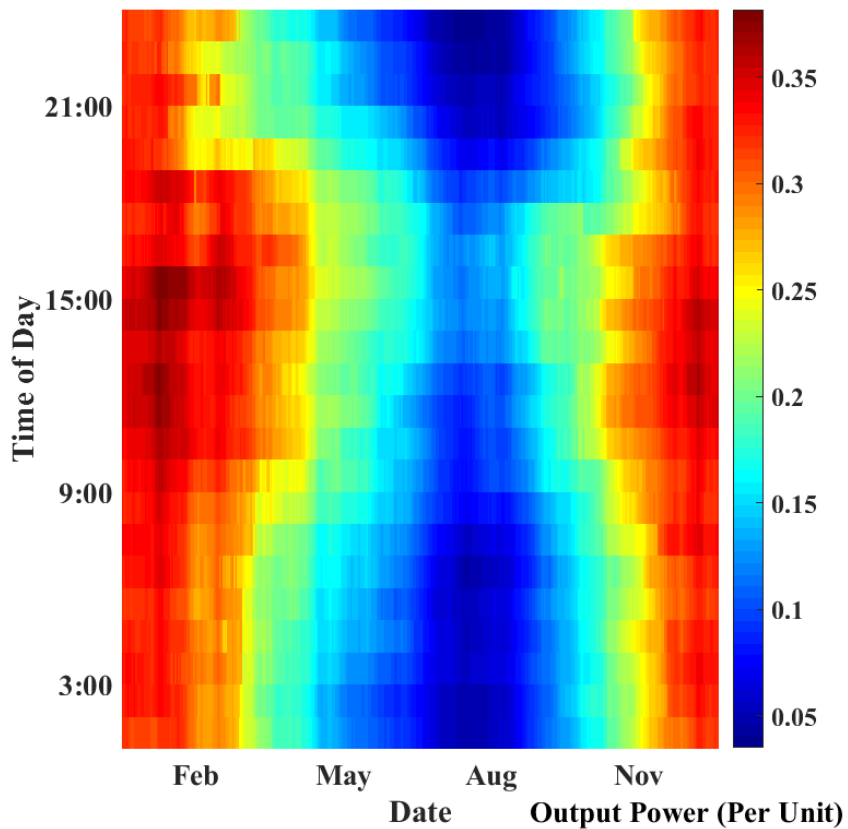


Figure 5.8(a): Expected Capacity Factor of the NPS-100c-21 at Cartwright

expected capacity factor to as high as 0.15 during the diurnal peak period, however it remains low enough to indicate a poor wind resource. In general, the NPS 100c-21 wind turbine is not optimized for Cartwright's wind regime and therefore exhibits poor performance.

Figure 5.8(b) displays the expected capacity factor of the NPS-100c-24 wind turbine. The general behavior due to the seasonal and diurnal cycle matches that of the NPS-100c-21, with the minima, maxima and seasonal-diurnal interrelation having a similar effect on wind turbine performance. However, the observed capacity factors are substantially higher. The peak capacity factor reaches 0.5 during January, with values in excess of 0.4 occurring from November to February throughout the day. The minimum capacity factor is roughly 0.08 during August, with the diurnal cycle increasing this value to 0.20 between 2:00 and 5:00 p.m. The NPS-100c-24 has a peak-period capacity factor of 0.15 per-unit higher than the NPS-100c-21, indicating an expected power output 15 kW higher (assuming a single 100 kW wind turbine). During the nadir, the NPS-100c-24 exhibits a capacity factor roughly 0.05 greater, reflecting a 5 kW increase in average power output. In general, the NPS-100c-24 is shown to probabilistically produce approximately one-third more energy than the NPS-100c-21. However, in each case the seasonal and diurnal cycle results in periods of relative quiescence (capacity factors less than 0.1) indicating that during these

periods wind generation would seldom be available. This demonstrates the large-scale intermittency of wind generation due to the influence of the seasonal and diurnal cycles.

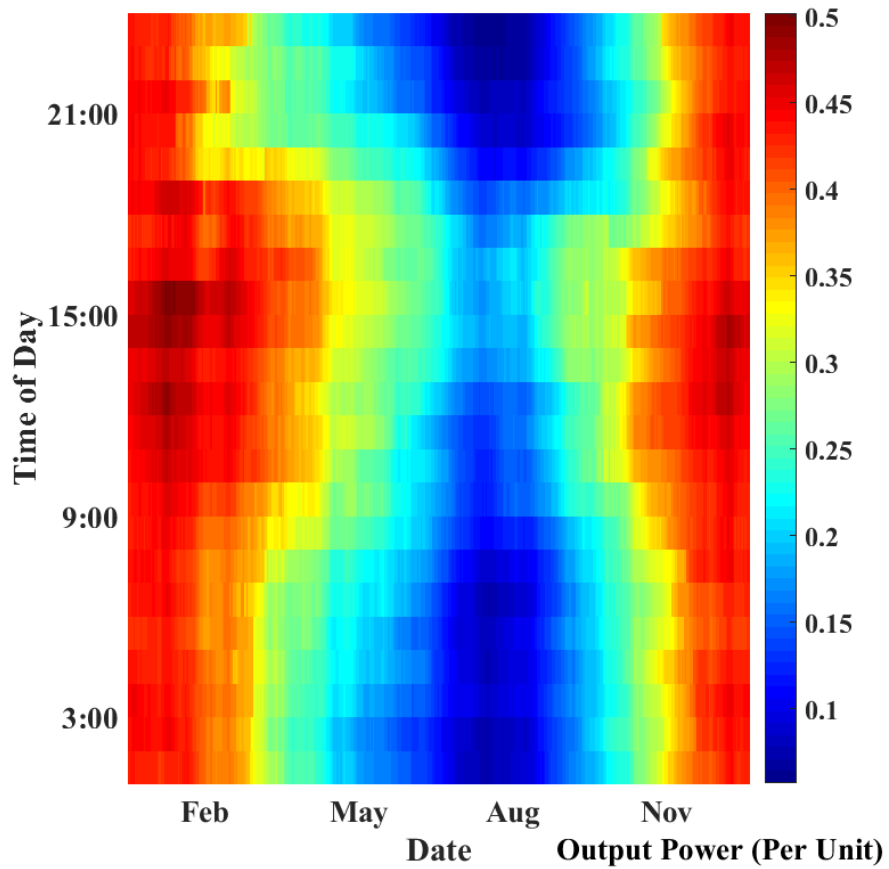


Figure 5.8(b): Expected Capacity Factor of the NPS-100c-24 at Cartwright

5.3: Wind Reserve Assessment

The wind reserve is the quantity of wind power available to meet secondary or peak electrical demand. It is a function of the site's wind resource, load profile and system architecture. Using environmental data, the wind resource of Cartwright has been modelled and the performance of two different wind turbine designs probabilistically investigated. Utilizing the wind resource, the amount, reliability and effect of the wind reserve can be quantified through a probabilistic comparison of wind generation, electrical demand their effects on microgrid operation. Continuing the case study, the electrical load profile of Cartwright is investigated to produce a probabilistic model of microgrid energy demand.

5.3.1: The Load Profile

The load profile of Cartwright was probabilistically modelled using 2 years of 15-minute data obtained from Nalcor. The univariate Kernel Density Estimation algorithm produced a time-variant probability distribution reflecting the observed electrical demand. Figures 5.9(a-d) present the probabilistic load profile, sampled at 3:00 a.m., 9:00 a.m., 3:00 p.m. and 9:00 p.m. and displaying the full seasonal cycle. Figure 5.9(a) displays the demand distribution at 3:00 a.m. The load profile is observed to have significant seasonal variability, with the most likely demand value varying from a peak of 600 kW during January to a minimum of 325 kW during September. A small secondary peak exists during

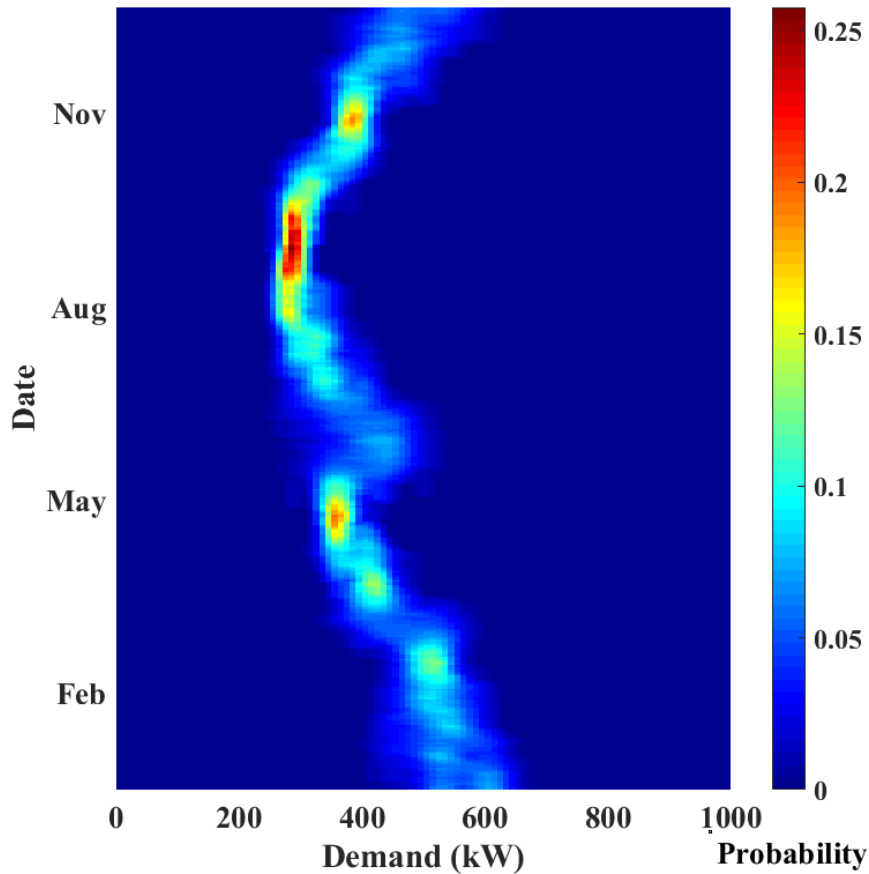


Figure 5.9(a): Cartwright Demand Distribution at 3:00 a.m.

June, correlating to the demand from shrimp plant during its season of operation. The distribution of demand values also exhibits variability, with higher demand variance during the winter months (likely due to variable heating requirements) and a tighter demand distribution near the late-summer load minimum. Figure 5.9(b) displays the load profile at 9 a.m. Due to the diurnal cycle, the demand values are consistently shifted upwards throughout the year. The most likely demand increases to 750 kW during January and 475 kW during September. In addition, the demand distributions are wider, indicating a greater degree of demand variability. The secondary peak during June is amplified, resulting in demand values reaching a range comparable to the winter maximum due to the increased industrial demand.

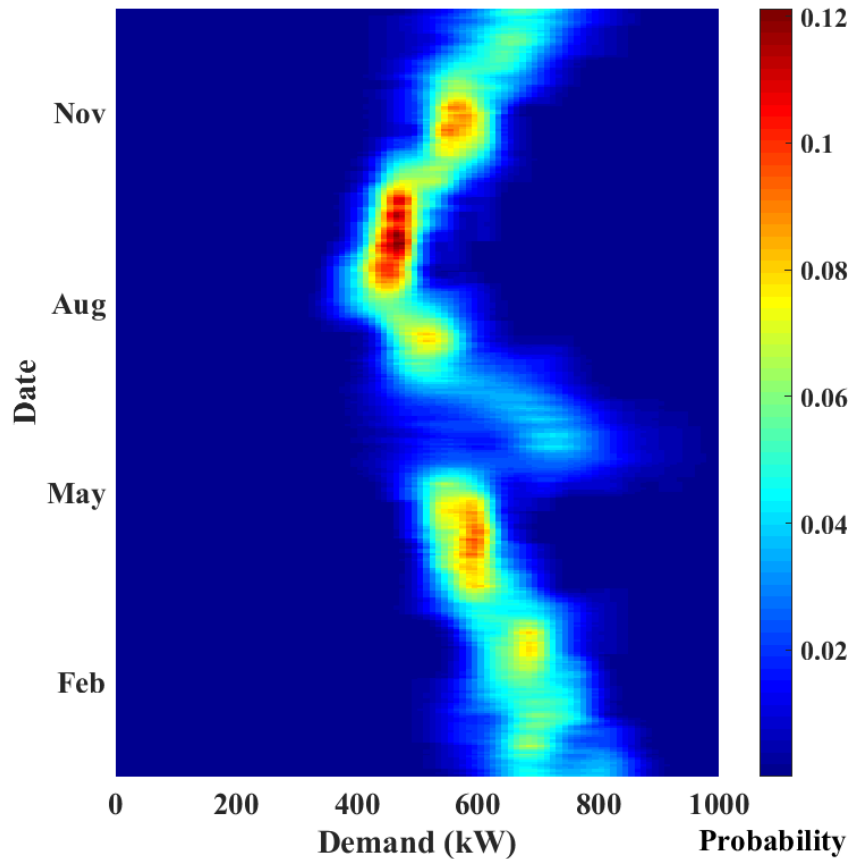


Figure 5.9(b): Cartwright Demand Distribution at 9:00 a.m.

Figure 5.9(c) displays the demand distribution at 3 p.m. The demand values are close to that observed at 9 a.m., with similar seasonal variability between 400 and 725 kW. However, the secondary peak is at its maximum amplitude – the shrimp plant is at this point likely responsible for nearly half of Cartwright’s electrical demand when operating at capacity. In general, the degree of demand variability has decreased slightly, resulting in an overall narrower demand distribution. A notable exception is during shrimp plant operation, where its more intermittent energy requirement has resulted in a very wide demand distribution ranging from 400 to 900 kW. Figure 5.9(d) displays the demand distribution at 9 p.m. At this point, the shrimp plant is less active, resulting in the secondary peak being shifted back towards the remainder of the demand distribution. At this time,

residential loads remain active, causing Cartwright’s electrical demand to maintain a 400 to 750 kW seasonal cycle – similar to the values observed at 9 a.m. and 3 p.m. The width of the distribution (indicating demand variability) is similar to that observed at 3 p.m., narrower than 9 a.m. and wider than 3 a.m. Essentially, a seasonal and diurnal cycle exists which effects both the mean electrical demand and the shape of the observed probability distribution. The shrimp plant is superimposed on this signal, and is more difficult to predict as its operation is defined more so by regulation of the shrimp season and economic factors such as prices and demand. Overall, the probabilistic model of Cartwright’s demand

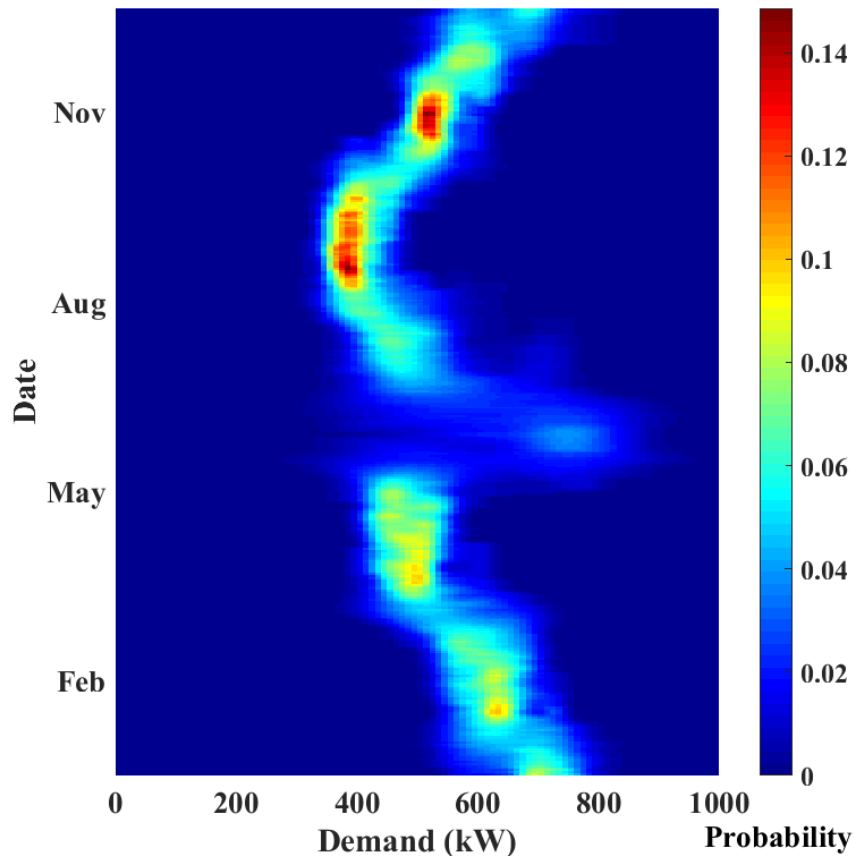


Figure 5.9(c): Cartwright Demand Distribution at 3:00 p.m.

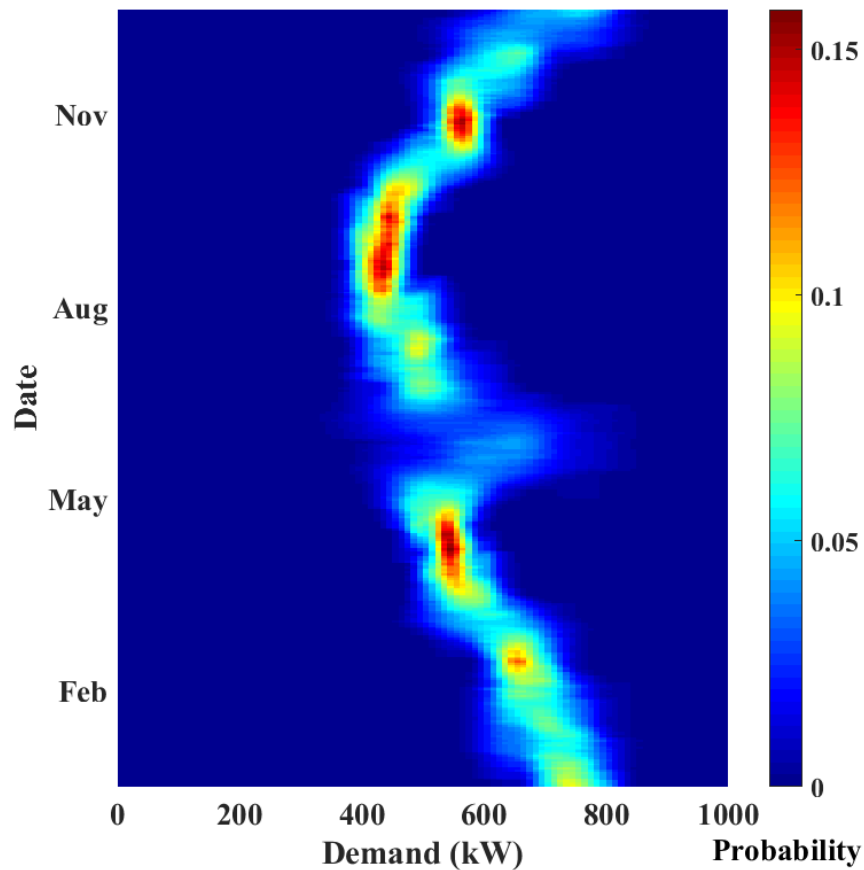


Figure 5.9(d): Cartwright Demand Distribution at 9:00 p.m.

provides the initial information required to begin further investigation into the effects of wind reserves on system operation.

The further investigation of Cartwright’s load profile requires the identification of the base, secondary and peak demand values, including their seasonal and diurnal variability. This is accomplished by analysis of the demand cumulative distribution function (CDF), calculated by integrating the probability distribution model described previously. Points within the CDF corresponding to specific cumulative probability values emerge, providing the information required to identify the base, secondary and peak demand. The CDFs themselves are clearly related to the corresponding load PDF, with the greatest CDF slope

occurring at the probabilistic peak demand value. The relative effects of the diurnal and seasonal cycle are clearly visible through their effects on the CDF. However, visual inspection of the CDF provides little information which has not previously been discussed with respect to the probability distribution model. Instead, the base, secondary and peak demand profiles are extracted from the CDF in order to display the information required for further assessment of wind reserves.

Figures 5.10 (a-d) display the base load, secondary load and peak load profiles (including their seasonal variability) sampled at 3:00 a.m., 9:00 a.m., 3:00 p.m. and 9:00 p.m. As discussed in Chapter 3, the base load corresponds to the 5th percentile of cumulative demand probability, the secondary load the 50th percentile and the peak load the 95th percentile. Figure 5.10(a) displays the demand profile at 3:00 a.m. The profile is winter-peaking, with the base load varying from 450 kW during January to 250 kW during August. The base load profile is nearly sinusoidal, with the annual-cycle dominating demand variation. The secondary demand follows a similar pattern, except it is shifted upwards by between 50 (during August) to 100 (during January) kW due to the presence of intermittently active customers. A slight secondary peak is evident during June due to Shrimp plant operation – the secondary load increases from 360 kW to 410 kW due to night-time plant operation. This increase is also evident (although more prominent) when examining the peak demand profile – the peak load increases from 410 to 500 kW before again declining towards an August minimum of 310 kW. The peak load reaches a maximum value of 650 kW during January, reinforcing the winter-peaking nature of Cartwright’s demand profile. In addition, the separation between the peak, secondary and base load

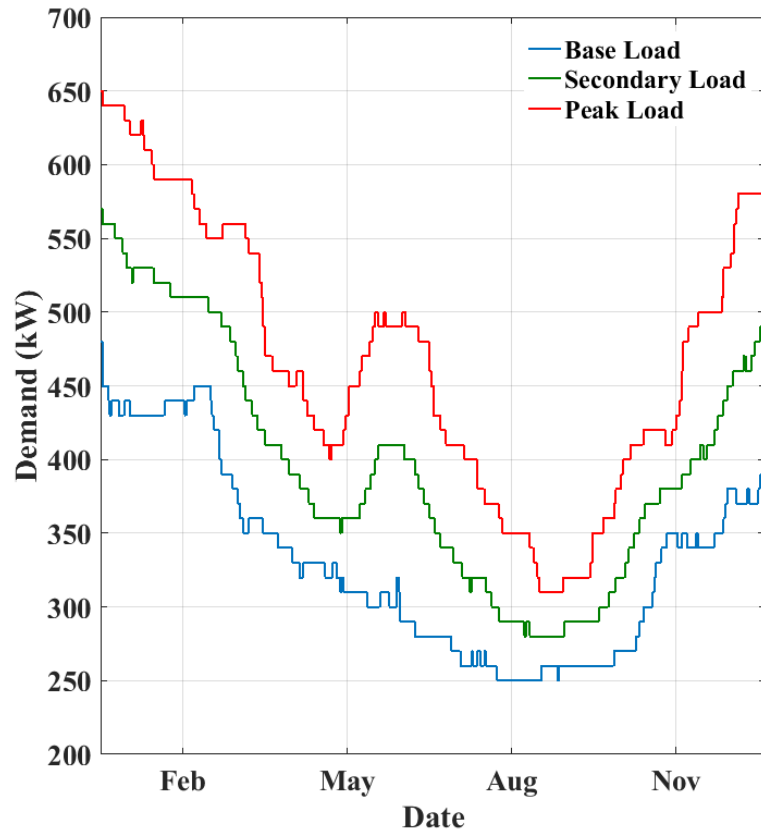


Figure 5.10(a): Base, Secondary and Peak Demand in Cartwright at 3:00 a.m.

profiles is highest during the winter load maximum, indicating the greatest degree of absolute variability in the expected electrical demand.

Figure 5.10(b) displays the demand profiles at 9:00 a.m. The standard winter-peaking pattern is evident, agreeing with the previously examined probabilistic load model. The base load varies from a peak of 600 kW during January to a minimum of 350 kW during August. There is no real secondary peak in the base load profile, indicating that the shrimp plant operates less than 95% of the time and therefore is counted as a secondary or peaking

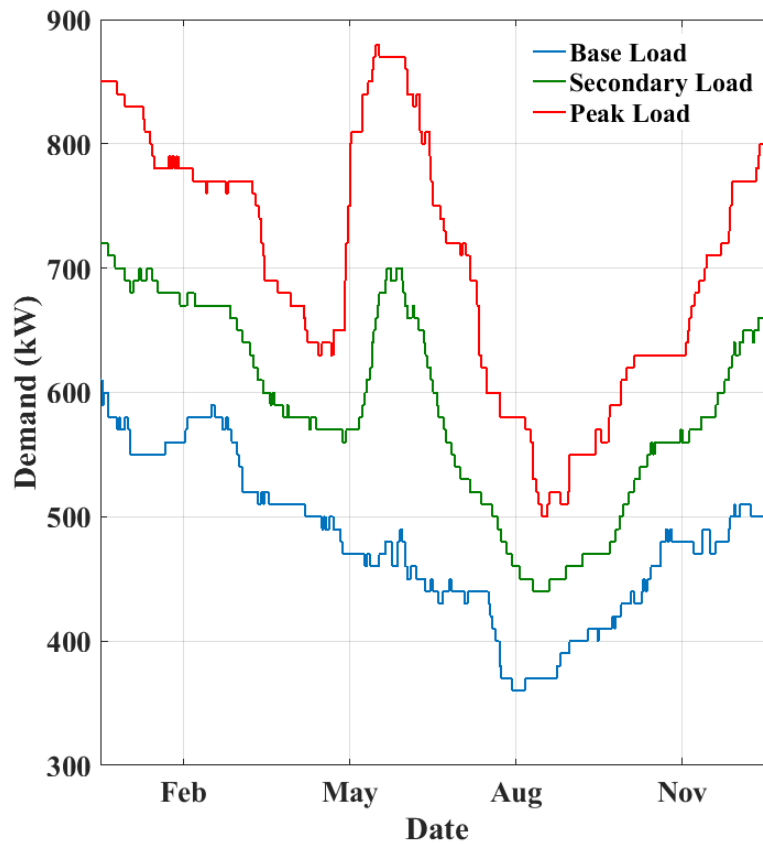


Figure 5.10(b): Base, Secondary and Peak Demand in Cartwright at 9:00 a.m.

customer. The secondary demand does show the secondary peaking behavior, increasing from 575 to 700 kW during the June operating period. The remainder of the year demonstrates similar behavior to the base load, with the secondary demand varying from a peak of 700 kW during January to a minimum of 450 kW during August. The secondary demand varies from approximately 100 kW above the base demand during January to 50 kW during July, indicating the seasonal-cycle changes in demand variability. The exception is during shrimp plant operation, where the secondary demand exceeds the base load by as much as 250 kW, indicating a highly variable and intermittent demand profile. The peak demand profile mirrors the behavior of the secondary demand profile, except for an even stronger secondary peak which actually exceeds the winter load maximum – the shrimp

plant operation period therefore exhibits the annual maximum peak demand of approximately 975 kW. The remainder of the year exhibits similar behavior to the secondary demand and the peak pattern from 3:00 a.m., being essentially a shifted secondary demand profile with the value varying from 850 kW during January to 500 kW during August.

Figure 5.10c displays Cartwright's base, secondary and peak demand profiles at 3:00 p.m. The general behavior is similar to that previously described, albeit the demand profiles are slightly lower. The base load varies from a peak of 575 kW during January to a minimum of 340 kW during August and September. The secondary demand follows a similar profile, varying from 700 kW to 390 kW. The seasonal cycle in demand variability is also intact. However, the secondary peak due to the shrimp plant operation is highly amplified – the secondary demand increases from 480 kW to 700 kW during the operating season. The peak demand profile also exhibits the amplified peak, increasing from 550 kW to 880 kW. Similar to at 9:00 a.m., the absolute peak demand is observed during plant operation as opposed to during the winter base load maximum. Figure 5.10(d) displays the load profiles at 9:00 p.m. The base load has not significantly changed, varying from a peak of 650 kW to a minimum of 375 kW. The secondary and peak load profiles also exhibit similar behavior. The secondary demand varies from 740 kW to 430 kW, with the secondary peak now having a lower amplitude, resulting in an increase from 525 kW to 610 kW. The peak load profile also displays this behavior – the secondary peak of 770 kW is slightly less than the winter peak of 810 kW, indicating a lesser degree of shrimp plant operation. The peak demand at this time is slightly higher than at 3:00 p.m. – this is most

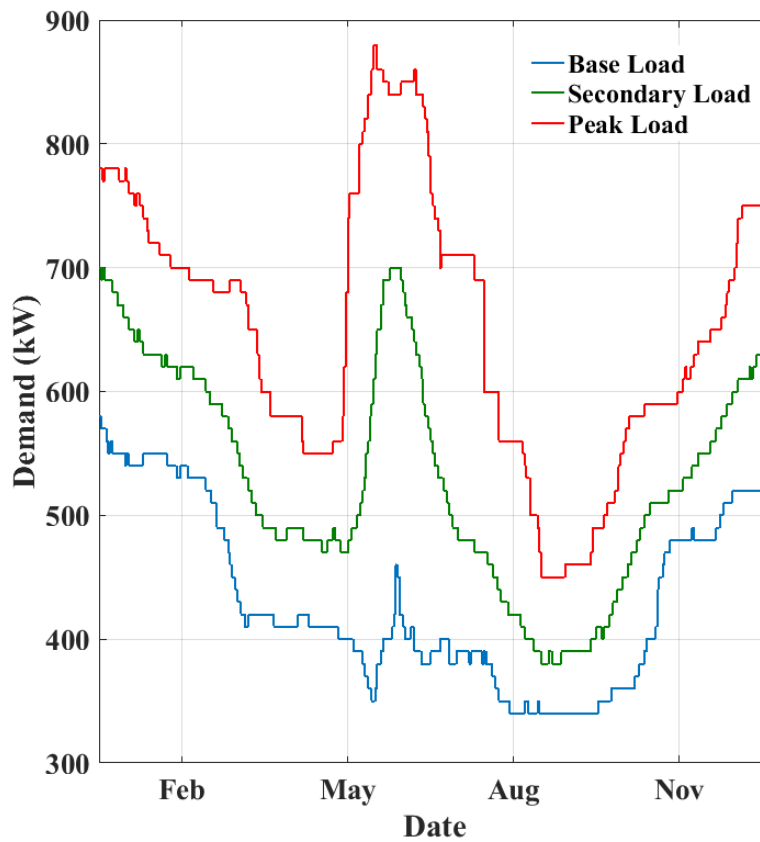


Figure 5.10(c): Base, Secondary and Peak Demand in Cartwright at 3:00 p.m.

likely due to greater activity in residential loads. However, the general seasonal and diurnal variability in load profiles is preserved, providing valuable information regarding the nature of electrical demand at Cartwright.

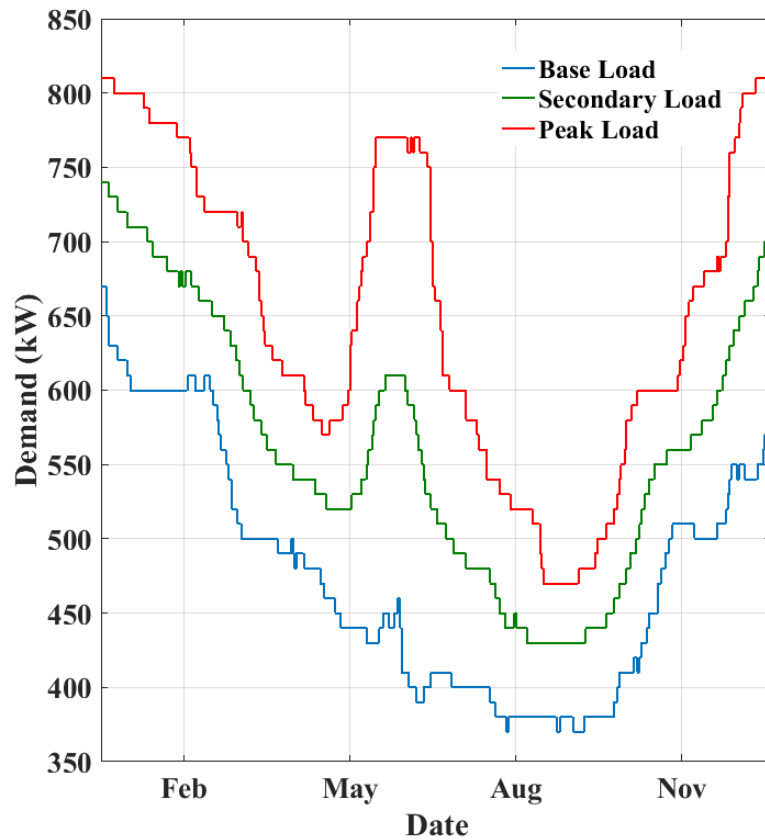


Figure 5.10(d): Base, Secondary and Peak Demand in Cartwright at 9:00 p.m.

The identification of the base, secondary and peak demand profiles allow modifications to the previously defined probabilistic load model. The base load can be removed from the load distribution, representing the effect of conventional base generation acting as a grid-forming system. The remaining demand represents that serviceable by wind generation – referred to as the secondary demand. Figure 5.11(a-d) displays the time-variant probability distribution of Cartwright’s secondary demand, sampled at 3:00 a.m., 9:00 a.m., 3:00 p.m. and 9:00 p.m. The characteristics of this probabilistic model provides information which can be utilized to predict the ability of wind turbines to supplement the conventional base

load generators. Figure 5.11(a) displays the secondary demand distribution at 3:00 a.m. A seasonal cycle is evident, with the demand distribution being wider during the winter months – the January secondary demand varies from 50 to 200 kW above the concurrent base load. During August and September, this distribution is more concentrated – the secondary demand varies between 10 and 100 kW and has a higher peak probability at approximately 30 kW. A secondary peak exists during June due to the shrimp plant – the secondary demand distribution shifts upwards and widens, now ranging between 50 and 250 kW as opposed to 10 and 100 kW. Figure 5.11(b) displays the secondary demand

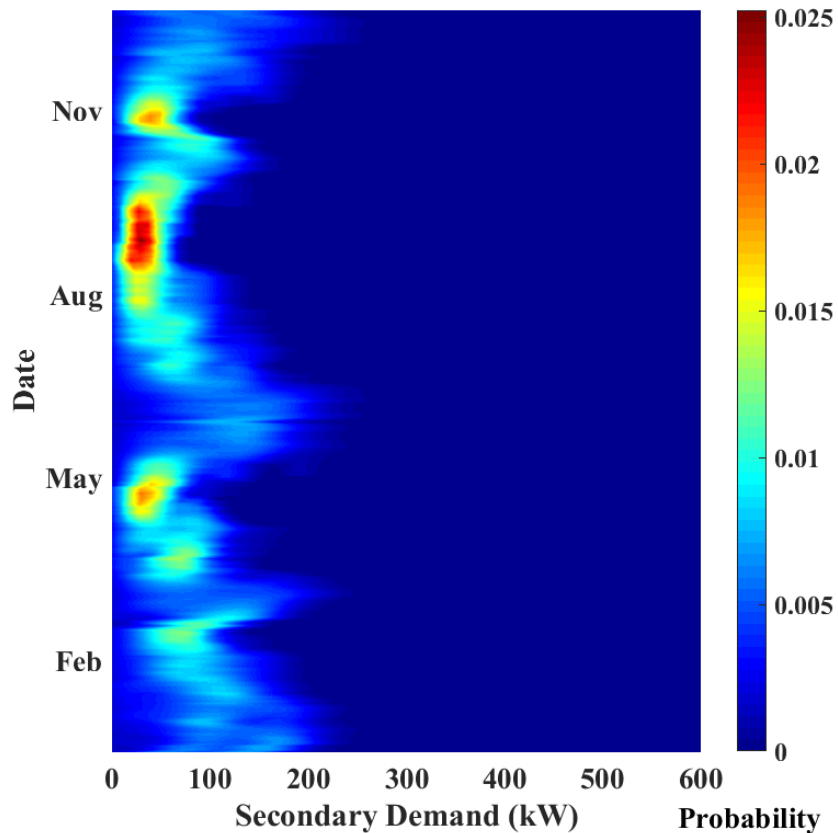


Figure 5.11(a): Secondary Demand Distribution in Cartwright at 3:00 a.m.

distribution at 9:00 am. A seasonal cycle still exists, however it is less significant, indicating that at this time the seasonal cycle is primarily manifested in shifting the base load as opposed to the secondary demand distribution. In general, the distribution of secondary demand has substantially higher variance, with values commonly ranging from 0 to 300 kW above the concurrent base load. The shrimp plant has a more significant effect on the secondary demand distribution, resulting in values between 150 and 350 kW becoming the most common secondary demand values, with isolated instances of up to 500 kW observed. This reflects the intermittent nature of this industrial customer, shifting the general demand distribution without significantly effecting the base load profile.

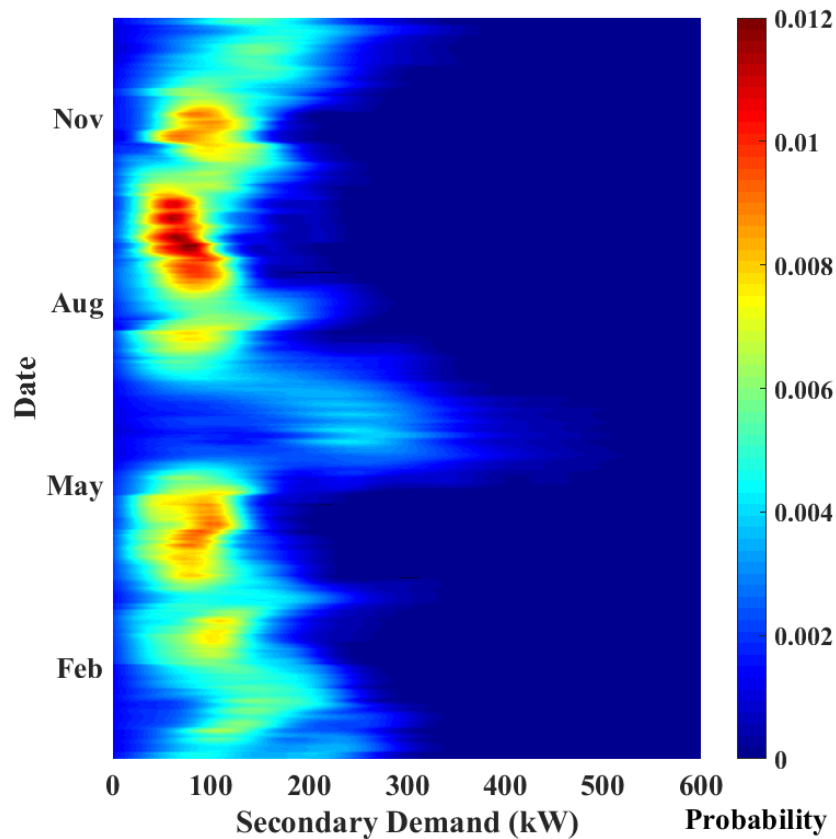


Figure 5.11(b): Secondary Demand Distribution in Cartwright at 9:00 a.m.

Figure 5.11(c) displays the secondary demand distribution at 3:00 p.m. In general, it is similar to that observed at 9:00 a.m. The seasonal cycle only weakly effects the probability distribution, indicating its primary effect remaining on the base load profile as investigated previously. The shrimp plant has by far the largest effect on the demand distribution, resulting in the secondary demand shifting from 0-200 kW to 200 to 450 kW, with isolated observations as high as 600 kW above the concurrent base load. Any installed wind generation must therefore be significantly oversized to meet this demand profile in comparison to that observed during the remainder of the year. Figure 5.11(d) displays the secondary demand distribution at 9:00 p.m. At this time, the shrimp plant is less active,

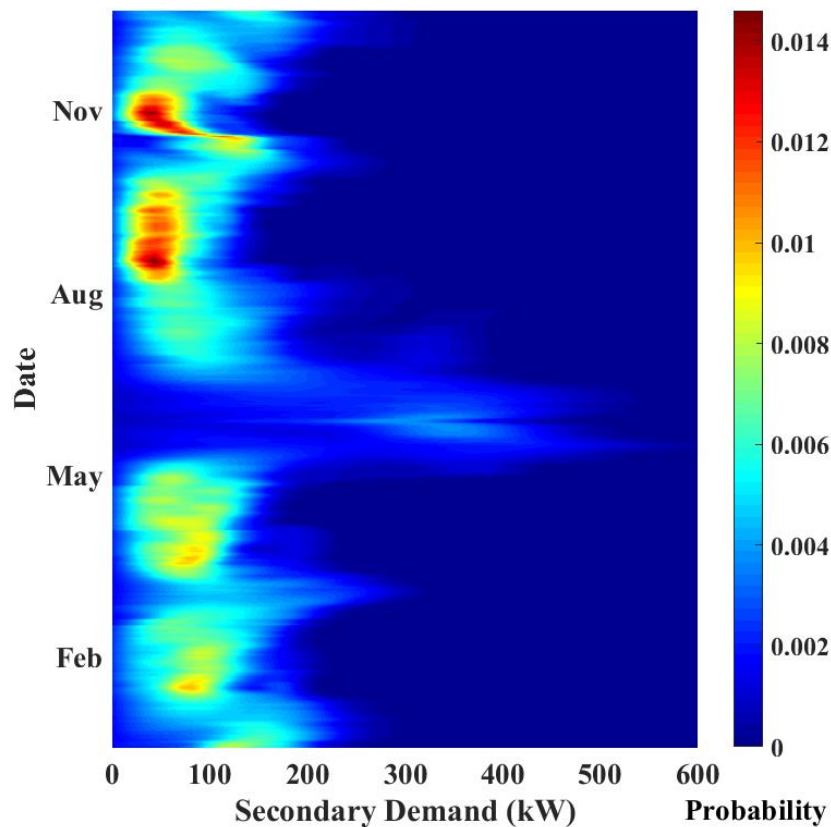


Figure 5.11(c): Secondary Demand Distribution in Cartwright at 3:00 p.m.

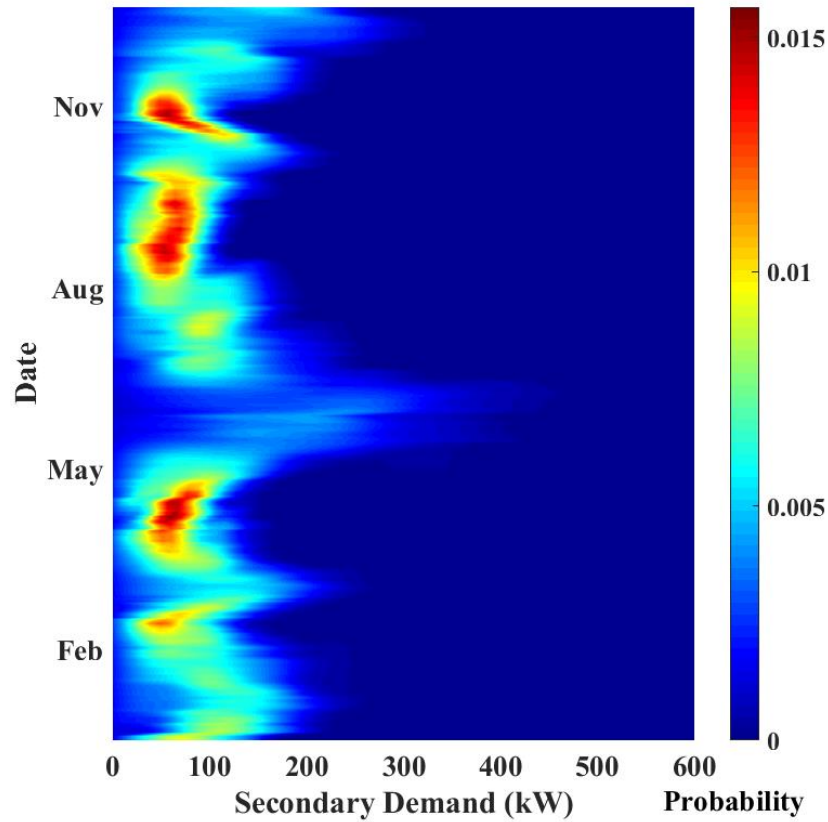


Figure 5.11(d): Secondary Demand Distribution in Cartwright at 9:00 p.m.

resulting in a smaller (albeit still significant) shift in the demand profile. In general, the secondary demand varies between 0 and 200 kW above the base load for most of the year, with slight probabilities of 300 kW values seen during December and especially when the shrimp plant is active – at this point isolated observation of up to 500 kW can be expected. Overall, the secondary demand profile displays significant diurnal variability, slight seasonal variability and clearly shows the effect a large industrial customer can have on a probabilistic load profile. To further refine this investigation, the peak demand profiles will also be examined to provide the information needed to evaluate the ability of wind turbines to provide demand response services by acting as a short-term peaking unit.

The peak demand is calculated by subtracting the appropriate seasonal and diurnal secondary (50% cumulative probability) demand from the load observations, keeping only positive values. This results in a dataset containing all load observations where a peaking unit would be used to provide demand response. The probabilistic load modeling algorithm presented in Chapter 3 is applied to this dataset, resulting in a time-variant distribution model of Cartwright’s peak demand. Figure 5.12(a-d) displays the peak demand probability distribution spanning the seasonal cycle, observed at 3:00 a.m., 9:00 a.m., 3:00 p.m. and 9:00 p.m. Figure 5.12(a) presents the peak demand distribution at 3:00 a.m. In general, the peak demand ranges from 0 to 100 kW above the appropriate secondary demand value.

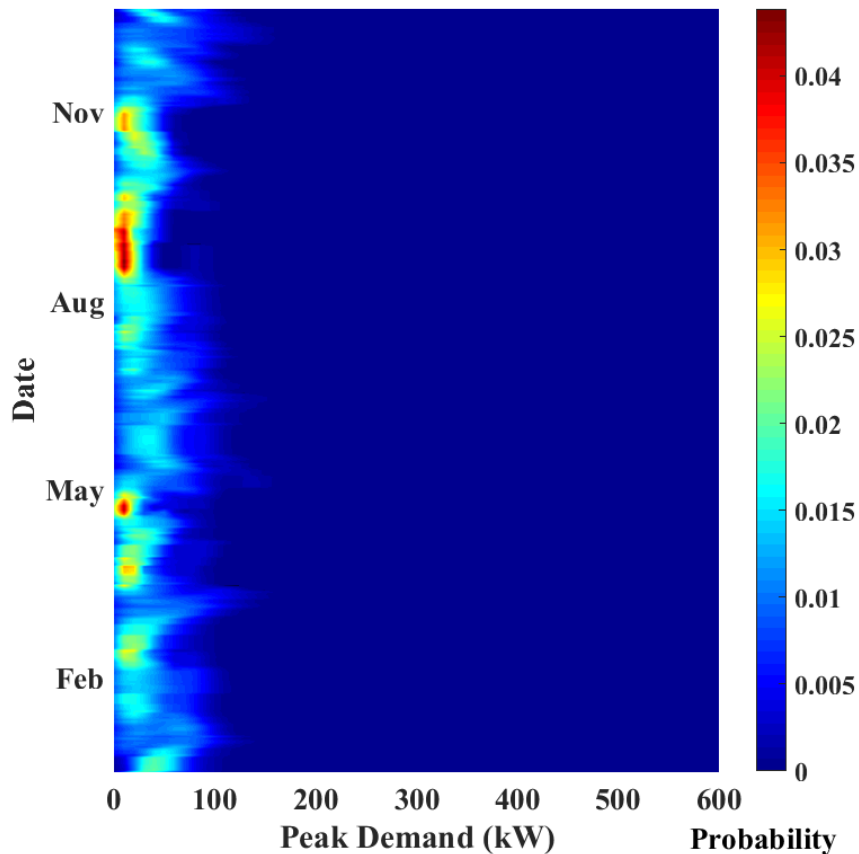


Figure 5.12(a): Peak Demand Distribution in Cartwright at 3:00 a.m.

Some seasonal-cycle variability is evident within the demand profile, with the winter months (December to March) exhibiting a higher degree of peak-demand variance (from 0 to 125 kW) while the months of May, July, August, September and October have the peak demand probability concentrated at values under 50 kW. The shrimp plant operates during June, and has the effect of interrupting the seasonal cycle with the return winter-type peak demand profile. However, as the shrimp plant is relatively inactive at 3 a.m., the overall effect is not as large as that observed later in the day. Figure 5.12(b) displays the peak demand profile at 9:00 a.m. The increase in residential and commercial demand results in a higher variance within the peak demand profile, with significant probability mass existing at values of up to 200 kW during the winter months and 150 kW during May-October. The

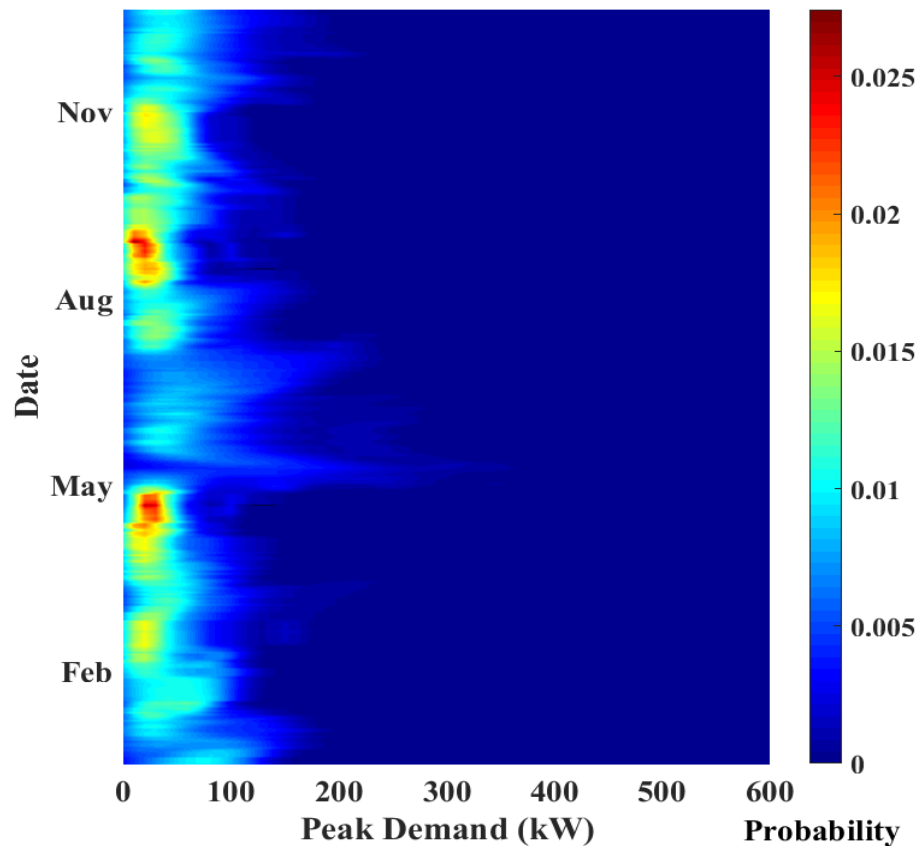


Figure 5.12(b): Peak Demand Distribution in Cartwright at 9:00 a.m.

shrimp plant now has a more significant effect on the demand profile, with the peak distribution shifting from the 0-150 kW distribution seen during May to 0-300 kW during early June, immediately afterwards. Essentially, peaking units must probabilistically supply more energy (when needed) during plant operation in comparison to the remainder of the year.

Figure 5.12(c) displays the peak demand distribution at 3:00 p.m. At this time, the peak demand distribution is somewhat more concentrated for the majority of the year, varying between 0 and 100 kW above the secondary load. The shrimp plant has the largest effect, being fully active. During June, the peak load distribution increases to as much as 400 kW

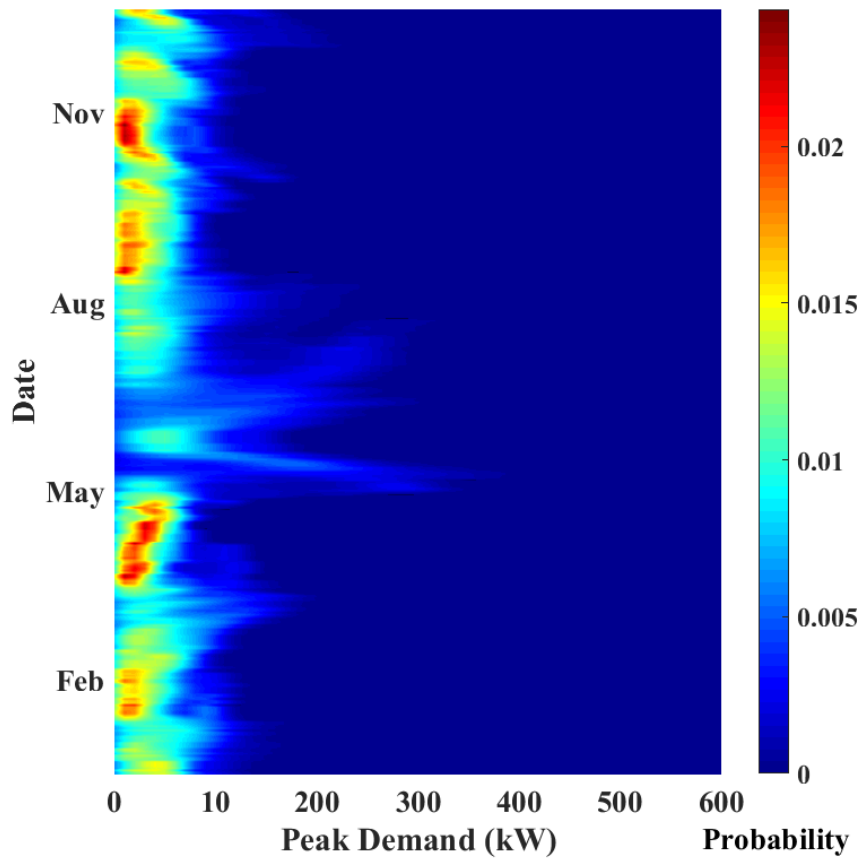


Figure 5.12(c): Peak Demand Distribution in Cartwright at 3:00 p.m.

above the secondary load value. In addition, a bimodal peak is revealed corresponding to early and late June, indicating that the shrimp plant is most active near the beginning and end of its operation season. Figure 5.12(d) displays the peak demand distribution at 9:00 p.m. At this time, the shrimp plant is mainly quiescent, only slightly shifting the peak demand distribution. The seasonal cycle is still observable, with a more concentrated demand profile during the May and July to October. During November to April, the demand distribution has higher variance, with values in excess of 100 kW more common. Overall, the peak demand distribution acts as a probabilistic load model for wind reserves implemented as peaking units. As the base load and secondary demand is supplied by

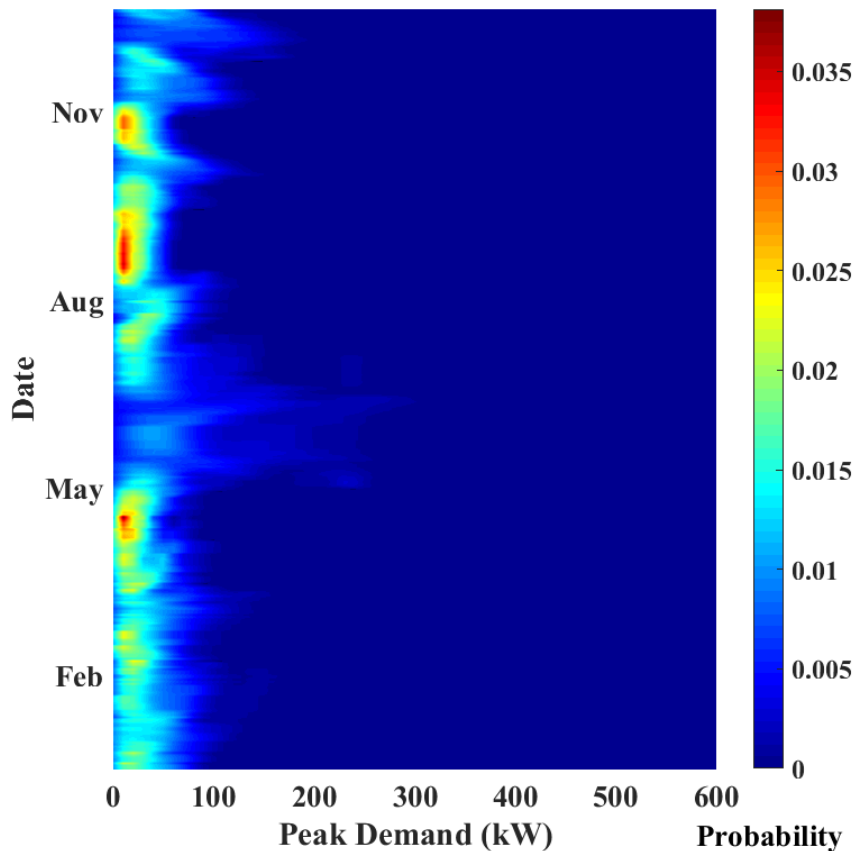


Figure 5.12(d): Peak Demand Distribution in Cartwright at 9:00 p.m.

conventional generation, the probability distribution of the peak demand allows the probabilistic evaluation of wind generation's ability to provide demand response, acting as an active reserve within Cartwright's islanded microgrid.

5.3.2: Probabilistic Reserve Modeling

The previously developed probabilistic wind turbine output model is combined with the secondary demand models to produce a probabilistic model of the instantaneous power balance. The power balance is the difference between the wind generation and the reserve requirement – either the secondary or peak demand profile. Positive values indicate sufficient wind reserve, with negative values indicating a shortfall which must be provided by conventional generation units to prevent loss of load. The properties of the power balance probability distribution therefore define the condition space of the operational microgrid and allows the optimization of wind turbine installation. Figure 5.13(a-d) displays the probabilistic power balance model assuming 250 kW of wind generation using the NPS-100c-21 power curve. In this case, the wind generation is used to meet the secondary demand, with conventional generators supplying only the base load. This will occur in situations when sufficient wind available for EMS systems to allocate wind generation to the microgrid, however when diesel generator operating requirements or a high degree of intermittency make wind incapable of meeting some of the base load requirements. The distribution model includes both seasonal and diurnal dimensions, with

Figure 5.13 displaying the full seasonal cycle at 3:00 a.m., 9:00 a.m., 3:00 p.m. and 9:00 p.m. respectively. The majority of the probability mass exists as a mirrored demand distribution, reflecting quiescent wind turbine operation. In this situation, no reserve generation is available. This situation is most common at 3:00 a.m., when the wind resource is suppressed. However, the largest negative power balance observations occur at 3:00 p.m., when the shrimp plant is active. At this time, the wind generation is capable of providing an active reserve some of the time, with probability mass existing at positive power balance values. The precise probability of wind reserve availability as well as the expected energy balance can be calculated using this distribution. In general, the power balance distribution follows the seasonal and diurnal-cycle variability discussed in the previous section, reflecting the observed changes in the wind resource and demand profile.

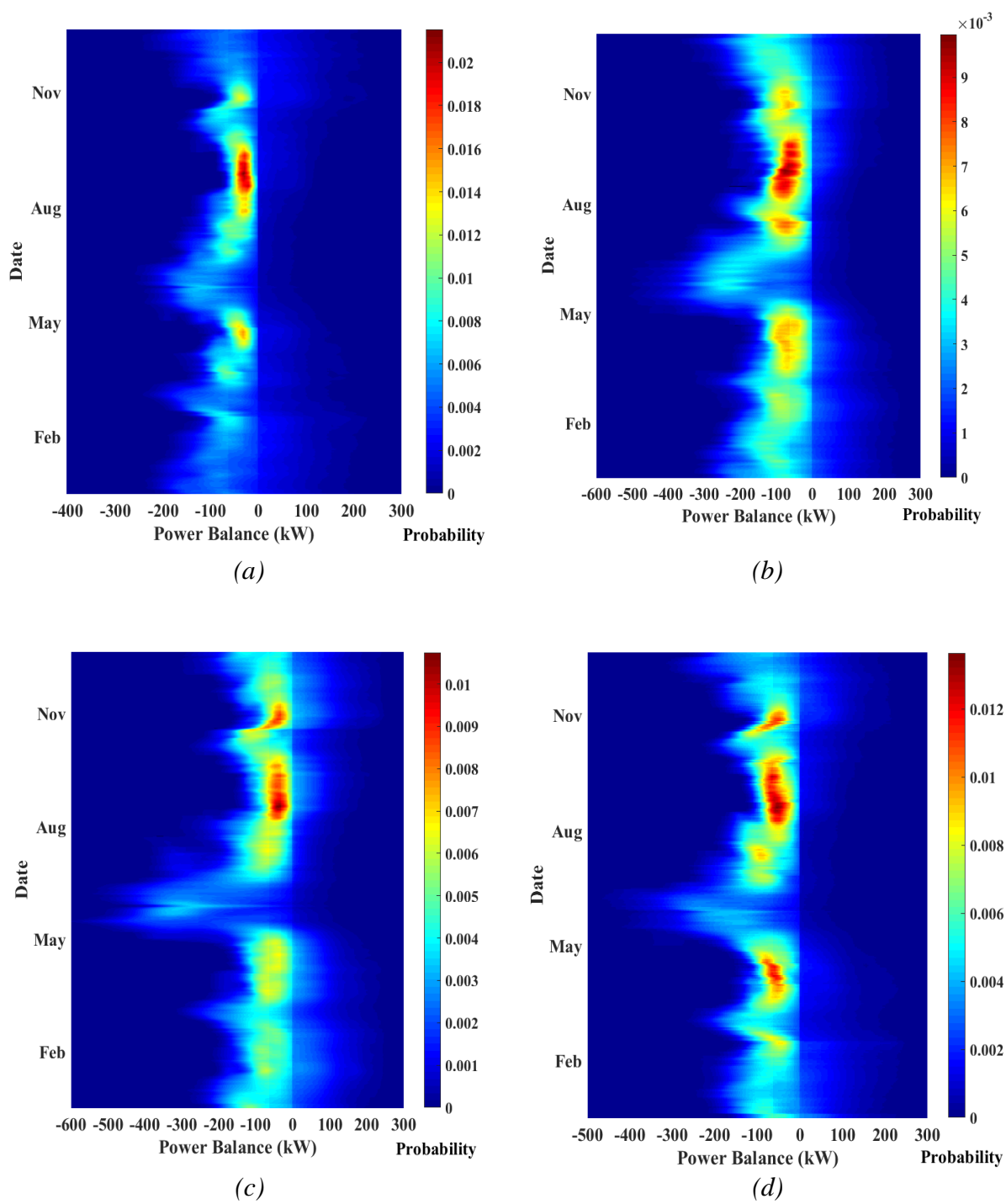


Figure 5.13: Power Balance Distribution in Cartwright at (a) 3:00 a.m., (b) 9:00 a.m., (c) 3:00 p.m. and (d) 9:00 p.m. using the NPS-100c-21

Figure 5.14 (a-d) presents the probabilistic power balance distribution assuming 250 kW of wind generation using the NPS-100c-24 wind turbine. Compared to the NPS-100c-21, a significantly greater positive-value probability mass is observed, especially at 9:00 a.m. and 3:00 p.m. (Figures 5.14(b) and 5.14(c)). During these times, the wind turbine is operating at rated power a significant fraction of the time, especially during the winter months. The 250 kW rated output is greater than the majority of secondary demand observations, resulting in a higher probability of a positive wind reserve. This behavior is less common during the summer months (due to the seasonal-cycle wind resource variation) and during shrimp plant operation, where the resultant increase in demand is not compensated by additional wind availability. Making the assumption that the aggregate positive probability is the measure of wind availability, the seasonal cycle dominates the resultant metric. However, the NPS-100c-24 is consistently more likely to provide a wind reserve due to its design better suiting the wind resource at Cartwright.

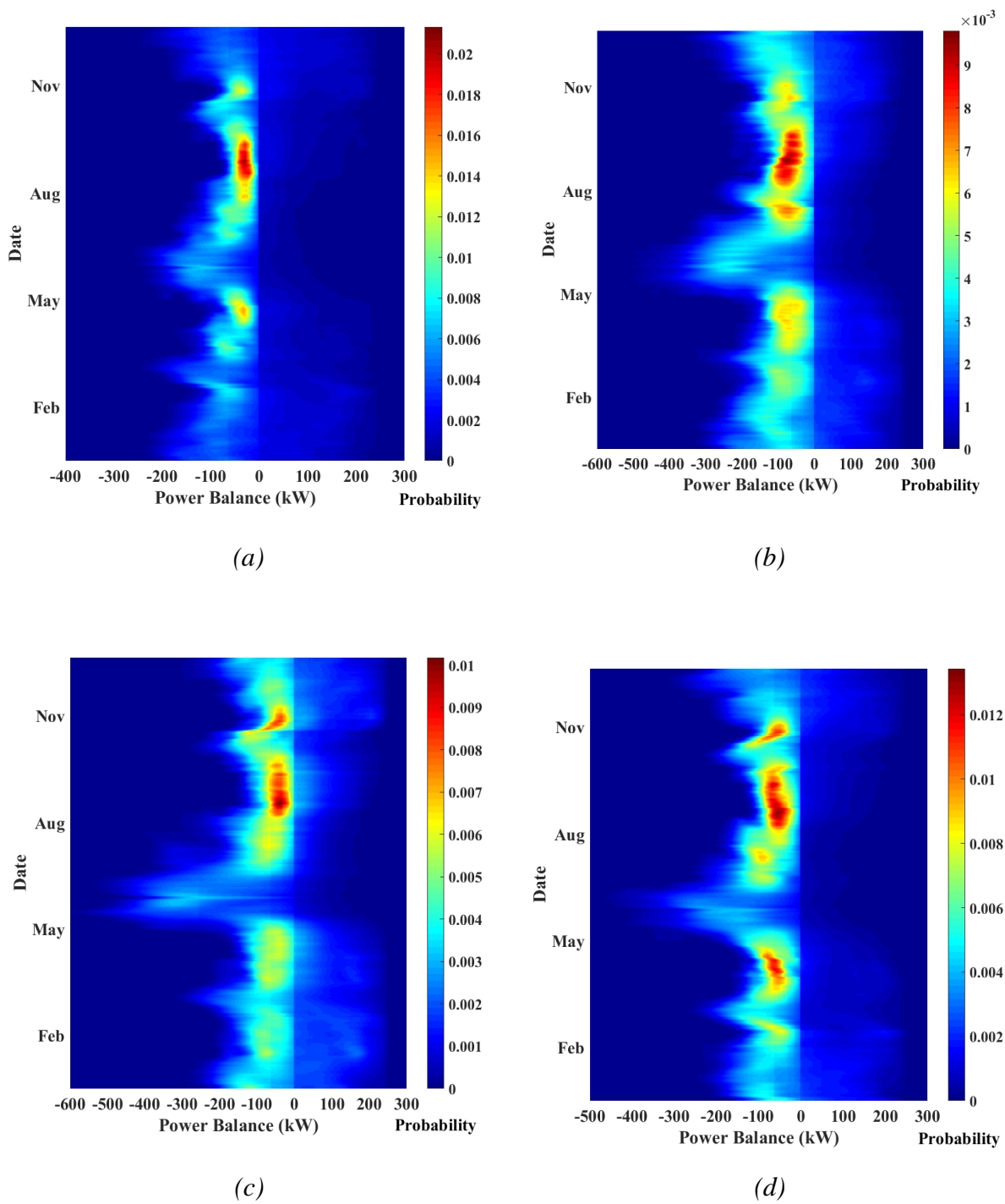
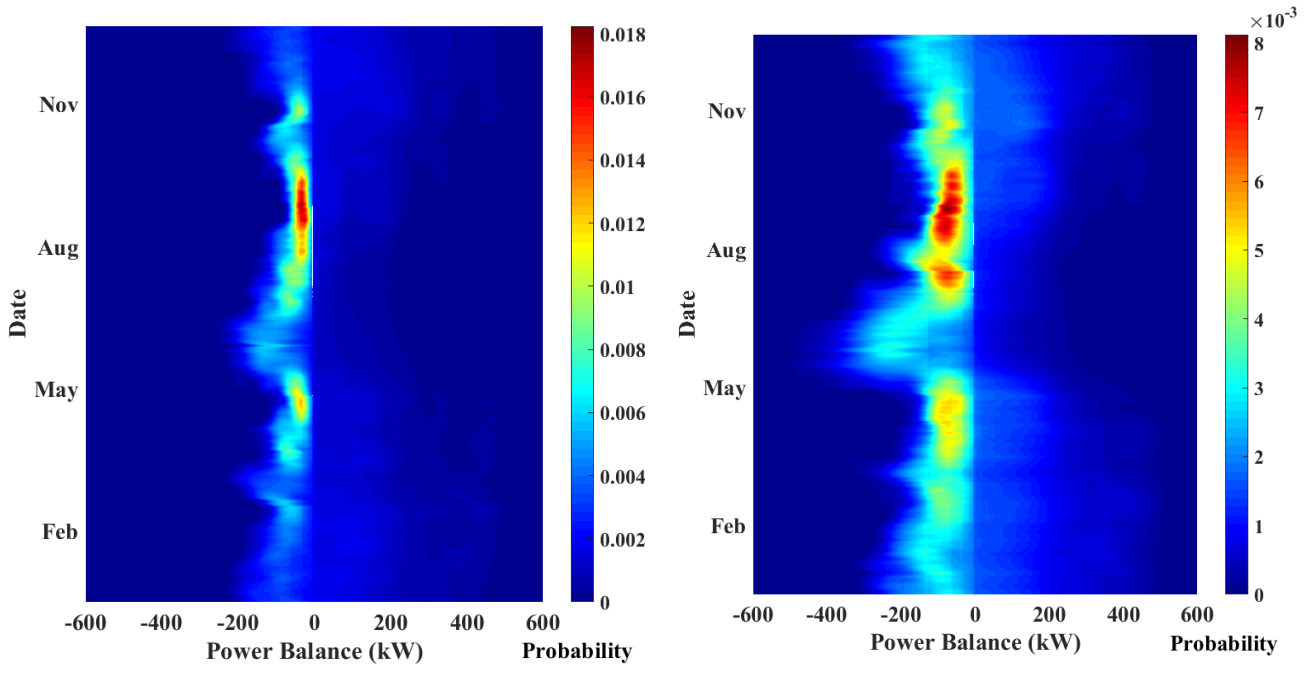


Figure 5.14: Power Balance Distribution in Cartwright at (a) 3:00 a.m., (b) 9:00 a.m., (c) 3:00 p.m. and (d) 9:00 p.m. using the NPS-100c-24

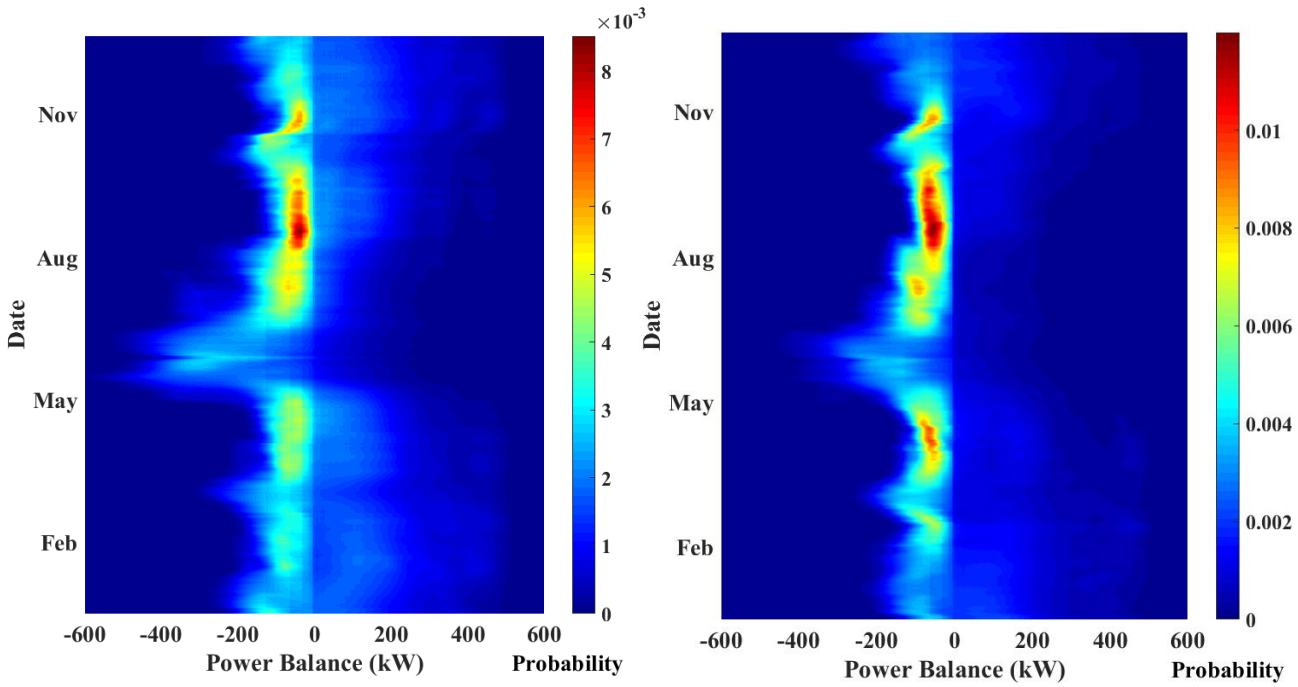
The effect of increased wind generation capacity on the probabilistic power balance is investigated by repeating the previous analysis assuming 500 kW of wind generation, - the equivalent of 5 operational wind turbines. Figure 5.15(a-d) presents the resulting probabilistic power balance when using the NPS-100c-21 wind turbine, observed at 3:00 a.m., 9:00 a.m., 3:00 p.m. and 9:00 p.m. to capture the diurnal wind reserve variability. In general, the probability distribution is not significantly changed, as the NPS-100c-21 is quiescent the majority of the time. However, the additional probability mass which is shifted to positive values is now spread over a larger area, with the potential for as much as 500 kW of excess wind energy during the winter months. At 9:00 a.m. and 3:00 p.m. (Figures 5.15(b) and 5.15(c)) the greater wind capacity does result in a greater probability of a positive wind reserve. However, the effect is fairly small except for during the seasonal wind maximum in December to February. Overall, the increase in wind capacity does result in a greater probability of a sufficient wind reserve. However, further analysis is needed to fully define its effect on Cartwright's microgrid.

Figure 5.16(a-d) presents the resulting probabilistic power balance when using the NPS-100c-24 wind turbine, again observed at 3:00 a.m., 9:00 a.m., 3:00 p.m. and 9:00 p.m. to capture the diurnal wind reserve variability. At 3:00 a.m., the distribution is not greatly changed, as the diurnal wind resource minimum results in a high probability of quiescent operation. However, the effect of both the design change (to the NPS-100c-24) and the increased capacity is clearly evident at 9:00 a.m. and 3:00 p.m., when the diurnal wind maximum increases the wind turbine output. Significant probability mass is shifted to



(a)

(b)



(c)

(d)

Figure 5.15: Power Balance Distribution in Cartwright at (a) 3:00 a.m., (b) 9:00 a.m., (c) 3:00 p.m. and (d) 9:00 p.m. using 500 kW of generation from the NPS-100c-21

significant probability for the small positive values which represent partial-load operation still meeting the reserve requirement. In general, the NPS-100c-24 has a higher likelihood of providing a wind reserve for secondary generation in comparison to the NPS-100c-21. In addition, the greater probability of rated output allows even the shrimp plant period to have some positive probability mass, indicating a wind reserve contributing to shaving this peak from Cartwright's load profile. The increased wind capacity does not have a linear effect on the wind reserve availability – the complex probabilistic interplay between the wind resource and the demand profile results in a non-linear relationship between wind capacity, probabilistic wind reserves and the resulting power balance.

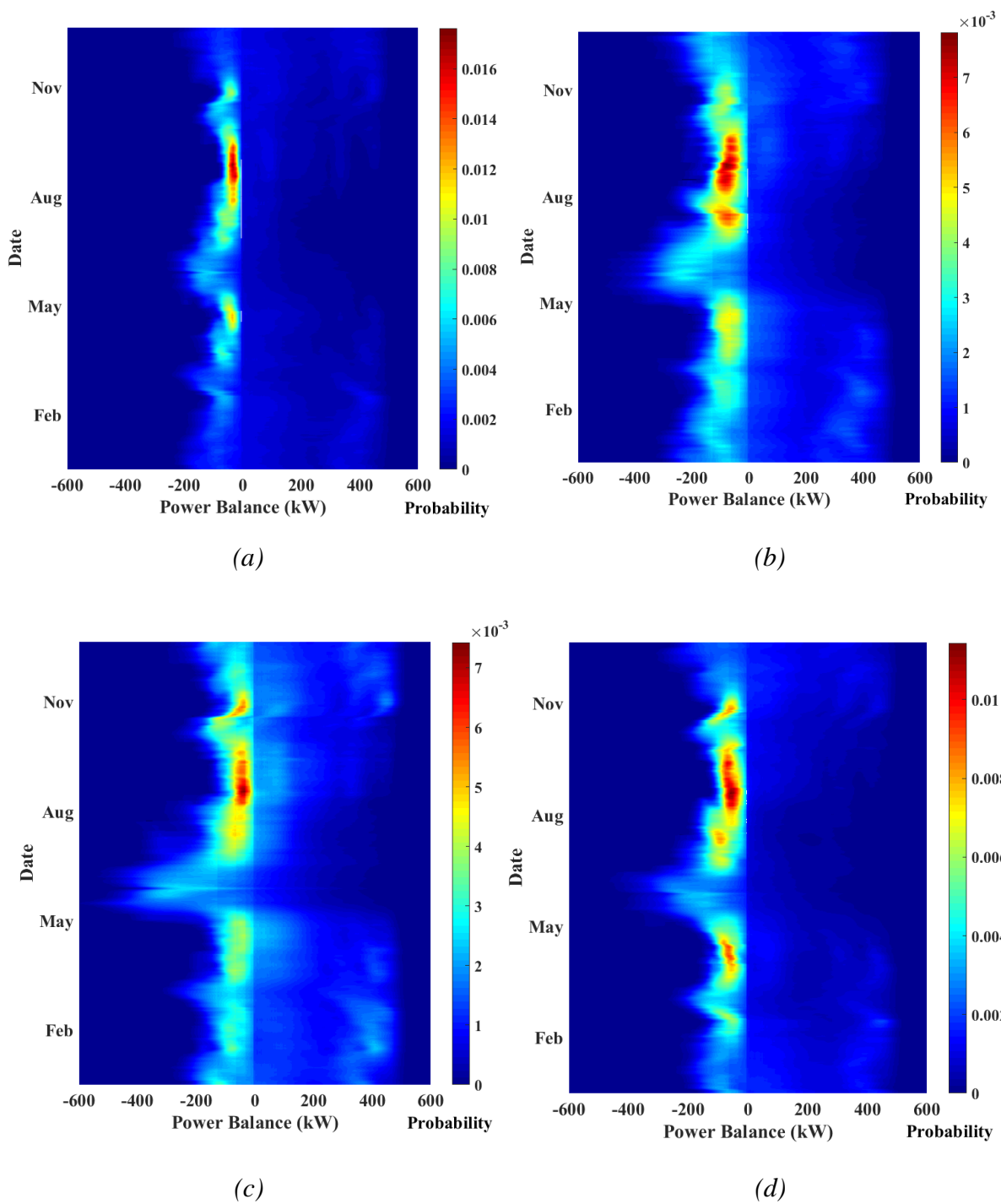
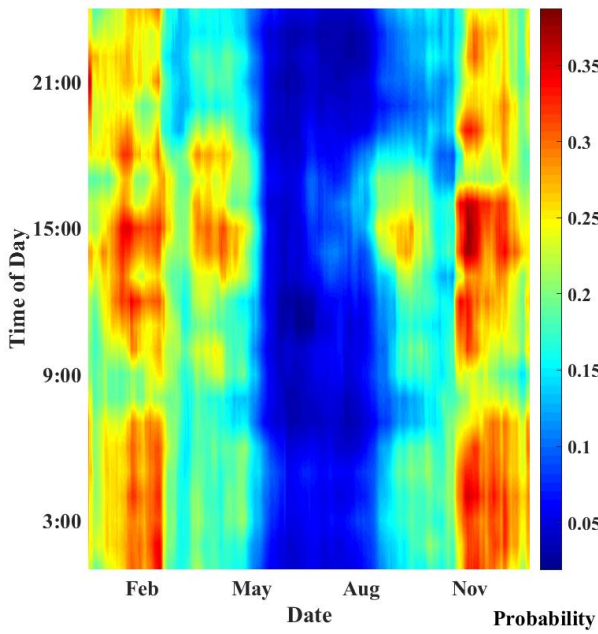
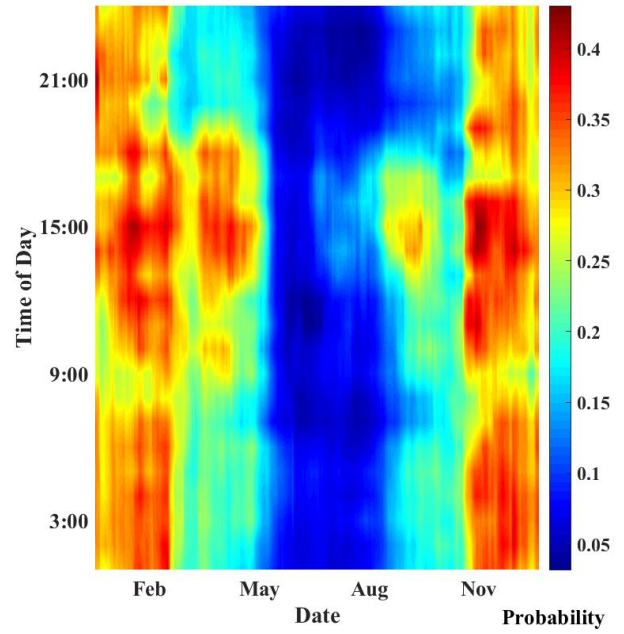


Figure 5.16: Power Balance Distribution in Cartwright at (a) 3:00 a.m., (b) 9:00 a.m., (c) 3:00 p.m. and (d) 9:00 p.m. using 500 kW of generation from the NPS-100c-24

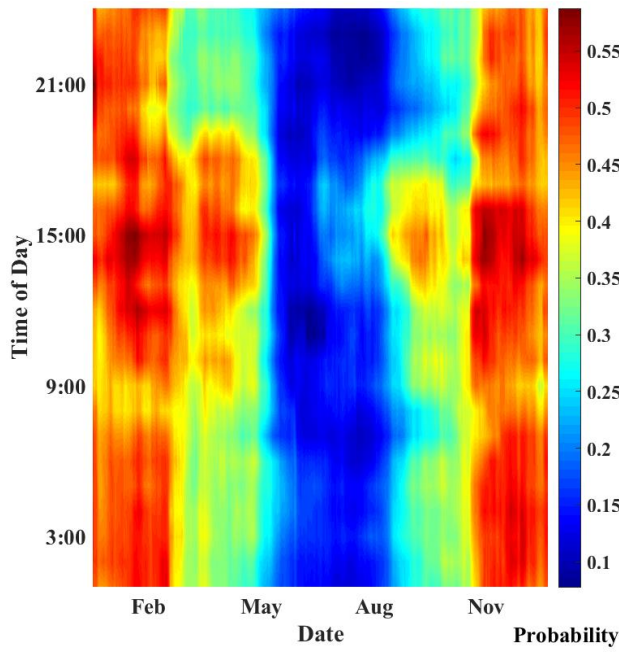
The probability of sufficient wind generation being available to meet the secondary demand is calculated by integrating the positive portion of the probabilistic power balance model. Excess energy is assumed to be dumped (or not generated) – the inclusion of storage is a subject of future investigations. The resulting wind reserve probability is a single value evaluated at each seasonal and diurnal phase, providing a time-variant wind reserve estimation which has applications in power system planning and wind turbine selection. Figure 5.17 (a-d) presents four of these probabilistic wind reserve models, evaluated assuming 250 kW of generation using the NPS-100c-21 (Figure 5.17(a)), the NPS-100c-24 (Figure 5.17(b)), 500 kW of generation using the NPS-100c-21 (Figure 5.17(c)) and the NPS-100c-24 (Figure 5.17(d)). The observed probability values clearly display the effects of wind turbine design, capacity, and the interplay between the demand profile and wind turbine output distribution during the course of seasonal and diurnal cycles. In the case of 250 kW capacity (Figures 5.17(a) and 5.17(b)), the NPS-100c-21 is shown to have a slightly lower probability of reserve, ranging from 0.03 (during June near 12:00 noon and June-August near 10:00 p.m.) to 0.36 during November at 3:00 p.m. During these periods, the NPS-100c-24 has probability values of 0.04 and 0.41, respectively – approximately 15% higher (in relative terms). The same pattern is evident when installing 500 kW of capacity (Figures 5.17(c) and 5.17(d)). The NPS-100c-21 exhibits reserve probabilities ranging from 0.09 to 0.57 – the seasonal diurnal pattern is unchanged. The NPS-100c-24 ranges from 0.11 to 0.64, slightly more than 10% higher. In general, the increase in capacity had a larger effect than the change in wind turbine design – at least 500 kW of capacity is required to provide a reliable wind reserve. However, this effect is asymptotic – a very large wind capacity would be required to meet reserve requirements during the summer wind resource



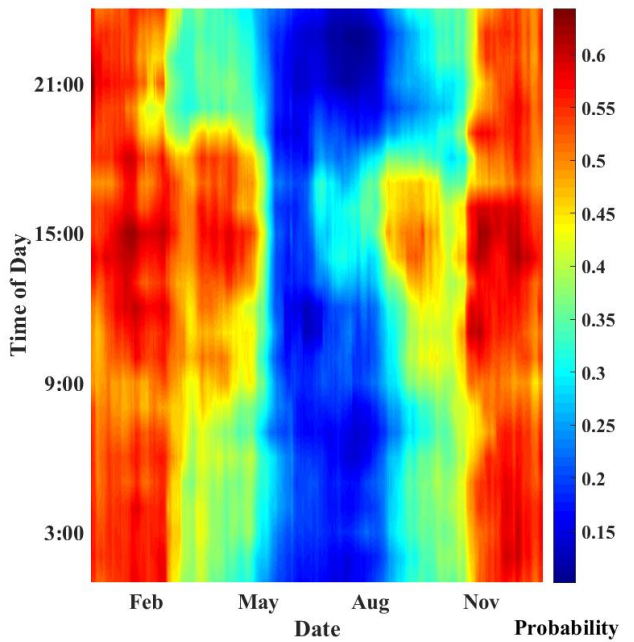
(a)



(b)



(c)



(d)

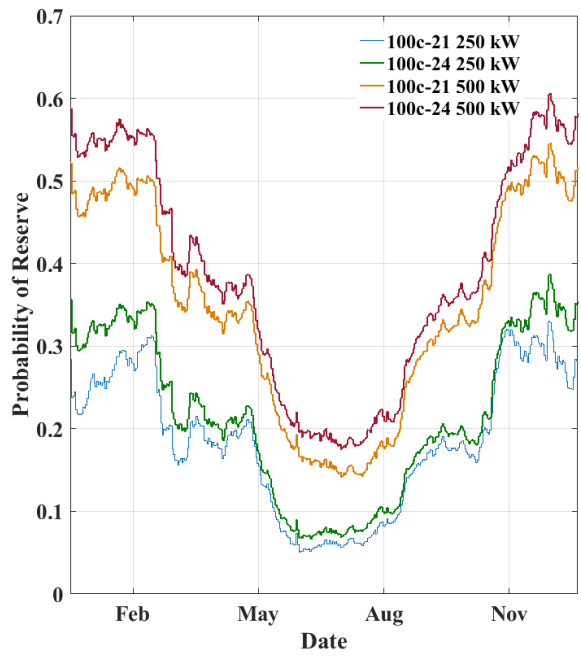
Figure 5.17: Probability of Meeting Secondary Reserve Requirements in Cartwright using (a) 250 kW of NPS-100c-21, (b) 250 kW of NPS-100c-24, (c) 500 kW of NPS-100c-21 and (d) 500 kW of NPS-100c-24

minimum or during shrimp plant operation, as the wind turbines are quiescent the majority

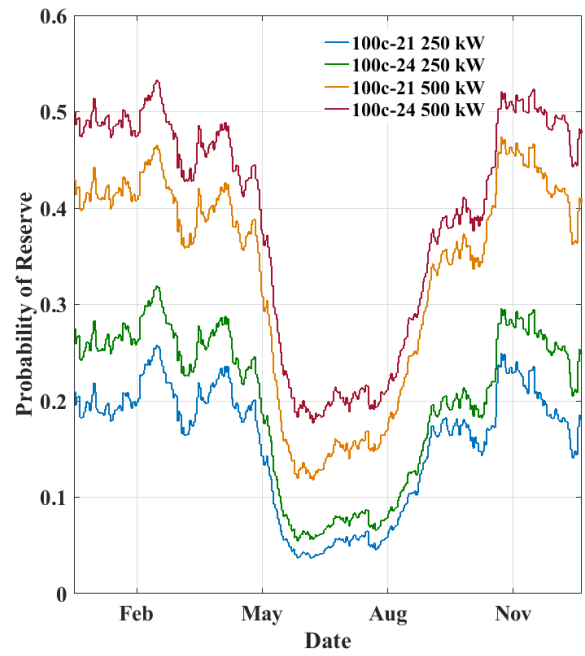
of the time, negating any rated capacity increase.

A further comparison of the effects of the seasonal and diurnal cycles as well as the wind turbine design and capacity on the wind reserve probability is presented by superimposing the resulting reserve probabilities which correspond to a single diurnal phase. Figure 5.18(a-d) presents the reserve probabilities of each wind turbine design/capacity combination, sampled at 3:00 a.m., 9:00 a.m., 3:00 p.m. and 9:00 p.m. respectively. In all cases, the seasonal cycle has the largest influence on the reserve probabilities. At 3:00 a.m. and 9:00 p.m. (Figures 5.18(a) and 5.18(d)) the reserve probabilities are generally sinusoidal, varying from a February peak of 0.3, 0.35, 0.5 and 0.6 for the listed design/capacity combinations. At 9:00 p.m. the peak reserve probability occurs slightly earlier, during January. However, the probability profiles are similar. The minimum reserve probability occurs during June and July, with values of 0.05, 0.08, 0.15 and 0.18 observed, respectively. These values are slightly lower at 9:00 p.m. due to the slightly higher demand profile at this time. The reserve probability profiles follow a different pattern at 9:00 a.m. and 3:00 p.m. (Figures 5.18(b) and 5.18(c)), with the shrimp plant operation visibly affecting the probability of wind reserve. At 9:00 a.m., the reserve probabilities peak at 0.25, 0.3, 0.45 and 0.52 during February and November. The minimum reserve probabilities occur in June, with a precipitous drop occurring as the shrimp plant operation begins. During this period, the reserve probabilities are as low as 0.04, 0.06, 0.12 and 0.18, respectively. Similar behavior is observed at 3:00 p.m., however the probability values are slightly higher during the winter peak (0.35, 0.4, 0.58 and 0.62, respectively) due to the diurnal wind resource maximum described previously. The effect of the shrimp

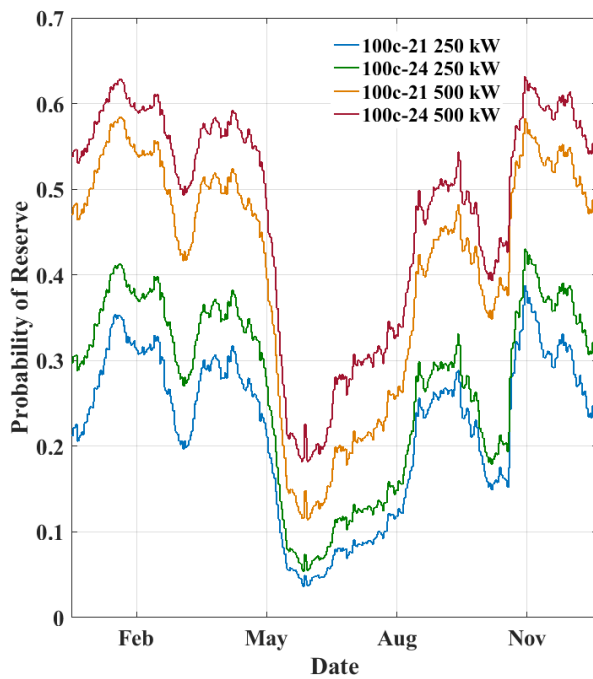
plant is at its most pronounced, with the reserve probabilities dropping to less than one third of their peak values during the June reserve minimum. At this time, the reserve probabilities are as low as 0.04, 0.06, 0.12 and 0.19 – nearly identical to the values at 9:00 a.m. Overall, Figures 5.17 and 5.18 have presented the significant annual and diurnal cycles in wind reserve probability where wind generation is used to meet Cartwright’s secondary demand. The effect of wind installation capacity and wind turbine design is observed. Note that during the peak periods, a doubling in capacity does not double the reserve probability – the behavior is asymptotic due to the fairly high probability of quiescent operation. Installation of more than 500 kW of wind generation would require additional microgrid reinforcement due to the high renewable penetration – these investigations are a subject of future research.



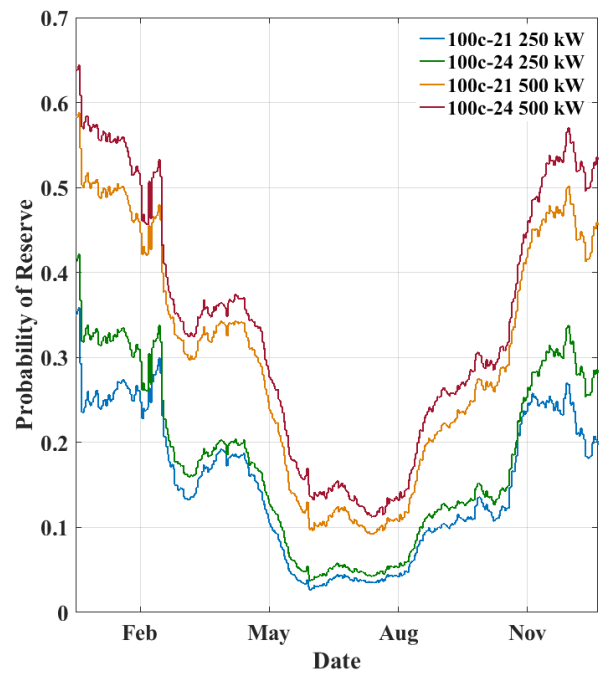
(a)



(b)



(c)



(d)

Figure 5.18: Probability of Meeting Secondary Reserve Requirements in Cartwright at (a) 3:00 a.m., (b) 9:00 a.m., (c) 3:00 p.m. and (d) 9:00 p.m.

Wind generation in an islanded microgrid can also be applied as a demand-response unit, performing “peak shaving” during periods of high demand. As opposed to the entire secondary demand, peaking units are only activated during peak-load periods, transferring the remaining generation requirement to the base-load or other secondary generators. In a microgrid, the conventional grid forming generators are fast enough to supply the secondary demand. However, they may have difficulty meeting the peak demand profile – operating at maximum capacity can reduce efficiency and reliability, especially when these conditions occur frequently. Wind generation is fast ramping and is capable of acting as a spinning reserve for peak-load demand response. Static reserves such as battery storage can also be used to meet transient load changes, however the limited capacity of such systems makes spinning reserves necessary in all but the smallest microgrids. Probabilistic evaluation of peak-load wind reserves is accomplished by repeating the use of probabilistic power balance algorithm from Chapter 3, with the secondary demand profile replaced by the peak demand profile developed in the previous section. The result is a probabilistic power balance model expressing the probability of any particular power surplus or shortfall value when wind generation is applied as a peak-shaving unit. Figure 5.19 (a-d) presents the probabilistic power balance model assuming 250 kW of rated capacity using the NPS-100c-21 wind turbine, evaluated at 3:00 a.m., 9:00 a.m., 3:00 p.m. and 9:00 p.m. respectively. In general, the observed behavior is similar to that from the secondary generation application. The wind turbine is quiescent the majority of the time, resulting in a reflected demand profile comprising the majority of probability mass. This trend is evident throughout the day. However, at 9:00 a.m. and 3:00 p.m. (Figures 5.19(b) and 5.19(c)), the diurnal wind resource cycle results in a more active wind turbine, placing more

probability mass at positive values. The effect of the seasonal wind resource cycle is evident, as well as the shrimp plant operation. There is also a slight seasonal trend in the peak demand profile, as described in the previous section.

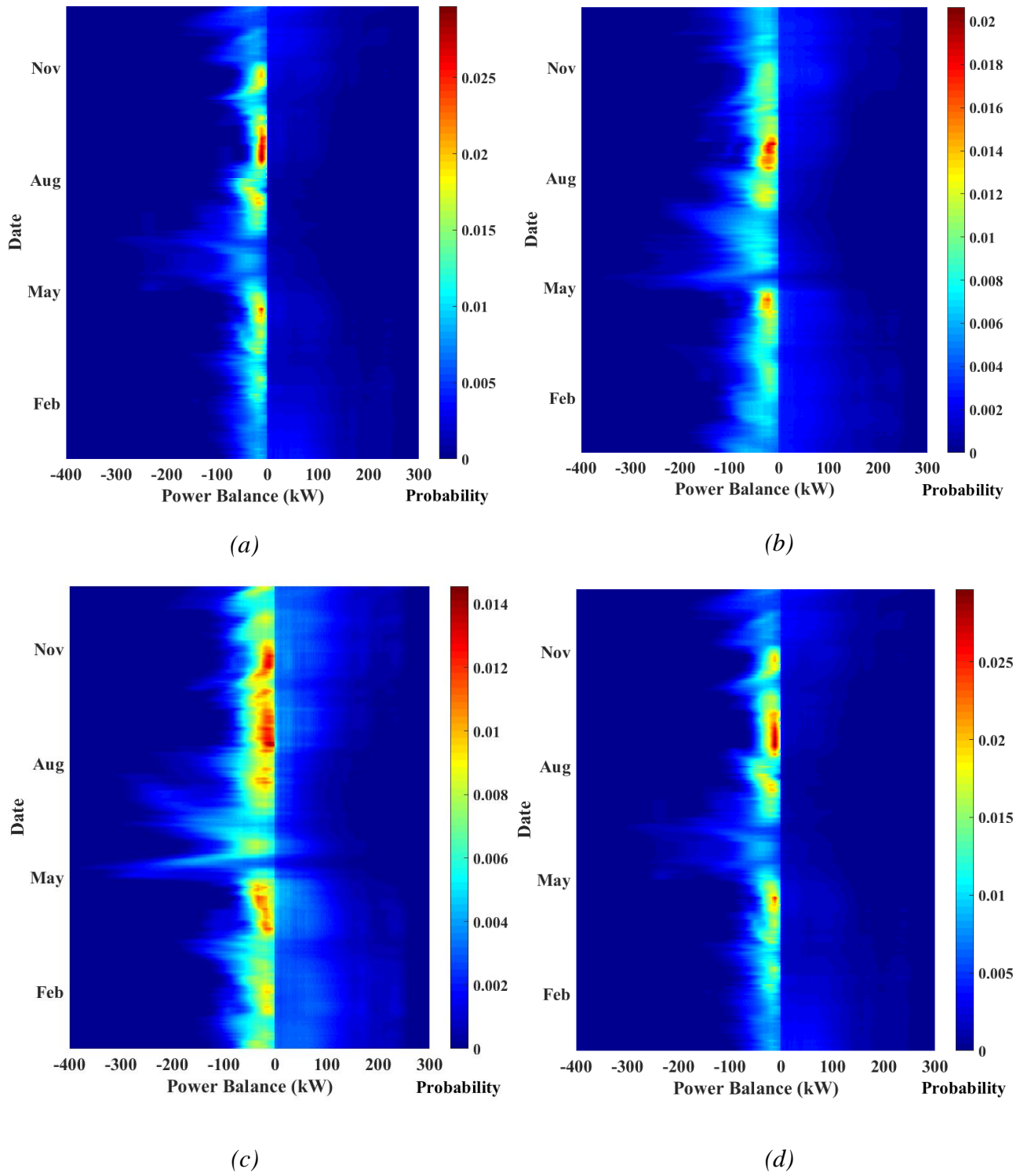
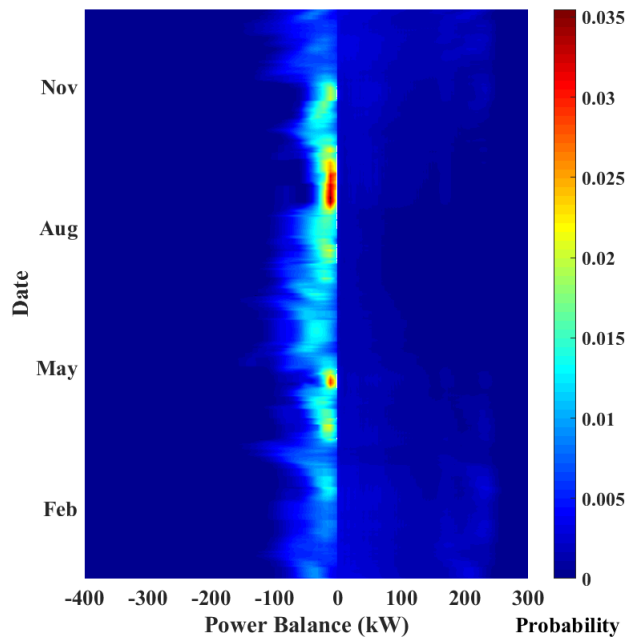
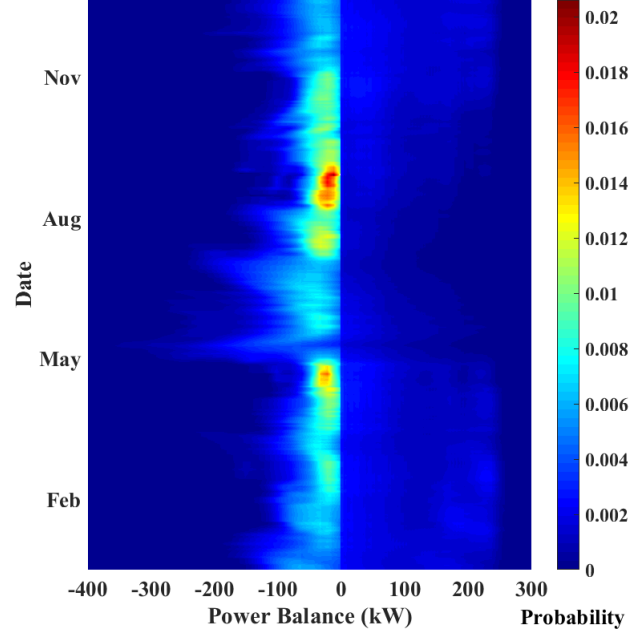


Figure 5.19: Peak Demand Power Balance Distribution in Cartwright at (a) 3:00 a.m., (b) 9:00 a.m., (c) 3:00 p.m. and (d) 9:00 p.m. using 250 kW of generation from the NPS-100c-21

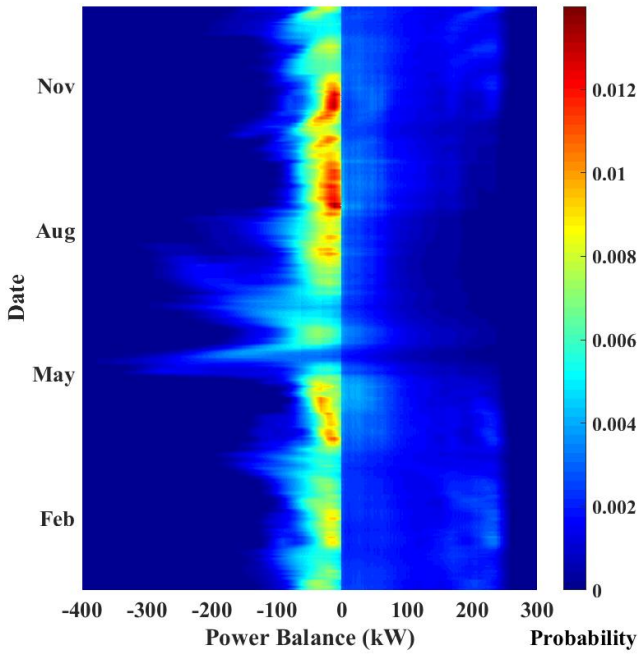
Figure 5.20(a-d) displays the probabilistic power balance when using the NPS-100c-24 wind turbine, again scaled to 250 kW of rated capacity. Overall, the NPS-100c-24 exhibits a slightly better power balance in comparison to the NPS-100c-21 – the higher likelihood of rated-output operation is clearly visible, especially at 3:00 p.m. (Figure 5.20c) during the diurnal wind resource maximum. There is consistently a greater proportion of probability mass at positive values, indicating the availability of wind reserves to meet the peak-shaving energy requirements. During the remainder of the day, the performance of the NPS-100c-24 is similar to the NPS-100c-21. While there is a slightly higher probability of rated power operation due to the wind turbine’s optimization for lower wind speeds, the base likelihood of this operating condition is low enough to damp the effect on the resultant wind reserve. The effects of the seasonal and diurnal cycles are similar across both turbine designs, and have been discussed in the previous sections. Regardless of the wind turbine design, the large proportion of negative value probability mass indicates that there is not enough wind capacity or a reliable enough wind resource to produce a consistently available wind reserve – the probability of wind turbine quiescence is too high.



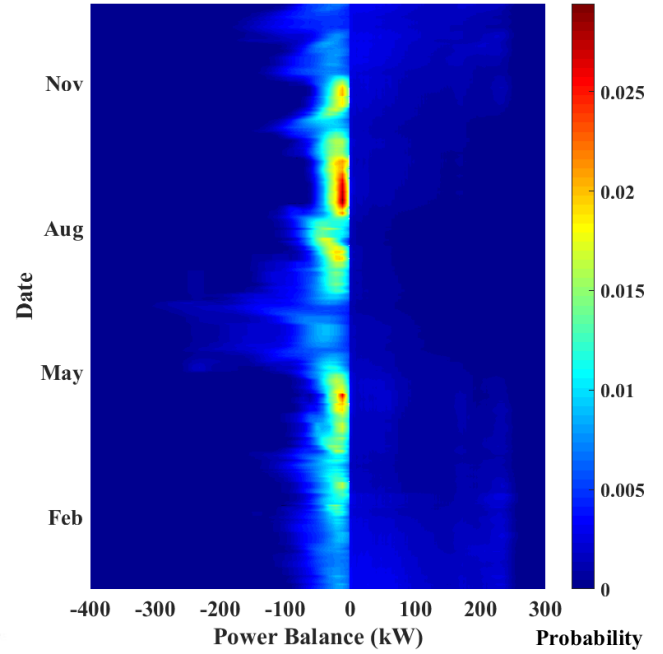
(a)



(b)



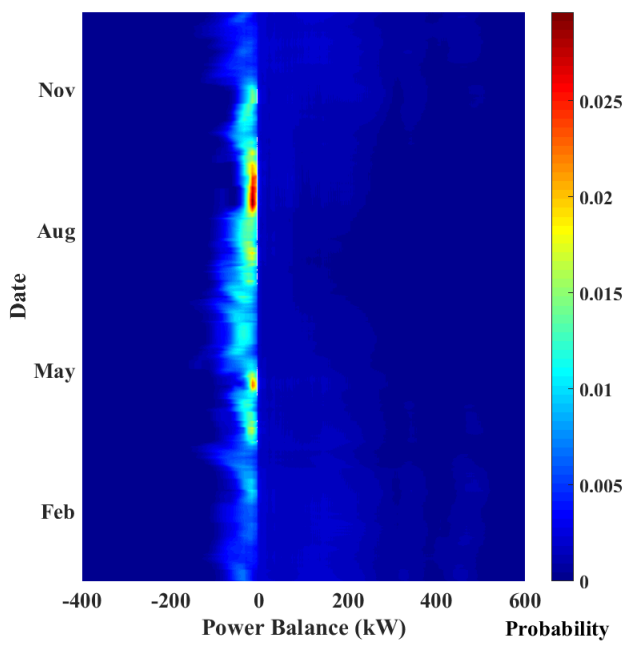
(c)



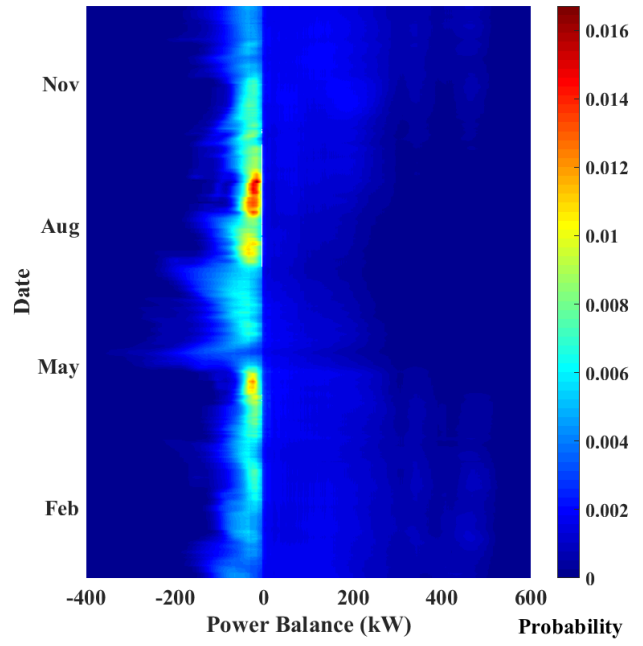
(d)

Figure 5.20: Peak Demand Power Balance Distribution in Cartwright at (a) 3:00 a.m., (b) 9:00 a.m., (c) 3:00 p.m. and (d) 9:00 p.m. using 250 kW of generation from the NPS-100c-24

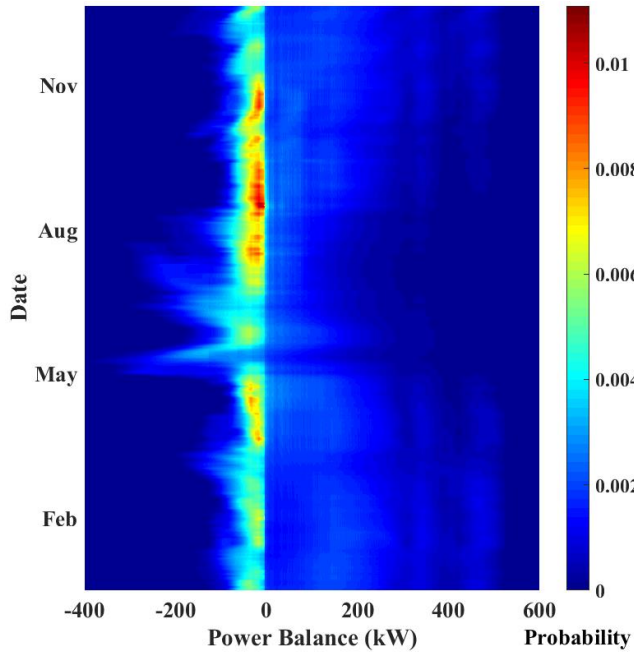
Figure 5.21 (a-d) displays the probabilistic power balance (when used for peak shaving) of a NPS-100c-21 wind turbine with 500 kW of rated capacity. As in previous figures, data is presented for 3:00 a.m., 9:00 a.m., 3:00 p.m. and 9:00 p.m. to display the diurnal-cycle effects on the resulting power balance probability distribution. The increased wind capacity results in a greater proportion of positive power balance values, however the majority of the probability mass is still a negative reflection of the load profile at 3:00 a.m. and 9:00 p.m. (Figures 5.21(a) and 5.21(d)). At 9:00 a.m. and 3:00 p.m. (Figures 5.21(b) and 5.21(c)) the increased capacity results in a higher probability of wind reserve, with the probability mass shifting to positive values. However, this is only valid during the winter wind resource maximum – during shrimp plant operation as well as the summer wind minimum, the wind reserve is not expected to be available the majority of the time due to wind turbine quiescence. It must be noted that the increased wind generation capacity produces a significant number of large positive values, indicating rated operation with little demand. During these situations, the produced energy would be wasted unless the base load units can be efficiently throttled down to take advantage of the wind energy. In addition, microgrid stability and power quality concerns appear with a high proportion of injected wind energy, further complicating the effects of increased wind generation capacity.



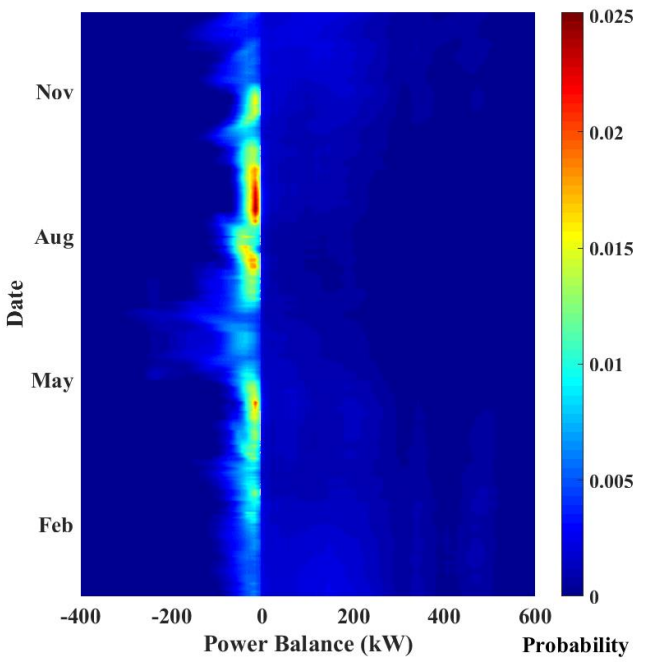
(a)



(b)



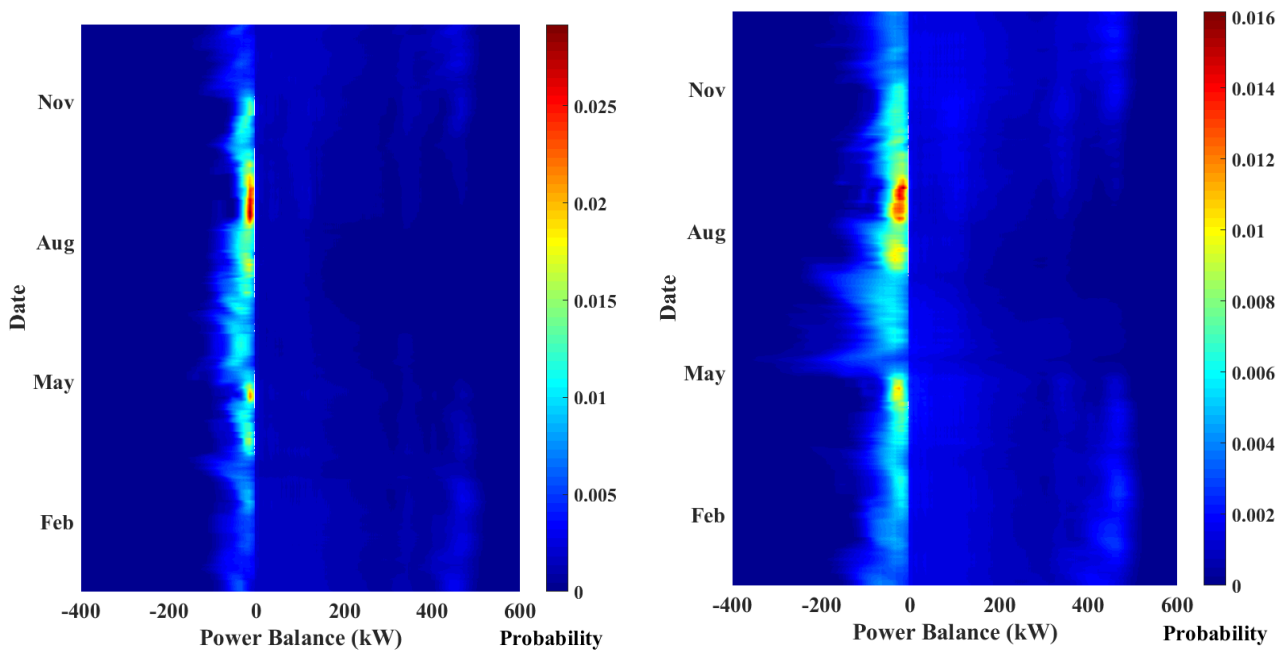
(c)



(d)

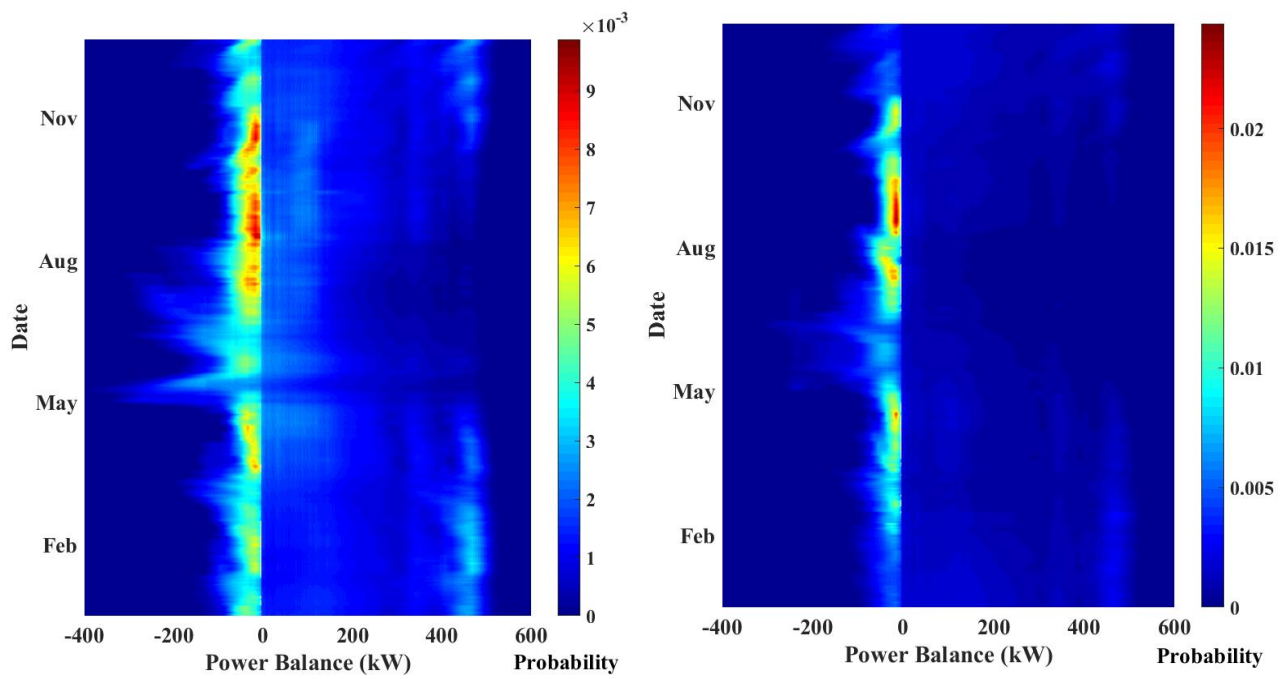
Figure 5.21: Peak Demand Power Balance Distribution in Cartwright at (a) 3:00 a.m., (b) 9:00 a.m., (c) 3:00 p.m. and (d) 9:00 p.m. using 500 kW of generation from the NPS-100c-21

Figure 5.22(a-d) displays the probabilistic power balance (for peak-shaving) when using the NPS-100c-24 wind turbine, this time scaled to 500 kW of capacity. As in the previous capacity application, the NPS-100c-24 exhibits a better power balance in comparison to the NPS-100c-21 due to the higher likelihood of rated-output operation. This effect is most prominent at 3:00 p.m. (Figure 5.22(c)) during the diurnal wind resource maximum. However, at all times of day a consistently greater proportion of probability mass is seen to exist at positive values. Therefore, the NPS-100c-24 wind turbine has a higher likelihood of providing a wind reserve adequate for peak-shaving applications. The effects of the seasonal and diurnal cycles are similar across both turbine designs, albeit the change in rated-operation probability is greater using the NPS-100c-24 due to the lower optimal wind speed being more common in general. Based on these probabilistic models (Figures 5.19-5.22) the NPS-100c-24 is more suitable for peak-shaving applications due to the higher probability of providing a wind reserve. However, a more quantitative analysis will also be conducted by determining the true probability of wind reserve availability for each design and capacity, as well as selecting samples of these resulting distribution models for direct comparison.



(a)

(b)

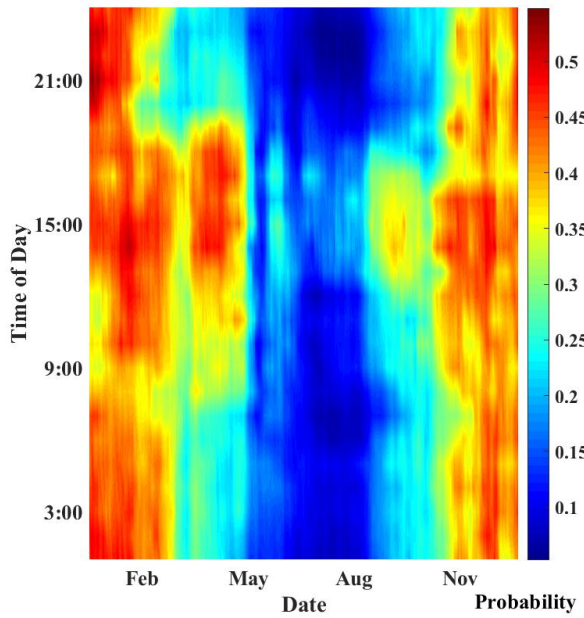


(c)

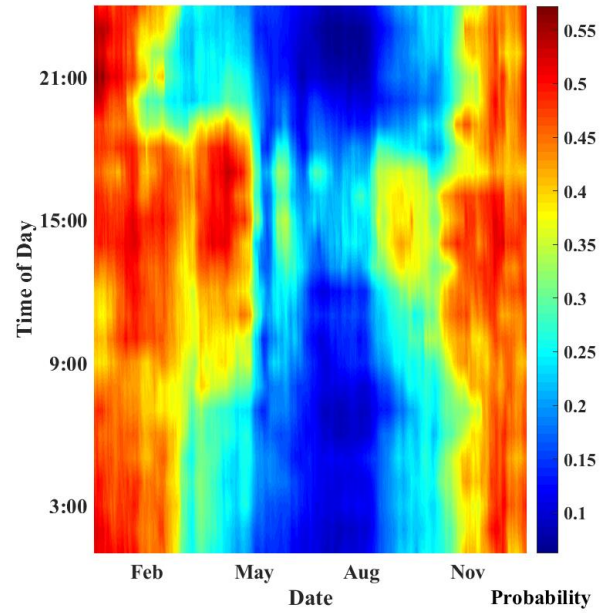
(d)

Figure 5.22: Peak Demand Power Balance Distribution in Cartwright at (a) 3:00 a.m., (b) 9:00 a.m., (c) 3:00 p.m. and (d) 9:00 p.m. using 500 kW of generation from the NPS-100c-24

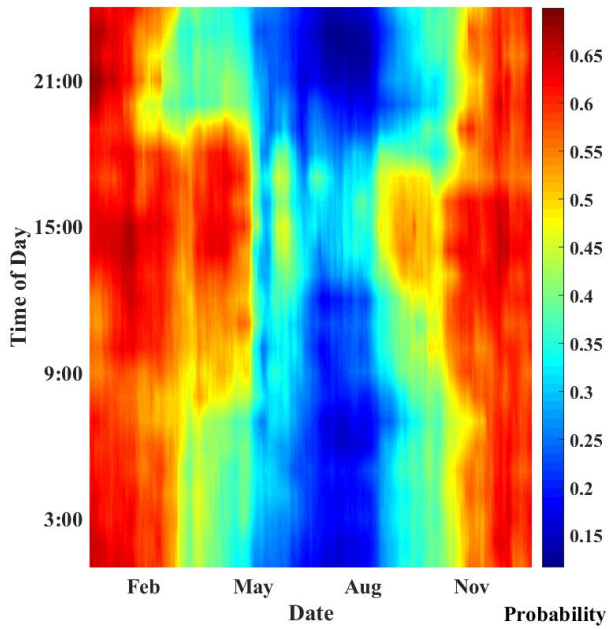
Figure 5.23 (a-d) presents the probability of sufficient wind energy being available to meet the peak-shaving reserve requirements, calculated assuming 250 kW (Figures 5.23(a) and 5.23(b)) and 500 kW (Figures 5.23(c) and 5.23(d)) of capacity in the form of the NPS-100c-21 (Figures 5.23(a) and 5.23(c)) or NPS-100c-24 (Figures 5.23(b) and 5.23(d)) wind turbine designs. The overall pattern of the reserve probabilities matches that observed when secondary generation was considered for application – the decrease in energy requirement for peak shaving and the slightly different demand distributions is not large enough to overcome the general effects of the seasonal and diurnally-driven wind resource variability. Regardless of the wind turbine design or capacity, the minimum reserve probability occurs during August at about 10:00 p.m., and is under 20%. When 250 kW of capacity is considered, both wind turbines exhibit a reserve probability under 10%. In each case, the NPS-100c-24 produces a slightly higher reserve probability, indicating stronger performance in Cartwright’s wind regime during these seasonal and diurnal periods. For each design combination, the maximum reserve probability occurs during January at 9:00pm. The pattern from previous investigations holds – the NPS-100c-24 has a higher reserve probability, although the difference between wind turbine designs is overshadowed by the effect of the doubling in generation capacity. In all cases, the maximum reserve probability is beneath 75%, being as low as 55% when using 250 kW of NPS-100c-21 based generation. Overall, the effect of the seasonal and diurnal cycles on wind reserve availability is clearly evident, with the effects of shrimp plant operation as well as wind resource variability clearly evident. Subsets of these plots will be examined to more quantitatively define the wind reserve probabilities.



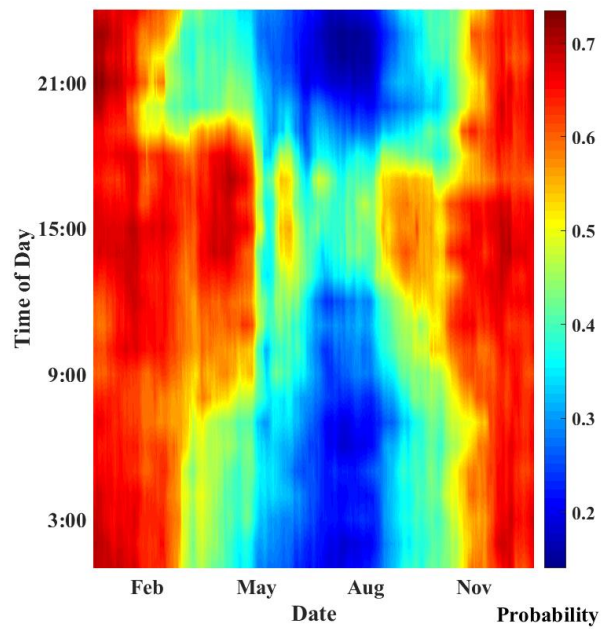
(a)



(b)



(c)



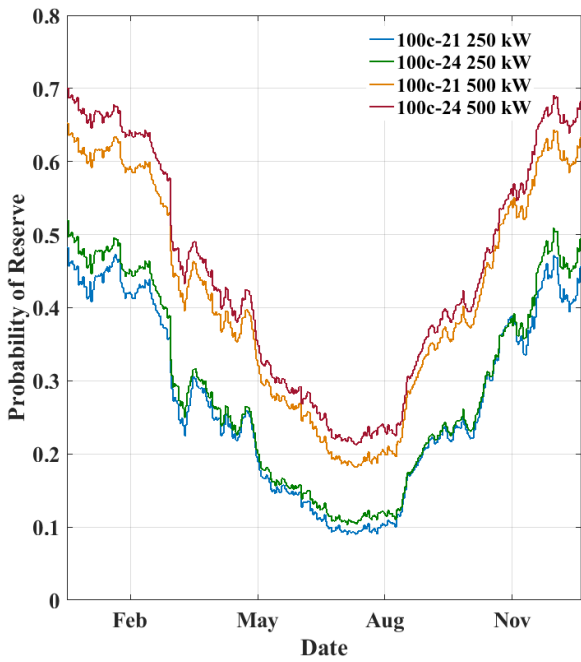
(d)

Figure 5.23: Probability of Meeting Peak Shaving Reserve Requirements in Cartwright at (a) 250 kW of NPS-100c-21, (b) 250 kW of NPS-100c-24, (c) 500 kW of NPS-100c-21 and (d) 500 kW of NPS-100c-24

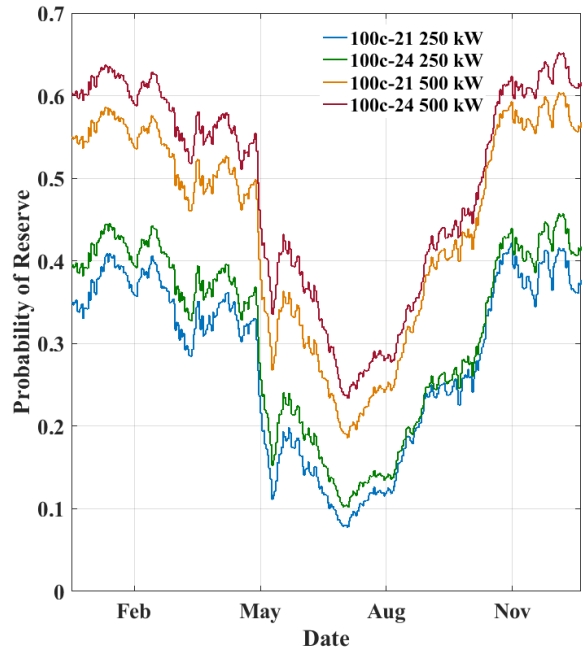
Similar to the previous application, a quantitative comparison of the effects of the seasonal and diurnal cycles as well as the wind turbine design and capacity on the wind reserve probability is presented by superimposing reserve probability samples as to display the seasonal cycle at a single diurnal phase. Figure 5.24(a-d) presents the peak-shaving reserve probabilities of each wind turbine design/capacity combination, sampled at 3:00 a.m., 9:00 a.m., 3:00 p.m. and 9:00 p.m. respectively. In all cases, the seasonal cycle has the largest influence on the reserve probabilities. At 3:00 a.m. and 9:00 p.m. (Figures 5.24(a) and 5.24(d)) the peak-shaving reserve probabilities remain sinusoidal. At 3:00 a.m., the reserve probabilities vary from a January peak of 0.48, 0.5, 0.65 and 0.7 for the listed design/capacity combinations to July minimum values of 0.09, 0.11, 0.18 and 0.22, respectively. These probabilities are somewhat higher than that of the secondary generation reserve application, due to the lower energy requirements for peak-shaving. At 9:00 p.m. the peak reserve probability profiles are similar, with the minimum reserve probability occurring during July, with values of 0.07, 0.08, 0.15 and 0.18 observed, respectively. The maximum reserve probabilities again occur during January, with respective values of 0.55, 0.57, 0.7 and 0.72. The range of values is slightly higher at 9:00 p.m. due to Cartwright's demand and wind regime.

The peak-shaving reserve probability profiles follow a significantly different pattern at 9:00 a.m. and 3:00 p.m. (Figures 5.24(b) and 5.24(c)) - the shrimp plant operation affects the probability of wind reserve by shifting the peak-demand distribution. At 9:00 a.m., the reserve probabilities peak at 0.4, 0.44, 0.58 and 0.62 during February and December. The minimum reserve probabilities again are observed in June, with a precipitous drop

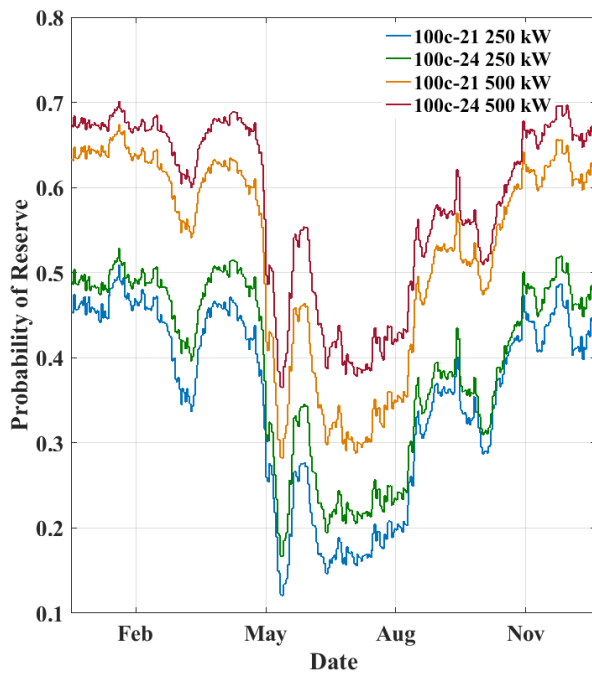
occurring as the shrimp plant operation begins. With the shrimp plant active, the reserve probabilities are as low as 0.11, 0.15, 0.28 and 0.33, respectively. These values recover by about 10% after the initial drop, then again decline to a July minimum of 0.08, 0.1, 0.19 and 0.25. This pattern is also evident at 3:00 p.m. The peak-shaving reserve probability values are slightly higher during the winter peak (0.5, 0.52, 0.66 and 0.7, respectively) due to the diurnal wind resource maximum increasing the wind turbine output. The effect of the shrimp plant very large - reserve probabilities drop to less than one third of their peak values. In this case, the absolute reserve minimum occurs during shrimp plant operation, with values declining to 0.12, 0.17, 0.28 and 0.37. In all cases, the NPS-100c-24 maintains reserve probability values between 0.05 and 0.10 higher than the NPS-100c-21, with the difference being carried through the capacity increase. As this profile holds for both peak-shaving (Figures 5.23 and 5.24) and secondary generation (Figures 5.17 and 5.18) applications, the NPS-100c-24 is verified to be a superior wind turbine design given Cartwright's wind resource. Further increases in capacity can be expected to increase the reserve probability. However, it is impractical to have wind generation larger than the grid-forming units, as wind turbine pickup will then have significant detrimental effects on microgrid stability. Further investigation in this area is a subject of future research, with a final goal of optimizing wind capacity from the viewpoint of wind reserve applications.



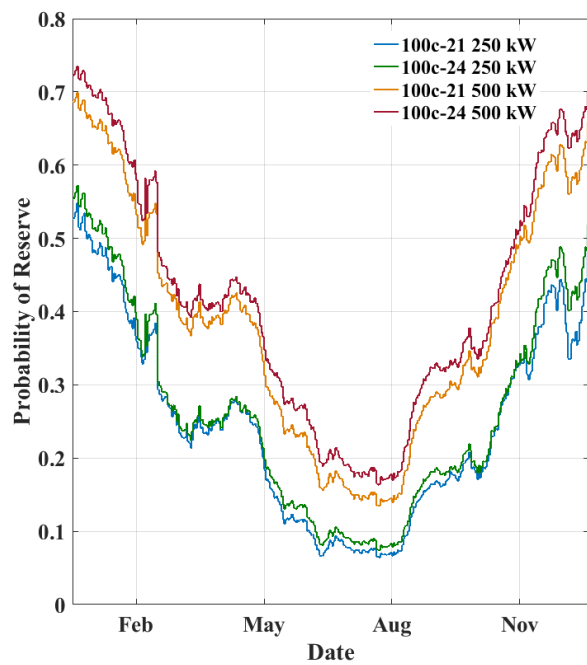
(a)



(b)



(c)



(d)

Figure 5.24: Probability of Meeting Peak Shaving Reserve Requirements in Cartwright at (a) 3:00 a.m., (b) 9:00 a.m., (c) 3:00 p.m. and (d) 9:00 p.m.

5.4: Conclusions

In this Chapter, field data from Cartwright has been used to probabilistically assess the ability of wind generation to act as an active reserve for microgrid regulation. The time-variant, multivariate probabilistic modeling algorithms proposed in previous Chapters successfully compensate for nonstationary behavior in the environmental and electrical demand datasets, providing an accurate assessment of the wind regime and demand profile, and its probabilistic transient variability. The results produced within the case study and provide valuable planning information with respect to wind generation's ability to meet demand response, secondary generation and frequency regulation in an islanded microgrid, with the seasonal, diurnal and generation-based variability in the probabilistic wind reserve being identified and quantified. The probabilistic microgrid power balance was developed for multiple wind installation topologies, including two wind turbine types and two generation capacities. The NPS-100c-24 wind turbine was shown to produce a superior wind reserve distribution compared to the NPS-100c-21, demonstrating the capacity of the proposed algorithm to compare the performance of different wind turbine designs. In addition, the effect of doubling generation capacity was fully defined probabilistically, allowing optimization to occur with respect to generation capacity in future cost-function based analysis.

Chapter 6: Cartwright – A Case Study: PLEXIM Implementation

6.1: Introduction

This Chapter continues the case study into implementing wind generation at Cartwright. Analysis in the previous Chapter has indicated that sufficient probabilistic wind reserves exist to justify further investigation – a reasonable amount (250-500 kW) of wind capacity can provide up to 70% of the reserve requirements for peak shaving and secondary demand response. The application of these wind reserves requires grid interconnection technology capable of interfacing wind generation with an islanded microgrid. To validate this wind interconnection topology (presented in Chapter 4) as well as the reserve applications investigated in Chapter 5, PLEXIM simulations are conducted which implement demand response, frequency regulation and voltage regulation of an islanded microgrid matching the general topology of Cartwright’s system. Essentially, a simulation framework in PLEXIM allows the study of wind reserve performance from a grid stability and control perspective. Topics of investigation include diesel generator control, grid synchronization of a power inverter, grid-supporting using wind reserves and the control of a PMSG wind turbine using an AC/DC/AC bidirectional back-to-back converter.

6.2: Implementation of Demand Response in a Microgrid

The implementation of demand response is tested by producing a variable demand profile within the islanded microgrid. Figure 6.1 presents the electrical demand used to validate the wind reserve topology. After a short grid-forming interval (neglected from future figures), a steady demand of 650 kW and 500 kVar is created, representing a base demand. After 3 seconds, a 200 kW and 150 kVar step signal is introduced, simulating an increase to peak demand values due to either the energization of a disconnected distribution feeder or the inrush period of a large rotating machine. Half of this load is then removed after 4 additional seconds, representing a decrease from peak demand after a large industrial or commercial load reaches steady state, or distribution transformers leave their inrush period. The microgrid is designed to operate at a 0.80 power factor, explaining the reactive power values and representing the design condition of the grid-forming diesel generator. The demand profile is suited for investigating demand response and frequency regulation, producing situations where both positive and negative frequency deviations are expected as well as intervals of insufficient demand due to the limited diesel generator response speed. In addition, the reactive power variability will introduce microgrid voltage changes which will verify the performance of droop and exciter control algorithms.

The demand profile in Figure 6.1 is used to run a dynamic simulation of the microgrid. The diesel generators form the grid upon initial start-up. The active and reactive power

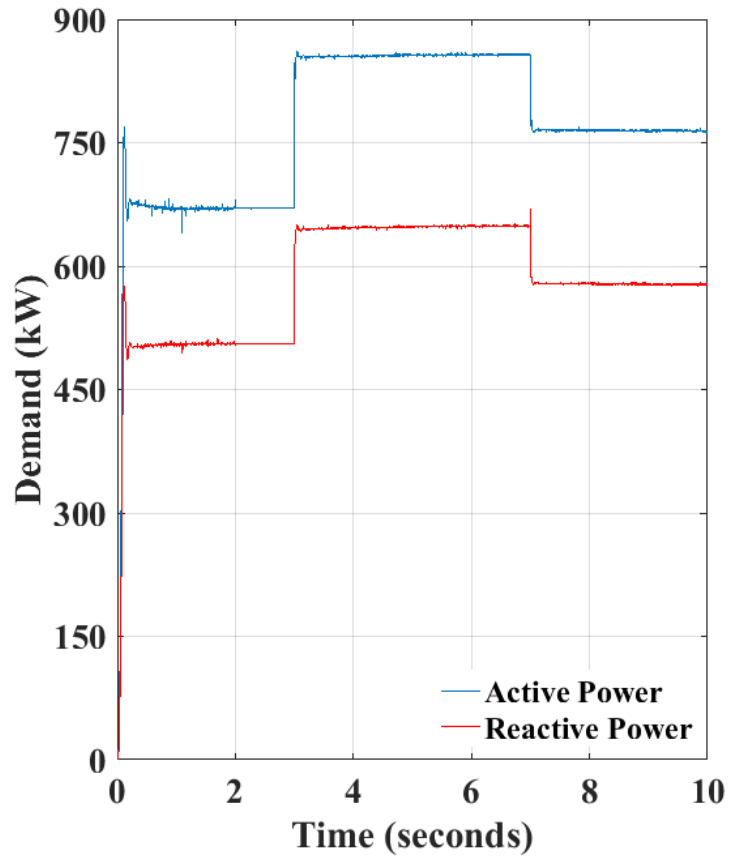


Figure 6.1: Microgrid Demand Profile

output of the diesel generators is regulated by the grid forming controller, in this case governor and excitation control. Figure 6.2 displays the active and reactive power output during the dynamic simulation, including both the generator terminal outputs and the power reaching the grid, accounting for line and unit transformer losses. The generator is initially in steady state, with the inverter connection at 2 seconds not significantly affecting the output. The demand increase at 3 seconds produces a transient drop in generator speed, increasing the power angle and therefore increasing the active power delivered to the microgrid. The initial spike in output power is quickly damped due to both the effects of the inverter droop regulation and the generator governor and exciter, which act to reach a steady state. This occurs quickly, with the slight change in output during the peak demand

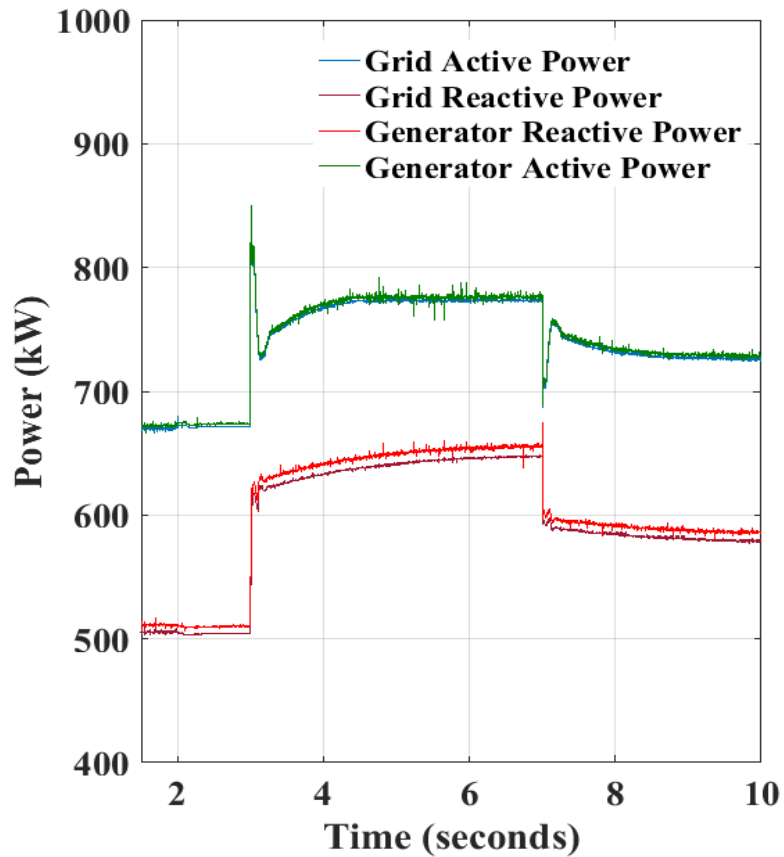


Figure 6.2: Synchronous Generator Power Output

interval resulting from the slower governor action as well as changes in the inverter droop output. Similar behavior is observed when the load is reduced at 7 seconds, with the initial departure being damped by fast droop and excitation controllers followed by a slower governor-based return to steady-state operations. Overall, the grid-forming generator remains stable during load variance, with no extreme active or reactive power departures and therefore reasonable stress on the generator assembly.

Figure 6.3 presents the microgrid frequency during the dynamic simulation. Initially, the microgrid is just converging to steady state after generator start-up. The inverter interconnection at 2 seconds causes a brief frequency rise due to the slight mismatch in

synchronization which is unavoidable when the grids are not directly connected. However, the DSOGI-FLL-based inverter synchronization and control algorithms quickly damp this frequency departure, resulting in steady-state operation resuming within 0.25 seconds. At 3 seconds, the load increase produces a frequency droop to just above 59.8 Hz. At this time, the inverter droop regulator begins to act to restore the grid frequency. The microgrid recovers to 59.9 Hz after less than 0.5 seconds, and reaches 59.95 Hz after 1 second. At this point, the frequency restoration controllers (the integral droop regulator and the generator governor) slowly restore the grid frequency back to 60 Hz over the next 3 seconds. Similar behavior (with opposite sign and roughly half the amplitude) occurs when the load is reduced – the microgrid frequency increases to 60.1 Hz before being near-exponentially reduced with a “half-life” of roughly 0.5 seconds. Essentially, the generator and inverter-based frequency regulation maintains microgrid stability and frequency even during significant step-changes in active and reactive demand, indicating the viability of using inverter-interconnected wind reserves for frequency regulation in an islanded microgrid.

Figure 6.4 displays the active power contributed by the inverter for the purpose of frequency regulation. Both the actual inverter output and the droop reference are included for comparison. The droop reference briefly becomes negative upon initial interconnection, however supervisory action prevents the actual inverter output from becoming negative. Instead, the slight frequency increase is handled by the synchronous governor. The inverter quickly settles into steady stage, essentially floating on the grid. Once the load increases at

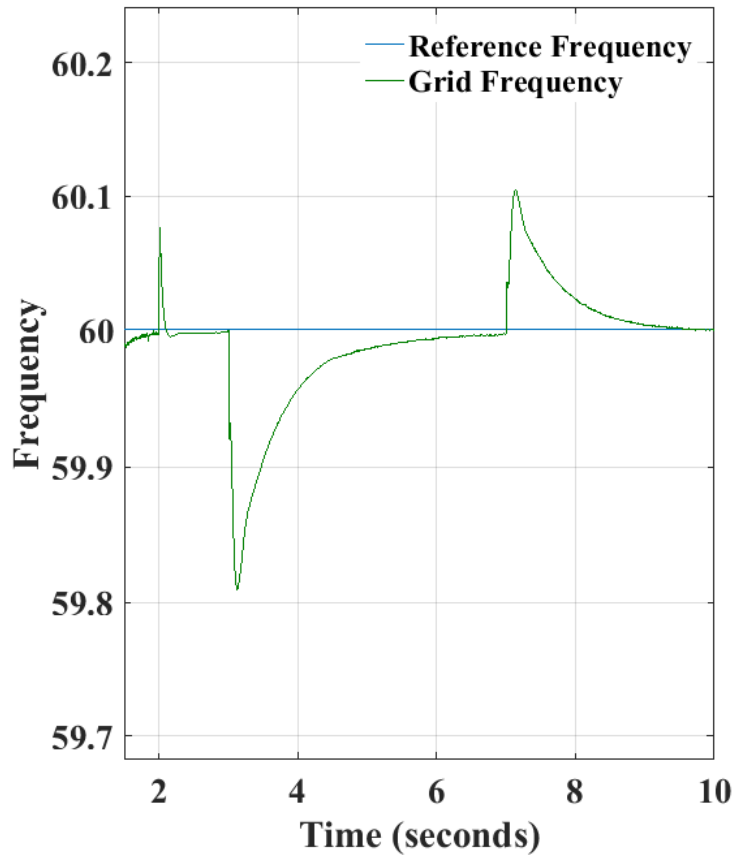


Figure 6.3: Grid Frequency

3 seconds, the droop controller instructs the inverter to inject 125 kW of real power into the microgrid. The injected power then varies according to the grid frequency, initially decreasing as the frequency is restored. However, after 1 second the injected power stabilizes at 75 kW due to the integral action of the droop regulator – the inverter is now supplying some of the demand by default, reducing the load uptake of the grid-forming generator. This is demand-response behavior, superimposed on the initial droop response. Similar behavior occurs after 7 seconds, when the load is reduced. The injected power decreases due to the droop action, serving to reduce the grid frequency from the peak observed in Figure 6.3(a). As the frequency is restored, the combination of proportional and integral droop regulation creates a new steady-state where the inverter is supplying 40

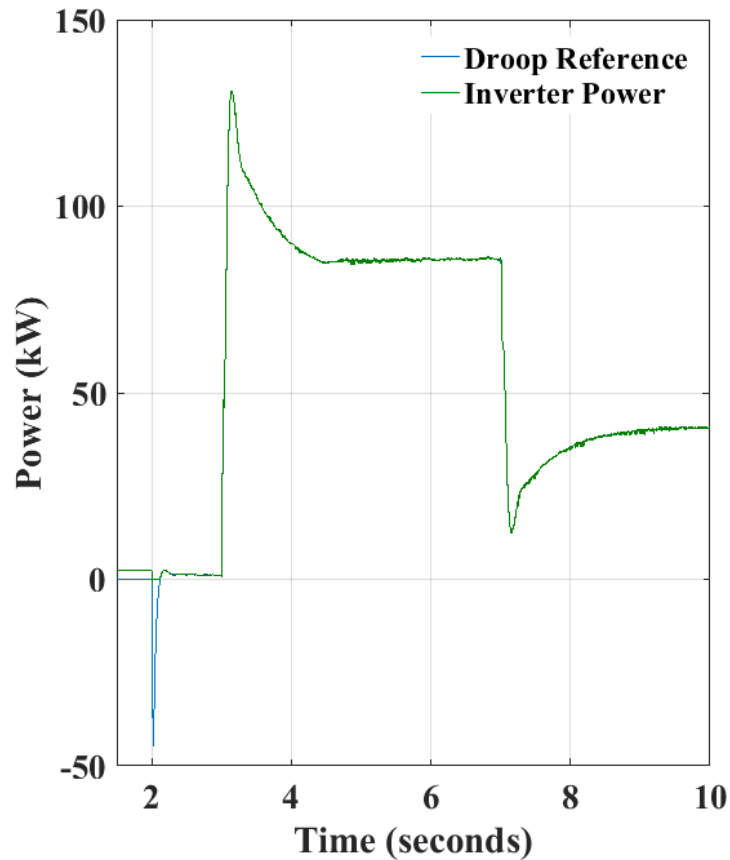


Figure 6.4 –Active Power from Droop Regulator

kW of active power to the grid, with the remainder being provided by the diesel generator. The magnitude of the droop excursions varies according to the droop gains – these must be set based on the inverter rating and microgrid operation standard required by the system operator. During the transient inverter output variations, the DC-link capacitor supplied the necessary energy until the PMSG stator current controller compensates for the increased demand. In these simulations, the system dynamics are accelerated to reduce the computational demand – insufficient memory and processing power is available for longer-period simulations.

Figure 6.5 displays the effect of the droop regulation on the microgrid frequency by comparing the observed performance with that of the generator governor alone (under identical grid conditions). With just the synchronous governor, the load change at 3 seconds causes a frequency drop to 59.6 Hz – essentially double the droop magnitude relative to the 60 Hz reference frequency. The droop regulator stops the frequency decline twice as fast after the load change, and quickly restores the grid frequency to within 0.1 Hz of the reference value. The smaller integral droop error does slightly increase the time to final frequency restoration – the governor control action is reduced while the inverter is limited in the amount of real power it can realistically inject. However, the microgrid frequency is within 0.1 Hz of the reference value during this period, essentially within the range of normal frequency variation. Similar behavior is evident when the load is decreased at 7 seconds – the magnitude of the microgrid frequency deviation is halved by the inverter action, at the cost of slight convergence delays. The large variations possible during

governor-only action are more likely to exceed the microgrid power quality standard with respect to frequency, justifying the use of droop-controlled inverters. The observed benefits of wind-reserve based frequency regulation using droop-controlled inverters are expected to be even greater when slower governors are present, either due to larger generators or isochronous generator groups regulated by slower supervisory control loops. Therefore, the application of wind reserves for frequency regulation is validated in the PLEXIM simulation environment.

The wind-reserve inverters also have the capacity to regulate microgrid voltage through injection of reactive power. This is accomplished through proportional Q/V droop

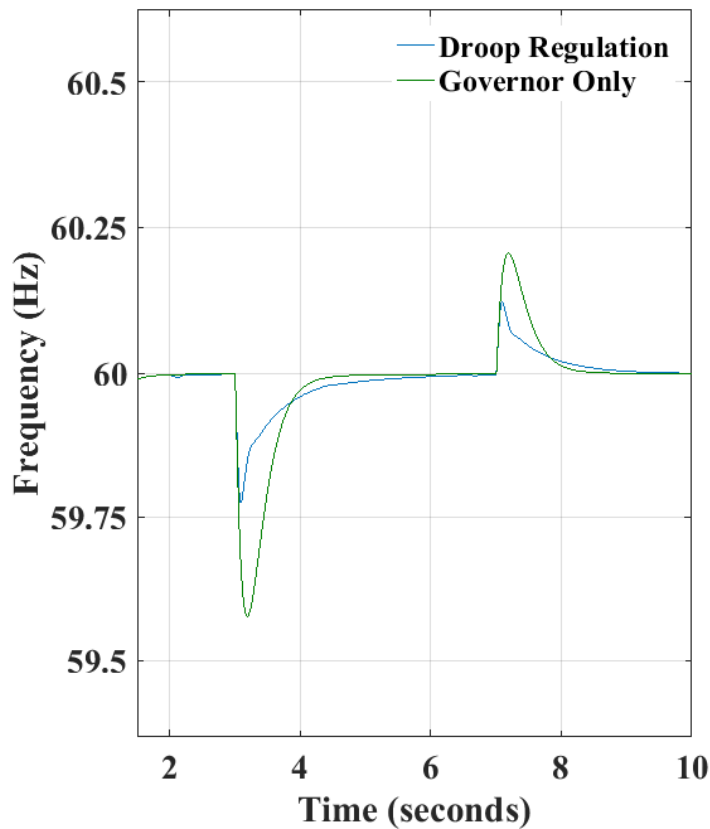


Figure 6.5: Performance Comparison of Microgrid Frequency Regulation

regulation on the wind reserve interconnection inverter. Power inverters are easily capable of injecting reactive power to the grid – power factor limitations are generally well beyond what is needed for droop regulation assuming a properly-tuned droop controller. The injected reactive power acts to compensate for voltage sag which primarily occurs during the activation of inductive loads. Figure 6.6 displays the generator terminal voltage error, measured on the low-voltage side of the unit transformer. Initially, the voltage is converging to the reference value after the start-up interval of the microgrid. Note that in this case, a positive error implies a lower than expected microgrid voltage. After 2 seconds, the increase in reactive demand (caused by the switching on of a large load at a power factor of 0.8 lagging) causes a voltage sag of approximately 2 volts – slightly more than 0.5% per-unit. The combination of excitation and droop control acts to exponentially restore the microgrid voltage – apart from the initial overshoot, the grid voltage is restored with a time constant of approximately 1 second. Similar behavior occurs when the load is reduced at 7 seconds, except the reduction in reactive demand causes an increase in microgrid voltage which is then restored by control action.

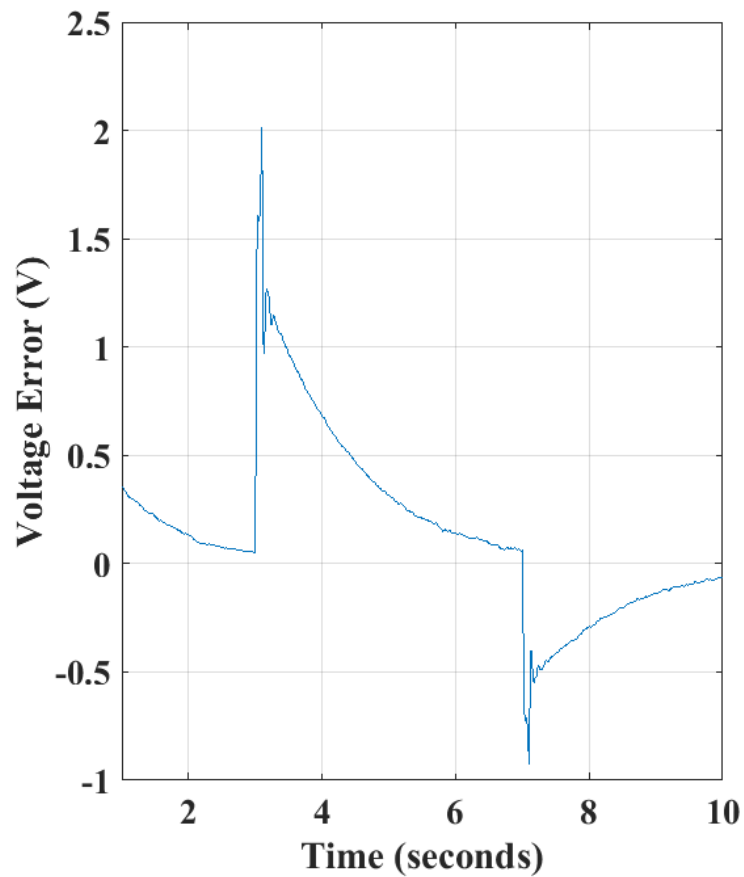


Figure 6.6: Microgrid Voltage Error

Figure 6.7 displays the reactive power injected by the power inverter, including both the actual power fed to the grid and the droop-control reference. Initially, both these values are zero, as the inverter is not connected. At 2 seconds, the inverter connects to the microgrid, and injects a small amount of reactive power due to the grid voltage being slightly under the reference value. At 3 seconds, the inductive load switches on, with the corresponding voltage sag resulting in the inverter injecting 40 kVar into the microgrid. The amount of injected power oscillates somewhat, following the slightly underdamped grid voltage in the face of the transient load change. However, within 0.5 seconds, the reactive power injection

converges to the exponential decay corresponding to the voltage restoration in Figure 6.4(a). Similar behavior is evident at 7 seconds, when a decrease in reactive demand causes a voltage rise which is then damped by the inverter consuming reactive power. In all cases, the actual injected reactive power very closely matches the droop reference. Some high-frequency oscillation is present due to the slight harmonic distortion inherent to any switch-mode inverter – the power filter does not perfectly remove these space harmonics. Any mismatch in inverter terminal frequency or angle would cause an offset and oscillation in the reactive power output which is not observed to any significant degree, indicating that the inverter is successfully synchronized to the microgrid even during these transient disturbances.

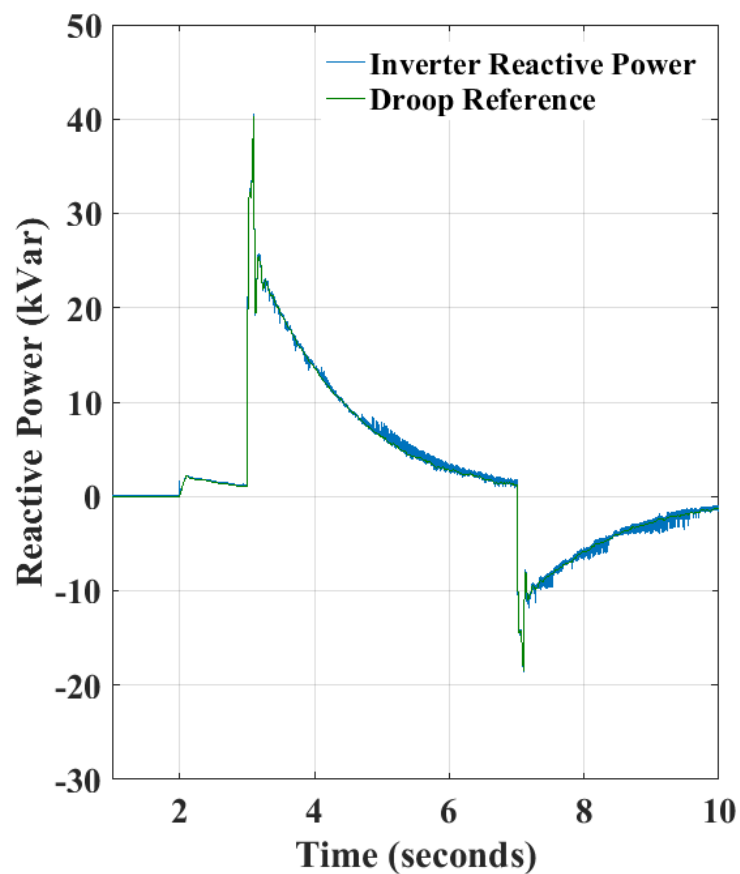


Figure 6.7: Reactive Power from Droop Regulator

The effect the inverter droop regulation has on the microgrid voltage is displayed in Figure 6.8. A comparison is made with the microgrid voltage observed during identical demand variations, except with the inverter disconnected and the synchronous exciter alone responsible for voltage regulation. The utility of the droop regulation is clearly visible. During exciter-only operation, the increase in reactive demand at 3 seconds results in a voltage sag of approximately 0.75% (per-unit). This sag then exponentially decays due to the exciter control action, with a decay determined by the electrical time constant of the synchronous generator. With droop regulation enabled, the sag magnitude is reduced by 50%, to approximately 0.5% per-unit. The subsequent decay is slightly slower (due to less integral action in the exciter), however, the microgrid voltage is within 0.1% per-unit before the exciter-only controller catches up. The reduced exciter action therefore does not affect microgrid voltage regulation to a significant degree, and exhibits less strain on the generator assembly by reducing the possibility of over or under-excitation due to large control actions. Similar behavior is apparent at 7 seconds when the reactive demand is decreased – the inverter droop regulation reduces the magnitude of the voltage sag while only minimally affecting the longer-term convergence to the microgrid reference voltage. Overall, the performance of the droop-regulated inverter validates the voltage regulation application of wind reserves. Whenever sufficient wind power is available, the wind turbine

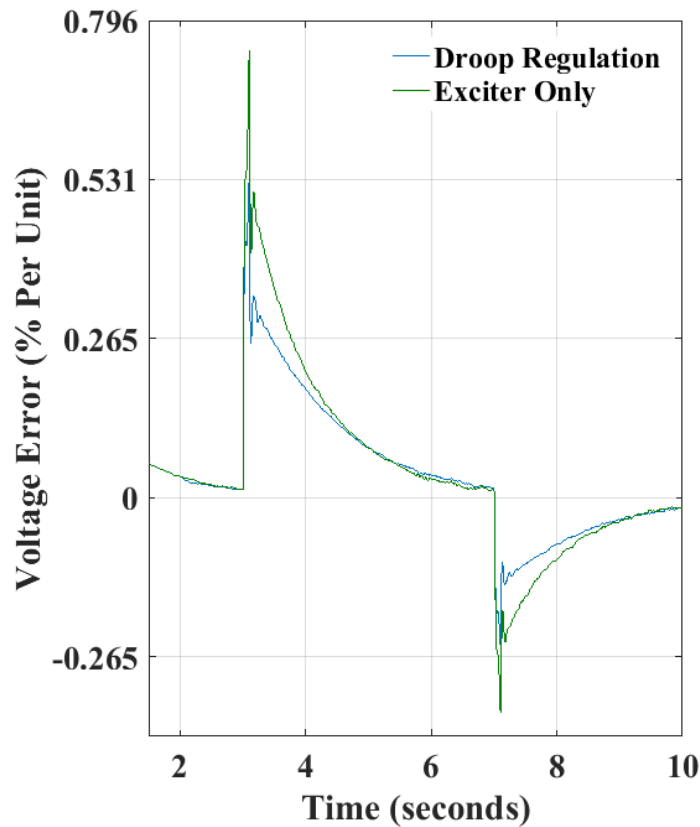


Figure 6.8: Performance Comparison of Microgrid Voltage Regulation

interconnection can provide both frequency and voltage regulation, improving the transient stability of the islanded microgrid during demand variation.

The successful operation of droop-controlled power inverters is reliant on fast, accurate synchronization with the surrounding microgrid. The synchronization system must be capable of maintaining synchronism during the frequency and voltage variability during load variations and other contingencies. Figure 6.9 displays the synchronization performance of the DSOGI-FLL based grid synchronizer implemented as the basis for the instantaneous power theory control of the voltage-source wind interconnection inverter. Initially, there is a slight disruption in grid synchronization when the inverter is first

connected to the microgrid. However, this is damped within 0.2 seconds, and never exceeds a magnitude of 0.1 Hz. At 3 seconds, the grid frequency decreases due to the activation of the additional demand. The grid frequency estimate from the DSOGI-FLL slightly lags this droop, slightly underestimating the frequency decrease initially then lagging the frequency restoration curve by approximately 0.1 seconds. However, the frequency estimation error remains at less than 0.05 Hz, falling to 0.01 Hz after the initial transient disturbance. Similar behavior is exhibited during the load decrease at 7 seconds – the DSOGI-FLL slightly lags and underestimates the droop, but overall maintains a high degree of accuracy in grid frequency estimation. The ability of the DSOGI-FLL to track these transient frequency changes ensures the accuracy of the inverter droop regulation, preventing a frequency or

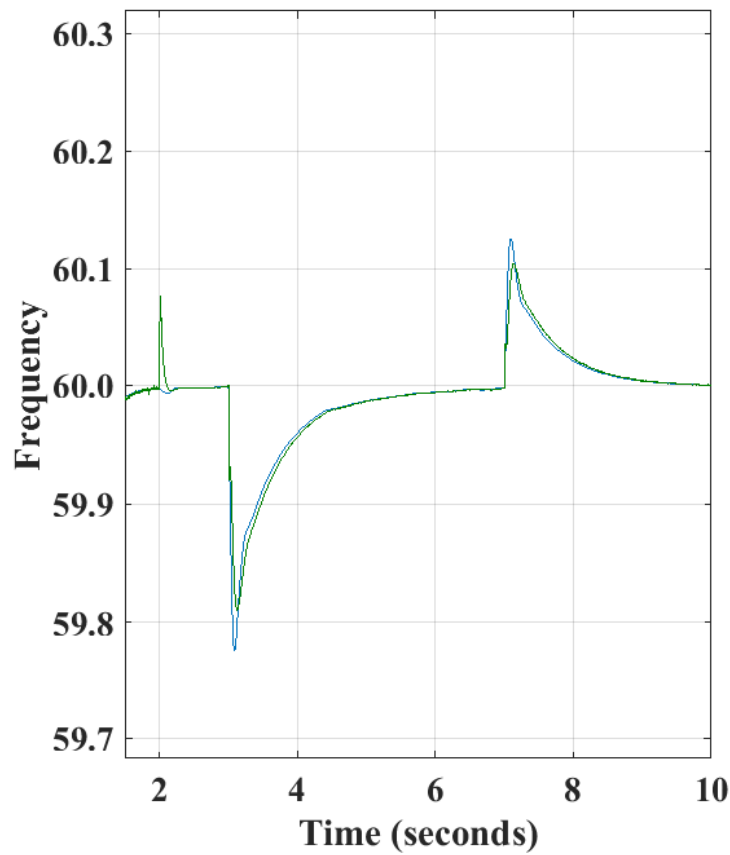


Figure 6.9: Grid Synchronization Performance

phase mismatch from occurring and therefore improving the stability and performance of the implemented frequency and voltage regulation.

The wind turbine interconnection inverter is configured using the VSI topology – the terminal voltage is adjusted to produce a desired output current while assuming a constant back-emf from the DC link. Therefore, during inverter operation the current flowing out of the terminals is the reference and control variable, determining the active and reactive power provided to (or received from) the islanded microgrid. Figure 6.10 displays the inverter current during the simulation interval, with a focus on the magnitude of the reference and measured currents as opposed to the waveforms. Prior to the grid interconnection at 2 seconds, a small current flows out of the inverter through the shunt branch of the LCL power filter as well as the primary side of the grid-interconnection transformer. During this period, the reference current is zero, and the inverter is instead programmed to match the grid voltage as closely as possible before interconnection and synchronization. Upon interconnection at 2 seconds, the inverter current decreases. The successful synchronization with the microgrid reduces the current flow out of the inverter, allowing it to essentially float on the grid. At 3 seconds, the current drastically increases to a maximum of 60 amperes (measured on the low voltage side of the transformer), providing the active and reactive power required by the droop controllers through references obtained using the instantaneous power theory. The inverter current stabilizes at 40 amps until the load decreases – then the reference current is also reduced by the droop regulators before stabilizing again at about 20 amps. Overall, the reference current very closely matches the

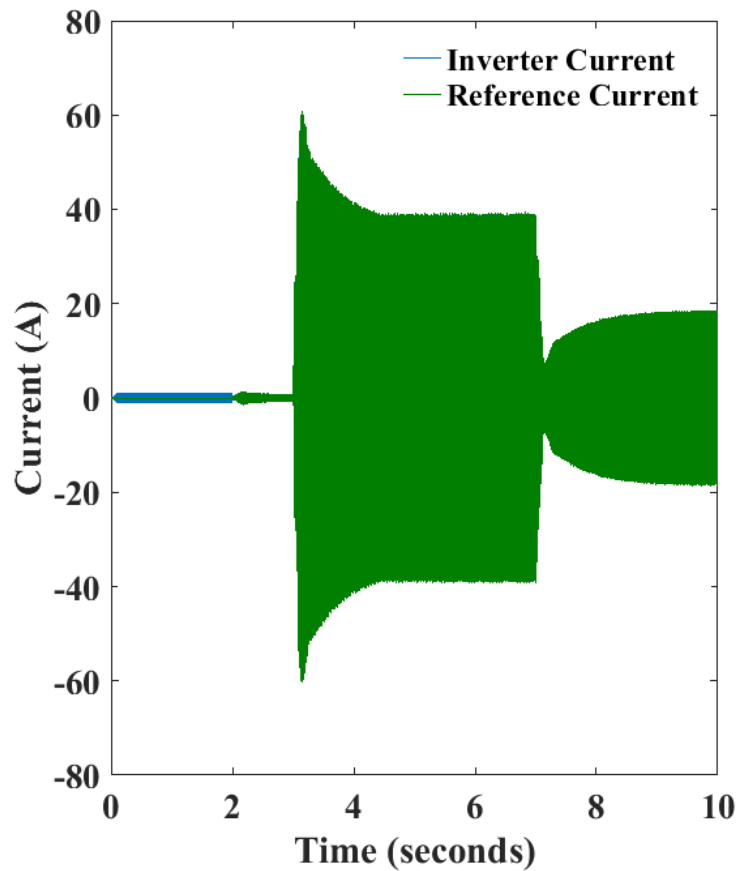
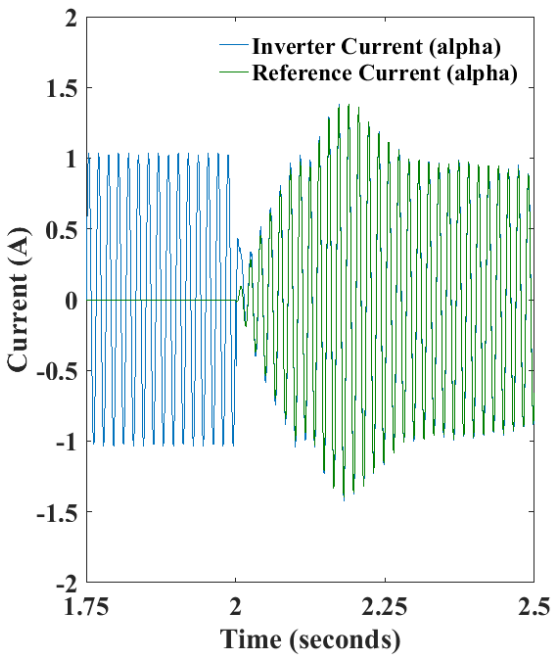


Figure 6.10: Inverter Terminal Current (Stationary Frame)

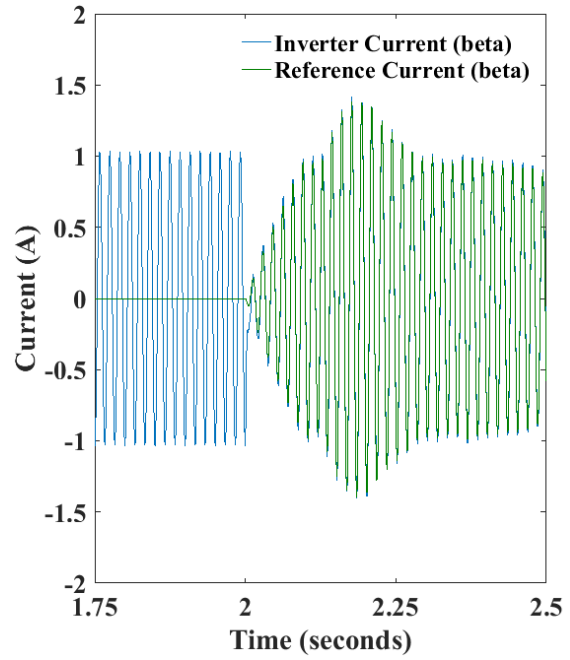
actual inverter current, with them being visually indistinguishable during steady-state operation.

Figure 6.11(a-d) displays the transient performance of the VSI current controller during the grid synchronization interval. The current is controlled in the stationary frame – Figures 6.11(a) and 6.11(c) display the alpha-axis current waveform while Figures 6.11(b) and 6.11(d) display the beta axis current. The general synchronization behavior is displayed in Figures 6.11(a) and 6.11(b), with 6.11(c) and 6.11(d) focusing on the immediate interconnection interval. Overall, the proportional-resonant current controller displays extremely fast and stable convergence to the reference current value. The PR controller is

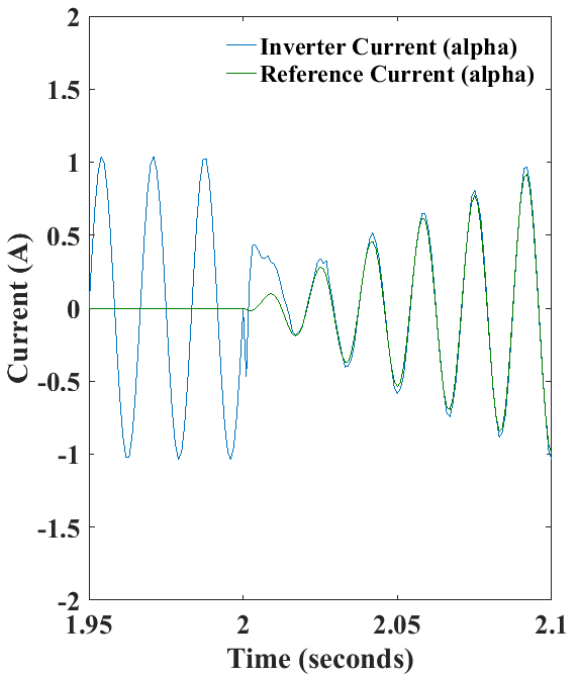
switched on at 2 seconds. Within 2 cycles of the current waveform, the inverter current in both axes has converged to within 5% of the reference value, with only a very slight error remaining due to the disturbances from the transformer and power filter losses. While some current distortion is evident during the immediate interconnection, this is quickly damped. Within 0.05 seconds of the initial synchronization, the inverter output current is essentially identical to the reference waveform, and maintains this behavior until a steady state is reached roughly 0.5 seconds after the initial interconnection. Based on the amplitude variability within the reference waveform, the resonant current controller is significantly faster than the instantaneous power theory based droop regulator, ensuring that the inverter controller dynamics can be safely neglected when evaluating the behavior of the droop controller during wind reserve applications.



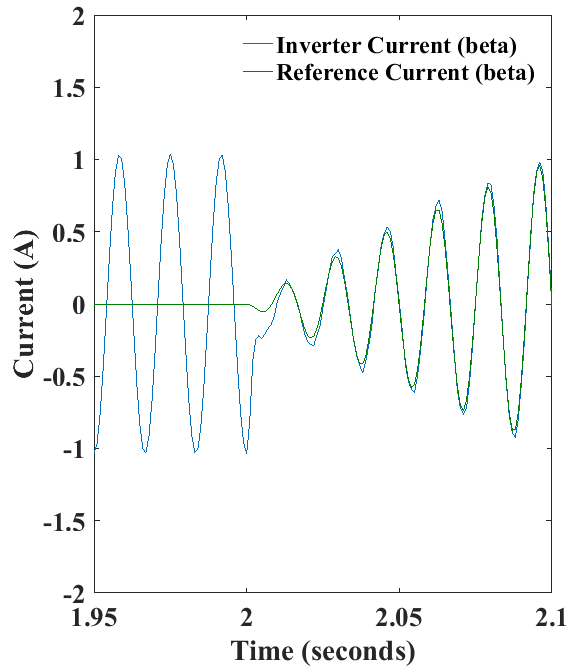
(a)



(b)



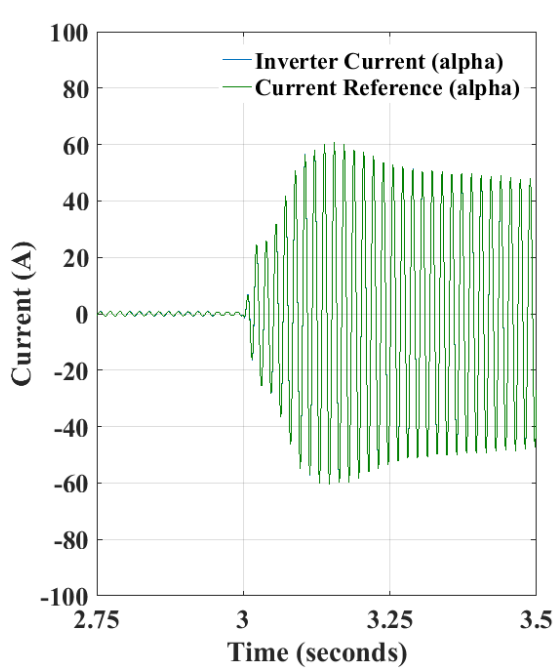
(c)



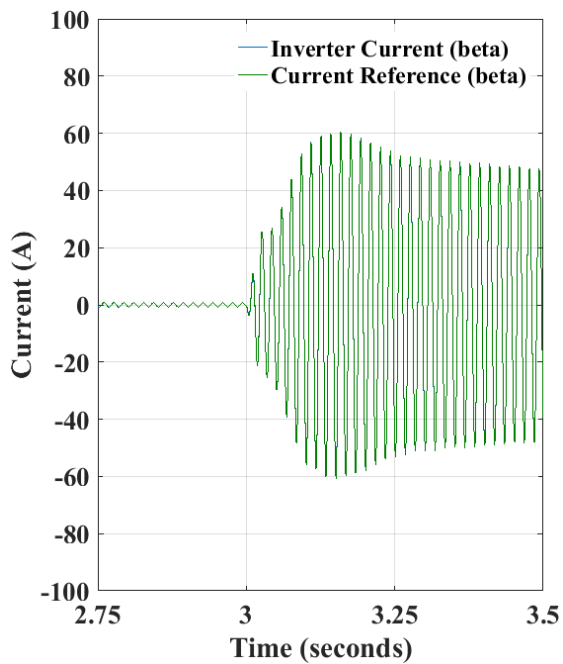
(d)

Figure 6.11: (a) Alpha-Axis Inverter Current (b) Beta Axis Inverter Current (c) Alpha Axis Transient Inverter Current and (d) Beta-Axis Transient Inverter Current during Grid Interconnection

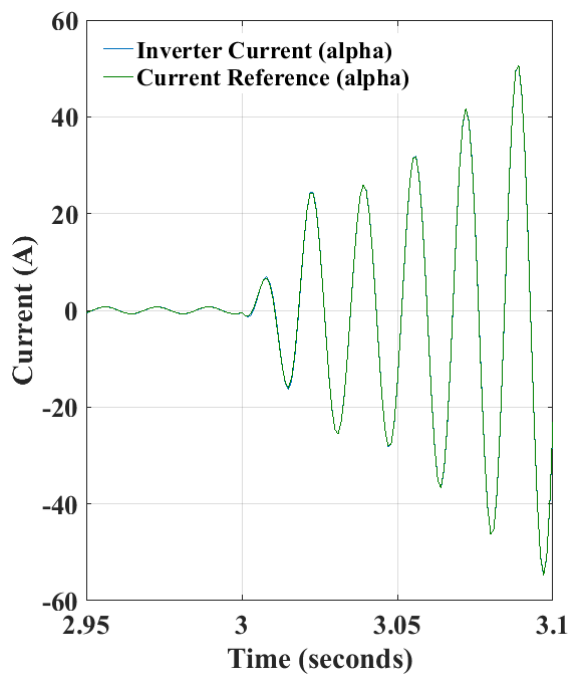
The stability and robustness of the current controller is displayed in Figure 6.12(a)-(d). The current reference drastically increases due to the load variability discussed previously, with the droop regulators requesting a significant amount of active and reactive power be injected into the microgrid in order to reduce the voltage sag and frequency reduction inherent to the activation of an inductive load. Figures 6.12(a) and 6.12(b) display an overview of the alpha and beta-axis current waveforms during the timescale of the droop regulator dynamics, with Figure 6.12(c) and 6.12(d) displaying the same waveforms focusing on the immediate transient reference change interval to display the effects of the faster inverter dynamics. In each case, no significant variation between the measured and reference currents are visible. The current reference magnitude varies from 1 to 15 amperes within a single cycle without disrupting the convergence of the resonant controller. This occurs despite the frequency change displacing the resonance frequency from that of the microgrid, reducing the effective integral gain of the current controllers. This further validates the robust behavior of the selected control topology. Similar behavior is displayed during the load decrease at 7 seconds - Figures 6.13(a)-(d) display the measured current and reference waveforms during the transient reference change and the steady-state convergence of the droop regulator. The PR controller maintains full reference tracking during the entire convergence interval. The strong performance of the inverter controller allows the integration of wind reserves with islanded microgrids, maintaining grid stability during reference changes and implementing any control action required from the supervisory level in order to implement demand response, droop regulation, or if desired grid-forming.



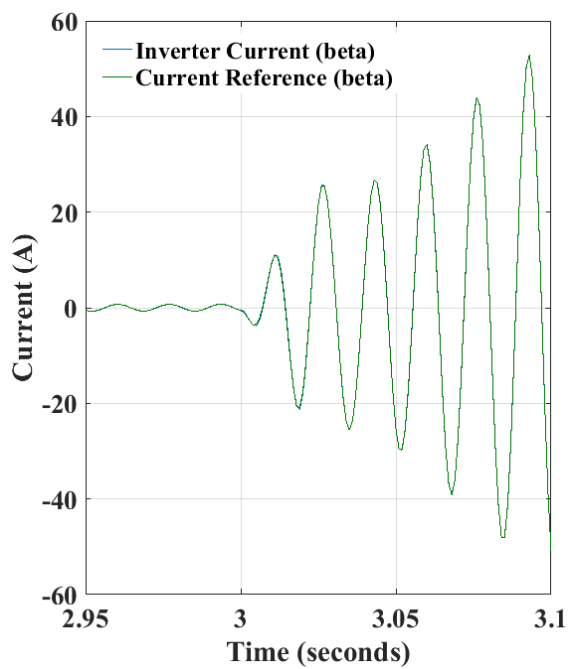
(a)



(b)

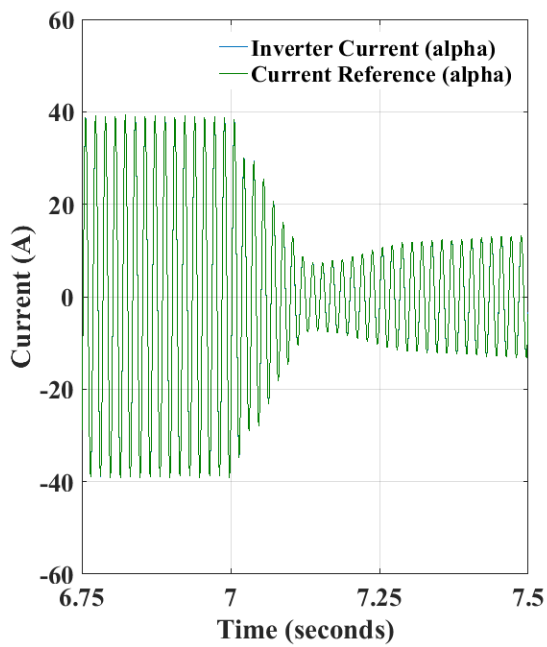


(c)

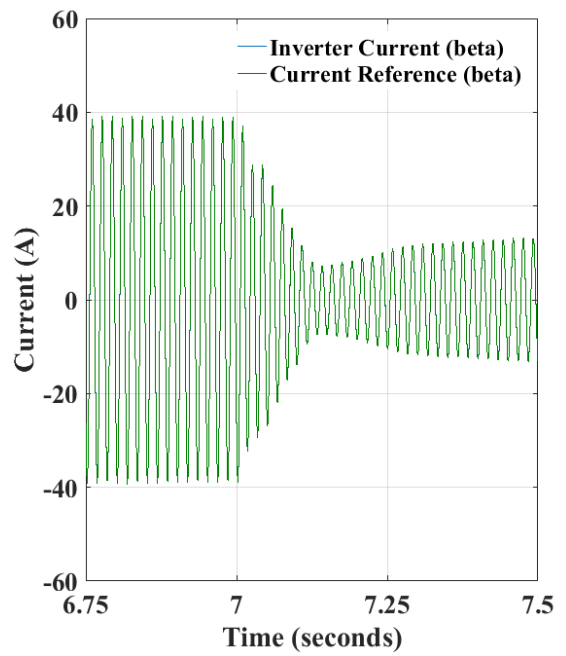


(d)

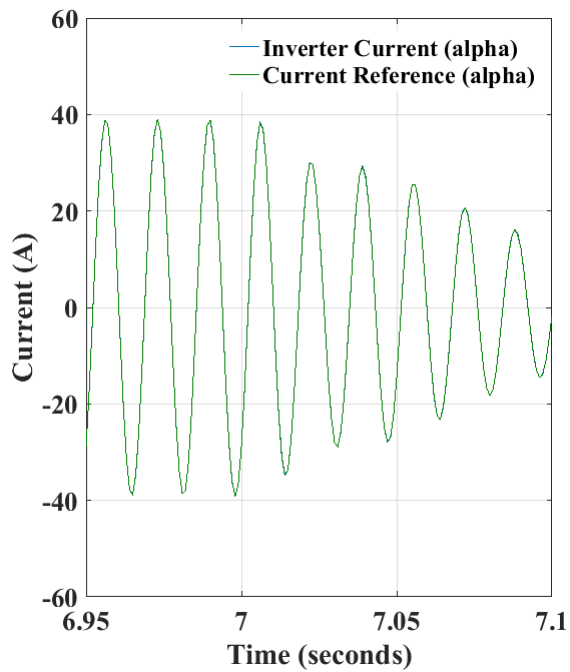
Figure 6.12: (a) Alpha-Axis Inverter Current (b) Beta Axis Inverter Current (c) Alpha Axis Transient Inverter Current and (d) Beta-Axis Transient Inverter Current during Demand Increase



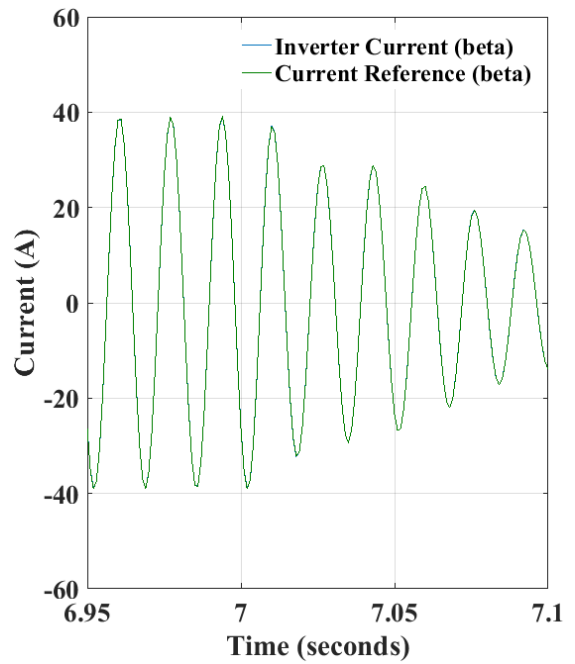
(a)



(b)



(c)



(d)

Figure 6.13: (a) Alpha-Axis Inverter Current (b) Beta Axis Inverter Current (c) Alpha Axis Transient Inverter Current and (d) Beta-Axis Transient Inverter Current during Demand Decrease

6.3: Wind Turbine Interconnection in PLEXIM

The wind turbine interconnection is computationally expensive to model in its entirety. Therefore, the interconnection topology has been split in order to isolate the microgrid performance simulations from the wind turbine and DC-Link dynamics. To validate the control topology of the PMSG-Direct-Drive wind turbine and DC-Link controllers, a DC load is used with a profile similar to that of the demand response simulations conducted previously. A PMSG-wind turbine (as described in Chapter 4) is connected to the DC-Link through an IGBT switch-mode controlled rectifier. The control topology is designed to maintain the DC-link voltage at a set value against the perturbations caused by demand variability. Figure 6.14 displays the DC-Link demand current. Initially (after the simulation starting transient) the DC-Link requires 2 amperes of current. After 4 seconds, the load is doubled to 4 amps, representing an increase in microgrid demand translated through a droop regulator or supervisory controller. After 7 seconds, the DC-link voltage set-point is reduced with the same load impedance, resulting in a decrease in demand to 3.6 amperes. The load is modelled as a variable resistor in series with a small inductance (to prevent transient singularities in the current derivatives), allowing for control over the DC-link demand without changing the system topology. A 1000 microfarad capacitor stabilizes the DC-Link and removes switching harmonics from the IGBT rectifier.

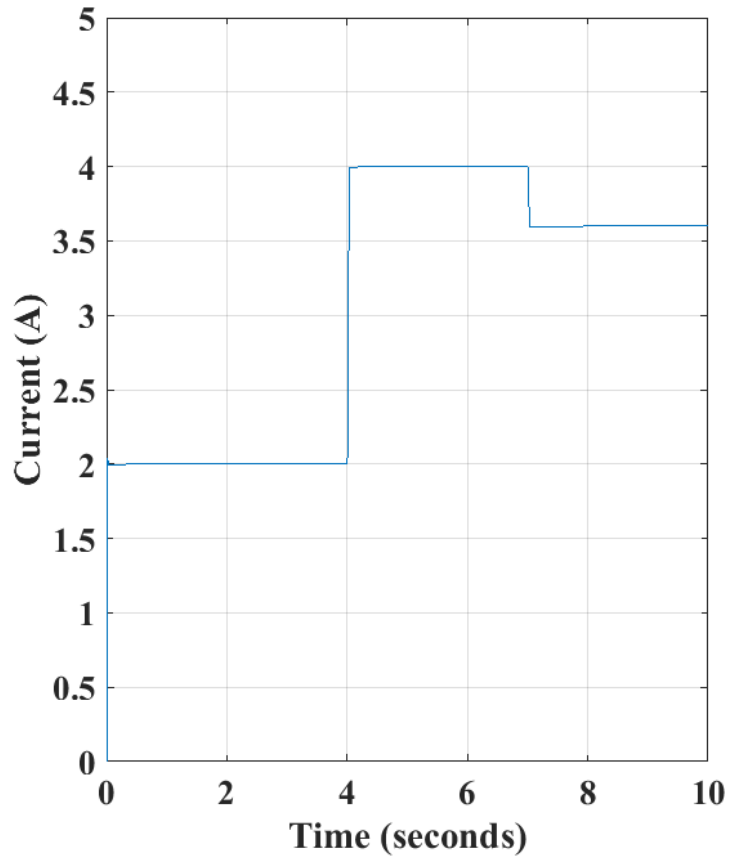


Figure 6.14: DC Link Current

Figures 6.15 and 6.16 display the DC Link voltage during the two demand variation periods – the first (Figure 15) due to an impedance change and the second (Figure 6.16) due to a DC-Link reference change. The DC link reference is set to 1000 volts, a value which allows the grid-side converter to operate at a modulation index near 0.5. However, a detailed investigation into DC link dynamics is required to determine the optimal DC link voltage value, requiring generator and grid data as well as advanced computational simulations. At 4 seconds, the DC link voltage decreases from 1000 to 998 volts. It quickly recovers to 999 volts due to energy being released from line inductances on the

PMSG side of the rectifier, before slowly returning to the reference value (1000 volts) with an exponential time constant dictated by the dynamic behavior of the PMSG controller. The time constant of this behavior is approximately 1 second, limited by the electrical time constant of the wind turbine PMSG and practical limits on the maximum and minimum PMSG stator current references. Figure 6.16 displays the reference-tracking behavior of the DC-Link controller. At 7 seconds, the reference voltage is decreased from 1000 volts to 900 volts. This simulates a worse-case scenario occurring during energization contingencies where the demand at the inverter can change extremely quickly. The DC link quickly responds, dropping to ~895 volts in less than 50 milliseconds as the DC Link capacitor is discharged. There is a slight overshoot beyond the reference value, which decays exponentially as the PMSG controller stabilizes the rectifier modulation index and therefore the PMSG stator currents. It must be noted that the DC link dynamics are non-linear (see Chapter 4), therefore standard first or second-order response forms are not observed. In either case, the DC Link controller successfully tracks the reference value in the face of load variation or set-point changes, indicating its ability to maintain DC Link stability during droop regulation. In addition, the control topology can accommodate a change in the PMSG back-emf requiring a lower (or higher) DC Link voltage to maintain a realistic rectifier modulation index.

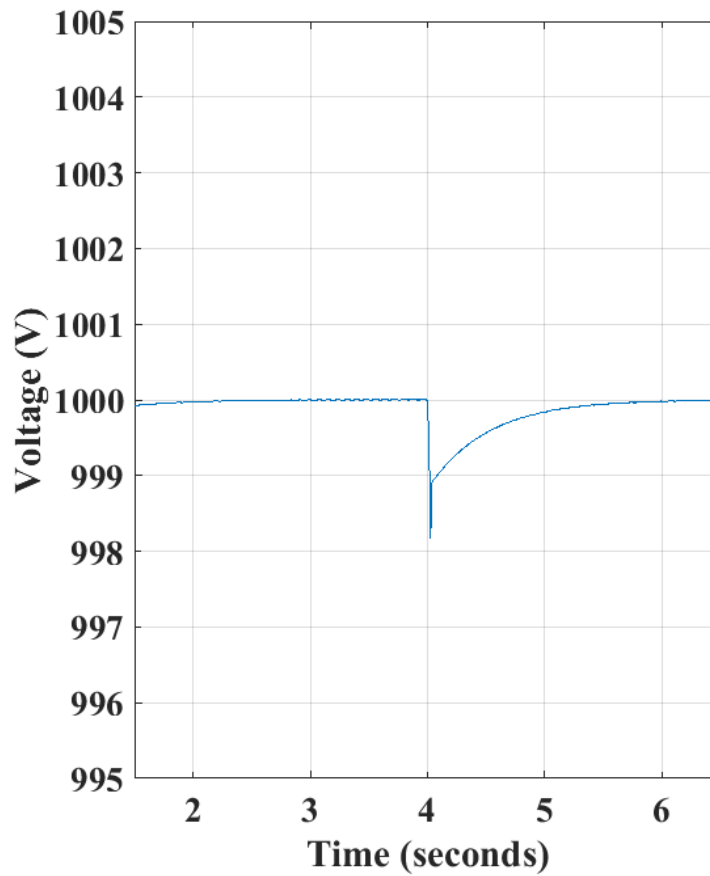


Figure 6.15: DC Link Voltage during Load Variation

The DC Link controller acts by changing the Q-axis current reference being fed to the PMSG controller. This acts in combination with zero D-axis current control to ensure unity power factor operation of the PMSG with a controlled, stable DC-Link voltage. The behavior of the DC Link is therefore limited by the performance of the PMSG controller. Figures 6.17-6.19 displays the PMSG stator currents and their reference values during the simulation period. Figure 6.17 displays an overview of the PMSG current magnitudes.

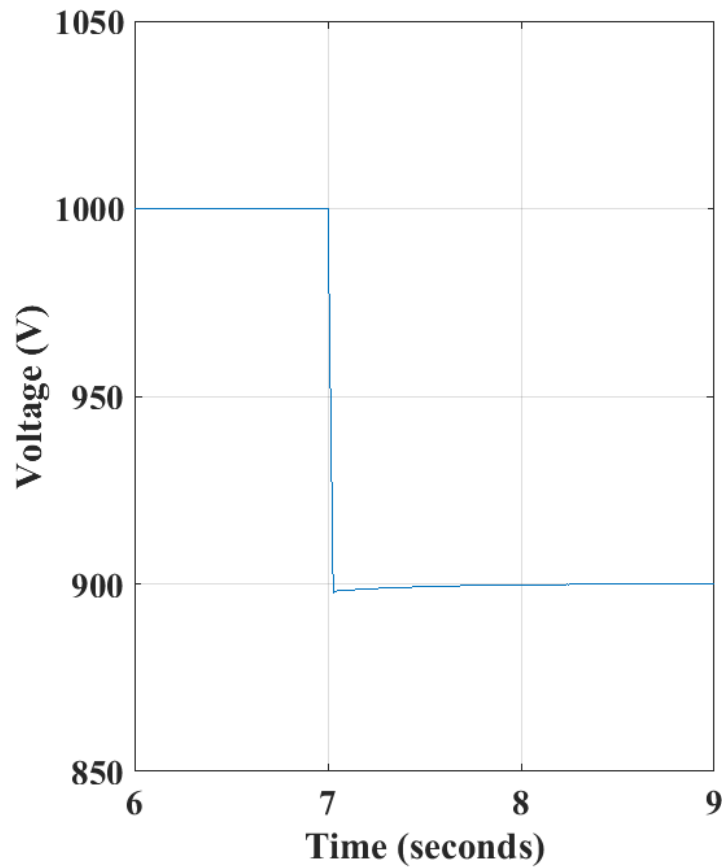


Figure 6.16: DC Link Voltage during Reference Change

After an initial simulation starting transient, the PMSG currents converge to their reference values of 0 (D-axis) and ~5 (Q-axis) amperes, respectively. The D-axis current reference remains zero throughout, with slight deviations in the observed D-axis current visible due to the cross-coupling with the Q-axis through the line and stator inductance. The Q-axis current increases to 10.5 amperes at 4 seconds due to the increase in DC Link current demand. While some controller transients are visible, no major deviations from the reference values occur. Similar behavior is evident at 7 seconds when the DC Link voltage set-point is changed. The large set-point change results in a 0 Q-axis current reference – the PMSG is essentially floating on the rectifier as the DC Link capacitor discharges through the load resistance. After a brief interval, the DC-Link reaches the new reference

value and the PMSG again delivers the current required by the load. Figure 6.18 displays the transient PMSG stator currents during the initial load increase. The D-axis current is not significantly affected, with the measured value remaining close to zero matching the reference value. The Q-axis current reference increases in a manner similar to a slightly underdamped step response, representing the behavior of the DC Link controller (PI with Feed Forward). The observed PMSG Q-Axis current slightly lags the reference value, however it never exhibits a significant tracking error and converges within 50 milliseconds to the reference value. Figure 6.19 displays the transient PMSG stator currents during the DC Link reference change. The D-axis current shows slight variations due to the large change in the Q-Axis current. However, the decoupling terms within the D-axis current

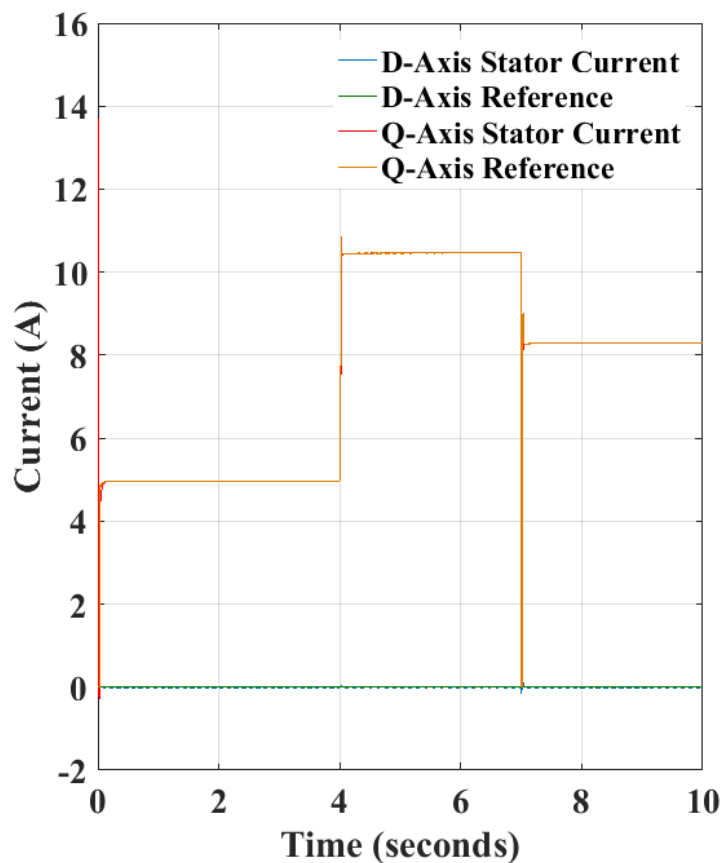


Figure 6.17: PMSG Stator Currents

controller prevents significant deviations from the reference value. The Q-axis current reference instantaneously decreases to zero due to the set-point step change. A realistic supervisory controller would not forward such a sharp command, however the step signal is useful for evaluating the stability of the current controller. The observed Q-axis current decays exponentially to zero, with the error converging to less than 1% of the step magnitude within 25 milliseconds. Once the DC Link capacitor discharges by 100 volts (after ~25 milliseconds) the Q-axis current reference increases, showing a slightly underdamped step change to its new stable value. The observed current displays a slight lag and undershoot initially, however it converges within 20 milliseconds, preventing a

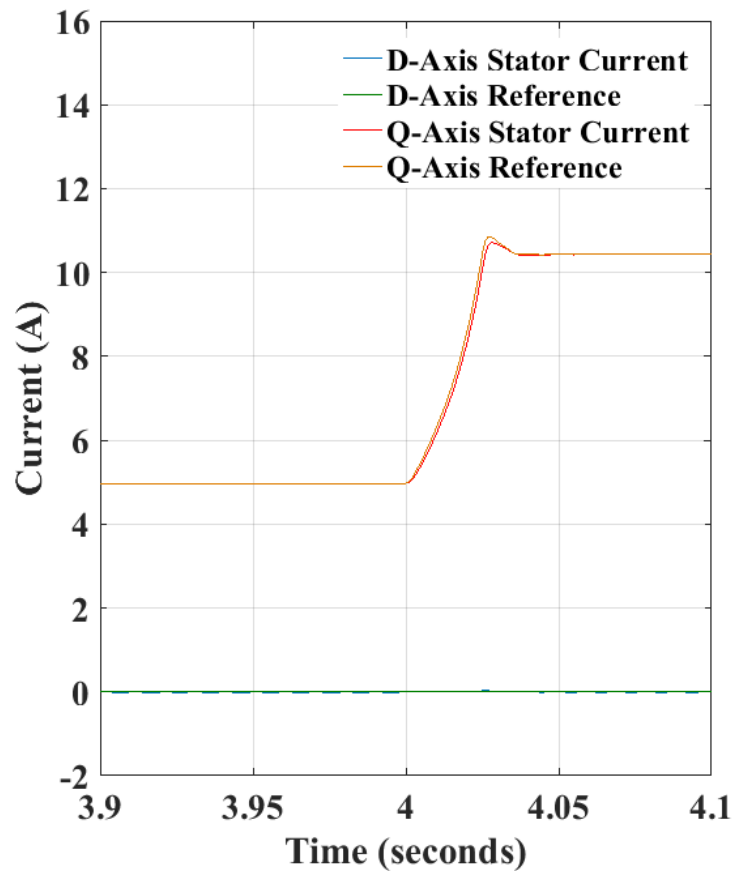


Figure 6.18: PMSG Stator Currents during Load Variation

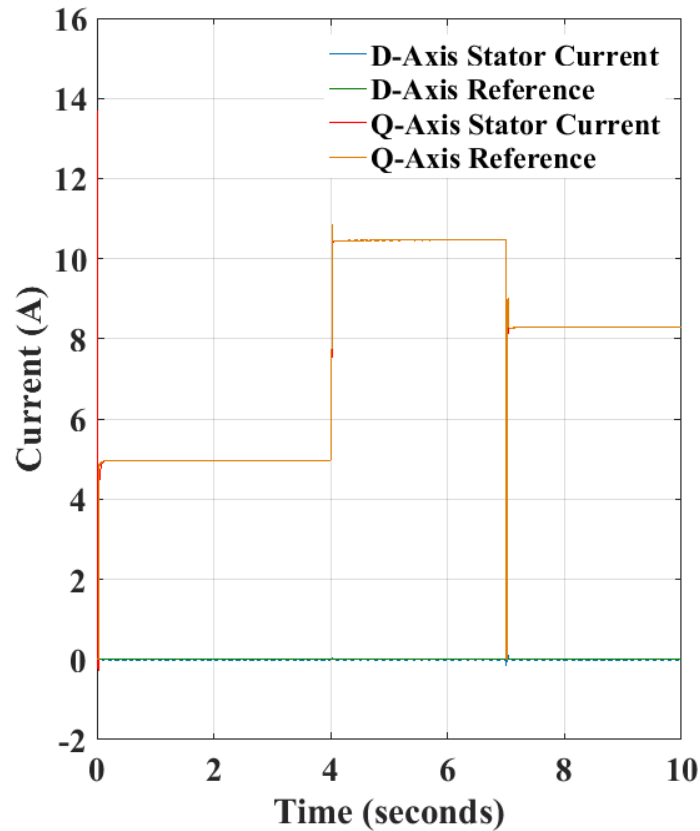


Figure 6.19: PMSG Stator Currents during DC Link Reference Change

significant error in the DC Link voltage. Overall, the PMSG current controllers are shown to successfully track the reference values provided by the DC Link regulator, displaying the ability of the PMSG wind turbine to supply variable loads through the chosen converter topology.

The PMSG current controllers act by varying the terminal voltage reference of the IGBT rectifier. Figures 6.20-6.22 display the measured D and Q axis inverter terminal voltages along with their reference values. The measured voltages are filtered through a short-period moving average to remove the switching commutation inherent to the IGBT converter. As the converter switching frequency is 10 kHz, no significant delay is introduced to the

signals. Figure 6.20 displays an overview of the PMSG voltages. After an initial starting transient, the inverter terminal voltages converge to a Q axis voltage of 275 volts and a D-axis voltage of ~5 volts. A slight offset is evident in the D-axis terminal voltage – this is due to the inability to perfectly remove the effects of cross-coupling - the D-axis voltage increases across the line inductance due to the Q-axis current. In general, no significant transient or steady state deviations from the voltage references are evident apart from the aforementioned cross-coupling compensation. Figure 6.21 displays the transient behavior of the converter terminal voltage during the load increase at 4 seconds. The increased current reference requires a decrease in the Q axis voltage reference from ~275 to ~250 volts, with a corresponding D-axis reference increase from ~5 to ~10 volts. The observed

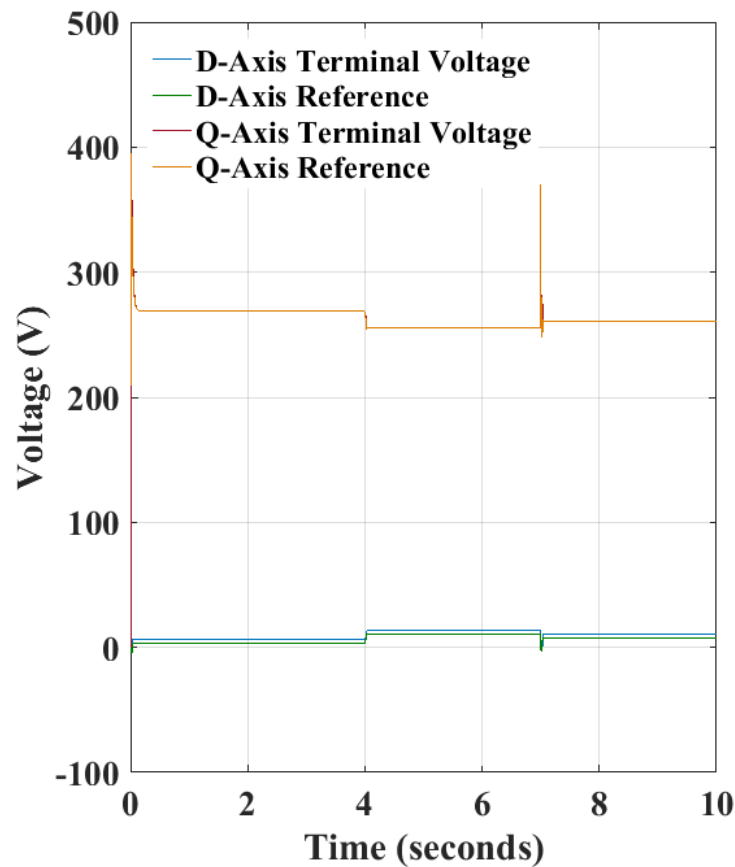


Figure 6.20: Converter Terminal Voltages

terminal voltages very closely follow this value, with a slight lag caused by the line and PMSG stator inductance. However, the overall converge is fast enough to provide the robust and stable dynamic behavior exhibited by the current waveform, demonstrating the effectiveness of the converter in tracking the PMSG stator current references by varying the terminal voltage. Figure 6.22 displays the transient terminal voltage behavior during the DC Link reference change at 7 seconds. The Q-axis voltage reference initially spikes to stop the current flow through the converter – the actual Q-axis voltage lags somewhat due to the inductance in the system. Similar behavior is evident when the reference voltage decreases again – it is impossible to instantaneously change the converter terminal voltage. However, both the Q and D-axis voltage waveforms closely match the reference value and

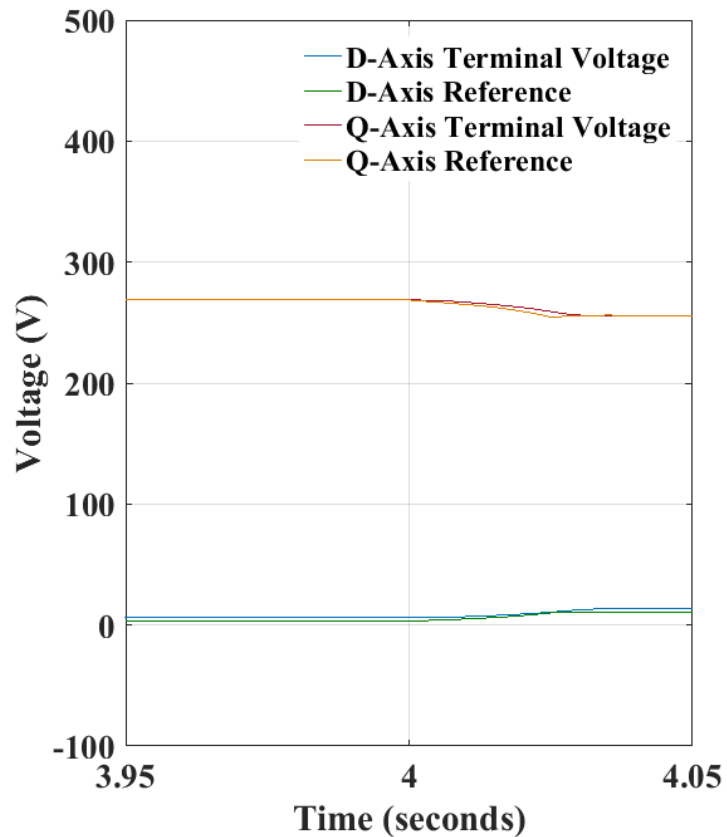


Figure 6.21: Converter Terminal Voltages during Load Variation

converge within 25 milliseconds. Only small changes in the converter reference are required to significantly affect the current flowing through the converter due to the low output impedance of larger PMSG systems. In any case, the time constant of the electrical control system is on the order of fractions of a second to seconds, significantly faster than the mechanical behavior of a large wind turbine and indicating the ability to control grid interconnection directly through manipulation of power electronic converters as opposed to the mechanical behavior of the wind turbine.

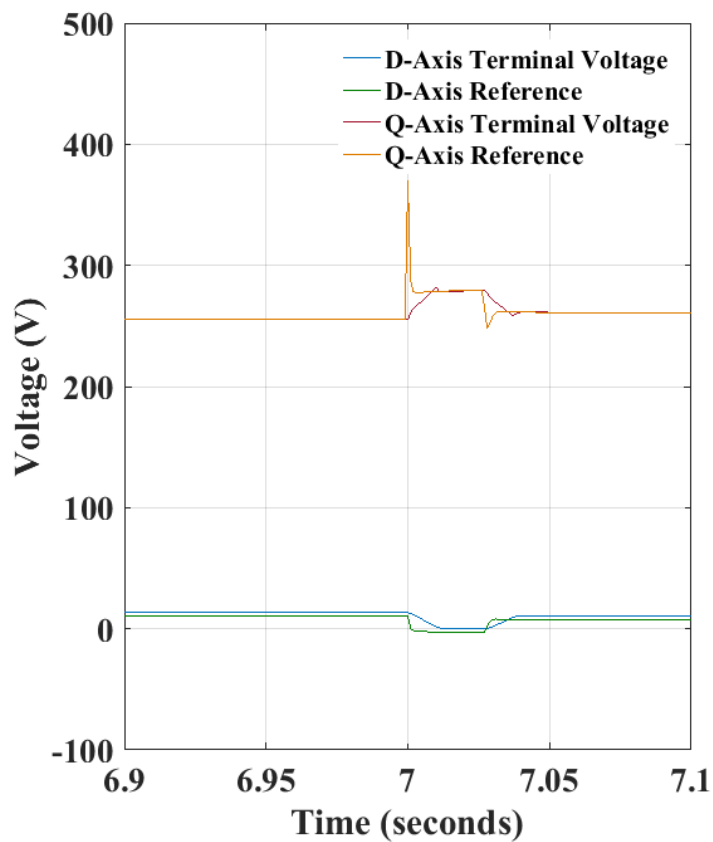


Figure 6.22: Converter Terminal Voltages during DC Link Reference Change

6.4: Conclusions

In this Chapter, PLEXIM simulations were conducted to validate the control and interconnection topology required to integrate wind reserved into an islanded microgrid. The performance of a power inverter in providing frequency and voltage regulation was investigated using a load profile matching common application of peak shaving or demand response in Cartwright. The performance of droop-based frequency regulation was compared to synchronous governor action and shown to improve the frequency stability of the microgrid by reducing the magnitude of frequency dips during demand increases. In addition, the ability of the power inverter to inject reactive power into the microgrid was used to perform voltage regulation through a Q/V droop algorithm, demonstrating a reduction in the magnitude of voltage sags during the activation of inductive loads compared to the performance of the synchronous exciter alone. The overall reference tracking ability of the PR VSI control algorithm was validated, with minimal THD and the ability to match fast droop reference changes. In addition, the DSOGI-FLL synchronization algorithm was shown to maintain an accurate estimate of the microgrid frequency during all frequency excursions, demonstrating the ability of wind reserves to provide demand response, frequency regulation and voltage regulation despite the lower inertia (and therefore greater frequency and voltage variability) of Cartwright's islanded microgrid. To conclude, the interconnection of a PMSG Direct-Drive wind turbine to a DC Link was investigated. The DC Link voltage control algorithm was shown to maintain a stable DC Link voltage despite significant demand variation and changes to the reference voltage. In

addition, the PMSG decoupled D-Q current controller was shown to exhibit robust and stable reference tracking, implementing unity power factor operation through zero D-Axis current control while also tracking the Q-axis current reference provided by the DC Link voltage regulator. Finally, the ability of the IGBT converter to implement current reference changes through terminal voltage variability was validated, demonstrating that power electronic converter control is capable of fully regulating the active and reactive power output of a wind turbine on a time scale significantly faster than the associated mechanical dynamics. The combination of PLEXIM simulations validates the previously discussed applications of wind reserves and demonstrates the ability of wind energy to improve the transient and dynamic stability of an islanded microgrid.

Chapter 7: Conclusions

This thesis provided improved probabilistic wind reserve assessment algorithms for use in islanded microgrids, including advanced multidimensional wind resource models, probabilistic wind reserve assessment techniques, studies into microgrid topologies and control as well as a case study which validated the utility of the proposed methodologies. An analysis and modeling framework was introduced for the probabilistic prediction of the performance of an islanded microgrid with wind generation installed as a dynamic reserve, allowing analysis of the feasibility of wind as well as providing a starting point for system optimization.

Chapter 2 presented a novel hybrid time/frequency analysis and modeling framework designed to identify and model time-variance within a bivariate environmental dataset. Frequency domain analysis identified and quantified statistically significant time-variance in the nonstationary site wind velocity and air density statistics. A feature extraction algorithm was formulated to extract these nonstationary components from the environmental dataset. The refined dataset was organized to allow an optimized nonparametric kernel smoothing algorithm, producing a multi-dimensional probabilistic model that numerically characterized the time-variant wind/density probability distribution. The proposed modeling methodology accounted for bivariate cross-correlation in addition to the inherent nonstationary behavior of the sample dataset. The performance of the probabilistic model was validated by splitting the environmental dataset into design and validation segments, with 5 years of additional environmental data used to

validate the probabilistic model. The multidimensional, nonparametric probabilistic model provides improved time resolution in addition to a more accurate time-variant bivariate probability distribution, allowing high resolution probabilistic assessment of a site wind resource. The development and implementation of this novel modeling methodology advanced the evaluation of a site's wind potential, turbine installation feasibility and allows probabilistic assessment of system contingencies, representing an improvement in the area of wind resource modeling.

Chapter 3 developed and presented a detailed methodology to enable the probabilistic modeling of wind reserves in an islanded microgrid. The modeling techniques were designed to produce strong results with respect to the feasibility, performance and dynamic behavior of islanded microgrids using wind power generation to augment base-load conventional sources. The proposed time-variant, multivariate probabilistic modeling algorithms successfully compensate for nonstationary behavior in the environmental and electrical demand datasets, providing an accurate assessment of the wind regime and demand profile in addition to its probabilistic transient variability. In addition, a probabilistic power-balance model was developed to evaluate the feasibility and general performance of wind generation when acting as a dynamic generation reserve. The use of advanced multidimensional kernel density estimators with optimized bandwidth selection improved the ability of the new model to capture multimodal probabilistic behavior in comparison to existing unimodal parametric distributions. The proposed modeling algorithm also provides improved accuracy compared to standard mixture models. The wind reserve assessment algorithm allows the provision of valuable planning information

with respect to wind generation's ability to meet demand response, secondary generation and frequency regulation in an islanded microgrid.

Chapter 4 presented an overview of various aspects of analysis, modeling and control of islanded Microgrids. An analytical and numerical framework for the implementation of wind-based reserve generation in islanded microgrids was developed within the PLEXIM simulation environment. The PLEXIM environment provides a framework for case-study analysis of wind reserve applications based on field data and microgrid topologies. Aspects of microgrid operation and modeling were reviewed, including grid forming techniques, grid synchronization of distributed generation and various droop-based grid interconnection schemes. These control techniques were applied to wind turbine installation and microgrid interconnection. Wind turbine generators were briefly reviewed, with direct-drive PMSG designed explored in greater detail. Their steady-state and dynamic behavior was reviewed, with decoupled rotating-frame control topologies implemented and analytically modeled to allow for interconnection with islanded microgrids. The grid interconnection topology was also reviewed, with the behavior of a back-to-back power converter modeled with respect to DC-link voltage regulation. The microgrid topology and PLEXIM implementation simulation environment was presented in a manner allowing future researchers to implement state-of-the-art microgrid models.

Chapter 5 presented a case study on wind reserve assessment for an islanded microgrid. Field data from Cartwright was used to probabilistically assess the ability of wind generation to act as an active reserve for microgrid frequency and voltage regulation. The time-variant, multivariate probabilistic modeling algorithms proposed in the previous

Chapters were used successfully compensate for nonstationary behavior in the environmental and electrical demand datasets, providing an accurate assessment of the wind regime and demand profile and its probabilistic transient variability. The results produced within the case study provided valuable planning information with respect to wind generation's ability to meet demand response, secondary generation and frequency regulation in an islanded microgrid, with the seasonal, diurnal and generation-based variability in the probabilistic wind reserve being identified and quantified. The probabilistic microgrid power balance was developed for multiple wind installation topologies, including two wind turbine types and two generation capacities. The NPS-100c-24 wind turbine was conclusively shown to produce a superior wind reserve distribution compared to the NPS-100c-21, demonstrating the capacity of the proposed algorithm to compare the performance of different wind turbine designs. In addition, the effect of a doubling in generation capacity was fully defined probabilistically, allowing optimization to occur with respect to generation capacity in future cost-function based analysis.

Chapter 6 presented PLEXIM simulations, conducted to validate the control and interconnection topology required to integrate wind reserved into an islanded microgrid. The performance of a power inverter in providing frequency and voltage regulation was investigated using a load profile matching a common application of peak shaving or demand response in Cartwright. The performance of droop-based frequency regulation was compared to synchronous governor action and shown to improve the frequency stability of the microgrid by reducing the magnitude of frequency dips during demand increases. In addition, the ability of the power inverter to inject reactive power into the microgrid was

used to perform voltage regulation through a Q/V droop algorithm, demonstrating a reduction in the magnitude of voltage sags during the activation of inductive loads compared to the performance of the synchronous exciter alone. The overall reference tracking ability of the PR VSI control algorithm was validated, with minimal THD and the ability to match fast droop reference changes. In addition, the DSOGI-FLL synchronization algorithm was shown to maintain an accurate estimate of the microgrid frequency during all frequency excursions, demonstrating the ability of wind reserves to provide demand response, frequency regulation and voltage regulation despite the lower inertia (and therefore greater frequency and voltage variability) of Cartwright's islanded microgrid. To conclude, the interconnection of a PMSG Direct-Drive wind turbine to a DC Link was investigated. The DC Link voltage control algorithm was shown to maintain a stable DC Link voltage despite significant demand variation and changes to the reference voltage. In addition, the PMSG decoupled D-Q current controller was shown to exhibit robust and stable reference tracking, implementing unity power factor operation through zero D-Axis current control while also tracking the Q-axis current reference provided by the DC Link voltage regulator. Finally, the ability of the IGBT converter to implement current reference changes through terminal voltage variability was validated, demonstrating that power electronic converter control is capable of fully regulating the active and reactive power output of a wind turbine on a time scale significantly faster than the associated mechanical dynamics. The combination of PLEXIM simulations validates the previously discussed applications of wind reserves and demonstrates the ability of wind energy to improve the transient and dynamic stability of an islanded microgrid.

7.1 Thesis Contribution

This thesis provided improved probabilistic wind reserve assessment algorithms for use in islanded microgrids. An advanced, time-variant multidimensional and multivariate wind resource modelling algorithm was developed to investigate wind turbine performance under nonstationary environmental conditions. This modeling algorithm was combined with electrical demand data to generate probabilistic wind reserve assessment techniques. An investigation into state-of-the-art microgrid topologies and control algorithms was also conducted to provide a framework for the analytical and numerical implementation of the probabilistically identified wind reserved. A case study was then conducted which validated the utility of the proposed methodologies, demonstrating the applications of wind reserves in an islanded microgrid. The overarching objective was to provide an analysis and modeling framework for the probabilistic prediction of the performance of an islanded microgrid when wind generation is installed as a dynamic reserve, allowing analysis of the feasibility of wind as well as providing a starting point for system optimization.

7.2: Future Work

The research presented in this thesis forms a framework for the assessment of wind reserves in islanded microgrid. Future work in this area is planned as follows:

- Conducting additional case studies for sites with fundamentally different climate regimes to investigate the results space produced by the assessment algorithm
- Implementing several existing deterministic wind reserve assessment algorithms with the objective of modifying them to produce results comparable to the proposed probabilistic model
- Investigating additional applications of wind energy in islanded microgrids, including unbalance compensation, power quality and system protection, including sensorless and non-linear control and operation algorithms
- Implementing supervisory and tertiary control layers which incorporate information developed from the probabilistic wind reserve assessment algorithm, with the goal of developing an Autonomous Intelligent Management System (AIMS) for islanded microgrids.
- Expanding and generalizing AIMS to work in both islanded and transmission-interconnected microgrids , optimizing microgrid stability and performance during transition intervals due to transmission contingencies or generation intermittency

References

Chapter 1

- [1] X. Xu, D. Niu, Q. Wang, P. Wang and D. Wu, "Intelligent Forecasting Model for Regional Power Grid With Distributed Generation", *IEEE Syst. J.*, to be published.
- [2] P. McSharry, S. Bouwman and G. Bloemhof, "Probabilistic Forecasts of the Magnitude and Timing of Peak Electricity Demand", *IEEE Trans. Power Syst.*, vol. 20, no. 2, pp. 1166-1172, May 2005.
- [3] H. Holttinen, et. al., "Methodologies to determine operating reserves due to increases wind power", *IEEE Trans. Sust. Energy*, vol. 3, no. 4, pp. 713-723, Oct. 2012.
- [4] Ye Wang, et. al., "Methods for assessing available wind primary reserve reserve", *IEEE Trans. Sust. Energy*, vol. 6, no. 1, pp. 272-280, Jan. 2015.
- [5] X. Xu, Z. Yan and S. Xu, "Estimating wind speed probability distribution by diffusion-based kernel density method", *Electric Pow. Syst. Res.*, vol. 121, pp. 28-37, April 2015.

Chapter 2

- [1] A. Vega Remesal, A. Ramos Millan, E. Conde Lazaro and P. Reina Peral, "Pre-feasibility study of hybrid wind power-H2 system connected to electrical grid", *IEEE Latin America Transactions*, vol. 9, no. 5, pp. 800-807, 2011.
- [2] D. Koussa and M. Koussa, "A feasibility and cost benefit prospection of grid connected hybrid power system (wind-photovoltaic) – Case study: An Algerian coastal site", *Renewable and Sustainable Energy Reviews*, vol. 50, pp. 628-642, 2015.
- [3] T. Iqbal, "Pre-Feasibility Study of a Wind-Diesel System for St. Brendan's, Newfoundland", *Wind Engineering*, vol. 27, no. 1, pp. 39-51, 2003.
- [4] E. Cheng, "Feasibility Study of a Wind-Powered Pumped-Storage Hydroelectric System", *Wind Engineering*, vol. 24, no. 2, pp. 111-117, 2000.
- [5] D. Saheb-Koussa, M. Koussa and N. Said, "Prospects of Wind-Diesel Generator-Battery Hybrid Power System: A Feasibility Study in Algeria", *Journal of Wind Energy*, vol. 2013, pp. 1-8, 2013.
- [6] M. Khan and M. Iqbal, "Pre-feasibility study of stand-alone hybrid energy systems for applications in Newfoundland", *Renewable Energy*, vol. 30, no. 6, pp. 835-854, 2005.
- [7] M. Nehrir, C. Wang, K. Strunz, H. Aki, R. Ramakumar, J. Bing, Z. Miao and Z. Salameh, "A Review of Hybrid Renewable/Alternative Energy Systems for Electric Power Generation: Configurations, Control, and Applications", *IEEE Trans. Sustain. Energy*, vol. 2, no. 4, pp. 392-403, 2011.
- [8] S. Upadhyay and M. Sharma, "A review on configurations, control and sizing methodologies of hybrid energy systems", *Renewable and Sustainable Energy Reviews*, vol. 38, pp. 47-63, 2014.
- [9] J. Bernal-Agustín and R. Dufo-López, "Simulation and optimization of stand-alone hybrid renewable energy systems", *Renewable and Sustainable Energy Reviews*, vol. 13, no. 8, pp. 2111-2118, 2009.
- [10] M. Deshmukh and S. Deshmukh, "Modeling of hybrid renewable energy systems", *Renewable and Sustainable Energy Reviews*, vol. 12, no. 1, pp. 235-249, 2008.
- [11] M. Fadaee and M. Radzi, "Multi-objective optimization of a stand-alone hybrid renewable energy system by using evolutionary algorithms: A review", *Renewable and Sustainable Energy Reviews*, vol. 16, no. 5, pp. 3364-3369, 2012.
- [12] B. DuPont and J. Cagan, "A hybrid extended pattern search/genetic algorithm for multi-stage wind farm optimization", *Optimization and Engineering*, vol. 17, no. 1, pp. 77-103, 2016.
- [13] L. Li and Z. Tan, "Optimization Design of Wind/Photovoltaic Hybrid Power Systems Based on Genetic Algorithms", *AMM*, vol. 278-280, pp. 1692-1695, 2013.
- [15] "Wind Energy | Canada's Wind TRM | Natural Resources Canada", *Nrcan.gc.ca*, 2015. [Online]. Available: <http://www.nrcan.gc.ca/energy/renewable-electricity/wind/7323>. Accessed: August 2016
- [16] *Irena.masdar.ac.ae*, 2016. [Online]. Available: <http://irena.masdar.ac.ae/>. Accessed: August 2016

- [17] R. Harris and N. Cook, 'The parent wind speed distribution: Why Weibull?', *Journal of Wind Engineering and Industrial Aerodynamics*, vol. 131, pp. 72-87, 2014.
- [18] J. III, J. Wiener and M. Smith, 'The Weibull Distribution: A New Method of Summarizing Survivorship Data', *Ecology*, vol. 59, no. 1, p. 175, 1978.
- [19] A. Watkins, 'On maximum likelihood estimation for the two parameter Weibull distribution', *Microelectronics Reliability*, vol. 36, no. 5, pp. 595-603, 1996.
- [20] F. Wang and J. Keats, 'Improved percentile estimation for the two- parameter Weibull distribution', *Microelectronics Reliability*, vol. 35, no. 6, pp. 883-892, 1995.
- [21] A. Watkins, 'On maximum likelihood estimation for the two parameter Weibull distribution', *Microelectronics Reliability*, vol. 36, no. 5, pp. 595-603, 1996.
- [22] F. Wang and J. Keats, 'Improved percentile estimation for the two- parameter Weibull distribution', *Microelectronics Reliability*, vol. 35, no. 6, pp. 883-892, 1995.
- [23] Y. Zewei and A. Tuzuner, 'Fractional Weibull Wind Speed Modeling For Wind Power Production Estimation', *Power and Energy Society General Meeting*, pp. 1-7, 2009.
- [24] A. Celik, "Assessing the suitability of wind speed probability distribution functions based on wind power density", *Renewable Energy*, vol. 28, no. 10, pp. 1563-1574, 2003.
- [25] J. Wang, J. Hu and K. Ma, "Wind speed probability distribution estimation and wind energy assessment", *Renewable and Sustainable Energy Reviews*, vol. 60, pp. 881-899, 2016.
- [26] X. Qu and J. Shi, "Bivariate Modeling of Wind Speed and Air Density Distribution for Long-Term Wind Energy Estimation", *International Journal of Green Energy*, vol. 7, no. 1, pp. 21-37, 2010.
- [27] J. Zhang, S. Chowdhury, A. Messac and L. Castillo, "A Multivariate and Multimodal Wind Distribution model", *Renewable Energy*, vol. 51, pp. 436-447, 2013.
- [28] J. Carta and D. Mentado, "A continuous bivariate model for wind power density and wind turbine energy output estimations", *Energy Conversion and Management*, vol. 48, no. 2, pp. 420-432, 2007.
- [29] K. Pope, R. Milman and G. Naterer, "Rotor dynamics correlation for maximum power and transient control of wind turbines", *International Journal of Energy Research*, 2009.
- [30] B. Malinga, J. Sneckenberger and A. Feliachi, "Modeling and Control of a Wind Turbine as a Distributed Resource", in *The 35th Annual Southeastern Symposium on System Theory*, West Virginia University, 2003, pp. 108-112.
- [31] H. Rinne, *The Weibull distribution*. Boca Raton: CRC Press, 2009.
- [32] J. III, J. Wiener and M. Smith, 'The Weibull Distribution: A New Method of Summarizing Survivorship Data', *Ecology*, vol. 59, no. 1, p. 175, 1978.
- [33] R. Harris and N. Cook, 'The parent wind speed distribution: Why Weibull?', *Journal of Wind Engineering and Industrial Aerodynamics*, vol. 131, pp. 72-87, 2014.
- [34] E. Kavak Akpinar and S. Akpinar, 'A statistical analysis of wind speed data used in installation of wind energy conversion systems', *Energy Conversion and Management*, vol. 46, no. 4, pp. 515-532, 2005.
- [35] X. Xu, Z. Yan and S. Xu, "Estimating wind speed probability distribution by diffusion-based kernel density method", *Electric Power Systems Research*, vol. 121, pp. 28-37, 2015.
- [36] B. Silverman, *Density estimation for statistics and data analysis*. London: Chapman and Hall, 1986.
- [37] M. Loève, *Probability Theory I*, New York: Springer-Verlag, 1977.
- [38] Howard G. Tucker, "A Generalization of the Glivenko-Cantelli Theorem". *The Annals of Mathematical Statistics*, vol. 30, pp. 828-830, 1959.
- [39] T. Burton, N. Jenkins, D. Sharpe and E. Bossanyi, *Wind Energy Handbook*, 2nd ed. Wiley, 2011.
- [40] K. Van Treuren, "Small-Scale Wind Turbine Testing in Wind Tunnels Under Low Reynolds Number Conditions", *J. Energy Resour. Technol*, vol. 137, no. 5, p. 051208, 2015.
- [41] M. Moran and H. Shapiro, *Principles of engineering thermodynamics*. [Singapore]: Wiley, 2012.
- [42] W. Haynes, *CRC handbook of chemistry and physics*. Boca Raton, FL.: CRC Press, 2011.
- [43] MATLAB r2016(a), Mathworks, 2016
- [44] M.L. Little and K. Pope, 'Modeling Seasonal Wind Resource Variation in a Maritime-Influenced Humid Continental Climate,' presented at the *Newfoundland Electrical and Computer Engineering Conference*, St. John's, NL, Nov. 5, 2015.
- [45] J. Apt, 'The spectrum of power from wind turbines', *Journal of Power Sources*, vol. 169, no. 2, pp. 369-374, 2007.

- [46] Kristan Matej, Leonardis Ales and Skocaj Danijel, "Multivariate Online Kernel Density Estimation with Gaussian Kernels", *Pattern Recognition*, vol. 44. no. 10, Oct. 2011.
- [47] M.P. Wand, M.C. Jones, *Kernel Smoothing*, Chapman & Hall/CRC (1995)
- [48] Ye Wang, et. al., "Methods for assessing available wind primary reserve reserve", *IEEE Trans. Sust. Energy*, vol. 6, no. 1, pp. 272-280, Jan. 2015.
- [49] X. Qu and J. Shi, "Bivariate Modeling of Wind Speed and Air Density Distribution for Long-Term Wind Energy Estimation", *International Journal of Green Energy*, vol. 7, no. 1, pp. 21-37, 2010.
- [50] J. Wang, J. Hu and K. Ma, "Wind speed probability distribution estimation and wind energy assessment", *Renewable and Sustainable Energy Reviews*, vol. 60, pp. 881-899, 2016.
- [51] Joseph Lee Rodgers and W. Alan Nicewander, "Thirteen Ways to Look at the Correlation Coefficient", *The American Statistician*, vol. 42, no. 1, 1988

Chapter 3

- [1] M. Bayat, K. Sheshyekani, M. Hamzeh and A. Rezaadeh, "Coordination of Distributed Energy Resources and Demand Response for Voltage and Frequency Support of MV Microgrids", *IEEE Trans. Power Syst.*, vol. 31, no. 2, pp. 1506-1516, March 2016.
- [2] C. De Jonghe, B. Hobbs and R. Belmans, "Optimal Generation Mix With Short-Term Demand Response and Wind Penetration", *IEEE Trans. Power Syst.*, vol. 27, no. 2, pp. 830-839, May 2012.
- [3] N. Mendis, K. M. Muttaqi and S. Perera, "Management of low- and high-frequency power components in demand-generation fluctuations of a DFIG-based wind-dominated RAPS system using hybrid energy storage", *IEEE Trans. Ind. Appl.*, vol. 50, no.3, pp. 2258-2268, May 2014.
- [4] N. Mendis, K. M. Muttaqi, S. Perera and S. Kamalasan, "An effective power management Strategy for a wind-diesel-hydrogen-based remote area power supply system to meet fluctuating demands under generation uncertainty", *IEEE Trans. Ind. Appl.*, vol. 51, no.2, pp. 1228-1238, March 2015.
- [5] J. Cardell and C. Anderson, "A Flexible Dispatch Margin for Wind Integration", *IEEE Trans. Power Syst.*, vol. 30, no. 3, pp. 1501-1510, May 2015.
- [6] A. Yousefi, H. Iu, T. Fernando and H. Trinh, "An Approach for Wind Power Integration Using Demand Side Resources", *IEEE Trans. Sust. Energy*, vol. 4, no. 4, pp. 917-924, October 2013.
- [7] J. Rocabert, A. Luna, F. Blaabjerg and P. Rodríguez, "Control of Power Converters in AC Microgrids", *IEEE Trans. Power Electron.*, vol. 27, no. 11, pp. 4734-4749, Nov. 2012.
- [8] Z. Ding and W. J. Lee, "A stochastic microgrid operation scheme to balance between system reliability and greenhouse gas emission", *IEEE Trans. Ind. Appl.*, vol. 52, no.2, pp. 1157-1166, March 2016.
- [9] J. Mitra, M. R. Vallem and C. Singh, "Optimal deployment of distributed generation using a reliability criterion", *IEEE Trans. Ind. Appl.*, vol. 52, no.3, pp. 1989-1997, May 2016.
- [10] T. Caldognetto, P. Tenti, A. Costabeber and P. Mattavelli, "Improving Microgrid Performance by Cooperative Control of Distributed Energy Sources", *IEEE Trans. Ind. Appl.*, vol. 50, no.6, pp. 3921-3930, Nov. 2014.
- [11] C. A. H. Aramburo, T. C. Green and N. Mugniot, "Fuel consumption minimization of a microgrid", *IEEE Trans. Ind. Appl.*, vol. 41, no.3, pp. 673-681, May 2015.
- [12] F. Katiraei and M. Irvani, "Power Management Strategies for a Microgrid With Multiple Distributed Generation Units", *IEEE Trans. Power Syst.*, vol. 21, no. 4, pp. 1821-1831, Nov. 2006.
- [13] M. Abdullah, K. Muttaqi, A. Agalgaonkar and D. Sutanto, "A Noniterative Method to Estimate Load Carrying Capability of Generating Units in a Renewable Energy Rich Power Grid", *IEEE Trans.on Sust. Energy*, vol. 5, no. 3, pp. 854-865, July 2014.
- [14] F. Adinolfi, G. Burt, P. Crolla, F. D'Agostino, M. Saviozzi and F. Silvestro, "Distributed Energy Resources Management in a Low-Voltage Test Facility", *IEEE Trans. Ind. Electron.*, vol. 62, no. 4, pp. 2593-2603, April 2015.
- [15] E. R. Hamilton, J. Undrill, P. S. Hamer and S. Manson, "Considerations for generation in an islanded operation", *IEEE Trans. Ind. Appl.*, vol. 46, no.6, pp. 2289-2298, Nov. 2010.
- [16] X. Xu, D. Niu, Q. Wang, P. Wang and D. Wu, "Intelligent Forecasting Model for Regional Power Grid With Distributed Generation", *IEEE Syst. J.*, to be published.

- [17] P. McSharry, S. Bouwman and G. Bloemhof, "Probabilistic Forecasts of the Magnitude and Timing of Peak Electricity Demand", *IEEE Trans. Power Syst.*, vol. 20, no. 2, pp. 1166-1172, May 2005.
- [18] H. Holttinen, et. al., "Methodologies to determine operating reserves due to increases wind power", *IEEE Trans. Sust. Energy*, vol. 3, no. 4, pp. 713-723, Oct. 2012.
- [19] Ye Wang, et. al., "Methods for assessing available wind primary reserve reserve", *IEEE Trans. Sust. Energy*, vol. 6, no. 1, pp. 272-280, Jan. 2015.
- [20] X. Xu, Z. Yan and S. Xu, "Estimating wind speed probability distribution by diffusion-based kernel density method", *Electric Pow. Syst. Res.*, vol. 121, pp. 28-37, April 2015.
- [21] Available: <http://northernpower.com/uk/wind-solutions/nps-10>

Chapter 4

- [1] F. Blaabjerg, R. Teodorescu, M. Liserre and A. Timbus, "Overview of Control and Grid Synchronization for Distributed Power Generation Systems", *IEEE Transactions on Industrial Electronics*, vol. 53, no. 5, pp. 1398-1409, 2006.
- [2] J. Mitra, M. Vallem and C. Singh, "Optimal Deployment of Distributed Generation Using a Reliability Criterion", *IEEE Transactions on Industry Applications*, vol. 52, no. 3, pp. 1989-1997, 2016.
- [3] D. Bernardon, A. Mello, L. Pfitscher, L. Canha, A. Abaide and A. Ferreira, "Real-time reconfiguration of distribution network with distributed generation", *Electric Power Systems Research*, vol. 107, pp. 59-67, 2014.
- [4] N. Mendis, K. M. Muttaqi, S. Perera, and S. Kamalasan, "An Effective Power Management Strategy for a Wind–Diesel–Hydrogen-Based Remote Area Power Supply System to Meet Fluctuating Demands Under Generation Uncertainty," *IEEE Transactions on Industry Applications*, vol. 51, no. 2, pp. 1228–1238, 2015.
- [5] F. Katiraei and M. Iravani, "Power Management Strategies for a Microgrid With Multiple Distributed Generation Units", *IEEE Transactions on Power Systems*, vol. 21, no. 4, pp. 1821-1831, 2006.
- [6] J. Rocabert, A. Luna, F. Blaabjerg and P. Rodríguez, "Control of Power Converters in AC Microgrids", *IEEE Transactions on Power Electronics*, vol. 27, no. 11, pp. 4734-4749, 2012.
- [7] S. Backhaus et. al, "DC Microgrids Scoping Study—Estimate of Technical and Economic Benefits", Los Alamos National Laboratory, 2015.
- [8] F. Nejabatkhah and Y. W. Li, "Overview of Power Management Strategies of Hybrid AC/DC Microgrid," *IEEE Transactions on Power Electronics*, vol. 30, no. 12, pp. 7072–7089, 2015.
- [9] M. Ahmed, Y. Kang, and Y.-C. Kim, "Communication Network Architectures for Smart-House with Renewable Energy Resources," *Energies*, vol. 8, no. 8, pp. 8716–8735, 2015.
- [10] U. B. Tayab, M. A. B. Roslan, L. J. Hwai, and M. Kashif, "A review of droop control techniques for microgrid," *Renewable and Sustainable Energy Reviews*, vol. 76, pp. 717–727, 2017.
- [11] *IEEE Standard for Interconnecting Distributed Resources with Electric Power Systems*, IEEE Standard 1547, Sept. 2008.
- [12] H. Han, X. Hou, J. Yang, J. Wu, M. Su and J. Guerrero, "Review of Power Sharing Control Strategies for Islanding Operation of AC Microgrids", *IEEE Trans. Smart Grid*, vol. 7, no. 1, pp. 200-215, Jan. 2016.
- [13] X. Wang, J. M. Guerrero, F. Blaabjerg and Z. Chen "A review of power electronics based microgrids" *J. of Power Electron.*, vol. 12, pp. 181-192, Jan. 2012.
- [14] S. M. Manson, A. Upreti and M. J. Thompson, "Case study: smart automatic synchronization in islanded power systems", *IEEE Trans. Ind. Appl.*, vol. 52, no.2, pp. 1241-1249, March 2016.
- [15] A. A. Renjit, A. Mondal, M. S. Illindala and A. S. Khalsa, "Analytical methods for characterizing frequency dynamics in islanded microgrids with gensets and energy storage, *IEEE Trans. Ind. Appl.*, to be published.
- [16] M. Bayat, K. Sheshyekani, M. Hamzeh and A. Rezaadeh, "Coordination of Distributed Energy Resources and Demand Response for Voltage and Frequency Support of MV Microgrids", *IEEE Trans. Power Syst.*, vol. 31, no. 2, pp. 1506-1516, March 2016.
- [17] C. De Jonghe, B. Hobbs and R. Belmans, "Optimal Generation Mix With Short-Term Demand Response and Wind Penetration", *IEEE Trans. Power Syst.*, vol. 27, no. 2, pp. 830-839, May 2012.

- [18] N. Mendis, K. M. Muttaqi and S. Perera, "Management of low- and high-frequency power components in demand-generation fluctuations of a DFIG-based wind-dominated RAPS system using hybrid energy storage", *IEEE Trans. Ind. Appl.*, vol. 50, no.3, pp. 2258-2268, May 2014.
- [19] N. Mendis, K. M. Muttaqi, S. Perera and S. Kamalasan, "An effective power management Strategy for a wind-diesel-hydrogen-based remote area power supply system to meet fluctuating demands under generation uncertainty", *IEEE Trans. Ind. Appl.*, vol. 51, no.2, pp. 1228-1238, March 2015.
- [20] S. Backhaus et. al, "DC Microgrids Scoping Study—Estimate of Technical and Economic Benefits", Los Alamos National Laboratory, 2015.
- [21] M. Babazadeh and H. Karimi, "A Robust Two-Degree-of-Freedom Control Strategy for an Islanded Microgrid", *IEEE Trans. Power Del.*, vol. 28, no. 3, pp. 1339-1347, July 2013.
- [22] J. He, Y. Li, J. Guerrero, F. Blaabjerg and J. Vasquez, "An Islanding Microgrid Power Sharing Approach Using Enhanced Virtual Impedance Control Scheme", *IEEE Trans. Power Electron.*, vol. 28, no. 11, pp. 5272-5282, Nov. 2013.
- [23] J. He and Y. W. Li, "Analysis, design, and implementation of virtual impedance for power electronics interfaced distributed generation", *IEEE Trans. Ind. Appl.*, vol. 47, no.6, pp. 2525-2538, Nov. 2016.
- [24] P. Rodríguez, A. Luna, R. Muñoz-Aguilar, I. Etxeberria-Otadui, R. Teodorescu and F. Blaabjerg, "A Stationary Reference Frame Grid Synchronization System for Three-Phase Grid-Connected Power Converters Under Adverse Grid Conditions", *IEEE Trans. Power Electron.*, vol. 27, no. 1, pp. 99-112, Jan. 2012.
- [25] P. Rodríguez, A. Luna, I. Candela, R. Mujal, R. Teodorescu and F. Blaabjerg, "Multiresonant Frequency-Locked Loop for Grid Synchronization of Power Converters Under Distorted Grid Conditions", *IEEE Trans. Ind. Electron.*, vol. 58, no. 1, pp. 127-138, Jan. 2011.
- [26] M. Hamzeh, A. Ghazanfari, H. Mokhtari, and H. Karimi, "Integrating Hybrid Power Source Into an Islanded MV Microgrid Using CHB Multilevel Inverter Under Unbalanced and Nonlinear Load Conditions," *IEEE Transactions on Energy Conversion*, vol. 28, no. 3, pp. 643–651, 2013.
- [27] F. Katiraei, M. Iravani, and P. Lehn, "Micro-Grid Autonomous Operation During and Subsequent to Islanding Process," *IEEE Transactions on Power Delivery*, vol. 20, no. 1, pp. 248–257, 2005.
- [28] J. Mitra, M. R. Vallem, and C. Singh, "Optimal Deployment of Distributed Generation Using a Reliability Criterion," *IEEE Transactions on Industry Applications*, vol. 52, no. 3, pp. 1989–1997, 2016.
- [29] T. L. Vandoorn, B. Meersman, J. D. M. D. Kooning, and L. Vandeveld, "Directly-Coupled Synchronous Generators With Converter Behavior in Islanded Microgrids," *IEEE Transactions on Power Systems*, vol. 27, no. 3, pp. 1395–1406, 2012.
- [30] S. T. Cady, A. D. Dominguez-Garcia, and C. N. Hadjicostis, "A Distributed Generation Control Architecture for Islanded AC Microgrids," *IEEE Transactions on Control Systems Technology*, vol. 23, no. 5, pp. 1717–1735, 2015.
- [31] R. J. Best, D. J. Morrow, D. J. McGowan, and P. A. Crossley, "Synchronous Islanded Operation of a Diesel Generator," *IEEE Transactions on Power Systems*, vol. 22, no. 4, pp. 2170–2176, 2007.
- [32] P. C. Krause, O. Wasynczuk, S. Pekarek, "Chapter 7: Synchronous Machines," in *Electromechanical motion devices*, Hoboken, NJ: Wiley-IEEE Press, 2012.
- [33] "IEEE Standard Definitions for Excitation Systems for Synchronous Machines." IEEE Standard 421.1-2007, July 2007.
- [34] S. Chung, "A phase tracking system for three phase utility interface inverters," *IEEE Transactions on Power Electronics*, vol. 15, pp. 431-438, May 2000.
- [35] P. Rodríguez, J. Pou, J. Bergas, I. Candela, R. Burgos, and D. Boroyevich, "Double synchronous reference frame PLL for power converters," in *Proc. IEEE Power Electronics Special Conference (PESC'05)*, 2005, pp. 1415-1421.
- [36] M. Karimi-Ghartemani and M.R. Iravani, "A method for synchronization of power electronic converters in polluted and variable-frequency environments," *IEEE Transactions on Power Systems*, vol. 19, pp. 1263-1270, Aug. 2004.
- [37] P. Rodríguez, A. Luna, M. Ciobotaru, R. Teodorescu, and F. Blaabjerg, "Advanced Grid Synchronization System for Power Converters under Unbalanced and Distorted Operating Conditions," *IECON 2006 - 32nd Annual Conference on IEEE Industrial Electronics*, 2006.
- [38] B. Wu and M. Narimani, *High-power converters and AC drives*. Hoboken, NJ: IEEE Press, 2017.

- [39] H. Akagi, E. H. Watanabe, and Aredes Mauricio, *Instantaneous power theory and applications to power conditioning*. Piscataway, NJ: IEEE Press, 2007.
- [40] A. Timbus, M. Ciobotaru, R. Teodorescu, and F. Blaabjerg, "Adaptive Resonant Controller for Grid-Connected Converters in Distributed Power Generation Systems," *Twenty-First Annual IEEE Applied Power Electronics Conference and Exposition, 2006. APEC '06*.
- [41] R. Teodorescu, F. Blaabjerg, M. Liserre, and P. Loh, "Proportional-resonant controllers and filters for grid-connected voltage-source converters," *IEE Proceedings - Electric Power Applications*, vol. 153, no. 5, p. 750, 2006.
- [42] H. Han, X. Hou, J. Yang, J. Wu, M. Su, and J. M. Guerrero, "Review of Power Sharing Control Strategies for Islanding Operation of AC Microgrids," *IEEE Transactions on Smart Grid*, vol. 7, no. 1, pp. 200–215, 2016.
- [43] Y. Mohamed and E. El-Saadany, "Adaptive Decentralized Droop Controller to Preserve Power Sharing Stability of Paralleled Inverters in Distributed Generation Microgrids," *IEEE Transactions on Power Electronics*, vol. 23, no. 6, pp. 2806–2816, 2008.
- [44] W. Yao, M. Chen, J. Matas, J. M. Guerrero, and Z.-M. Qian, "Design and Analysis of the Droop Control Method for Parallel Inverters Considering the Impact of the Complex Impedance on the Power Sharing," *IEEE Transactions on Industrial Electronics*, vol. 58, no. 2, pp. 576–588, 2011.
- [45] X. Chen, Y. Zhang, S. Wang, J. Chen, and C. Gong, "Impedance-Phased Dynamic Control Method for Grid-Connected Inverters in a Weak Grid," *IEEE Transactions on Power Electronics*, vol. 32, no. 1, pp. 274–283, 2017.
- [46] C. Blanco, D. Reigosa, J. C. Vasquez, J. M. Guerrero, and F. Briz, "Virtual Admittance Loop for Voltage Harmonic Compensation in Microgrids," *IEEE Transactions on Industry Applications*, vol. 52, no. 4, pp. 3348–3356, 2016.
- [47] A. Elrayyah, F. Cingoz, and Y. Sozer, "Construction of Nonlinear Droop Relations to Optimize Islanded Microgrid Operation," *IEEE Transactions on Industry Applications*, vol. 51, no. 4, pp. 3404–3413, 2015.
- [48] T. Ackermann, *Wind power in power systems*. Chichester: Wiley, 2012.
- [49] T. Wildi, *Electrical machines, drives, and power systems*. Upper Saddle River: Prentice Hall. Pearson Education International, 2002.
- [50] H. J. Herbein, *Rotating machinery*. San Francisco, 1971.
- [51] Nicholas W. Miller, Juan J. Sanchez-Gasca, William W. Price, Robert W. Delmerico, "DYNAMIC MODELING OF GE 1.5 AND 3.6 MW WIND TURBINE-GENERATORS FOR STABILITY SIMULATIONS," *GE Power Systems Energy Consulting*, IEEE WTG Modeling Panel, Session July 2003
- [52] R. Pena, J.C. Clare, G.M. Asher, "Doubly fed induction generator using back-to-back PWM converters and its application to variable-speed wind-energy generation," *IEEE Proc.-Electr. Power Appl.*, Vol. 143, No. 3, May 1996
- [53] Vladislav Akhmatov, "Variable-Speed Wind Turbines with Doubly-Fed Induction Generators, Part I: Modelling in Dynamic Simulation Tools," *Wind Engineering* vol. 26, no. 2, 2002
- [54] M. Kuschke and K. Strunz, "Energy-Efficient Dynamic Drive Control for Wind Power Conversion With PMSG: Modeling and Application of Transfer Function Analysis," *IEEE Journal of Emerging and Selected Topics in Power Electronics*, vol. 2, no. 1, pp. 35–46, 2014.
- [55] Kundur, P. *Power System Stability and Control*. New York, NY: McGraw Hill, 1993
- [56] D. Hanselman, "Brushless permanent magnet motor design, 2nd ed.", The Writers' Collective, Mar. 2003.
- [57] P. Pillay, R. Krishnan, "Modeling, simulation, and analysis of permanent-magnet motor drives, Part II: The brushless DC motor drive", *IEEE Trans. on Ind. App.*, Vol. 25, No. 2, Mar./Apr. 1989
- [58] J. Manwell, *Wind energy explained*. New York: John Wiley, 2001.
- [59] S. Heier, "Grid Integration of Wind Energy Conversion Systems," *John Wiley & Sons Ltd*, 1998, ISBN 0-471-97143-X.
- [60] N. A. Orlando, M. Liserre, R. A. Mastromauro, and A. Dell'aquila, "A Survey of Control Issues in PMSG-Based Small Wind-Turbine Systems," *IEEE Transactions on Industrial Informatics*, vol. 9, no. 3, pp. 1211–1221, 2013.